Analysis & Design of Non-Linear Amplifiers for Efficient Microwave Transmitters

by

Michael Dean Roberg

B.S., Bucknell University, 2003

M.S., University of Pennsylvania, 2006

A thesis submitted to the

Faculty of the Graduate School of the

University of Colorado in partial fulfillment

of the requirements for the degree of

Doctor of Philosophy

Department of Electrical, Computer, and Energy Engineering

2012

This thesis entitled:

Analysis & Design of Non-Linear Amplifiers for Efficient Microwave Transmitters

written by Michael Dean Roberg

has been approved for the Department of Electrical, Computer, and Energy Engineering

_____

Zoya Popović

_____

Edward Kuester

Date _____

The final copy of this thesis has been examined by the signatories, and we

Find that both the content and the form meet acceptable presentation standards

Of scholarly work in the above mentioned discipline.

Roberg, Michael Dean (Ph.D., Electrical Engineering)

Analysis & Design of Non-Linear Amplifiers for Efficient Microwave Transmitters

Thesis directed by Professor Zoya Popović

This thesis addresses analysis and design of high efficiency microwave power amplifiers and rectifiers. The focus of this body of work is to optimize narrow band power amplifiers for maximization of Power-Added-Efficiency (PAE) and rectifiers for maximization of RF-DC power conversion efficiency. A power amplifier performs DC-RF conversion while a rectifier performs RF-DC conversion, therefore a strong analogy exists between the two.

Design with non-linear devices suffers from lack of accurate models characterizing large signal behavior, therefore measurement based techniques are often adopted in order to create high performance designs. The theoretical analysis presented in this thesis provides the microwave circuit designer intuition concerning performance expectations of design options rather than a recipe for creating a successful design. The complexity of non-linear device physics results in behavior which is often limited to qualitative description, complicating accurate model development.

The presented theoretical analysis is applied to load-pull based design of S-Band and X-Band power amplifiers and S-Band power rectifiers. The measured circuits exhibit high efficiency consistent with the analysis. An implementation of a high efficiency pulsed S-band AM radar transmitter is presented along with measured results. An extension of the presented analysis is investigated in the form of a harmonic injection amplifier, which conceptually allows realization of a high power, high efficiency broadband amplifier.

In summary, this thesis details 1) the load-pull measurement based design technique applied to microwave power amplifiers and rectifiers, 2) a theoretical analysis technique characterizing the performance limitations of harmonically terminated power amplifiers which may be applied to power rectifiers as well, 3) the design and measurement of several successful high efficiency power amplifiers and rectifiers and 4) interesting implementations of the presented theory in a system context.

Dedication

I dedicate this thesis to my family which includes my parents Craig & Deb Roberg, my sister Becky Mashburn, my brother-in-law Justin Mashburn and my two pugs Alice & Stella. Thank you all for the support and for keeping my perspective on life grounded!

Personal

Acknowledgments

First and foremost I would like to thank former research group member John Hoversten for teaching me the foundations on which the research I performed was based. His hard work and attention to detail are things which I attempted to carry forward in the lab since his graduation. I would also like to thank Jon Chisum, Erez Falkenstein and Rob Scheeler for keeping the mood in the lab light and not letting things get too serious. It's always important to have a little bit of fun at work in my opinion. I would like to thank Asmita Dani and Jennifer Imperial for helping me solidify my knowledge of many concepts relative to amplifiers through helping them with their projects. To the other group members I have had the pleasure of working with, including Frank Trang, Scott Schafer, Andrew Zai, Ignacio Ramos, Xavi Palomer, Ceśar Sańchez-Peŕez, David Sardin, Evan Cullens, Nicola Kinzie, Brad Lindseth, Dan Kuester, Leonardo Ranzani, Negar Ehsan, Mike Elsbury, Milos Janković and Luke Sankey, I thank you for the many helpful discussions and good times in the lab.

Professional

Acknowledgments

CONTENTS

List of Tables

L IST OF F IGURES

CHAPTER 1

INTRODUCTION

CONTENTS

The requirements of modern radar and communication systems are driving the use of advanced waveforms. Conceptually, the use of these advanced waveforms allows efficient use of available spectrum while meeting system performance goals. However, advanced waveforms are both phase and amplitude modulated resulting in a varying envelope signal, which stresses the capability of the transmitting portion of the microwave system, particularly in terms of efficiency. The impacts and consequently the research problems are addressed in Section 1.2. However, prior to the discussion of the research problems, some background information in basic concepts is required, which is presented in Section 1.1. Section 1.2 also provides the reader with an overview of the chapters contained within this thesis and the specific research problems they address.

As an example of the importance of efficiency, consider current cellular base stations. As of 2011, a typical third generation (3G) base station consumes between 500-1000 W of power to generate 60-120 W of RF output power, resulting in an average total efficiency of 12 % [3]. A 3G base station consumes between 4.9-9.0 MWh yearly, and in China there are approximately 700,000 base stations. Therefore, the cost in powering the base station portion of a cellular network is very high and any improvement in efficiency can have a dramatic impact on the operating cost of a cellular network. Additionally, improving amplifier efficiency will not only reduce the power consumed by the PA, but will also reduce the energy consumption of the associated power and cooling systems.

The main theme of the work presented in this thesis is improving efficiency of PAs for microwave communication and radar transmitters. In order to provide an understanding of the role of the impedance presented to the active device at the harmonic frequencies, a generalized Fourier analysis was developed and applied not only to amplifiers with harmonic terminations at the output, but also to microwave rectifiers and power amplifiers with external injection of waves at harmonic frequencies. In addition, the challenge of simultaneous efficiency and linearity in a transmitter is addressed for radar waveforms, and a possible approach to solving the even more challenging problem of simultaneous efficiency, linearity and bandwidth is proposed.

1.1 Basic Efficiency Concepts

Section 1.1 is not intended to be a power amplifier tutorial; it is intended to address the very basics of power added efficiency and impacts of input power back-off. For an introduction to microwave power amplifiers, a number of excellent books are recommended, e.g. [4, 5, 6, 7]. Fig. 1.1 shows the basic block diagram of a microwave transmitter. A baseband digital signal is converted to an analog signal using a Digital to Analog Converter (DAC), which is then upconverted to the fundamental frequency f_0 using a mixer. The output of the mixer is passed through a bandpass filter to remove unwanted mixing artifacts and then amplified by the driver amplifier and Power Amplifier (PA) prior to transmission. In general, the number of mixing

stages, filters, and amplifiers varies but the basic block diagram allows simplified explanation of the concepts contained herein.

The prime focus of this thesis is the PA stage which typically dominates the power-added-efficiency (PAE) of the transmitter, where the PAE is defined as

$$\eta_{PAE} = \frac{P_{out} - P_{in}}{P_{DC}} \tag{1.1}$$

where P_{out} is the average microwave output power, P_{in} is the average microwave input power, and P_{DC} is the consumed DC power. For continuous-wave (CW) signals, P_{out} and P_{in} are simply the average output and input powers at the fundamental transmission frequency. Another efficiency metric often encountered is drain efficiency, which is defined by

$$\eta_D = \frac{P_{out}}{P_{DC}} \tag{1.2}$$

where it is evident that the drain efficiency and power added efficiency are related by

$$PAE = \left(1 - \frac{1}{G}\right)\eta_D \tag{1.3}$$

where G is the gain of the stage. The PAE may be defined between any two points within the microwave transmitter chain, but for the purposes of investigating the driving factor in the PAE, the input will be considered as the input to the driver amplifier and the output as the output of the power amplifier as shown in Fig. 1.1.
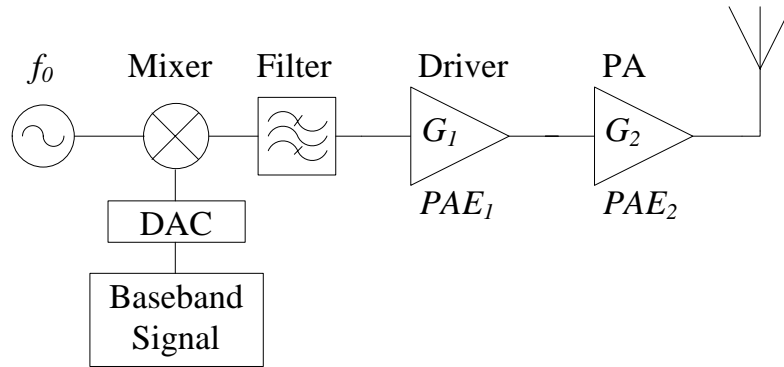
Figure 1.1: Generic microwave transmitter block diagram.
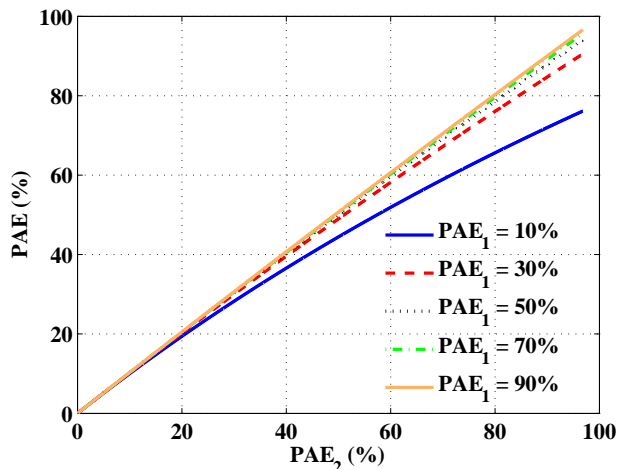
Figure 1.2: Total PAE as a function of output stage PAE (PAE_2) assuming $G_1 = 20$ dB and $G_2 = 15$ dB.

Assume that the driver amplifier has a PAE and gain given by PAE_1 and G_1 while the power amplifier has a gain and PAE given by PAE_2 and G_2. It is straightforward to derive the total PAE, which is given by

$$\eta_{PAE} = \frac{1 - \frac{1}{G_1 G_2}}{\frac{1 - \frac{1}{G_2}}{PAE_2} + \frac{1 - \frac{1}{G_1}}{G_2 PAE_1}} \tag{1.4}$$

Equation (1.4) allows investigation of the impact of the driver amplifier and power amplifier parameters on the cascaded PAE. For example, consider the case where $G_1 = 20$ dB and $G_2 = 15$ dB. Fig. 1.2 shows the impact of the driver and power amplifier PAE on the total PAE. It is evident that the driver PAE starts to impact the total PAE when it is significantly lower than the power amplifier PAE. For reasonable driver PAE, the total PAE is approximately that of the power amplifier. Of course in some scenarios the driver PAE has an impact on the total PAE, but for most microwave transmitters the output power amplifier PAE dominates the total PAE.

The other basic concept to understand is how the efficiency is impacted by input power back-off. A very basic example will serve to demonstrate the problem. Consider a class-A power amplifier, which is the most basic of all power amplifiers where both the voltage and current can vary without distortion. When the input power to the class-A amplifier is such that the voltage and current could swing no more without distortion, the amplifier exhibits a theoretical efficiency

4
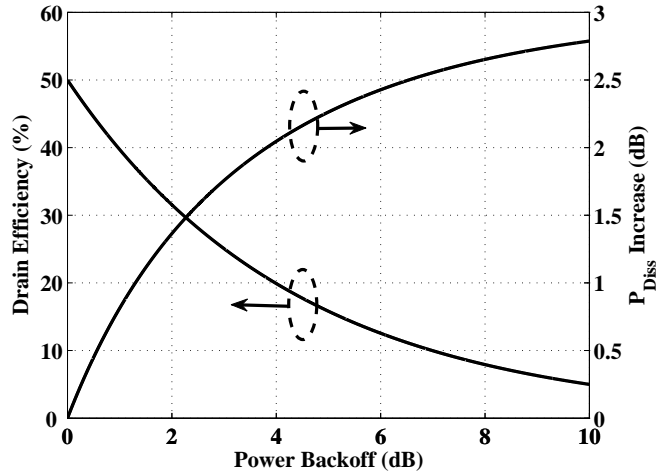
Figure 1.3: Class-A amplifier performance versus input power back-off.

drain efficiency of 50 %. However, if the input power to the amplifier is reduced (power back-off), the efficiency is reduced. Fig. 1.3 depicts the reduction of drain efficiency as a function of input power back-off. If the input power is reduced by half, the efficiency is halved corresponding in a 1.76 dB increase in power dissipation along with the 3 dB reduction in output power. Although more exotic power amplifiers will deviate from the performance shown in Fig. 1.3, the general trend is the same: the efficiency is reduced as the input drive is reduced from the optimally efficient operating point.

1.2 Research Problems & Chapter Overview

The work presented in each chapter is summarized below, with Chapter 7 concluding the completed work and presenting future work. Rather than giving an overview of background in this chapter, summaries of previous work and the context of the work in this thesis are given at the beginning of each chapter.

1.2.1 Chapter 2 Overview

Chapter 2 provides an overview of the measurement based PA design technique known as load-pull. Theoretical derivations relevant to proper input and output network design for performing

load-pull are presented. A method for characterizing and calibrating a single-slug load pull tuner is presented along with measured results. Many of the load-pull and tuner calibration concepts were applied to the work in [8]. A load-pull based design of a hybrid S-band power amplifier using a GaN transistor is presented with measured performance [9]. MMIC circuit designs for performing load-pull on-wafer are also presented with measured results. The specific research problems addressed are as follows:

- Proper design of input and output load pull fixtures

- Characterization and calibration of single-slug load pull tuners

- Application of load-pull measurements to a high efficiency hybrid PA design

- On-wafer load-pull design considerations

1.2.2 CHAPTER 3 OVERVIEW

Chapter 3 presents a harmonically terminated power amplifier analysis developed by the author which was published in [10]. The analysis investigates the performance of power amplifiers subject to a finite set of arbitrary harmonic terminations. The main goals of the analysis include investigating the

(1) Fidelity of harmonic terminations required to achieve a specified efficiency.

(2) Impact of resistive, reactive and complex harmonic terminations on maximum PA efficiency and corresponding fundamental output power and load resistance.

(3) Impact of fundamental frequency reactance on maximum PA efficiency and corresponding fundamental output power and load resistance.

Extensions of the analysis to devices with a linear parasitic output network are presented along with examples. A qualitative validation of the theory is presented based on measurements of a GaN device.

1.2.3 Chapter 4 Overview

Chapter 4 discusses the design and analysis of a supply modulated radar transmitter, of which portions are contained in [11, 12]. The motivation for using a supply modulated radar transmitter in terms of spectral confinement is presented. The impact on radar system performance in terms of several relevant metrics is analyzed. These include transmitted spectrum, range resolution, time side-lobe level and signal-to-noise ratio. A test-bed demonstrating the performance of an implemented supply modulated radar transmitter is presented along with measured efficiency and occupied spectrum. Specific attention is paid to linearity of the transmitter, which is necessary for achieving the desired amplitude and phase modulated radar signal at the output of the transmitter.

1.2.4 Chapter 5 Overview

Chapter 5 investigates harmonically terminated power rectifiers based on the prior analysis done in harmonically terminated power amplifiers. Analysis of different classes of power rectifiers is presented, including Class-C, Class-F and Class-F^{-1}. The analysis of each class focuses on

- Derivation of the ideal current and voltage waveforms based up an ideal rectifying element

- Relationships between fundamental frequency and DC load resistance

- Impact of on-resistance and threshold voltage parasitics

A measurement based design of a class-C rectifier using a Schottky diode as the rectifying element is presented along with measured output power and efficiency results [13].

1.2.5 Chapter 6 Overview

Chapter 6 presents the concept of the harmonic injection amplifier, which offers the possibility of a broadband high efficiency power amplifier. This amplifier shapes the drain waveforms through injection of harmonic power into the device output, which can result in efficiency improvement if done appropriately. Specifically, the cases of second harmonic only and third harmonic only

injection are analyzed, of which some of the second harmonic only theory is contained in [14]. The analysis provides

- Derivation of the ideal current and voltage waveforms

- Total efficiency as a function of how efficiently the harmonic power can be injected (e.g. injector efficiency)

- Expression of the injected power and impedance for optimal efficiency as a function of injector efficiency

In order to allow injection of harmonic power into the device output a special three-port network is required. The requirements of this network are analyzed fully and a methodology for achieving a broadband injection network is conceptualized.

CHAPTER 2

LOAD PULL BASED POWER

AMPLIFIER DESIGN

CONTENTS

2.1 Introduction

Microwave transistors often lack a non-linear model suitable for efficient PA design, or an existing non-linear model fails to accurately reproduce measured performance in high efficiency operation points near the I-V axes. This usually means that several design iterations are required in order to realize an efficient PA. Alternatively, a measurement-based design technique involving source pull and load pull may be adopted [6].

Traditional passive source pull and load pull make use of fundamental-frequency mechanical tuners to vary drain (output) and gate (input) impedance for a common source device [15]. Source pull refers to characterizing transistor performance as function of the impedance presented to the input while load pull refers to characterizing transistor performance as a function of the impedance presented to the output. However, for the remainder of this chapter the term load pull will be assumed to refer to both source pull and load pull.

Using traditional passive load pull, transistor performance is measured over a constellation of fundamental frequency impedances while the impedances at the harmonics of the fundamental are allowed to vary arbitrarily. Passive harmonic load pull incorporates additional mechanical slugs in order to control both the fundamental-frequency and harmonic impedances [16]. Active load pull, introduced in [17], uses signal injection to electrically synthesize load impedances. Elaborate active and passive harmonic load pull techniques [18] are available but are less common and significantly more expensive. Recently, a large signal network analyzer was used to perform real-time active harmonic load pull in development of a $2\,\mathrm{GHz}$ PA having 75% PAE [19].

In Section 2.2, load pull measurement theory using passive tuners is presented with Section 2.3 discussing the measurement network design. Section 2.4 discusses a method for characterizing and calibrating single-slug passive tuners. Section 2.5 discusses the implementation of fundamental frequency (f_0) load pull with Class-F^{-1} harmonic terminations (up to third harmonic) on a TriQuint $12\,\mathrm{W}$ $0.25\,\mu\mathrm{m}$ GaN device at $2.14\,\mathrm{GHz}$. Section 2.5.1 presents the prototype PA designed based upon the measurements presented in Section 2.5 and includes measured performance. The PA exhibits $7\,\mathrm{W}$ output power and 84.6% PAE with a drain voltage of $31\,\mathrm{V}$ at 2.14 GHz. A
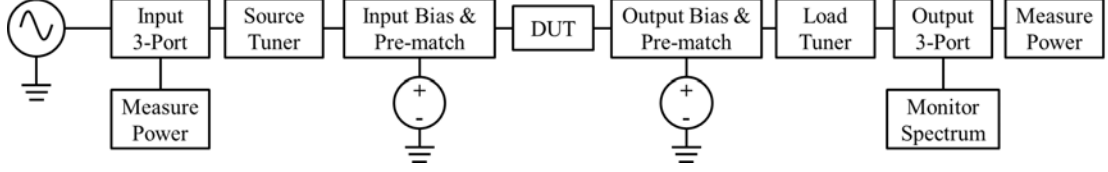
Figure 2.1: Basic fundamental frequency load pull block diagram.

0.69 dB improvement in output power and 84.9% PAE is obtained at 2.15 GHz. Full wave EM modeling of the die-to-matching-network transition is used in order to accurately determine the $2f_0$ and $3f_0$ impedances at the virtual drain. Input and output pre-match circuits are designed and class-F^{-1} harmonic traps are verified. Fundamental frequency source and load pull with class-F^{-1} harmonic terminations are performed to determine optimal fundamental frequency source Z_S and load Z_L impedance. Finally, the prototype PA is designed with integrated bias lines. The straightforward design procedure results in a first-pass success, yielding an efficient PA using an un-modeled device. It is noted that Class-F and class-E PAs having greater than 80% PAE and over 5 W output power near 2 GHz have been reported [20]-[21]. However, this chapter details a class-F^{-1} design which achieves over 80% PAE, with the results being published in [9]. Section 2.6 discusses the design of X-Band load pull circuits using the TriQuint $0.25\,\mu$m GaN MMIC process. The calibration technique is discussed and measured load pull results are presented. Future work for developing a high efficiency PA design based upon the collected measurements is discussed.

2.2 Load Pull Measurement Theory

Fig. 2.1 shows a basic block diagram of a fundamental frequency load pull measurement setup. The Device Under Test (DUT) is connected in some fashion to an input pre-matching and output pre-matching circuit which provide DC bias to the DUT as well as pre-matching the impedance to reasonable values. Proper design of the pre-matching circuits is vital to taking good load pull measurements. The designs of the pre-matching circuits should take into account the following:

- The pre-matching circuit should have low insertion loss (or more appropriately, low dissipative loss [22]). Any power dissipated in the pre-matching circuits will reduce the tuning

11

range which the tuners can achieve at the DUT reference planes.

- The pre-matching circuits should pre-match the input and output impedances such that minimal tuning of the source and load tuners is required. This improves measurement accuracy due to the limited range over which the tuners are required to tune. For example, if it is expected that the optimal output impedance should be in the neighborhood of $10\,\Omega$, then the output pre-match should be designed such that $10\,\Omega$ is presented to the DUT with the load tuner set to the $50\,\Omega$ position.

- The pre-matching circuits should fix the harmonic terminations presented to the DUT, particularly at the output. Device performance is strongly impacted by output harmonic terminations as discussed in Chapter 3. It would be incorrect to make conclusions based on fundamental frequency load pull where the harmonic terminations varied as a function of fundamental frequency impedance.

- The pre-matching circuits should incorporate a well designed bias-tee in order to stabilize the device (e.g. prevent low frequency oscillations) and minimize insertion loss.

- The pre-matching circuits should be measurable at the fundamental and harmonic frequencies. This is important for impedance verification of the pre-matches. It is also necessary for power measurement calibration in the load pull setup. It is necessary to have the full 2-port scattering parameters of the pre-matching fixtures in order to properly calibrate the load pull setup.

- The characterization of the output pre-matching circuit should incorporate the parasitics associated with the attachment to the DUT as well as the internal parasitics of the DUT which are relevant to theoretical amplifier classes. Most amplifier classes are defined at the virtual drain of the DUT. For example, the characterization should take into account the parasitic output capacitance of the DUT as well as the bond wire parasitics in the case of a discrete device. For a packaged device, the additional packaging parasitics should be characterized. This is vital to theoretical interpretation of load pull measurements and

making valid conclusions based upon the measurements.

The source tuner and load tuner in Fig. 2.1 allow tuning of the input impedance and output impedance presented to the DUT. These tuners can be thought of as individual scattering parameters boxes which are a function of some controllable physical parameters of the tuners themselves. For performing load pull, it is important to be able to control the impedances presented to the DUT, and therefore it is necessary to know how to control the tuners to synthesize the desired impedances. Section 2.4 discusses this in more detail.

The input 3-port network allows an input signal to drive the DUT and also be coupled to a power measurement device in order to measure the available input power to the DUT. The available power is measured rather than the delivered power because, in general, the DUT serves as an unknown termination which does not allow calculation of delivered power. The output 3-port network allows the delivered output power from the DUT to be measured as well as the spectral content. The spectral content is typically monitored in order to ensure the DUT is not oscillating. For high power devices, it is important that the network sufficiently attenuate the signal output from the DUT in order to measure the power with standard laboratory equipment, which typically limits input power to 20 dBm. In the case of the output network, the delivered output power is calibrated rather than the available output power because, in general, the DUT again serves as an unknown termination which does not allow the available output power to be determined. Section 2.3 discusses the specific requirements of the input 3-port and output 3-port networks in more detail.

2.3   Load Pull Measurement Network Design

As discussed in Section 2.2, appropriate design of the input 3-port and output 3-port networks depicted in Fig. 2.1 is vital to taking good load pull measurements. To understand the requirements placed upon the networks, a scattering parameter analysis may be performed. The input 3-port network shown in Fig. 2.2 is analyzed first. For the purposes of this analysis, it is assumed that the 3-port network incorporates the source tuner, input bias & pre-match, and any additional

parasitics that are desired to be absorbed in the network. The reflection coefficients at each network port in Fig. 2.2 are expressed as

$$\Gamma_S = \frac{Z_S - Z_0}{Z_S + Z_0} \tag{2.1}$$

$$\Gamma_L = \frac{Z_L - Z_0}{Z_L + Z_0} \tag{2.2}$$

$$\Gamma_P = \frac{Z_P - Z_0}{Z_P + Z_0} \tag{2.3}$$

where Z_0 is the system impedance, Z_S is the source impedance (e.g. the RF signal generator impedance), Z_L is the terminating impedance on the DUT port and Z_P is the terminating impedance on the power measurement port. The relationship between the forward and reflected waves at each port can be written given the scattering parameters as

$$\begin{pmatrix} b_1 \\ b_2 \\ b_3 \end{pmatrix} = \begin{pmatrix} S_{11}a_1 + S_{12}a_2 + S_{13}a_3 \\ S_{21}a_1 + S_{22}a_2 + S_{23}a_3 \\ S_{31}a_1 + S_{32}a_2 + S_{33}a_3 \end{pmatrix} \tag{2.4}$$

When only port-1 is driven, the input waves at the remaining ports are the product of the outgoing wave from the port and the reflection coefficient at that port, which allows (2.4) to be expressed as

$$\begin{pmatrix} b_1 \\ b_2 \\ b_3 \end{pmatrix} = \begin{pmatrix} S_{11}a_1 + S_{12}\Gamma_L b_2 + S_{13}\Gamma_P b_3 \\ S_{21}a_1 + S_{22}\Gamma_L b_2 + S_{23}\Gamma_P b_3 \\ S_{31}a_1 + S_{32}\Gamma_L b_2 + S_{33}\Gamma_P b_3 \end{pmatrix} \tag{2.5}$$
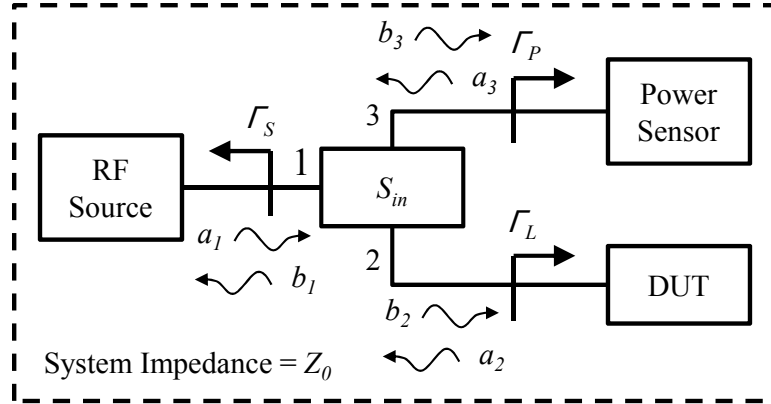
Figure 2.2: Load pull 3-port input network analysis block diagram.

The goal is to solve for b_1, the reflected wave at port-1, in terms of a_1, the incident wave, and the remaining known quantities. Therefore, it is first necessary to solve for the reflected waves at port-2 and port-3 in terms of the incident wave at port-1 and the remaining known quantities. The second and third row of (2.5) may be written as

$$\begin{pmatrix} 1 - S_{22}\Gamma_L & -S_{23}\Gamma_P \\ -S_{32}\Gamma_L & 1 - S_{33}\Gamma_P \end{pmatrix} \begin{pmatrix} b_2 \\ b_3 \end{pmatrix} = \begin{pmatrix} S_{21} \\ S_{31} \end{pmatrix} a_1 \tag{2.6}$$

Solving (2.6) results in

$$\begin{pmatrix} b_2 \\ b_3 \end{pmatrix} = \frac{a_1}{1 - \Gamma_L S_{22} - \Gamma_P S_{33} + \Gamma_L \Gamma_P (S_{22}S_{33} - S_{23}S_{32})} \begin{pmatrix} S_{21} - \Gamma_P S_{21}S_{33} + \Gamma_P S_{23}S_{31} \\ S_{31} + \Gamma_L S_{21}S_{32} - \Gamma_L S_{22}S_{31} \end{pmatrix}$$
$$\tag{2.7}$$

Given that the reflected waves at port-2 and port-3 are solved for, the reflected wave at port-1 may be solved for by substitution of (2.7) into the first row of (2.5), resulting in

$$b_1 = S_{11}a_1 + \frac{a_1 \left[S_{12}\Gamma_L (S_{21} - \Gamma_P S_{21}S_{33} + \Gamma_P S_{23}S_{31}) + S_{13}\Gamma_P (S_{31} + \Gamma_L S_{21}S_{32} - \Gamma_L S_{22}S_{31}) \right]}{1 - \Gamma_L S_{22} - \Gamma_P S_{33} + \Gamma_L \Gamma_P (S_{22}S_{33} - S_{23}S_{32})}$$
$$\tag{2.8}$$

The input reflection coefficient $\Gamma_{in,1}$ at port-1 is then given by

$$\Gamma_{in,1} = \frac{b_1}{a_1} = S_{11} + \frac{S_{12}\Gamma_L (S_{21} - \Gamma_P S_{21}S_{33} + \Gamma_P S_{23}S_{31}) + S_{13}\Gamma_P (S_{31} + \Gamma_L S_{21}S_{32} - \Gamma_L S_{22}S_{31})}{1 - \Gamma_L S_{22} - \Gamma_P S_{33} + \Gamma_L \Gamma_P (S_{22}S_{33} - S_{23}S_{32})}$$
$$\tag{2.9}$$

Similar expressions for the input reflection coefficients at the other ports can be derived when only the respective port is being driven, and are given by

$$\Gamma_{in,2} = \frac{b_2}{a_2} = S_{22} + \frac{S_{21}\Gamma_S (S_{12} - \Gamma_P S_{12}S_{33} + \Gamma_P S_{13}S_{32}) + S_{23}\Gamma_P (S_{32} + \Gamma_S S_{12}S_{31} - \Gamma_S S_{11}S_{32})}{1 - \Gamma_S S_{11} - \Gamma_P S_{33} + \Gamma_S \Gamma_P (S_{11}S_{33} - S_{13}S_{31})}$$
$$\tag{2.10}$$

$$\Gamma_{in,3} = \frac{b_3}{a_3} = S_{33} + \frac{S_{32}\Gamma_L (S_{23} - \Gamma_S S_{23}S_{11} + \Gamma_S S_{21}S_{13}) + S_{31}\Gamma_S (S_{13} + \Gamma_L S_{23}S_{12} - \Gamma_L S_{22}S_{13})}{1 - \Gamma_L S_{22} - \Gamma_S S_{11} + \Gamma_L \Gamma_S (S_{22}S_{11} - S_{21}S_{12})}$$
$$\tag{2.11}$$

Equations (2.9)-(2.11) are in general complicated, but many simplifications can be made starting from these general cases. However, it is important to have the general expressions if an error analysis of calibration factors is to be performed, for example. Typically a power

sensor matched to the system impedance Z_0 is used to measure power on port-3, therefore $\Gamma_P \approx 0$. Additionally, the RF source is typically matched to the network, therefore $\Gamma_S \approx 0$. These assumptions simplify (2.9)-(2.11) to

$$\Gamma_{in,1} = S_{11} + \frac{S_{12}\Gamma_L S_{21}}{1 - \Gamma_L S_{22}} \tag{2.12}$$

$$\Gamma_{in,2} = S_{22} \tag{2.13}$$

$$\Gamma_{in,3} = S_{33} + \frac{S_{32}\Gamma_L S_{23}}{1 - \Gamma_L S_{22}} \tag{2.14}$$

As discussed in Section 2.2, it is desirable to measure the available input power to the DUT. A straightforward manner to do this is to measure the power delivered to a power measurement device on port-3 and use this measurement along with the 3-port network parameters to determine available power to the DUT at port-2. Following [23], the average power delivered to the load at port-3 and available power from port-1 are given by

$$P_{D,3} = \frac{|b_3|^2}{2Z_0}(1 - |\Gamma_P|^2) \tag{2.15}$$

$$P_{A,1} = \frac{\left| \frac{2a_1(1 - \Gamma_S \Gamma_{in,1})}{1 - \Gamma_S} \right|^2}{8Z_0} \frac{|1 - \Gamma_S|^2}{1 - |\Gamma_S|^2} \tag{2.16}$$

The transducer gain from port-1 to port-3 is then given by

$$G_{T,31} = \frac{P_{D,3}}{P_{A,1}} = \frac{\frac{|b_3|^2}{2Z_0}(1 - |\Gamma_P|^2)}{\frac{\left| \frac{2a_1(1 - \Gamma_S \Gamma_{in,1})}{1 - \Gamma_S} \right|^2}{8Z_0} \frac{|1 - \Gamma_S|^2}{1 - |\Gamma_S|^2}} \tag{2.17}$$

which simplifies to

$$G_{T,31} = \frac{P_{D,3}}{P_{A,1}} = \frac{|b_3|^2}{|a_1|^2} \frac{(1 - |\Gamma_P|^2)(1 - |\Gamma_S|^2)}{|(1 - \Gamma_S \Gamma_{in,1})|^2} \tag{2.18}$$

Substituting in the solution for b_3 from (2.7) results in

$$G_{T,31} = \frac{P_{D,3}}{P_{A,1}} = \left| \frac{S_{31} + \Gamma_L S_{21} S_{32} - \Gamma_L S_{22} S_{31}}{1 - \Gamma_L S_{22} - \Gamma_P S_{33} + \Gamma_L \Gamma_P(S_{22}S_{33} - S_{23}S_{32})} \right|^2 \frac{(1 - |\Gamma_P|^2)(1 - |\Gamma_S|^2)}{|(1 - \Gamma_S \Gamma_{in,1})|^2}$$
$$\tag{2.19}$$

At this point it is necessary to make design choices concerning the input network to allow practical measurements to be taken. The issue with the generality presented in (2.19) is that the transducer gain from port-1 to port-3 is a function of Γ_L which is an unknown value due to the

DUT. At this point it is assumed that an isolator is placed between the 3-port input network and the source tuner at port-2. This effectively results in $\Gamma_L = 0$, reducing (2.19) to

$$G_{T,31} = \frac{P_{D,3}}{P_{A,1}} = |S_{31}|^2 \frac{(1 - |\Gamma_P|^2)(1 - |\Gamma_S|^2)}{|1 - \Gamma_P S_{33}|^2 |(1 - \Gamma_S \Gamma_{in,1})|^2} \tag{2.20}$$

For a practical application, port-3 is typically well matched given that it is terminated with a power sensor having a high return loss. Additionally, the source is typically well matched. Given these assumptions, the transducer gain simplifies to

$$G_{T,31} = |S_{31}|^2 \tag{2.21}$$

which is most often the expression used in practice for this application. Using this expression, the available input power at port-1 is easily calculated from the measured power at port-3 by the equation

$$P_{A,1} = \frac{P_{D,3}}{G_{T,31}} = \frac{P_{D,3}}{|S_{31}|^2} \tag{2.22}$$

Basically, what has been concluded from the theoretical analysis of the input 3-port relevant to load pull measurements is the following:

- An isolator should be placed on port-2 of the input network prior to the source tuner in order to eliminate variation in the transducer gain from port-1 to port-3 as a function of load impedance.

- The input network should be well matched to the RF source and power measurement device, allowing the simplified form of the transducer gain given in (2.21) to be used.

An additional practical requirement is that typically only 20 dBm of input power can be delivered to the power measurement device. This is an absolute maximum limit, so a good rule to follow is try to optimize $G_{T,31}$ such that at the maximum available input power required for driving the DUT, only 0 dBm of input power is delivered to the power measurement device.

Now that measurement of the available input power at port-1 has been made possible, it is necessary to scale this measurement to determine the available input power to the DUT at port-2.

The scaling factor is a byproduct of deriving the available gain from port-1 to port-2, given by

$$G_{A,21} = \frac{P_{A,2}}{P_{A,1}} \tag{2.23}$$

Given that $P_{A,1}$ is known based upon the measurement at port-3, $P_{A,2}$ is directly related to $P_{D,3}$ by

$$P_{A,2} = G_{A,21} \frac{P_{D,3}}{|S_{31}|^2} \tag{2.24}$$

The assumptions made up to this point allow the available gain from port-1 to port-2 to be simply expressed as given in [23] as

$$G_{A,21} = \frac{|S_{21}|^2}{1 - |S_{22}|^2} \tag{2.25}$$

The load pull calibration factor Θ_{in} yielding the available input power to the DUT based on the measurement at port-3 is then given by

$$\Theta_{in} = \frac{|S_{21}|^2}{|S_{31}|^2 (1 - |S_{22}|^2)} \tag{2.26}$$

Using a similar procedure, the load pull calibration factor yielding the delivered output power from the DUT based upon the measurement at port-2 of the output network (assuming port-3 is connected to a well-matched spectrum analyzer) is given by

$$\Theta_{out} = \frac{1 - |S_{11}|^2}{|S_{21}|^2} \tag{2.27}$$

where the scattering parameters in (2.27) refer to those of the cascade of the network connected to the output of the DUT rather than the input. The main additional requirement for the output 3-port network is that it must have sufficient attenuation based upon the maximum output power of the DUT to prevent damage to both the spectrum analyzer and power measurement device.

2.4 TUNER CHARACTERIZATION & CALIBRATION

For the load-pull measurements performed within this thesis, FOCUS Microwaves single slug computer controlled mechanical tuners were used. Due to the desired measurement flexibility, custom load-pull software was developed in MATLAB®. However, given the choice was made
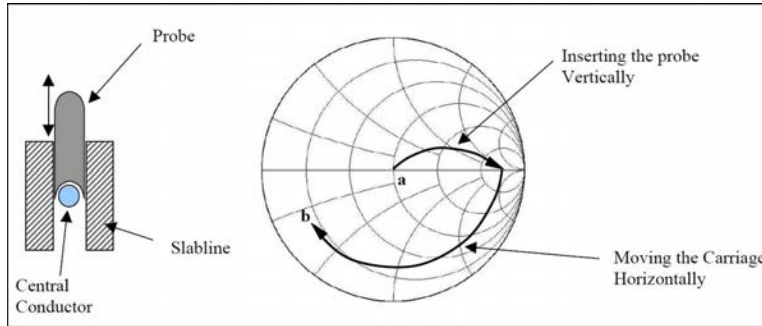
Figure 2.3: Mechanism by which single slug mechanical tuner synthesizes impedances. A metallic probe is inserted vertically towards the center conductor of a slab-line to increase the reflection coefficient magnitude, and moved horizontally along the slab-line to shift the reflection coefficient phase.

to develop custom software, it became necessary to calibrate the tuners in the absence of manufacturer provided calibration software. This section discusses the method developed for performing tuner calibration. The method is general, and certainly could be extended to other single slug type tuners.

Fig. 2.3 depicts the mechanism by which a single slug mechanical tuner is able to synthesize impedances [24]. A slug, denoted by the probe in Fig. 2.3, may be moved vertically in towards the central conductor of a slab-line as well as horizontally along the slab-line. With the probe at a fixed vertical distance from the central conductor, motion along the horizontal axis corresponds to a phase shift in the reflection coefficient shown as arc b in Fig. 2.3. At a fixed horizontal location, motion vertically towards the central conductor of the slab-line transforms the $50\,\Omega$ impedance to a highly reflective impedance shown as arc a. Therefore, characterization of this type of tuner simplifies to modeling the phase shift in the reflection coefficient as a function of the horizontal slug position x and the reflection coefficient phase and magnitude behavior as a function of the vertical slug position y.

At this point, a reasonable question to ask is, "Why not measure the scattering parameters at each (x,y) tuner position?" The answer to this question is simple: This would take an unreasonable amount of time. The tuners used for this research have approximately 7,000 unique x positions and 2,800 unique y positions, resulting in 19.6 million positions. Taking into account that the tuner is mechanical, assume it takes approximately $0.5\,\text{s}$ to move from one unique (x,y) to another.

Measuring all unique positions would then take about 113 days. Considering two tuners are required to perform source pull and load pull, the better part of an entire year would be spent just calibrating the tuners, which certainly is unreasonable.

In order to calibrate a tuner, a small set of data is collected such that the reflection coefficient phase as a function of x and the phase and magnitude as a function of y can be modeled. In general, this simply requires measuring the scattering parameter of interest on a network analyzer at constant x as a function of y as well as the same scattering parameter at a constant y as a function of x. Once the phase as a function of x and the magnitude and additional phase as a function of y have been modeled, the (x,y) pair required to synthesize a target reflection coefficient can be predicted.

As an example of the procedure, the calibration of a tuner at $4.9\,\mathrm{GHz}$ will be described, where it is assumed that port-2 of the tuner is connected to the DUT. In this case the scattering parameter of interest is S_{22}. First, S_{22} is measured as a function of y for several unique x positions as shown in Fig. 2.4. Note how the shape of each arc appears the same with the exception of the initial phase for each arc. If each arc is normalized by its initial phase and re-plotted, Fig. 2.5 results, validating the assumption that the arcs have relatively consistent shape as a function of y.

The measured and modeled initial phases as a function of x are plotted in Fig. 2.6(a). As expected, the initial phase exhibits linear behavior as a function of x and can be modeled as such. The error in the model of the initial phase is shown in Fig. 2.6(b), with the error being limited to $\pm 2.5°$. The magnitude and phase behavior as a function of y following normalization by the initial phase as a function of x can be modeled using polynomial fits. Through experimentation, it was found that fourth-order polynomial fits to the phase in degrees and magnitude in decibels yielded accurate results. The measured magnitude and phase behavior versus the fitted magnitude and phase behavior is shown in Fig. 2.7. The fit errors are shown in Fig. 2.8. The phase error is within $\pm 0.3°$ while the magnitude error is within $\pm 0.1\,\mathrm{dB}$.

Following the development of the mathematical model which describes the magnitude and
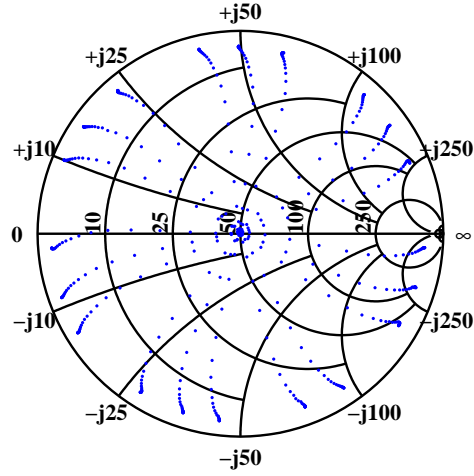
Figure 2.4: Initial points measured for tuner characterization at $4.9\,\mathrm{GHz}$. Points at the center of the Smith chart correspond to the slug being fully retracted from the slab-line while points at the edge correspond to full insertion of the slug.
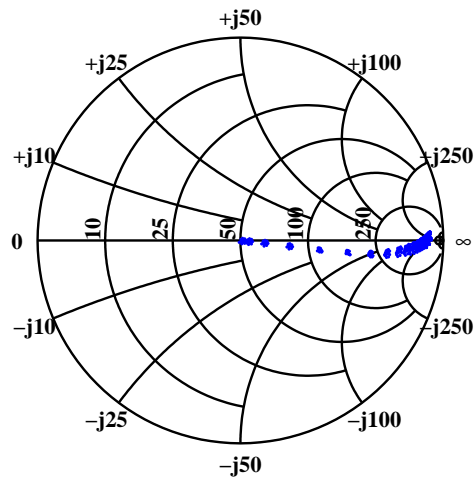
Figure 2.5: Initial measured points following phase normalization.

phase of the scattering parameter versus (x,y), a set of impedances can be defined for which to calibrate the tuner. This means that it is desired to use the tuner to synthesize this set of impedances, and the full 2-port scattering parameters of the tuner must be measured for proper calibration as discussed in the previous section. Once this set of points is defined, the magnitude and phase of the scattering parameter associated with each point is evaluated and the mathematical models are used in an inverse fashion to calculate the (x,y) to measure the tuner at. Fig. 2.9(a) shows the desired calibration points which cover the entirety of the Smith
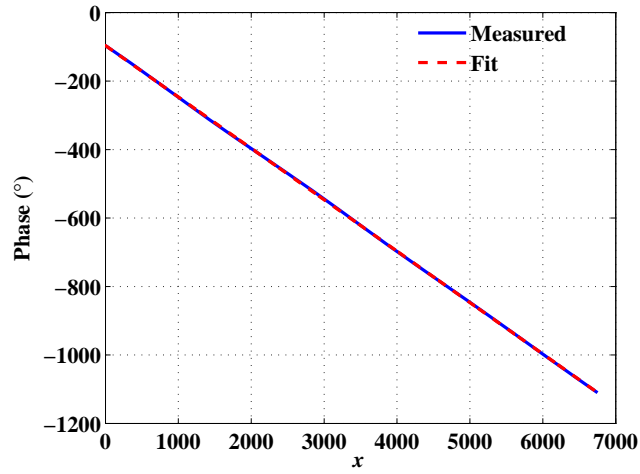
(a)
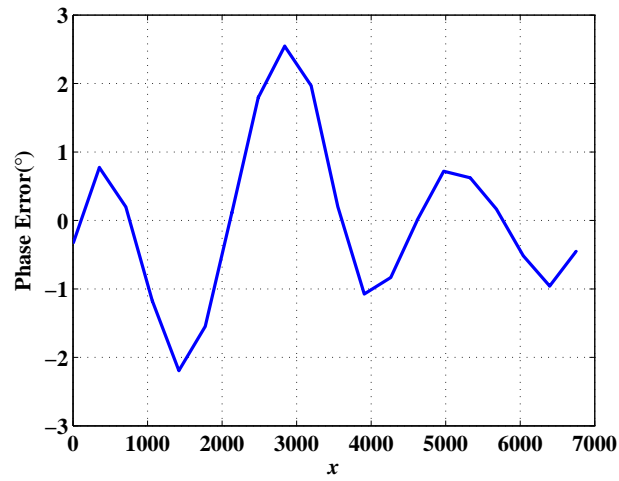
(b)

Figure 2.6: (a) Initial measured and modeled reflection coefficient phase as a function of horizontal slug position x. A first-order polynomial (line) was used to fit the measured data. (b) Error between the measured and modeled phase as a function of x.
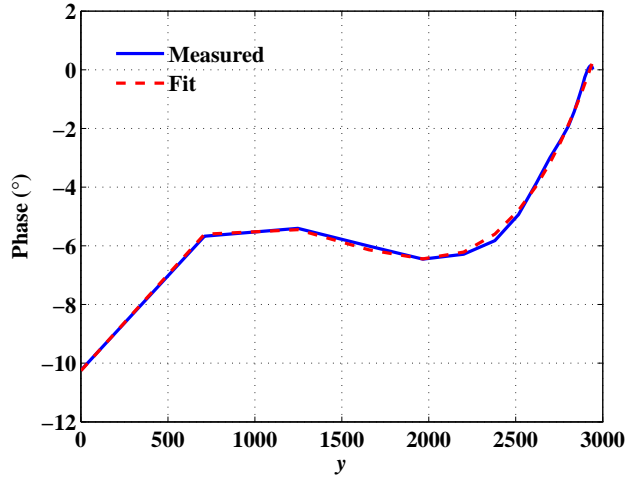
(a)
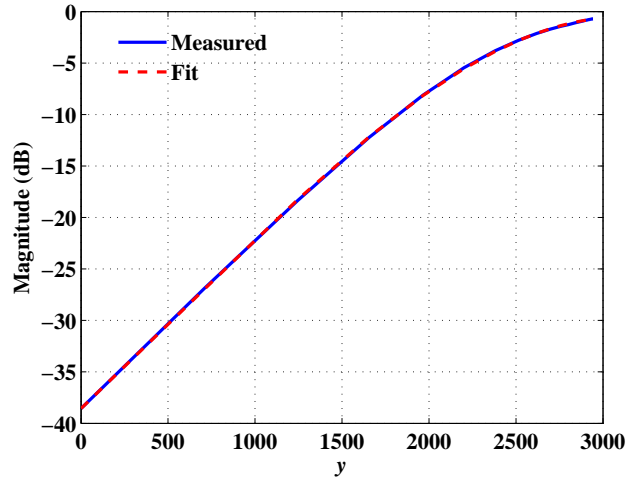
(b)

Figure 2.7: (a) Measured and fitted reflection coefficient phase as a function of vertical slug position y. A fourth-order polynomial was used to fit the measured data. (b) Measured and fitted magnitude behavior as a function of y. A fourth-order polynomial was used to fit the measured data. Note that $y = 0$ corresponds to the slug being fully retracted from the slab-line.
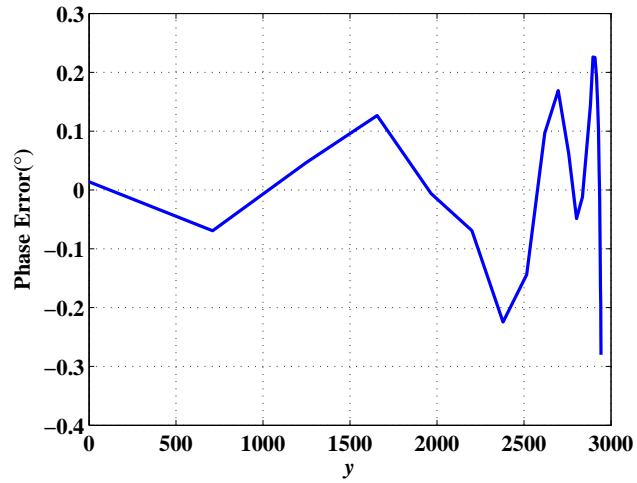
(a)
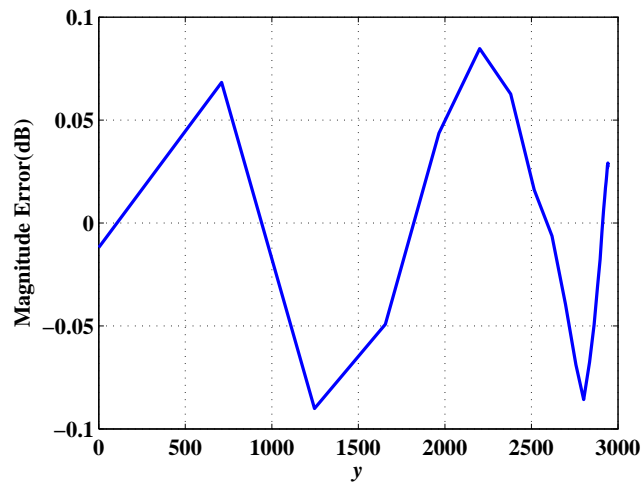
(b)

Figure 2.8: (a) Error between the measured and modeled reflection coefficient phase as a function of y. (b) Error between the measured and modeled reflection coefficient magnitude as a function of y.
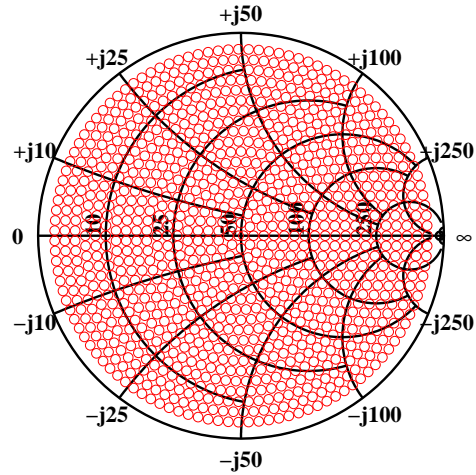
(a)
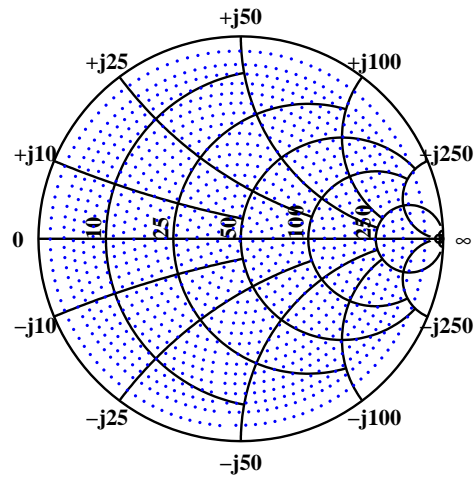
(b)

Figure 2.9: (a) Measured calibration points. (b) Predicted calibration points.

Chart, with Fig. 2.9(b) showing the measured calibrated points. It is evident that the method does a very good job at allowing the user to determine the appropriate (x,y) points to move the tuner to in order to synthesize an impedance and to calibrate the necessary power measurements for load pull.
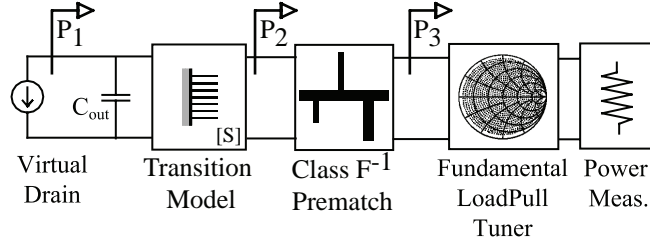
Figure 2.10: Load pull block diagram with defined reference planes for impedances. The transition model characterizes the S-parameters of the bare die to microstrip two-port network. For a two harmonic class-F^{-1} PA, open circuit and short circuit terminations are presented at plane P1 at $2f_0$ and $3f_0$, respectively.

2.5 Load Pull With Fixed Class-F^{-1} Harmonic Terminations

A specific application of the theory presented in Sections 2.2-2.4 is the fabrication of a high efficiency PA in the absence of a device model. The DUT was the TriQuint TGF2023-02 12 W bare die power GaN on SiC which operates up to 18 GHz [25]. A 0.68 pF output capacitance (C_{out}) was calculated using the linear model provided in the device data-sheet. The low C_{out} of the device coupled with significant gain at multiple harmonics of 2.14 GHz made this device an excellent candidate for a high efficiency PA design. A full wave EM model of the transition model indicated in Fig. 2.10 was developed in Ansoft HFSS™ to model the impedance transformation due to the fringing capacitance from the die to the ground plane, as well as the impact of the two bond wires connecting the die to the microstrip [8]. The two port S-parameters from plane P_1 to P_2 were calculated by cascading the S-parameters of the ideal C_{out} with the S-parameters of the transition model exported from HFSS™. Fig. 2.11 depicts the resultant S_{11} and S_{22} of the model from 2 to 7 GHz, showing that the C_{out} and transition model must be taken into account in order to present specific impedances at the virtual drain (plane P_1).

Using the impedance transformation model, a microstrip pre-match was designed on a 30-mil Rogers 4350B substrate. The load pre-match was designed to present the ideal class-F^{-1} $2f_0$ and $3f_0$ terminations at plane P_1 shown in Fig. 2.10. A source pre-match was designed without any specific input harmonic terminations. The S-parameters of the pre-match circuits were
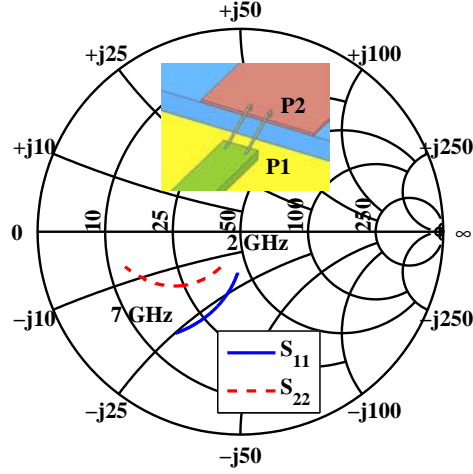
Figure 2.11: Simulated S_{11} and S_{22} versus frequency from $2\,\mathrm{GHz}$ to $7\,\mathrm{GHz}$. The transformation from plane P_1 to P_2 depicted in Fig. 2.10 is significant and must be accounted for in order to present harmonic terminations at the virtual drain. Additionally, the impact of the transformation increases with frequency.

measured using modular fixtures as mentioned in [26] to verify the harmonic terminations of the output pre-match and calibrate the load pull measurements. The DUT bias current was set to approximately $50\,\mathrm{mA}$ with a drain voltage of $30\,\mathrm{V}$. An initial approximation to the optimal Z_S of $3.1 + \mathrm{j}13.8\,\Omega$ was determined by performing a small signal fundamental frequency source pull for gain using a single slug tuner from FOCUS Microwaves. Z_S is referenced to the bonding plane on the input pre-match. It was found that the initial Z_S did not change for drain voltages between $25\,\mathrm{V}$ and $35\,\mathrm{V}$.

Large signal load pulls were performed to determine the optimal Z_L having maximum PAE, with at least $5\,\mathrm{W}$ output power. For each fundamental impedance point, a small input power sweep was performed to find the input drive level resulting in maximum PAE. An optimal Z_L of $164.5 - \mathrm{j}4.5\,\Omega$ was determined for a drain voltage of $30\,\mathrm{V}$ resulting in a PAE of 84.2%. A final large signal source pull was performed to refine the source impedance, resulting in an optimal Z_S of $1.5 + \mathrm{j}10.4\,\Omega$, resulting in a PAE of 85.7%.
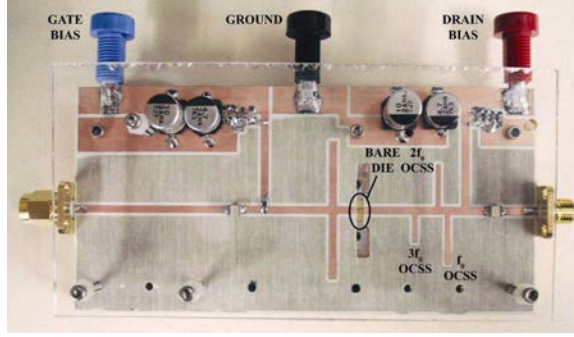
Figure 2.12: Photo of prototype amplifier. Note that no tuning of the amplifier was required to achieve the presented performance. Bias lines are implemented with $\lambda\backslash4$ transmission lines shorted to ground with resonant capacitors at 2.14 GHz. Several decades of capacitors (100 pF - 10 μF) are implemented in the design to suppress low frequency oscillations. A 10 Ω series resistor on the gate bias line is used to improve stability.

2.5.1 PROTOTYPE PA & MEASURED PERFORMANCE

The prototype PA is shown in Fig. 2.12. The circuit was fabricated using an LPKF S62 milling machine. The input matching section was realized with parallel Open Circuit Shunt Stubs (OCSS) to present the low Z_S while reducing insertion loss. The output matching section used $\lambda\backslash4$ OCSSs to present open and short circuits at $2f_0$ and $3f_0$, respectively. An additional OCSS is used to match the fundamental Z_L. American Technical Ceramics 100B and 600S capacitors were used for the DC block and bias line resonant capacitors, respectively. The microstrip ground plane is sweat soldered to a copper block, which serves as both a heat sink and continuous ground plane.

The PA exhibited over 80% PAE at $V_{DD} = 30$ V for a wide range of drain currents (50 mA - 200 mA). The best balance of PAE, output power, and gain performance was measured using a drain current of 170 mA at 30 V, therefore all subsequent measurements were taken at this corresponding gate bias point. Measurements of the prototype PA performance at 2.14 GHz versus input power are shown in Fig. 2.13 for the design point drain voltage of 30 V. The non-linearity of the amplifier is evident by investigation of the gain versus input power. The peak 2.14 GHz PAE is achieved under 3.6 dB gain compression. The harmonic powers relative to the carrier power at

Table 2.1: Harmonic power at PA output

Harmonic	$2f_0$	$3f_0$	$4f_0$	$5f_0$
Power (dBc)	-47.2	-52.3	-32.9	-49.5
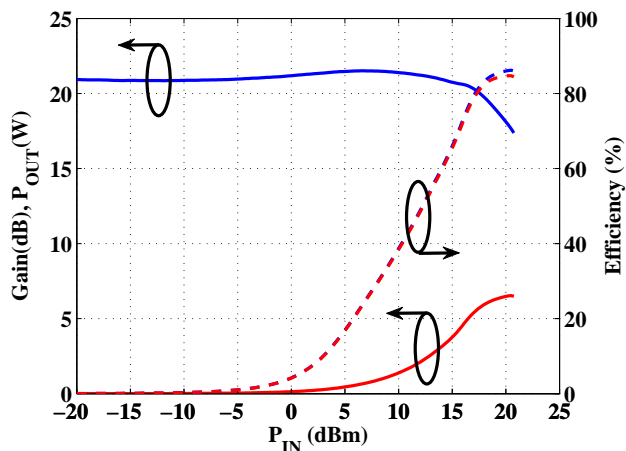
Figure 2.13: Measured PA performance at design point of $2.14\,\mathrm{GHz}$ versus input power, $\mathrm{V}_{DD} = 30\,\mathrm{V}$. The gain undergoes a slight expansion from $21.0\,\mathrm{dB}$ to $21.5\,\mathrm{dB}$ prior to entering compression. A peak PAE of over 84% is realized at the $3.6\,\mathrm{dB}$ gain compression point, corresponding to $20.2\,\mathrm{dBm}$ input power and $6.5\,\mathrm{W}$ output power at the design point.

the $2.14\,\mathrm{GHz}$, $30\,\mathrm{V}$ peak PAE operating point are listed in Table 2.1 up to $5\mathrm{f}_0$. The second and third harmonics are on the order of $-50\,\mathrm{dBc}$, while the fourth harmonic is significantly higher at $-32.9\,\mathrm{dBc}$. This is most likely due to the fourth harmonic termination not being explicitly controlled in the design. The significant harmonic power measured at $4\mathrm{f}_0$ and $5\mathrm{f}_0$ suggests that additional efficiency may be realized by terminating these harmonics in short and open circuits, respectively. However, it is possible that the additional insertion loss incurred by the matching topology would negate the benefits of terminating additional harmonics or degrade the efficiency achieved with only $2\mathrm{f}_0$ and $3\mathrm{f}_0$ terminations.

The prototype PA peak PAE performance at $2.14\,\mathrm{GHz}$ versus supply voltage is shown in Fig. 2.14. The PA exhibits over 80% PAE from $20\,\mathrm{V}$ to $35\,\mathrm{V}$ with over $15\,\mathrm{dB}$ of gain. The PA exhibits over $10\,\mathrm{dB}$ of gain and 65% PAE for supply voltages greater than $10\,\mathrm{V}$, making it well suited for envelope tracking applications [27]. The output power exceeds $5\,\mathrm{W}$ for supply voltages greater than $26\,\mathrm{V}$, peaking at $8.8\,\mathrm{W}$ output power for a supply voltage of $35\,\mathrm{V}$.

The performance of the PA over the 2.10 - $2.18\,\mathrm{GHz}$ bandwidth is shown in Fig. 2.15 for a supply voltage of $34\,\mathrm{V}$ (chosen to show peak measured PAE operating point). The PA exhibited its peak PAE of 84.9% at $2.15\,\mathrm{GHz}$ while maintaining over 70% PAE from 2.11 - $2.17\,\mathrm{GHz}$. The
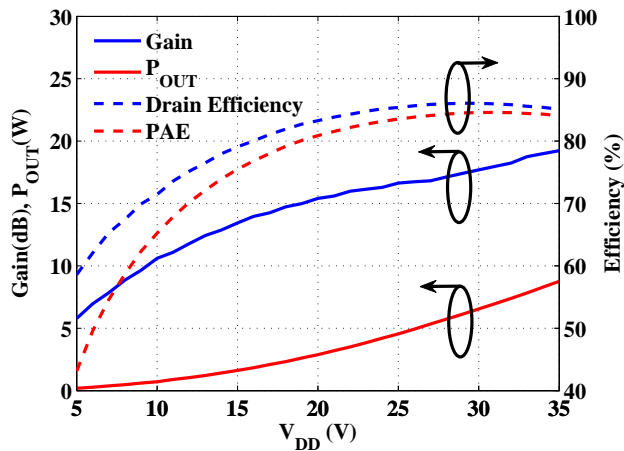
Figure 2.14: Measurements of transducer gain, delivered output power, drain efficiency and PAE at 2.14 GHz. Peak 2.14 GHz PAE of 84.6% occurs at $V_{DD} = 31$ V, having 7 W output power, 18 dB Gain, and 86% drain efficiency.
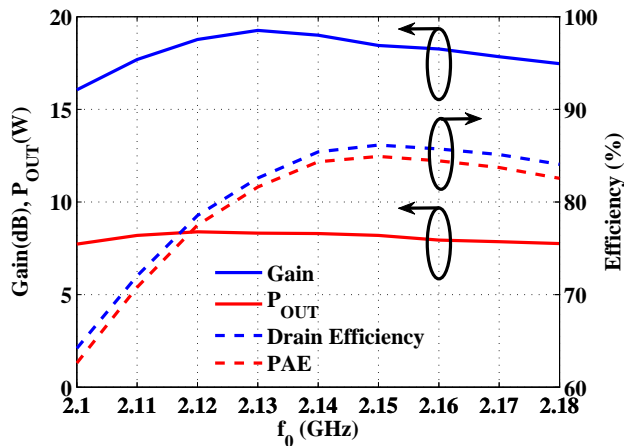
Figure 2.15: Measurements of transducer gain, delivered output power, drain efficiency and PAE versus frequency at $V_{DD} = 34$ V. Peak PAE of 84.9% occurs at 2.15 GHz. The amplifier exhibits over 70% peak PAE, 7.8 W output power, and 17.7 dB gain over the entire 2.11 - 2.17 GHz W-CDMA bandwidth. For most of the W-CDMA bandwidth, the peak PAE exceeds 80%.

significant reduction in PAE realized as the frequency departs from 2.14 GHz is expected, due to the narrow-band harmonic terminations presented by the OCSSs. An output power level between 7.7 W and 8.4 W was maintained, while the gain exceeded 16 dB across the bandwidth, peaking at 19.3 dB at 2.13 GHz.

This particular power amplifier was submitted to the IEEE IMS 2010 PA Student Competition.

PAs entered to the competition must have an operating frequency between 1 GHz and 20 GHz, produce greater than 5 W output power and require less than 25 dBm input power. The entrant must inform the engineer measuring the amplifier at the competition (a representative from Agilent) of the DC bias points, input drive level and frequency. The Agilent representative then measures the PA and the entrant's score is calculated as the the PAE multiplied by $f_0^{0.25}$. The PAE of the prototype amplifier was measured as 82.6% with 38.20 dBm output power at 2.15 GHz for a score of 100.02, good enough for second place [28]. The winning design was a class-J design which achieved a PAE of 74.67 % at 3.50 GHz for a score of 102.13.

2.6   X-Band MMIC Load Pull

High power X-band amplifiers are necessary for radar and communication system transmitters. As an example, the B1B Bomber uses the APQ-164 X-band pulse-doppler radar for navigation and weapon delivery [29]. Military communication systems, such as MILSATCOM, operate in lower X-band (7-8 GHz). For high power X-band transmitters, both power consumption and heat dissipation become important design constraints. Improvement of the transmitter efficiency reduces both the power consumption and heat dissipation and is therefore highly desirable. Typically, the output stage power amplifier is the dominant component of the transmitter efficiency, therefore this is often the component which receives the most attention [5].

In order to achieve high output power and efficiency, the active device is driven until it operates non-linearly [30]. Therefore, linear design techniques are non-applicable and either non-linear model-based techniques or measurement-based techniques are used for design. Non-linear models are often created by using data collected from source pull and load pull measurements [6]. However, often times the models fail to accurately model the performance of power amplifiers operating with high efficiency. Therefore, power amplifier design often involves taking source pull and load pull measurements, then designing the final power amplifier based upon the measurements.

Monolithic Microwave Integrated Circuit (MMIC) technology offers the ability to miniaturize microwave circuits and limit the parasitics entailed with fabrication. Not surprisingly, many

X-band power amplifiers have been realized in MMICs. The state of the art in terms of efficiency with over 5 W output power was achieved by Tayrani using a class-E design where he achieved 67% power added efficiency with 6 W output power at 7.5 GHz under 10% duty cycle pulsed conditions [31]. Recently, MMIC processes using GaN as the semiconductor have become available which allow the possibility of realizing power amplifiers with improved efficiency for a given output power. This is mainly due to the higher power density achievable with GaN relative to other semiconductors [32]. For the work presented in this section, TriQuint's $0.25\,\mu$m GaN on SiC MMIC process is used. This process has been used to created impressive wide-band power amplifiers with over 9 W of power and 20% power added efficiency from 1.5 GHz to 17 GHz [33].

The following subsections detail the design of the MMIC structures necessary to perform on-wafer source pull and load pull in order to realize a high efficiency X-band PA using the TriQuint GaN on SiC process. Prior to discussing the specific structures, Section 2.6.1 discusses the calibration procedure to motivate the development of the test structures. Section 2.6.2 discusses some of the TriQuint GaN on SiC design parameters and their impact on the test structure design. Section 2.6.3 details the design and performance of the individual test structures. Section 2.6.4 presents measurements of the test structures along with source pull and load pull measurements.

2.6.1 CALIBRATION PROCEDURE

First it is important to define the relevant calibration reference planes for the test setup. The term "calibration reference plane" refers to a reference plane at which a the network analyzer measurement is calibrated to. Fig. 2.16 provides a definition of the calibration reference planes which will be used for the remainder of the subsection.

A network analyzer may be calibrated to reference plane A through use of a commercial calibration kit, such as a Short-Open-Load-Through (SOLT) or Through-Reflect-Line (TRL) kit. However, calibrating to the other planes requires more care. The scattering parameters of the source tuner and load tuner can easily be measured, however this is unnecessary because
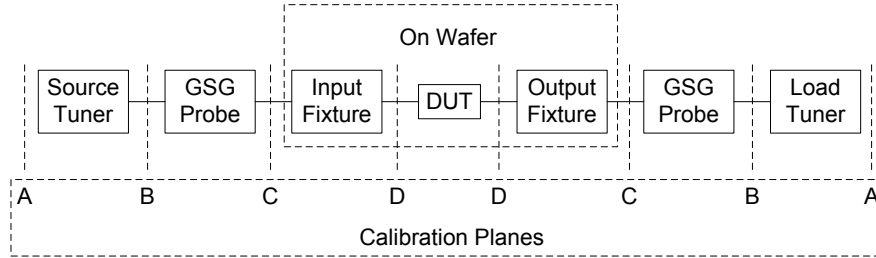
Figure 2.16: Definition of the calibration reference planes. The calibration method drives the required on-wafer test structures.

the tuners will never be used in absence of the probes. Additionally, it is undesirable to have any circuitry between the tuners and the Ground-Signal-Ground (GSG) Coplanar Waveguide (CPW) probes because this will further restrict tuning range due to dissipative loss. Therefore, it is reasonable to measure at least the cascade of the tuners and their respective probes.

It must be decided whether or not to measure the cascade of the tuner, probe and its respective on-wafer fixture. This is a more difficult decision to make. Measuring the full cascade involves a single calibration step, which is an advantage. The disadvantage is the scattering parameters of the tuner cascaded with its respective probe are unknown, therefore using a different on-wafer fixture would require full re-calibration. The disadvantage of not measuring the full cascade is that two distinct calibration procedures are required: one in which the cascade of the tuner and its respective probe are measured and one in which the scattering parameters of the individual fixtures are measured. The full cascade is then performed by cascading the scattering parameters collected from the separate measurements. However, due to the flexibility this method provides, it has been selected by the author. This method does require two distinct on-wafer TRL kits: one which allows calibration of the tuner and probe cascades, and one which allows measurement of the fixtures. The calibration steps are summarized as follows:

- Calibrate the network analyzer up to plane A depicted in Fig. 2.16 using a commercial calibration kit.

- Use an on-wafer TRL calibration kit to calibrate the source tuner - probe and probe - load tuner cascades. This procedure begins by performing on-wafer TRL calibration with the

33

tuners in their $50\,\Omega$ positions to extract de-embedding blocks. Then the source tuner - probe cascade scattering parameters are measured as a function of position by changing the source tuner position with the load tuner in its $50\,\Omega$ position and de-embedding the probe - load tuner cascade which was characterized from the on-wafer TRL calibration. The characterization of the probe - load tuner cascade as a function of position is analogous.

- Use a TRL calibration kit to measure the input fixture and output fixture. To perform this step the tuners are tuned to their $50\,\Omega$ positions and a TRL calibration is performed to extract the de-embedding blocks following the probes. The scattering parameters of the input and output fixtures are then measured by cascading them with the appropriate TRL section and de-embedding accordingly.

The TRL algorithm which allows extraction of de-embedding blocks is found in [34] and has been implemented in MATLAB® by the author. Given the calibration procedure, the required set of on-wafer test circuits is the following:

- TRL Kit 1: input section - output section cascade

- TRL Kit 1: input section - line - output section cascade

- TRL Kit 1: input section reflect

- TRL Kit 1: output section reflect

- TRL Kit 2: input section - output section cascade

- TRL Kit 2: input section - line - output section cascade

- TRL Kit 2: input section reflect

- TRL Kit 2: output section reflect

- Input Fixture - TRL Kit 2 output section cascade

- TRL Kit 2 input section - output Fixture cascade

Table 2.2: SiC Substrate Parameters

Dielectric Constant	9.7
Loss Tangent	0.001
Conductivity	$2.05 \times 10^7 (\frac{\text{S}}{\text{m}})$
Height	$100\,\mu\text{m}$
Thickness	$6.77\,\mu\text{m}$
DC Current Handling	$16\,\frac{\text{mA}}{\mu\text{m}}$

- Input Fixture - DUT - output Fixture cascade

It is also important to design a well matched, low loss probe pad to allow good on-wafer measurements. Since Cascade Microtech $150\,\mu\text{m}$ pitch GSG CPW probes are available, corresponding probe pads were designed. The design of the probe pads and each of the test structures is discussed in Section 2.6.3. Prior to discussing the designs, some relevant GaN on SiC design parameters are highlighted and their impact on the test circuit design is presented in Section 2.6.2.

2.6.2 RELEVANT GaN ON SiC DESIGN PARAMETERS AND LIMITATIONS

TriQuint's $0.25\,\mu\text{m}$ GaN on SiC MMIC process is a 3-Metal-Interconnect (3MI) process [35]. Microstrip transmission lines have been used by the author where applicable. In order to minimize the conduction losses of the microstrip lines, Type 7 lines are used which form the top conductor of the microstrip lines from all three metal layers (M0, M1, and M2). The substrate parameters which dictate the transmission line parameters of the Type 7 line are summarized in Table. 2.2.

Using the parameters in Table. 2.2 as inputs to TX-LINE®, the line width corresponding to a $50\,\Omega$ characteristic impedance at $10\,\text{GHz}$ is $93.6\,\mu\text{m}$. The DC current handling capability of this line is then evaluated as approximately $1500\,\text{mA}$. For an amplifier having $5\,\text{W}$ output power at a $40\,\text{V}$ drain bias, this line width could support an amplifier with down to 8.34% drain efficiency, which should be more than adequate for performing load pull measurements. Further discussion of DC current handling capability will be presented during discussion of the drain bias tee design.

2.6.3 TEST STRUCTURES

PROBE PADS

It was necessary to develop RF probe pads to allow on-wafer measurements of the testing structures using GSG CPW probes. Given the availability of 150 μm pitch GSG RF probes, 150 μm pitch probe pads were designed. The design goals were to minimize the parasitics of the probe pad while providing a transition from the CPW probe to an on-wafer 50 Ω microstrip line. The layout of the probe pad design is shown in Fig. 2.17.

The red squares in Fig. 2.17 depict the landing pads for the RF probe, where the passivation layer has been removed. The ground pads are 75 μm long x 100 μm wide. The signal pad is 75 μm long x 75 μm wide. This is larger than the minimum pad size of 35 μm long x 25 μm wide suggested by Cascade Microtech [36]. Although Cascade suggests using 100 μm square pads, the presented design achieves significant improvement in parasitics.

The ground landing pads are grounded using substrate vias as depicted in Fig. 2.17. The signal landing pad tapers to a 50 Ω line width of 93.6 μm. The design was initially arrived at using a linear simulator in Microwave Office® which modeled the CPW to microstrip transition. The design was then verified using AXIEM®, which is a Method of Moments simulator offered in the AWR Design Environment™. Fig. 2.18 depicts the scattering parameters of the probe pad resultant from the AXIEM® simulation. The return loss is in excess of 35 dB up to 36 GHz.
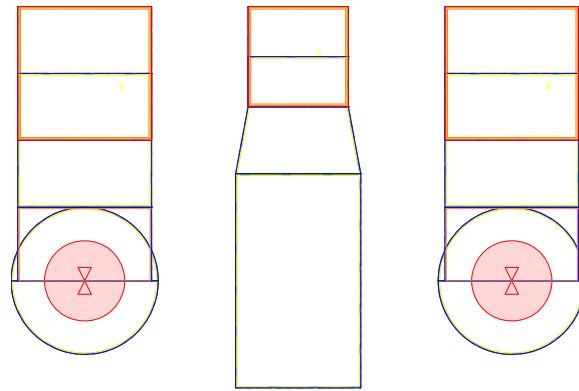
Figure 2.17: Layout of the RF probe pad, with the central structure being the signal and the remaining structures being ground. The pad is design for use with 150 μm pitch GSG probes.
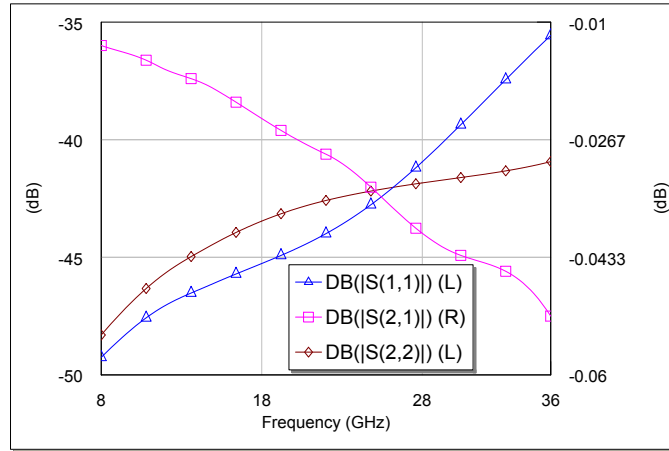
Figure 2.18: AXIEM® simulation of RF probe pad layout. Minimal parasitics are realized up to 36 GHz, which was chosen as the highest simulation frequency because if is the third harmonic of the highest X-band frequency (12 GHz).

Given the excellent match, the insertion loss is set by the scattering parameter S_{21} and is less than 0.05 dB up to 36 GHz. This design provides a low parasitic probe to microstrip transition which will be useful not only for RF probing but for bonding to if the MMIC is used within a hybrid circuit.

DEVICE SELECTION

The device selected for fabrication is shown in Fig. 2.19 and has a 70 μm gate width with 10 gate fingers, corresponding to 700 μm of gate periphery. This device was selected because it was the largest available device in the design kit library and therefore the device which is capable of delivering the most output power. The 0.25 μm GaN 3MI process data sheet quotes 5-7 W/mm for output power, therefore a rough estimate of output power for this device is 4.9 W [37]. This is lower than the required 5 W, however this is just a rough estimate of the output power. Simulation using the non-linear model provided by TriQuint indicated that more than 5 W output power could be achieved with this device. The dimension of the microstrip line which would mate seamlessly with the gate and drain manifold for this device is 300 μm. This is an important dimension which will drive the input/output matching circuits as well as the TRL kit used for characterization of the respective structures.

37
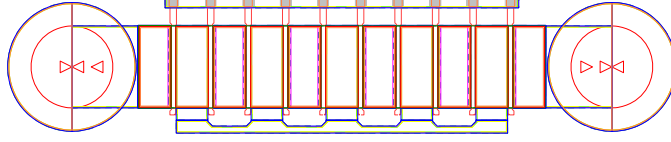
Figure 2.19: Active device selected for load pull measurement. The gate is the top side, with the drain being the bottom side. The circular structures are substrate vias. The device has a $70\,\mu$m gate width with 10 gate fingers, corresponding to $700\,\mu$m of gate periphery.

It is important to characterize the output capacitance of the device in order to allow termination of harmonics at the virtual drain of the device [8]. The output capacitance of the device was extracted using the method presented in [38]. This is done by measuring the small signal scattering parameters at $10\,$MHz as a function of bias point and then converting these to small signal admittance parameters Y. The gate-to-source, gate-to-drain, and drain-to-source capacitances are then calculated using the following equations, where port-1 is the gate and port-2 is the drain.

$$C_{GD} = -\frac{\text{Im}(Y_{12})}{2\pi \times 10^7} \tag{2.28}$$

$$C_{DS} = \frac{\text{Im}(Y_{22})}{2\pi \times 10^7} - C_{GD} \tag{2.29}$$

$$C_{GS} = \frac{|Y_{11} + Y_{12}|^2}{2\pi \times 10^7 \times \text{Im}(Y_{11} + Y_{12})} \tag{2.30}$$

The output capacitance C_{OUT} of the transistor is then calculated using the following expression.

$$C_{OUT} = C_{DS} + C_{GD}||C_{GS} \tag{2.31}$$

Initially, the non-linear model from the design kit was used with the above procedure to calculate C_{OUT} but invalid results were arrived at (e.g. C_{OUT} was negative). The linear model was then used to calculate an output capacitance of $0.2478\,$pF. Given the author's experience with TriQuint's discrete $0.25\,\mu$m GaN on SiC devices, this is a reasonable result for the output capacitance, corresponding to $0.354\,$pF per mm of gate periphery.
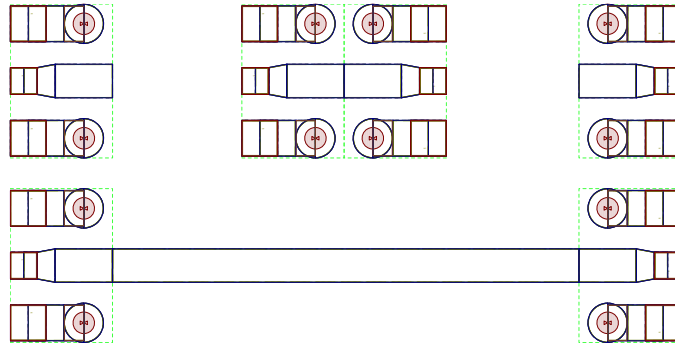
Figure 2.20: 50 Ω TRL kit. The line length is 1300 μm and the reflect standards are open circuits.

TRL CALIBRATION KITS

Section 2.6.1 discussed the calibration technique selected by the author in order to calibrate the load pull measurements. Given the selected technique, design of two TRL kits was required. The first TRL kit has a 50 Ω line that should allow calibration between 8 GHz and 36 GHz. This provides coverage down to the lowest X-band frequency and the third harmonic of the highest X-band frequency. The designed 50 Ω TRL kit is shown in Fig. 2.20. The line phase resultant from an AXIEM® simulation is shown in Fig. 2.21.

The second TRL kit requires a taper to a 300 μm line given the width of the active device which was discussed in Section 2.6.3. Due to the wider line width, a different line length than the previous TRL kit is required. The designed TRL kit with a 300 μm line width is shown in Fig. 2.22. The line phase resultant from an AXIEM® simulation is shown in Fig. 2.23.
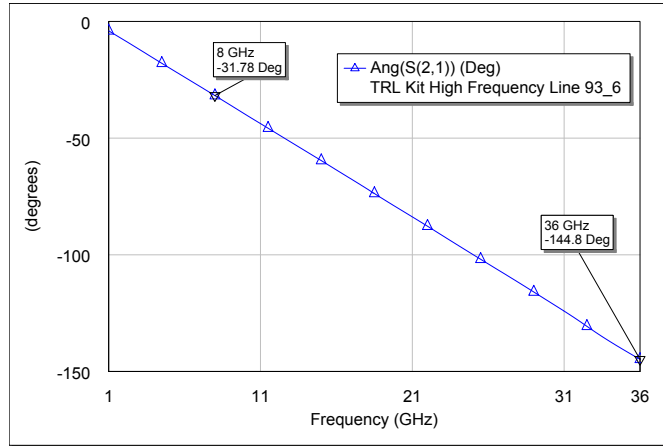
Figure 2.21: 50 Ω TRL kit line phase simulated with AXIEM®. The phase is well within the recommended range of 20° - 160° over the frequency range 8 GHz - 36 GHz [1].
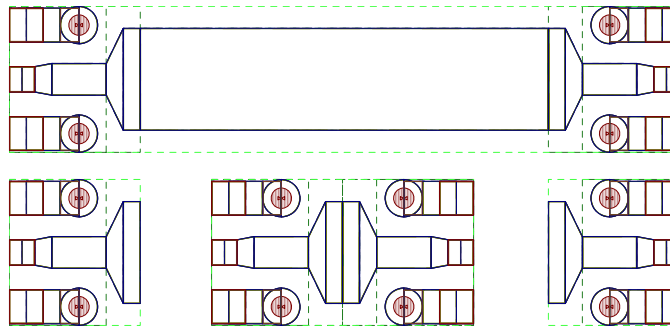
Figure 2.22: 300 µm line width TRL kit. The line length is 1200 µm and the reflect standards are open circuits.
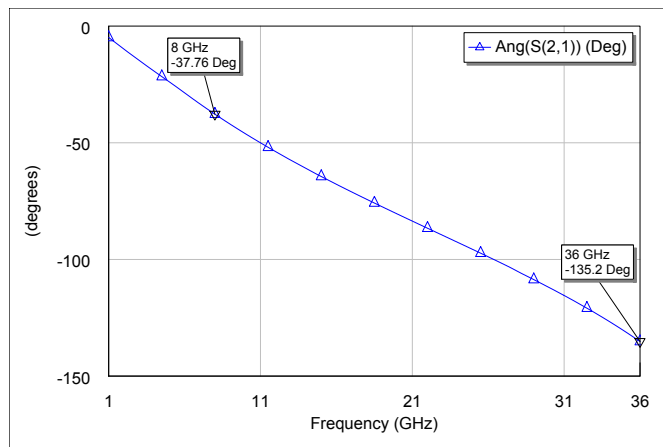
Figure 2.23: 300 µm line width TRL kit line phase simulated with AXIEM®. The phase is well within the recommended range of 30° - 150° over the frequency range 8 GHz - 36 GHz.
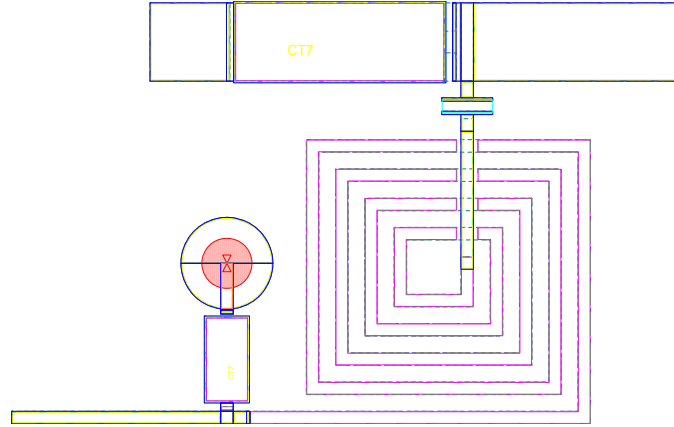
Figure 2.24: Gate bias tee layout. The upper left is the RF input port (port-1), the upper right is the RF+DC output port (port-2) and the lower open ended trace is the DC input port (port-3)

GATE BIAS TEE

The gate bias tee design is significantly simpler than the drain bias tee design, however it still presents its own design challenges. The insertion loss and isolation of the bias tee are paramount in order to maximize the compressed gain of the amplifier, thus maximizing power added efficiency and minimizing the waste of input drive power. For design simplicity, a bias tee matched to $50\,\Omega$ on both RF ports is designed such that once the matching circuit is designed the bias tee can simply be added to the circuit without transforming the match. The main reason the gate bias tee design is simpler is DC current handling requirements. Minimal current is drawn into the gate of the transistor, and in compression minimal current is sunk into the supply, therefore the current handling capability of the bias tee is not substantial. From experience, it has been found that maximum PAE is obtained when the current draw is less than $1\,\text{mA}$. Given the minimal current draw, use of a spiral inductor as the RF choke presents no problem. Fig. 2.24 depicts the gate bias tee design layout.

The design includes a blocking capacitor and a $10\,\Omega$ low frequency stabilization resistor on the DC line prior to the spiral inductor. The spiral inductor acts as a $90°$ transmission line at $10\,\text{GHz}$ and is shunted to ground through a resonant capacitor to optimize RF-DC isolation. The DC current handling capability of this design is limited by the stabilization resistor current handling and the inductor's under-bridge current handling which is based on its width. The

41
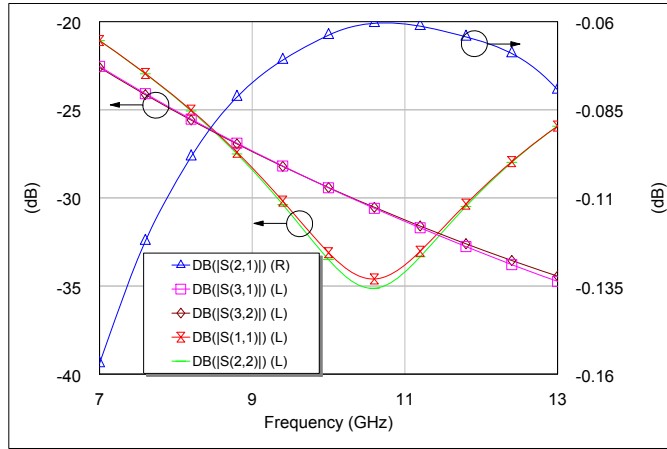
Figure 2.25: Gate bias tee relevant scattering parameters.

resistor is designed to support up to 54 mA of current while the under-bridge line type can support 6.4 mA/μm line width. The line width of the under-bridge was designed as 15 μm, therefore the under-bridge can handle 96 mA of DC current. Therefore the stabilization resistor limits the DC current handling capability of the gate bias tee to 54 mA. However, 54 mA is more than sufficient for performing the necessary tests as discussed above.

Fig. 2.25 depicts the AXIEM® simulation of the gate bias tee scattering parameters. Port-1 is the RF input port, port-2 is the RF+DC output port, and port-3 is the DC input port. The match at port-1 and port-2 is excellent, exhibiting better than 24 dB return loss over the entire 8-12 GHz band. The isolation is better than 25 dB over the entire band. Given the excellent match and isolation, the insertion loss is driven by S_{21} and is less than 0.10 dB over the entire band. While the performance of the bias tee is excellent, another very important parameter is size. The size of the rectangle fully enclosing the bias tee is approximately 640 μm long by 500 μm wide. This is relatively large, but as will be shown later is not a driving factor in the total MMIC size.

Input Matching Circuit

Prior to designing the load pull input matching circuit, the nominal impedance to present to the device must be defined. This was done by using the non-linear model provided by TriQuint and measuring the fundamental frequency input impedance to the gate of the transistor while varying
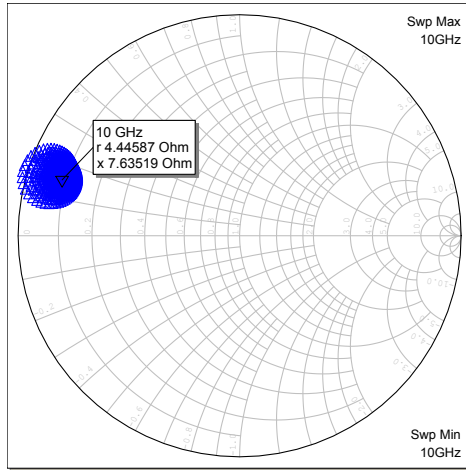
Figure 2.26: Constellation of optimal small-signal source pre-match fundamental impedances. Given the constellation, a $5\,\Omega$ pre-match is selected.

the fundamental frequency load presented to the drain in small-signal. For these measurements a bias point of -3.5 V on the gate and 40 V on the drain was used. The conjugate of these measured impedances gives a good approximation of the impedance to present to the gate of the transistor. Of course the source tuner will be used to modify this impedance, but it is preferable to pre-match to a good location to maximize the validity of the calibration. Fig. 2.26 shows the constellation of optimal input impedances to present to the gate at $10\,\text{GHz}$ as a function of the termination at the drain. Based upon the results, a $5\,\Omega$ pre-match impedance at the fundamental frequency is selected. The harmonic terminations at the input to the transistor will not be specifically terminated, although that is an option for future work.

Fig. 2.27 shows the layout of the designed input matching circuit. The input match includes the gate bias tee as discussed in the previous subsection and uses a linear taper and two shunt capacitors to realize the impedance match. The impedance presented to the gate of the transistor from 7-13 GHz is shown in Fig. 2.28 with the insertion loss being shown in Fig. 2.29. The circuit provides an inductive match with near $5\,\Omega$ real part which should allow source pull over the 8-12 GHz frequency band. The insertion loss of the match at $10\,\text{GHz}$ is $0.63\,\text{dB}$ which is large but expected due to the dramatic impedance transformation (10:1). The size of the rectangle fully enclosing the matching circuit is approximately $1400\,\mu\text{m}$ long by $700\,\mu\text{m}$ wide.
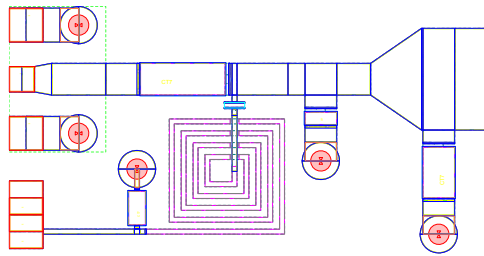
Figure 2.27: Input matching circuit with bias tee layout.
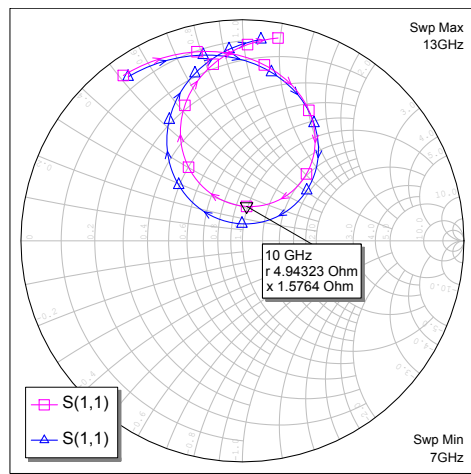
Figure 2.28: Input matching circuit with bias tee input impedance. The blue trace is from the linear simulator while the pink trace is from simulation using AXIEM®.
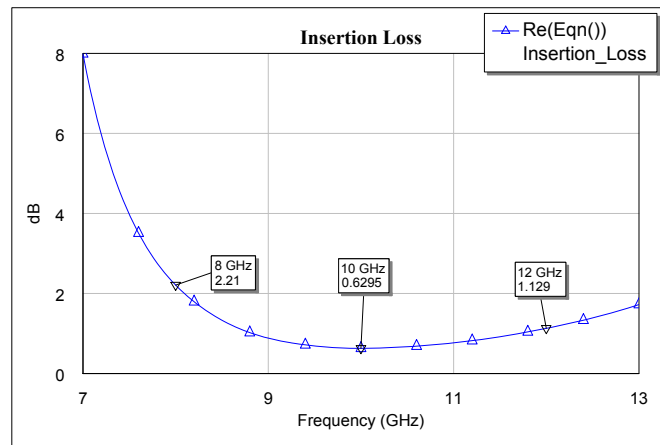
Figure 2.29: Input matching circuit with bias tee insertion loss simulated with AXIEM®.
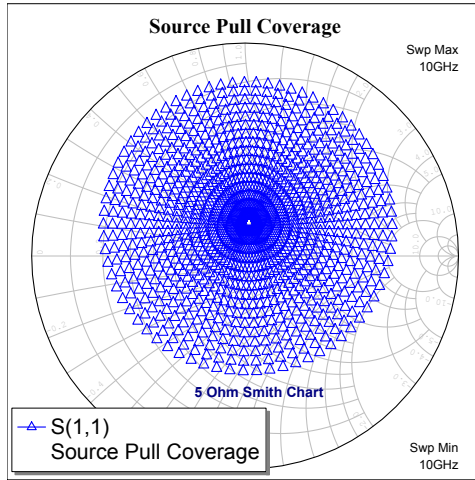
Figure 2.30: Source pull coverage at 10 GHz assuming tuner with maximum reflection coefficient of 0.8.

Since this structure will be used to perform source pull, it is important to look at the fundamental impedance tuning range when a tuner is used. Fig. 2.30 shows the range over which the input impedance the gate of the transistor sees can be tuned at 10 GHz. A tuner with maximum reflection coefficient magnitude of 0.8 has been assumed. It is expected that this tuning range is sufficient to find the optimum source impedance.

DRAIN BIAS TEE

Design of the drain bias tee proved more difficult than the design of the gate bias tee due to the DC current handling requirements. Using a spiral inductor would have required a prohibitively large bridge width. Therefore, a design was adopted which used a meandered transmission line to effectively act as the RF choke inductor. Fig. 2.31 shows the layout of the drain bias tee. A coupled line model was used to arrive at a design which yielded 90° of phase at the design frequency of 10 GHz. The design was then refined using the AXIEM®. The meandered transmission line is then shorted to ground through a 10 GHz shunt resonant capacitor to cause the bias line to look like an open circuit at RF at its connection point to the through line. The scattering parameters of the structure are plotted in Fig. 2.32. The insertion loss at 10 GHz is approximately 0.18 dB, with approximately 30 dB of RF-DC isolation. The structure is large, taking up a footprint of

45
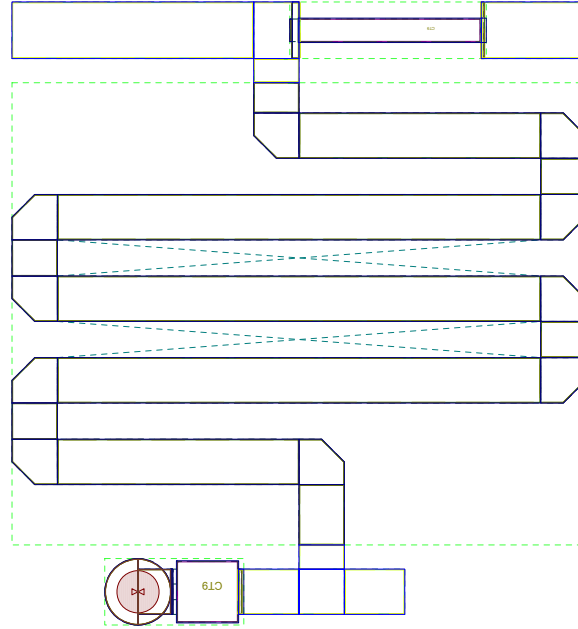
Figure 2.31: Drain bias tee layout. The upper left is the RF+DC output port (port-1), the upper right is the RF output port (port-2) and the lower open ended trace is the DC input port (port-3).
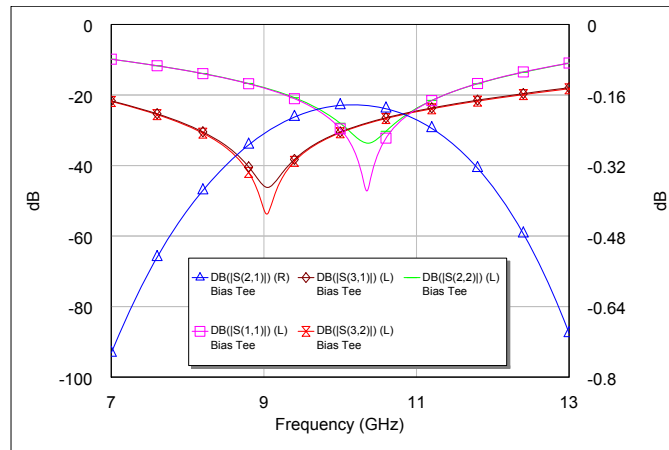
Figure 2.32: Drain bias tee S-parameters.

approximately $1\,\mathrm{mm}^2$.

OUTPUT MATCHING CIRCUIT

The output matching circuit is shown if Fig. 2.33. It implements fixed class-F^{-1} terminations at the virtual drain using shunt capacitors for resonators. The size of the rectangle fully enclosing the output matching circuit is approximately $2000\,\mu\mathrm{m}$ long by $1100\,\mu\mathrm{m}$ wide. The fundamental
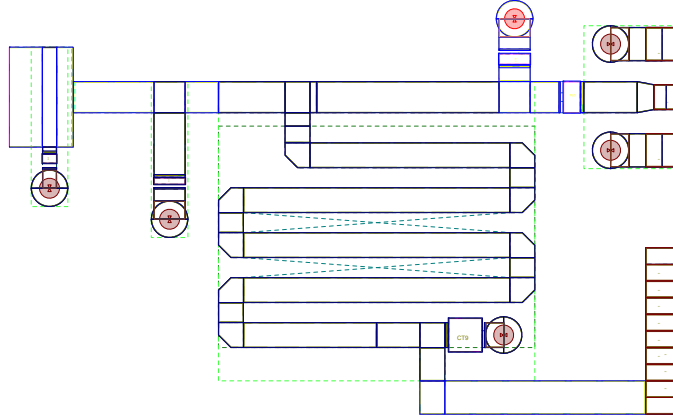
Figure 2.33: Layout of output matching circuit. The far left connects to the transistor drain.
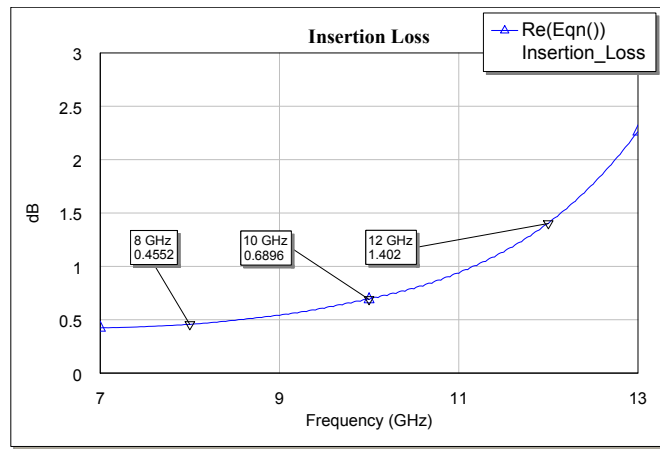
Figure 2.34: Insertion loss of the output matching circuit.

impedance at the virtual drain is pre-matched to approximately $70\,\Omega$ at $10\,\text{GHz}$, with an open circuit at $20\,\text{GHz}$ and a short circuit at $30\,\text{GHz}$. The insertion loss of the structure versus frequency is shown in Fig. 2.34. Less than $0.7\,\text{dB}$ insertion loss is achieved at $10\,\text{GHz}$.

As with the input fixture, the tuning range of the fundamental impedance is important. Additionally, it is desired that the harmonic terminations are fixed, which given the topology of the match should be the case. Fig. 2.35 shows the tuning range at the fundamental frequency of $10\,\text{GHz}$ and its second and third harmonics. The terminations at the second and third harmonics are relatively fixed, while the fundamental impedance may be tuned substantially.
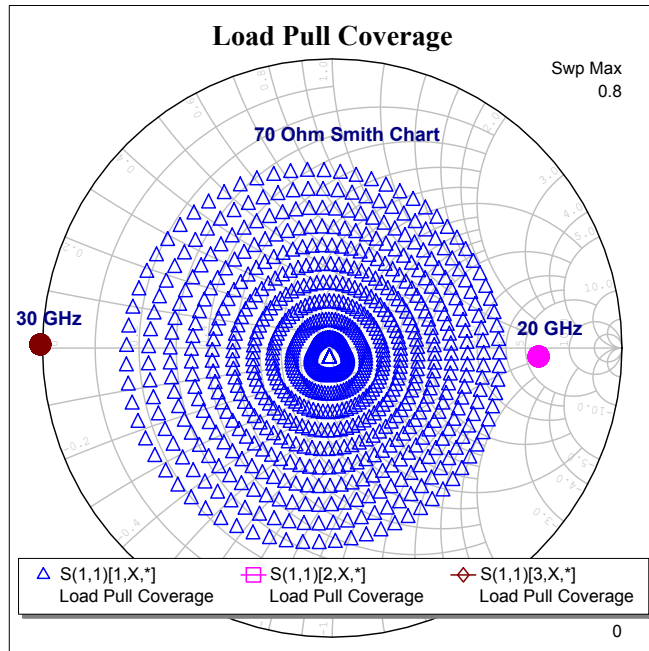
Figure 2.35: Load pull coverage at 10 GHz and harmonics assuming tuner with maximum reflection coefficient of 0.8.

2.6.4 MMIC Measurements

The MMIC designs presented in the previous section were fabricated at the TriQuint foundry in Richardson, TX. The foundry made the decision to split the circuits up into two separate 2 mm x 4 mm MMICs, of which photos are shown in Fig. 2.36. The structures on the MMICs have been labeled with the lettering corresponding to the list below.

- (A) TRL Kit 1: input section - output section cascade

- (B) TRL Kit 1: input section - line - output section cascade

- (C) TRL Kit 1: input section reflect

- (D) TRL Kit 1: output section reflect

- (E) TRL Kit 2: input section - output section cascade

- (F) TRL Kit 2: input section - line - output section cascade

- (G) TRL Kit 2: input section reflect
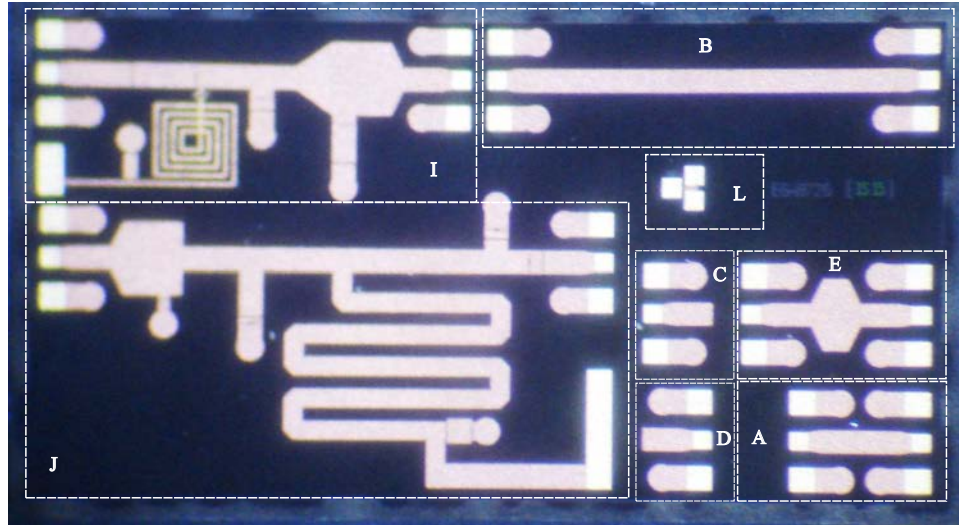
(a)
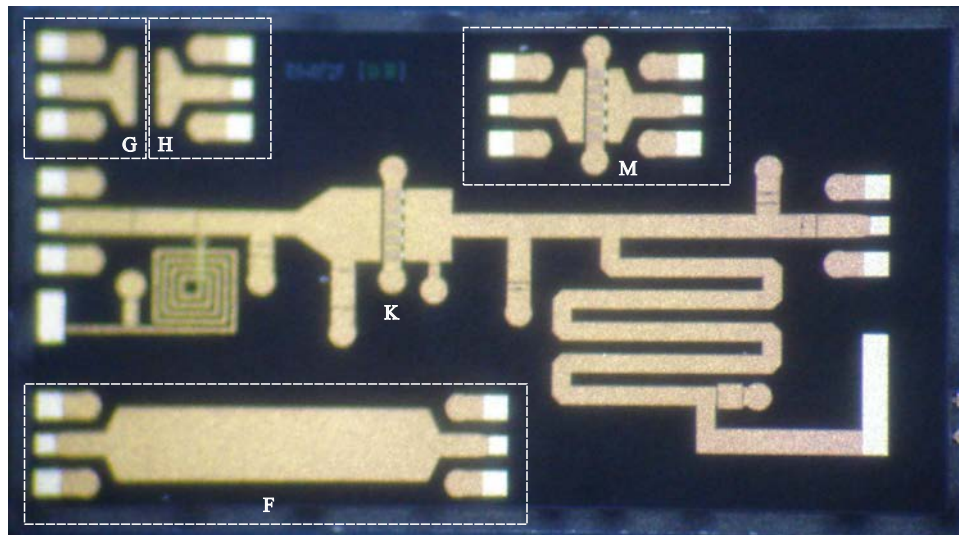
(b)

Figure 2.36: (a) MMIC 1 containing the majority of the TRL calibration kits and impedance verification structures. (b) MMIC 2 containing the remainder of TRL calibration structures, a device for measuring scattering parameters and the full cascade for load pull measurements. Each MMIC is 2 mm x 4 mm.

- (H) TRL Kit 2: output section reflect

- (I) Input Fixture - TRL Kit 2 output section cascade

- (J) TRL Kit 2 input section - output Fixture cascade

- (K) Input Fixture - DUT - output Fixture cascade

- (L) Foundry test structure (process requirement)

- (M) Device with TRL Kit 2 standards

The scattering parameters of the input and output pre-matching circuits were measured in order for calibrated load pull measurements to be taken, as well as for impedance verification. Fig. 2.37 shows the simulated and measured input pre-matching fixture impedance match versus frequency. The measured impedance is slightly shifted in frequency from the simulation. However, the impedance presented by the measured fixture is more than sufficient for load pull measurements. The insertion loss of the measured fixture at $10\,\mathrm{GHz}$ was $0.60\,\mathrm{dB}$, with the simulated value being $0.62\,\mathrm{dB}$. For all intensive purposes, the measured and simulated input pre-matching fixture behaved very much the same. Given the agreement in insertion loss and presented impedance, it can be inferred that the RF-DC isolation of the structure is satisfactory. It was also noted during testing that the termination on the DC port did not impact the measured scattering parameters.

Fig. 2.38 shows the simulated and measured output pre-matching fixture impedance match versus frequency. The measured impedance is slightly shifted in frequency from the simulation. However, the impedance presented by the measured fixture is more than sufficient for load pull measurements. The insertion loss of the measured fixture at $10\,\mathrm{GHz}$ was $0.47\,\mathrm{dB}$, with the simulated value being $0.63\,\mathrm{dB}$. This is a welcomed improvement in insertion loss of the fixture. The improvement in insertion loss is attributed to inaccurate modeling of the conductor loss in the AXIEM® stackup, as both the input and output pre-matching fixtures measured as having lower loss than the expected loss from simulation.
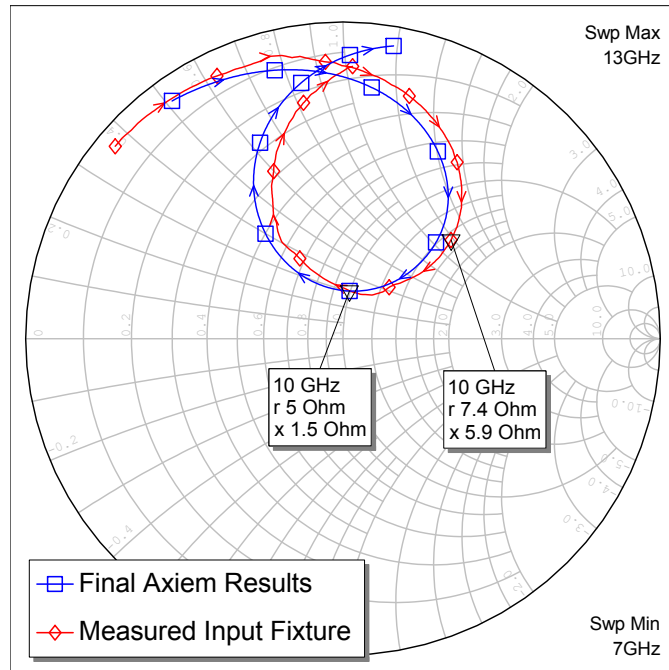
Figure 2.37: Simulated versus measured input pre-matching fixture impedance match. The measured results are slightly shifted in frequency relative to the simulation. The Smith Chart is normalized to $5\,\Omega$.
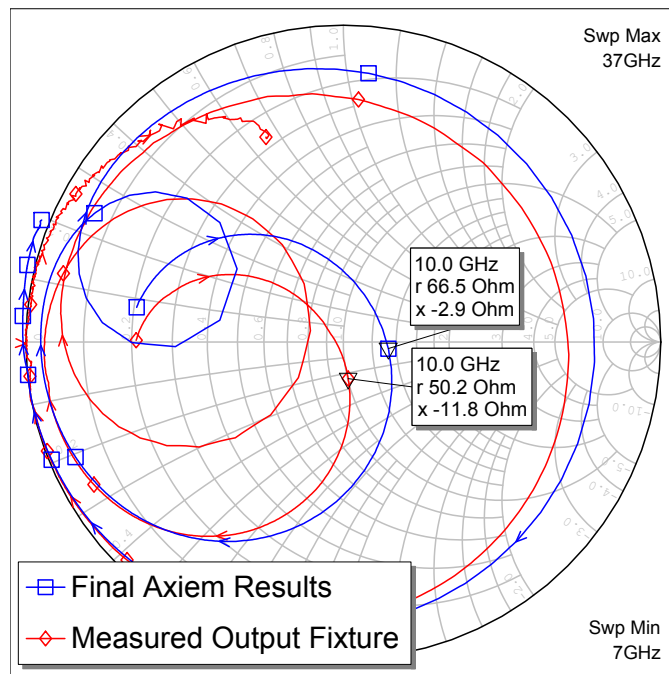
Figure 2.38: Simulated versus measured output pre-matching fixture impedance match. The measured results are slightly shifted in frequency relative to the simulation. The Smith Chart is normalized to $50\,\Omega$.

Table 2.3: Output Impedance vs. Frequency

$f_0 = 10\,\text{GHz}$	$f_0 = 9.79\,\text{GHz}$
$Z(f_0) = 50.2 - \text{j}11.8\,\Omega$	$Z(f_0) = 48.3 - \text{j}1.1\,\Omega$
$Z(2f_0) = 25.9 - \text{j}90.6\,\Omega$	$Z(2f_0) = 291.8 - \text{j}1.0\,\Omega$
$Z(3f_0) = 0.0 + \text{j}0.9\,\Omega$	$Z(3f_0) = 0.0 - \text{j}0.5\,\Omega$

For the output pre-matching fixture, the harmonic terminations are also important. Table 2.3 lists the measured fundamental frequency and up to third harmonic terminations for the output fixture at both 10 GHz and 9.79 GHz. It is evident that the phase of the second harmonic termination at 20 GHz is significantly off from the design, however at harmonics of 9.79 GHz the harmonic terminations are very good. Given the fidelity of the harmonic terminations at 9.79 GHz, this frequency was selected as the frequency at which load pull measurements would be performed.

Initially, fundamental frequency source pull at 9.79 GHz was performed in small signal. For these measurements, the DC drain voltage was set to 30 V and the quiescent drain current was set to 40 mA. The load impedance was set to 50 Ω for these measurements. The small signal gain contours are shown in Fig. 2.39. The peak small signal gain of 15.1 dB occurred at 3.1 + j16.3 Ω.

Load pull was then performed with the same quiescent drain voltage and current, with the input impedance set to 3.1 + j16.3 Ω. The PAE contours are shown in Fig. 2.40. A peak PAE of 51.4 % occurred with a load impedance of 139.1 + j45.1 Ω, which isn't particularly far from the real axis, verifying the model of the output capacitance. It is evident that the PAE contours are not closed, therefore the optimal impedance was not found. Unfortunately, the tuning range was was limited to $|\Gamma| = 0.5$ due to the loss of the matching circuit and probe-tuner cascade. The load tuner is particularly lossy due to a second harmonic resonator carriage, which limits how close the fundamental frequency carriage can be placed to the DUT. For comparison, the tuning range of the load tuner - probe cascade is approximately $|\Gamma| = 0.65$, while the tuning range of the source tuner - probe cascade is approximately $|\Gamma| = 0.75$, demonstrating the impact which the harmonic resonator carriage has on the tuning range. The power contours are not interesting to investigate due to the tuning range achieved. In this case, the power varied between

Source Pull - Small Signal Gain

Swp Max
15.08

15.1
r 3.1 Ohm
x 16.3 Ohm

— Gain Contours

□ Peak Gain

p1: Gain = 10.0 dB
p2: Gain = 10.5 dB
p3: Gain = 11.0 dB
p4: Gain = 11.5 dB
p5: Gain = 12.0 dB
p6: Gain = 12.5 dB
p7: Gain = 13.0 dB
p8: Gain = 13.5 dB
p9: Gain = 14.0 dB
p10: Gain = 14.5 dB
p11: Gain = 15.0 dB
p12: Gain = 15.1 dB

Swp Min
10
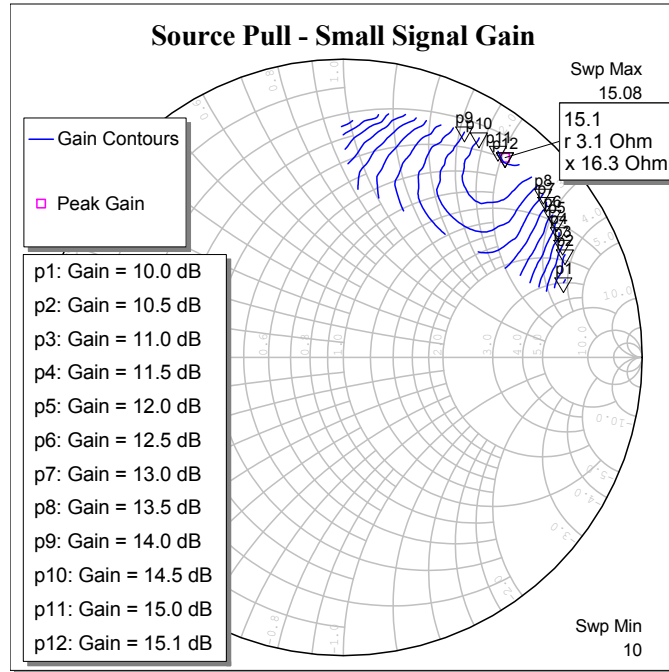
Figure 2.39: Measured small signal gain contours with 30 V drain voltage and 40 mA quiescent current. The Smith Chart is normalized to 5 Ω.

34.0 dBm and 35.5 dBm over the range measured in Fig. 2.40, with the output power at the peak PAE being 34.5 dBm (2.8 W). Further testing at 35 V improved the output power to 35.5 dBm (3.6 W) with an associated PAE of 49.6 %. No significant change in the optimal input and output impedances was noted between 30 V and 35 V. Testing at 15 V showed a shift in the optimal output impedance, with no significant shift in the input impedance.

Given the tuning range of the output cascade was limited to $|\Gamma| = 0.5$, the usefulness of the measurements is limited. It is also evident that the output impedance yielding optimal PAE is going to be high for a device of this size, and comparable to an achievable open circuit harmonic termination. Therefore, for a future design it would be desirable to increase the device size to improve the difference between the fundamental impedance and achievable open circuit termination at the second harmonic, or to investigate a different class of amplifier with the same device size. Most likely, this class should have a short circuit second harmonic termination given the high fundamental impedance required for optimal PAE.
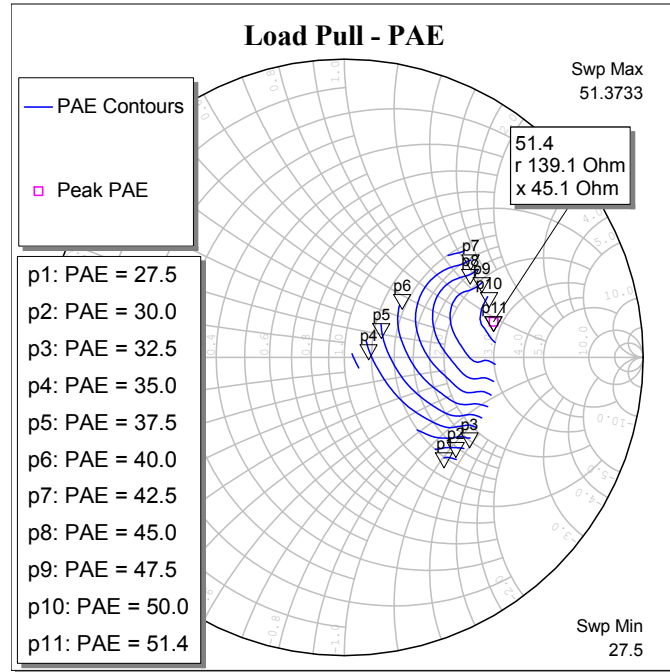
Figure 2.40: Measured power added efficiency contours with 30 V drain voltage and 40 mA quiescent current. The Smith Chart is normalized to 50 Ω.

2.6.5 ACKNOWLEDGEMENTS

The author would like to acknowledge Dr. Charles Campbell of TriQuint for useful discussions concerning the GaN on SiC process.

2.7 CONCLUSION

This chapter presented some of the basics of load pull based power amplifier design, including some basic load-pull theory and measurement network design. A method for calibrating and measuring a single slug mechanical tuner was presented and verified with a FOCUS Microwaves tuner. The load pull method is necessary for high-efficiency PA design when good models are not available, which is commonly the case, especially for new device technologies such as GaN used in this thesis. The specific contributions described in this chapter are:

- Application of the basic load pull theory to the design of a high-efficiency 2.14 GHz cell-phone band PA.

- The resulting design was implemented in a hybrid circuit with a TriQuint 12 W GaN die. This PA was measured independently by Agilent at the 2010 IEEE International Microwave Symposium, resulting in 82.6 % PAE with 38.2 dBm output power and 18 dB large signal gain. This PA won second place at the 2010 IMS PA Student Competition and is also reported in [9].

- The load-pull design method was scaled to 10 GHz in a GaN MMIC test structure with implicit harmonic terminations on-chip. The TriQuint 0.25 μm GaN process was used and resulted in an efficiency of 50 % at 10 GHz with 3.5 W of output power in a test MMIC. The measured results from this test circuit serve as input characterization information for the next iteration of a high-efficiency 10 GHz PA design, with estimated potential PAE of 70 %.

CHAPTER 3

Harmonically Terminated Power Amplifier Analysis

CONTENTS

3.1 Introduction

Power amplifier (PA) efficiency is traditionally controlled by the current conduction angle of the transistor, which results in sinusoidal voltage and clipped sinusoidal current time-domain waveforms at the virtual drain (collector) [6]. In the frequency domain, the clipped sinusoidal current waveforms correspond to generation of harmonic current components by the transistor. Given that the voltage waveform is a pure sinusoid, no harmonic voltage components are produced, requiring that harmonic shorts are presented to the transistor at the virtual drain. Other classes of PAs, such as class-F and class-F^{-1}, present specific harmonic impedances at the virtual drain, using either harmonic voltage or current components to shape the drain waveforms, therefore improving efficiency. Non-linearities inherent to the transistor such as knee voltage, etc. are viable methods of producing harmonic voltage components [5]. At higher microwave frequencies, parasitics inherent to the transistor, as well as its package can limit the ability to present specific harmonic impedances.

Investigation of PAs via Fourier analysis was published as early as 1932 [39]. In [40], Raab analyzed efficiency and output power capability of an ideal PA having a finite number of reactive harmonic terminations. This method maximized PA efficiency through optimization of the drain voltage and current waveform Fourier coefficients and fundamental frequency reactance, under the restriction of a finite set of harmonic terminations. In [41], an analytical treatment of ideal class-F amplifiers subject to finite harmonic terminations was presented, in which purely reactive harmonic terminations were also assumed. Using a technique similar to [40], a set of PA classes with class-B efficiency has been treated [42]. In [43], an analytical solution to finite harmonic class-C PA maximum efficiency was derived, which is equally applicable to analysis of a finite harmonic class-C^{-1} PA. Cripps recently discussed the waveform analysis of a second-harmonic only PA in [44].

To the best of the authors' knowledge, a general analysis with arbitrary sets of resistive and reactive harmonic terminations has not been presented to date. However, in practice harmonic terminations are complex due to resistive loss of the PA output network. Therefore, it is of interest to understand the impact of arbitrary impedances at harmonic frequencies on PA efficiency, output power, and load impedance. This chapter generalizes the classical method of [40] in order to investigate several issues of practical interest:

(1) Fidelity of harmonic terminations required to achieve a specified efficiency.

(2) Impact of resistive, reactive and complex harmonic terminations on maximum PA efficiency and corresponding fundamental output power and load resistance.

(3) Impact of fundamental frequency reactance on maximum PA efficiency and corresponding fundamental output power and load resistance.

In Section 3.2, a generalized theoretical analysis of PA efficiency, output power, and load impedance is presented. Section 3.3 presents the optimization procedure by which the optimal waveforms for a given set of finite harmonic terminations are evaluated. Sections 3.4 and 3.5 detail the results for PAs having up to third harmonic voltage and current components for real and complex fundamental load impedances, respectively. Section 3.6 presents a practical application of the theoretical analysis for a 2.14 GHz PA with a constant device output capacitance assumed. Section 3.7 discusses an alternate set of normalization conditions which can be applied to the analysis presented in Section 3.2. Section 3.8 contains an example of harmonic load pull data using a practical 50 W GaN HEMT demonstrating trends predicted by the theory.
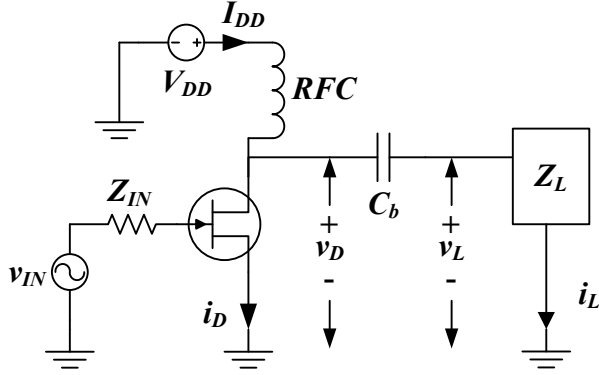
Figure 3.1: Circuit diagram of ideal common source FET-based PA. The DC Block (C_b) and RF Choke (RFC) are assumed to be ideal, therefore Z_L is equivalent to the impedance Z_D presented to the virtual drain at the fundamental and harmonic frequencies.

3.2   HARMONICALLY TERMINATED PA ANALYSIS APPROACH

Fig. 3.1 depicts an ideal PA, which will be described in terms of a Field Effect Transistor (FET) without loss of generality, and with the following assumptions:

- The device has zero on-state resistance, R_{on}. While non-zero R_{on} may be considered, the intention of the following analysis is to investigate the performance ceiling rather than the performance as a function of R_{on}.

- The drain is biased through an ideal RF Choke (RFC).

- The load Z_L is DC isolated from the supply by an ideal blocking capacitor C_b that acts as a short circuit at the operating frequency f_0 and corresponding harmonics.

- A sinusoidal voltage at f_0 is applied to the gate. Harmonics are present only at the output of the transistor, and they are assumed to be generated by the various non-linearities of the transistor, which include non-linear capacitances such as gate-to-source capacitance.

- The DC drain voltage V_{DD} and DC drain current I_{DD} are strictly greater than or equal to zero.

- The drain current and voltage waveforms have fixed maximum values I_{max} and V_{max}, regardless of harmonic content. This allows a fair comparison of output power and funda-

mental load impedance for amplifiers having different harmonic terminations. Alternate parameters may be fixed as discussed in the Appendix.

The time-harmonic drain voltage $v_D(\theta)$ and current $i_D(\theta)$ waveforms of an ideal PA limited to m harmonics can be represented by Fourier series as

$$v_D(\theta) = V_{DD} + \sum_{n=1}^{m}[a_{v,n}\cos(n\theta) - b_{v,n}\sin(n\theta)] \quad \text{(V)} \tag{3.1}$$

$$i_D(\theta) = I_{DD} + \sum_{n=1}^{m}[a_{i,n}\cos(n\theta) - b_{i,n}\sin(n\theta)] \quad \text{(A)} \tag{3.2}$$

where $\theta = 2\pi f_0 t$ is angular time [7]. In principle, m may extend to ∞, but practically is finite due to the device gain roll-off in frequency and in the case of this chapter up to $m = 3$ is analyzed. The minimum values of the drain waveforms defined in (3.1) and (3.2) are required to be greater than or equal to zero, where the case when the waveforms have minima of zero corresponds to (3.17) being maximized. This corresponds to the DC power being minimized for the given fundamental output power. Under this restriction, the ideal PA with no harmonic voltage or current components corresponds to a class-A PA with full $360°$ conduction angle, as expected. By inspection of Fig. 3.1, the load network voltage $v_L(\theta)$ and current $i_L(\theta)$ waveforms are given by

$$v_L(\theta) = \sum_{n=1}^{m}[a_{v,n}\cos(n\theta) - b_{v,n}\sin(n\theta)] \quad \text{(V)} \tag{3.3}$$

$$i_L(\theta) = -\sum_{n=1}^{m}[a_{i,n}\cos(n\theta) - b_{i,n}\sin(n\theta)] \quad \text{(A)} \tag{3.4}$$

Due to the definitions of the load voltage in (3.3) and current waveforms in (3.4), the voltage and current fundamental frequency and harmonics components are expressed as

$$V_L(nf_0) = a_{v,n} + jb_{v,n} \quad \text{(V)} \tag{3.5}$$

$$I_L(nf_0) = -a_{i,n} - jb_{i,n} \quad \text{(A)} \tag{3.6}$$

The load impedance at frequency nf_0 is given by

$$Z_L(nf_0) = \frac{V_L(nf_0)}{I_L(nf_0)} = -\frac{a_{v,n} + jb_{v,n}}{a_{i,n} + jb_{i,n}} \quad (\Omega) \tag{3.7}$$

The time average power delivered to the load at frequency nf_0 is given by

$$P_L(nf_0) = \frac{\text{Re}\{V_L(nf_0)I_L^*(nf_0)\}}{2}$$
$$= -\frac{a_{v,n}a_{i,n} + b_{v,n}b_{i,n}}{2} \quad \text{(W)}$$

(3.8)

where $*$ denotes the complex conjugate operator. For analysis of an ideal PA, it is convenient to define the fundamental frequency drain voltage Fourier coefficient $a_{v,1}$ as

$$a_{v,1} = 0 \quad \text{(V)}$$

(3.9)

Any other choice of $a_{v,1}$ would simply shift the phase of the fundamental component of the drain voltage waveform with respect to the higher order components, therefore requiring the same phase shift to higher order components to restore waveform alignment. Consequently, the time average power delivered to the load at the fundamental frequency simplifies to

$$P_L(f_0) = -\frac{b_{v,1}b_{i,1}}{2} \quad \text{(W)}$$

(3.10)

In order to perform a generalized analysis of an ideal PA, it is convenient to normalize the drain and load waveforms by the maximum drain voltage V_{max}, which can be withstood without device breakdown, and the maximum drain current I_{max} the device can support, such that

$$\bar{v}_D(\theta) = \frac{1}{\alpha V_{max}} v_D(\theta) \quad \text{(V)}$$

(3.11)

$$\bar{i}_D(\theta) = \frac{1}{\beta I_{max}} i_D(\theta) \quad \text{(A)}$$

(3.12)

$$\bar{v}_L(\theta) = \frac{1}{\alpha V_{max}} v_L(\theta) \quad \text{(V)}$$

(3.13)

$$\bar{i}_L(\theta) = \frac{1}{\beta I_{max}} i_L(\theta) \quad \text{(A)}$$

(3.14)

where α and β are scaling factors defined as

$$\alpha = \frac{1}{\max[\bar{v}_D(\theta)]} \quad \text{(V}^{-1}\text{)}$$

(3.15)

$$\beta = \frac{1}{\max[\bar{i}_D(\theta)]} \quad \text{(A}^{-1}\text{)}$$

(3.16)

The maximum values of the drain voltage and current waveforms are fixed at V_{max} and I_{max}, respectively, regardless of the harmonic content and are easily scaled. PA efficiency is expressed

as

$$\eta = \frac{P_L(f_0)}{V_{DD}I_{DD}} = \frac{\bar{P}_L(f_0)}{\bar{V}_{DD}\bar{I}_{DD}} \tag{3.17}$$

where $\bar{P}_L(f_0)$, $\bar{V}_{DD}$ and $\bar{I}_{DD}$ are the fundamental power, DC drain voltage, and DC drain current, respectively, calculated via optimization of the normalized equations (3.11) - (3.14). (3.17) refers to drain efficiency, or an upper bound to power added efficiency. (3.17) shows that PA efficiency can be maximized using the normalized equations. Once efficiency optimization using the normalized equations is performed, the corresponding fundamental output power and fundamental load impedance are calculated. Let the normalized fundamental frequency voltage Fourier coefficient and normalized fundamental frequency load impedance be defined as

$$\bar{b}_{v,1} = -\sqrt{2} \quad \text{(V)} \tag{3.18}$$

$$z_L(f_0) = 1 + jx_L(f_0) \quad (\Omega) \tag{3.19}$$

where the normalized fundamental load resistance $r_L(f_0)$ is unity and $x_L(f_0)$ is the normalized fundamental load reactance. Defining $\bar{b}_{v,1}$ and $z_L(f_0)$ in this manner results in $1\,\text{W}$ normalized output power when $x_L(f_0) = 0$. The freedom to choose convenient definitions of these quantities is due to the normalized equations given in (3.11) - (3.14). Alternate definitions would simply result in different values for the normalized quantities $\bar{V}_{DD}$, $\bar{I}_{DD}$, $\max[\bar{v}_D(\theta)]$ and $\max[\bar{i}_D(\theta)]$ without impacting the efficiency, fundamental output power, and fundamental load impedance. Given the definitions of (3.18) and (3.19), the normalized fundamental frequency Fourier coefficients of the drain current are derived as

$$\bar{a}_{i,1} = \frac{\sqrt{2}x_L(f_0)}{x_L^2(f_0) + 1} \quad \text{(A)} \tag{3.20}$$

$$\bar{b}_{i,1} = \frac{\sqrt{2}}{x_L^2(f_0) + 1} \quad \text{(A)} \tag{3.21}$$

Substituting (3.18) and (3.21) into (3.10) yields an expression for the normalized fundamental frequency average power, given by

$$\bar{P}_L(f_0) = \frac{1}{x_L^2(f_0) + 1} \quad \text{(W)} \tag{3.22}$$

The fundamental frequency average power is then expressed as

$$P_L(f_0) = \alpha\beta V_{max}I_{max}\bar{P}_L(f_0) \quad \text{(W)} \tag{3.23}$$

which through substitution of (3.15) and (4.54) simplifies the fundamental frequency average power to

$$P_L(f_0) = \frac{V_{max}I_{max}\bar{P}_L(f_0)}{\max[\bar{v}_D(\theta)]\max[\bar{i}_D(\theta)]} \quad \text{(W)} \tag{3.24}$$

In order to compare PA's having different sets of arbitrary harmonic terminations with constant V_{max} and I_{max}, the output power is normalized by the output power of a class-A amplifier, which is given by

$$P_A = \frac{V_{max}I_{max}}{8} \quad \text{(W)} \tag{3.25}$$

Dividing (3.24) by (3.25) produces an expression for fundamental output power normalized to class-A output power given by

$$p_{LA}(f_0) = \frac{8\bar{P}_L(f_0)}{\max[\bar{v}_D(\theta)]\max[\bar{i}_D(\theta)]} \tag{3.26}$$

The fundamental frequency resistance is expressed as

$$R_L(f_0) = \text{Re}\left\{\frac{\alpha V_{max}}{\beta I_{max}}(1 + jx_L(f_0))\right\} = \frac{\alpha V_{max}}{\beta I_{max}} \quad (\Omega) \tag{3.27}$$

which by substitution of (3.15) and (4.54) becomes

$$R_L(f_0) = \frac{\max[\bar{i}_D(\theta)]V_{max}}{\max[\bar{v}_D(\theta)]I_{max}} \quad (\Omega) \tag{3.28}$$

To compare the impact of harmonic terminations on the fundamental frequency resistance, it is useful to normalize by the class-A load line resistance given by

$$R_A = \frac{V_{max}}{I_{max}} \quad (\Omega) \tag{3.29}$$

Dividing (3.28) by (3.29) produces an expression for fundamental load resistance normalized to the class-A load line resistance given by

$$r_{LA}(f_0) = \frac{\max[\bar{i}_D(\theta)]}{\max[\bar{v}_D(\theta)]} \tag{3.30}$$

Similarly, the fundamental load reactance normalized to the class-A load line resistance is given by

$$x_{LA}(f_0) = \frac{\max[\bar{i}_D(\theta)]}{\max[\bar{v}_D(\theta)]} x_L(f_0) \tag{3.31}$$

Additional parameters of interest include the drain waveform peaking factors δ_V and δ_I as discussed in [45]. These factors relate the peak values of the drain waveforms to their respective DC components, and are defined as

$$\delta_V = \frac{\max[\bar{v}_D(\theta)]}{\bar{V}_{DD}} \tag{3.32}$$

and

$$\delta_I = \frac{\max[\bar{i}_D(\theta)]}{\bar{I}_{DD}} \tag{3.33}$$

These parameters give insight into the waveform peaking characteristics of different amplifier classes, allowing the designer to scale DC supply values in order to operate within the peak voltage and current limitations of the amplifying device. Note that $\delta_V = \delta_I = 2$ corresponds to a class-A PA.

3.3 Efficiency Optimization Procedure

In general, maximization of efficiency given a finite set of harmonic terminations must be performed numerically via a global optimization procedure, although special cases exist in which explicit expressions have been obtained [45]-[46]. A general procedure for numerical maximization of efficiency given a finite set of harmonic terminations is as follows:

- Define a finite set of m normalized harmonic load impedances $z_L(2f_0), z_L(3f_0), ..., z_L(mf_0)$ where voltage and current harmonics greater than m are not generated by the active device.

- Apply a global optimization algorithm to maximize the efficiency by optimizing the normalized fundamental frequency reactance $x_L(f_0)$ and the normalized drain waveform Fourier coefficients given the set of normalized harmonic load impedances. Either the current or voltage coefficients may be optimized as convenient, given the remaining coefficients are explicitly defined by the harmonic impedances.

- Once efficiency optimization is complete, use (3.26) to calculate the fundamental frequency output power normalized to class-A output power. Use (3.30) and (3.31) to calculate the fundamental frequency resistance and reactance, respectively, normalized to the class-A load line resistance.

The implementation of the general efficiency maximization procedure is performed with the MATLAB® optimization toolbox using the *fminsearch* function, which implements the direct search Nelder-Mead simplex method described in [47]. The method does not require a gradient of the function being minimized, and it is well suited for problems that exhibit discontinuities. Because the *fminsearch* function may result in a local solution, multiple sets of drain waveform Fourier coefficients and $x_L(f_0)$ initial conditions are used to ensure the global maximum efficiency is found. Given that *fminsearch* is a minimization function, the cost function is defined as negative efficiency $(-\eta)$ in order to solve for maximum efficiency. Solved efficiency, Fourier coefficients, and $x_L(f_0)$ results for specific sets of harmonic impedances were in agreement with those found using alternate optimization methods, e.g. genetic and simulated annealing [48], [49].

The detailed efficiency optimization process which is applied given a finite set of normalized harmonic load impedance constraints is as follows:

- Define the configuration parameters of the *fminsearch* function. These include the termination tolerances of the optimizer, the maximum number of cost function evaluations and the maximum number of optimizer iterations.

- Initialize the fundamental frequency reactance and the normalized harmonic drain waveform Fourier coefficients.

- Call the *fminsearch* function using the configuration parameters, $-\eta$ cost function, normalized harmonic load impedances, fundamental frequency reactance initial condition and normalized harmonic drain waveform Fourier coefficients as inputs. As mentioned above, multiple sets of initial conditions are used to ensure the global optimum is found by *fminsearch.*

The cost function evaluates $-\eta$ using values of fundamental frequency reactance and harmonic drain waveform Fourier coefficients pass to it by the *fminsearch* function along with the normalized harmonic load impedance constraints and is implemented as follows:

- Evaluate the normalized fundamental frequency drain current waveform Fourier coefficients using (3.20) and (3.21).

- Evaluate the normalized fundamental frequency average power using (3.22).

- Evaluate the global minima of the normalized drain current and voltage waveforms in the absence of their DC terms in order to find the values of $\bar{V}_{DD}$ and $\bar{I}_{DD}$ which are added to the normalized waveforms such that their minima is zero.

- Evaluate $-\eta$ using the calculated values of $\bar{P}_L(f_0)$, $\bar{V}_{DD}$ and $\bar{I}_{DD}$.

The evaluation of the global minima of the normalized drain current and voltage waveforms presents and interesting problem, especially as the number of finite harmonics assumed in the analysis increases. While discrete evaluation of the waveforms may be used to approximately find their minima, this would require increasingly fine evaluation steps as the number of harmonics increases in order to ensure that the global minimum is found. A straightforward procedure for evaluating the global minimum without requiring discrete evaluations of the drain waveforms is presented in the following subsection.

3.3.1 Evaluating the Global Minimum of a Function From Its Fourier Series Representation

Many engineering and optimization problems require evaluation of the global minimum or global maximum of a function. It is often the case that the function is of a single variable. For example, a periodic voltage or current waveform may be expressed as a single variable function, where time is the variable. A straightforward manner in which to find the critical points of any single variable function is to differentiate the function and solve for the points at which the first derivative is equal to zero. Unfortunately, as the Fourier series representation requires terms of increasing

order to accurately represent the periodic function, this method presents significant difficulty. As an example, a waveform having a Fourier series representation of order m will have a first derivative with terms up to order m. A general analytical solution to the zeroes of the first derivative do not exist in this case, therefore numerical techniques must be used to find the zeroes. However, directly applying numerical techniques to the Fourier series can be problematic, due to the large number of critical points which must be found when the order m is high.

The Weierstrass substitution is particularly applicable to the problem of finding the critical points of function given it's Fourier series representation [50]. This substitution allows expression of the sine and cosine terms of the Fourier series as polynomials in an auxiliary variable, which ultimately allows the evaluation of the waveform critical points to simplify to the problem of finding the zeroes of a polynomial. The following sections present the method and provide an example application of the method.

Method

Consider the problem of evaluating the critical points of a real valued function with a Fourier series representation given by

$$f(x) = C + \sum_{n=1}^{m}[a_n \cos(nx) - b_n \sin(nx)] \tag{3.34}$$

The standard procedure for evaluating the critical points is to differentiate (3.34) w.r.t x and set it equal to zero, yielding

$$\sum_{n=1}^{m} n[a_n \sin(nx) + b_n \cos(nx)] = 0 \tag{3.35}$$

Solving (3.35) in its present form is rather cumbersome in the general case. However, consider using the Weierstrass substitution. This substitution defines an auxiliary variable t as

$$t = \tan\left(\frac{x}{2}\right) \tag{3.36}$$

It can be shown that $\sin x$ and $\cos x$ can be expressed as ratios of polynomials, given by

$$\cos x = \frac{1 - t^2}{1 + t^2} \tag{3.37}$$

$$\sin x = \frac{2t}{1 + t^2} \tag{3.38}$$

Additionally, $\sin(nx)$ and $\cos(nx)$ may be expressed as ratios of polynomials as well using the generalized multiple angle formulas given by

$$\cos nx = \sum_{k=0}^{n} \binom{n}{k} \cos^k x \, \sin^{n-k} x \, \cos\left(\frac{1}{2}(n-k)\pi\right) \tag{3.39}$$

$$\sin nx = \sum_{k=0}^{n} \binom{n}{k} \cos^k x \, \sin^{n-k} x \, \sin\left(\frac{1}{2}(n-k)\pi\right) \tag{3.40}$$

Using (3.37) - (3.40), (3.35) can be expressed as a polynomial in t, for which robust root finding techniques exist, such as Laguerre's method [51]. Once the roots t_{root} are found, the reverse substitution is performed to determined the critical points in terms of x, given by

$$x_{critical} = 2 \tan^{-1} t_{root} \tag{3.41}$$

The values of the original function at the critical points may now be directly evaluated using (3.34) with the global minimum and global maximum being easily obtained. The polynomial will have $2m$ roots, therefore requiring up to $2m$ evaluations of (3.34) in order to find the global minimum and maximum. Fortunately, the complex roots are eliminated due to (3.41). If a root exists at $t_{root} = 0$, then it is necessary to ensure that both $x_{critical} = 0$ and $x_{critical} = \pi$ are evaluated due to the periodicity of the tangent function. It is important to note that the coefficients of the polynomial in t have closed-form expressions for any arbitrary Fourier series of order m. Therefore, the accuracy of the solved critical points depends on the numerical accuracy of the zero finding technique alone.

EXAMPLE

Consider an example where a waveform contains only up to second harmonic terms and is represented as

$$f(x) = C + \sum_{n=1}^{2} [a_n \cos(nx) - b_n \sin(nx)] \tag{3.42}$$

68

Table 3.1: Polynomial Coefficients for Waveform Containing up to Second Harmonic Terms

Term	Coefficient
t^4	$2b_2 - b_1$
t^3	$2a_1 - 8a_2$
t^2	$-12b_2$
t^1	$2a_1 + 8a_2$
t^0	$b_1 + 2b_2$

Using the method in the previous section, the coefficients of the polynomial in t which allows evaluation of the critical points are evaluated and listed in Table 3.1. Using the expressions for the polynomial coefficients in Table 3.1, the critical points of any waveform which can be represented by a Fourier series limited to order $m = 2$ can be determined. For example, consider a waveform represented by the Fourier coefficients given in Table 3.2. Table 3.3 lists the resultant roots of the polynomial and associated critical points of waveform rounded to the fourth decimal place. The critical points normalized to the waveform period are also listed in Table 3.3. Fig. 3.2 shows a single period of the resultant waveform, as well as the critical points calculated using the presented algorithm. Fig. 3.3 shows an example of the evaluated critical points for a waveform with the Fourier series limited to order $m = 10$ to demonstrate the ability of the presented method. It is evident that each critical point is precisely evaluated by the presented method, allowing for direct evaluation of the global minimum or maximum of the waveform by simply finding either the minimum or maximum of the waveform evaluated at the critical points. For these examples, the roots of the polynomial were determined using the MATLAB® function roots(), which evaluates the eigenvalues of the companion matrix formed from the polynomial coefficients.

Table 3.2: Example Fourier Coefficients

Term	Value
C	1
a_1	0.3
b_1	-0.6
a_2	0.1
b_2	0.5

Table 3.3: Example Roots and Critical Points

t_{root}	$x_{critical}$	$\frac{x_{critical}}{2\pi}$
-1.9706	4.0808	0.6495
+1.8539	2.1523	0.3425
+0.4090	0.7765	0.1236
-0.1673	5.9516	0.9472
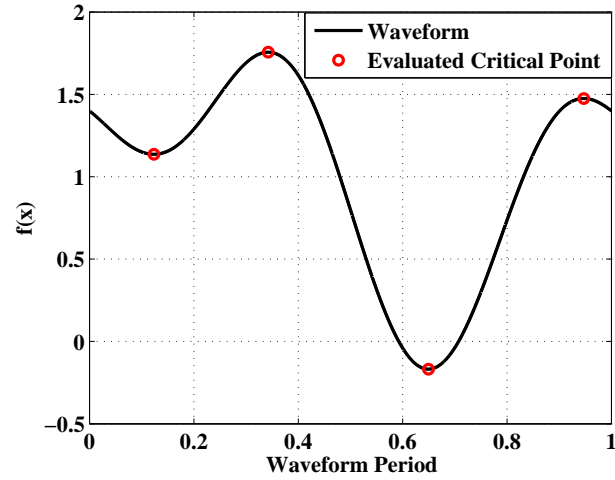
Figure 3.2: Second-order critical point evaluation example.
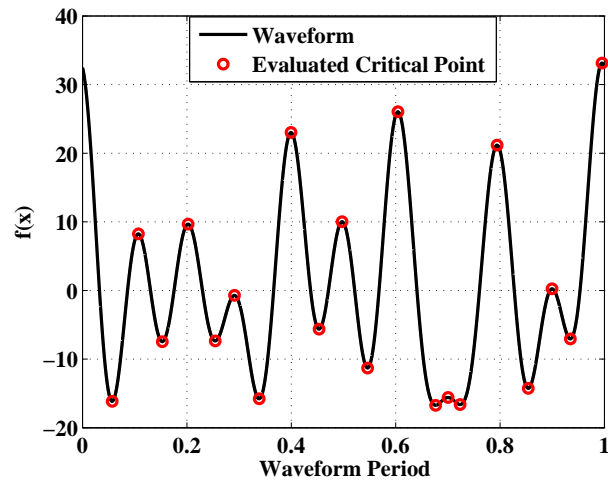
Figure 3.3: Tenth-order critical point evaluation example.

3.4 Real Fundamental Load Impedance

In this section, the method is applied to optimizing a PA with real valued fundamental load impedance with arbitrary complex harmonic terminations. The parameters of interest are efficiency, fundamental output power, and fundamental load resistance. In particular, their sensitivity to harmonic terminations is investigated.

3.4.1 Second-Harmonic Only PA

The real fundamental load impedance represents the PA configuration that will deliver maximum power given fixed values of peak voltage and current. From (3.22), the normalized power $\bar{P}_L(f_0)$ remains constant at $1\,\mathrm{W}$, independent of harmonic termination(s). Efficiency optimization is performed for second harmonic terminations spaced uniformly over the Smith Chart. For each harmonic termination, either the drain voltage coefficients $(\bar{a}_{v,2}, \bar{b}_{v,2})$ or the drain current coefficients $(\bar{a}_{i,2}, \bar{b}_{i,2})$ are selected for optimization. In the case where $z_L(2f_0) = 0$, the voltage coefficients cannot be optimized because they are necessarily zero. Therefore the current coefficients must be optimized instead. Similarly, when $z_L(2f_0) = \infty$ the current coefficients cannot be optimized because they are necessarily zero.

Fig. 3.4(a) shows efficiency contours as a function of second harmonic impedance. Maximum efficiency of 70.71% occurs under conditions of an ideal short or open circuit in agreement with [43], with degraded efficiency elsewhere. The ideal short circuit case corresponds to a second harmonic class-C PA, while the ideal open circuit case corresponds to a second harmonic class-C^{-1} PA.

A subset of the data shown in Fig. 3.4(a) is plotted in Fig. 3.4(b), which shows efficiency as a function of $\Gamma_L(2f_0)$ when $|\Gamma_L(2f_0)| = 1$, and when $\Gamma_L(2f_0)$ is purely real. For a purely reactive second harmonic termination (i.e. $|\Gamma_L(2f_0)| = 1$), 70% efficiency is achieved within $\pm 22.5°$ of a short and open circuit. For a purely real second harmonic termination (i.e. $\angle\Gamma_L(2f_0) = 0°, 180°$), 70% efficiency is achieved when $|\Gamma_L(2f_0)| \geq 0.944$.

In practice, this analysis gives insight to the PA designer concerning how closely the fabricated

second harmonic termination must be to an ideal short or open circuit to achieve a desired efficiency. For example, $\frac{R_L(f_0)}{34.7}$ must be achieved for an approximate short circuit and $34.7R_L(f_0)$ for an approximate open circuit given an ideal termination phase to achieve 70% efficiency, which is rather restrictive. A more reasonable goal would be to achieve $|\Gamma_L(2f_0)| \geq 0.8$ which would result in greater than 68% efficiency. This corresponds to $\frac{R_L(f_0)}{9}$ for an approximate short circuit and $9R_L(f_0)$ for an approximate open circuit, which is a more practical.

Fig. 3.5(a) shows contours of fundamental frequency output power, normalized to class-A. Fig. 3.5(b) shows $p_{LA}(f_0)$ from (3.26) as a function of $\Gamma_L(2f_0)$ when $|\Gamma_L(2f_0)| = 1$, and when $\Gamma_L(2f_0)$ is purely real. An output power of $0.971P_A$ is realized under conditions of maximum efficiency. A minimum output power of $0.879P_A$ occurs when $z_L(2f_0) = \pm j$, corresponding to a $0.56\,\text{dB}$ reduction relative to class-A output power. It is evident that output power may not be improved over class-A output power with only a second harmonic termination when peak current and voltage are held fixed.

Fig. 3.6(a) shows contours of fundamental frequency load resistance, normalized to the class-A load line. Fig. 3.6(b) shows $r_{LA}(f_0)$ as a function of $\Gamma_L(2f_0)$ when $|\Gamma_L(2f_0)| = 1$, and when $\Gamma_L(2f_0)$ is purely real. The load resistance exhibits a discontinuity about the imaginary axis. The load resistance under conditions of maximum efficiency is $1.03R_A$ when $z_L(2f_0) = 0$ and $0.97R_A = 1.03^{-1}R_A$ when $z_L(2f_0) = \infty$. This is due to the swapping of normalized current and voltage waveforms when the normalized load is changed from 0 to ∞, which effectively inverts (3.30). For example, when $z_L(2f_0) = \infty$, the peak voltage is increased over the class-A case, while the peak current stays the same, implying the load resistance must decrease to maintain constant V_{max} and I_{max}. In general, if the load resistance for one half of the Smith Chart (e.g. the left half) is calculated, the load resistance for the other half can be directly calculated by inverting the data, resulting in a discontinuity about the imaginary axis. In other words, the solutions from the left half of the Smith Chart correspond to current peaking drain waveforms, while the right half solutions correspond to voltage peaking.

Investigation of the waveform peaking factors defined in (3.32)-(3.33) provide insight into the

(a)

(b)
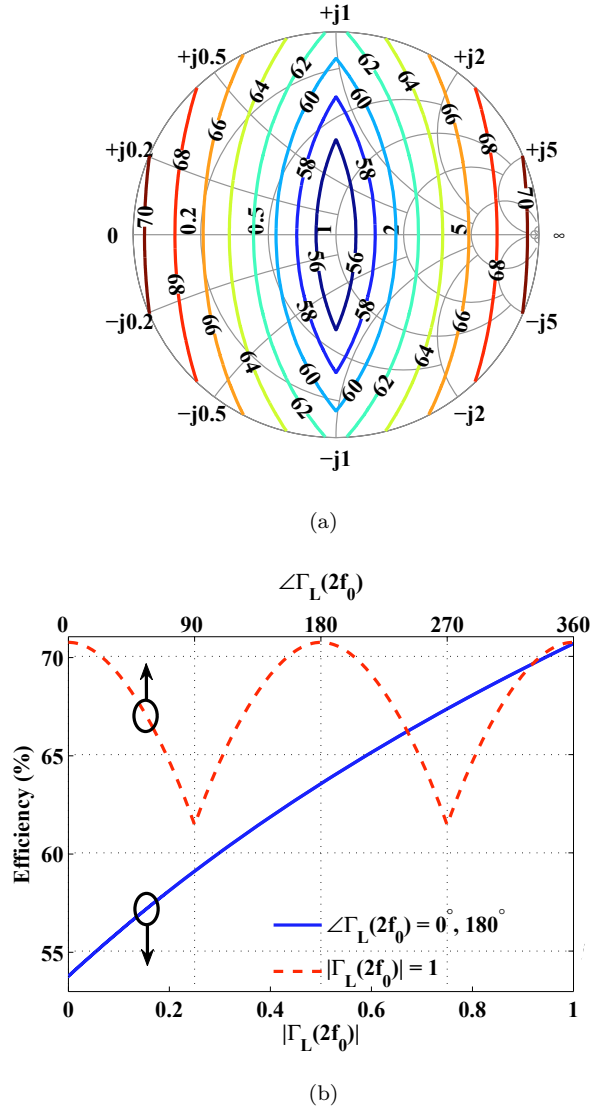
Figure 3.4: (a) Ideal second harmonic PA efficiency contours vs. $z_L(2f_0)$. The minimum efficiency of 53.76% occurs when $z_L(2f_0) = 1$. The maximum efficiency of 70.71% occurs when $z_L(2f_0) = 0$ or $z_L(2f_0) = \infty$. (b) Ideal second harmonic PA efficiency for purely resistive and purely reactive $z_L(2f_0)$. The fundamental frequency impedance $z_L(f_0)$ is purely real.

(a)

(b)
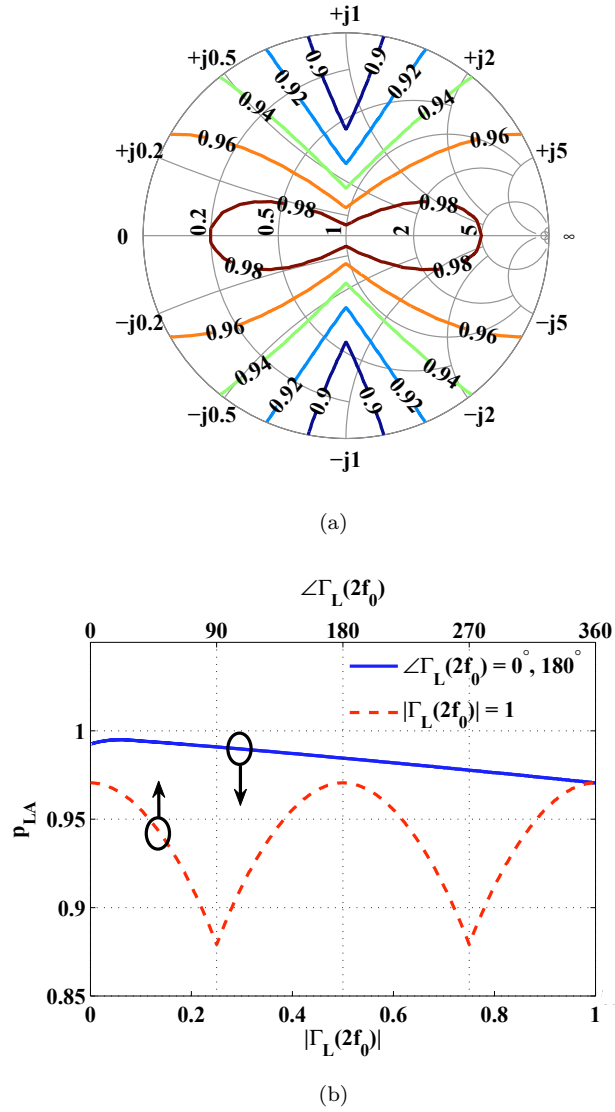
Figure 3.5: (a) Ideal second harmonic PA normalized power $p_{LA}(f_0)$ contours vs. $z_L(2f_0)$. (b) Ideal second harmonic PA $p_{LA}(f_0)$ for purely resistive and purely reactive $z_L(2f_0)$. The fundamental frequency impedance $z_L(f_0)$ is purely real.
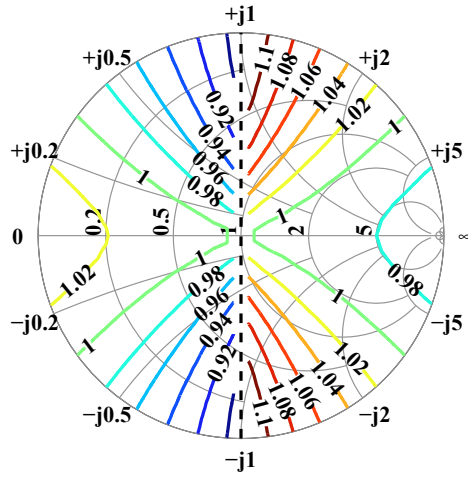
(a)
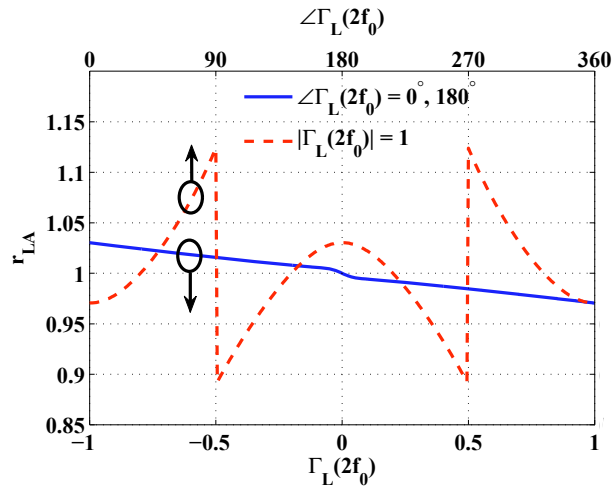
(b)

Figure 3.6: (a) Ideal second harmonic PA normalized load resistance $r_{LA}(f_0)$ contours vs. $z_L(2f_0)$. (b) Ideal second harmonic PA $r_{LA}(f_0)$ for purely resistive and purely reactive $z_L(2f_0)$. The fundamental frequency impedance $z_L(f_0)$ is purely real.
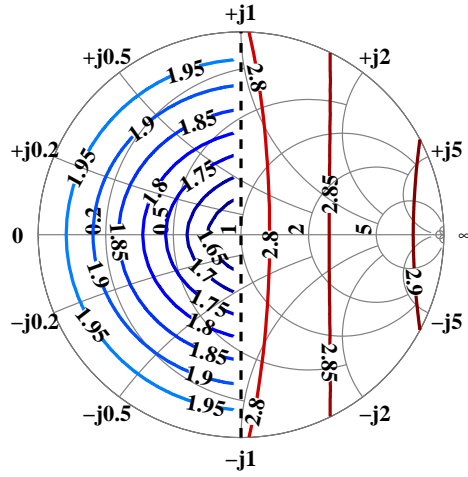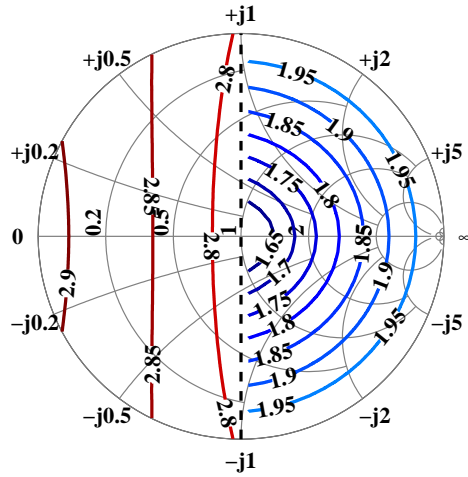
Figure 3.7: (a) Ideal second harmonic PA voltage peaking factor contours vs. $z_L(2f_0)$. The maximum voltage peaking factor of 2.9142 occurs when $z_L(2f_0) = \infty$. (b) Ideal second harmonic PA current peaking factor contours vs. $z_L(2f_0)$. The maximum current peaking factor of 2.9142 occurs when $z_L(2f_0) = 0$.
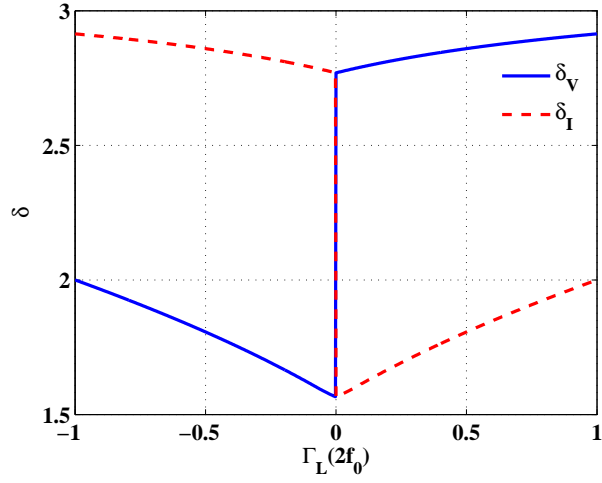
(a)
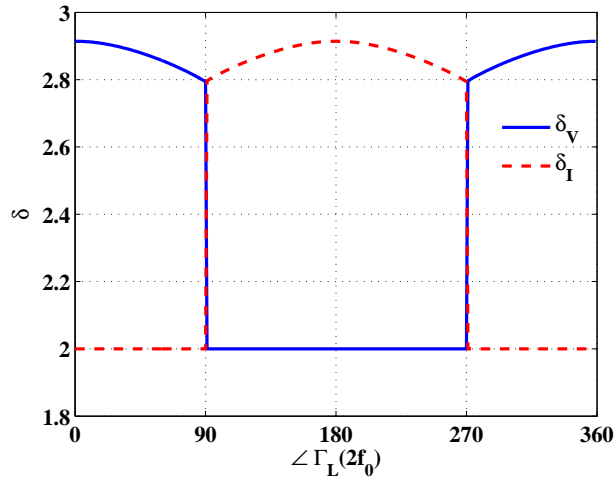
(b)

Figure 3.8: Ideal second harmonic PA peaking factors for purely resistive $z_L(2f_0)$. The fundamental frequency impedance $z_L(f_0)$ is purely real. (b) Ideal second harmonic PA $r_{LA}(f_0)$ for purely reactive $z_L(2f_0)$. The fundamental frequency impedance $z_L(f_0)$ is purely real.

structure of the optimal waveforms as a function of the second harmonic termination. Fig. 3.7 shows the peaking factor contours as a function of the second harmonic termination. It is evident that the peaking factors exhibit a discontinuity about the imaginary axis, as was the case with the resistance contours. Investigation of the peaking factors indeed shows that the transition from left to right across the imaginary axis shows the optimal efficiency PA transitions from a current peaking amplifier to a voltage peaking amplifier. At the discontinuity, there are two amplifier configurations yielding optimal efficiency; one corresponding to a current peaking PA and one corresponding to a voltage peaking PA. Fig. 3.8 shows the peaking factors as a function of $\Gamma_L(2f_0)$ when $|\Gamma_L(2f_0)| = 1$, and when $\Gamma_L(2f_0)$ is purely real. Note that for a fixed $|\Gamma_L(2f_0)|$, the voltage peaking factor remains constant on the left side of the imaginary axis, while the current peaking factor remains constant on the right side of the imaginary axis.

3.4.2 SECOND & THIRD HARMONIC PA

As demonstrated, second harmonic short and open circuits are optimal terminations from the standpoint of PA efficiency, which is in agreement with [40]. Efficiency is next re-optimized for an added third harmonic under conditions of an ideal second harmonic termination. When $z_L(2f_0)$ = 0, a peak efficiency of 81.65% is realized when $z_L(3f_0) = \infty$ as shown in Fig. 3.9(a). This set of harmonic terminations corresponds to a second & third harmonic class-F amplifier. Under the short circuit condition $z_L(2f_0) = z_L(3f_0) = 0$, an efficiency of 80.90% is simulated, which is in agreement with analysis of a finite harmonic class-C amplifier [43]. Fig. 3.9(b) shows the corresponding contours of output power normalized to class-A output power. The class-F output power is improved by $0.5\,\mathrm{dB}$ relative to class-A output power, while class-C output power is reduced $0.69\,\mathrm{dB}$ relative to class-A output power. Fig. 3.9(c) shows the corresponding contours of fundamental load resistance normalized to class-A load resistance. The class-F and class-C load resistance are $1.19R_A$ and $1.17R_A$, respectively.

Alternatively, efficiency optimization can be performed under the condition that $z_L(2f_0)$ = ∞. In this case, the resultant efficiency and power contours may be obtained by rotating

Table 3.4: Harmonically Terminated Amplifier Parameters

Class	η	$p_{LA}(f_0)$	$r_{LA}(f_0)$
Class-F $(2f_0 \ \& \ 3f_0)$	81.65 %	1.121	1.19
Class-F^{-1} $(2f_0 \ \& \ 3f_0)$	81.65 %	1.121	0.84
Class-C $(2f_0)$	70.71 %	0.971	1.03
Class-C $(2f_0 \ \& \ 3f_0)$	80.90 %	0.853	1.17
Class-C^{-1} $(2f_0)$	70.71 %	0.971	0.97
Class-C^{-1} $(2f_0 \ \& \ 3f_0)$	80.90 %	0.853	0.86

Fig. 3.9(a) and Fig. 3.9(b) 180° about the imaginary axis. The resultant resistance contours are obtained by inverting the contour values shown in Fig. 3.9(c) and rotating them 180° about the imaginary axis. The transformed contours may be used to extract the efficiency, output power, and load resistance of second and third harmonic class-F^{-1} and class-C^{-1} amplifiers. The efficiencies and output powers of the inverted amplifier classes are equivalent to those quoted for the non-inverted classes, while the load resistance is found to be the reciprocal of that for the non-inverted class. Consequently, the second and third harmonic class-F^{-1} and class-C^{-1} amplifiers require a smaller load resistance than their class-F and class-C counterparts to produce equivalent output power with maximum efficiency under conditions of fixed peak voltage and current. Table 3.4 summarizes the efficiency, fundamental output power and fundamental load resistance for second-harmonic only and second & third harmonic Class-F, Class-C, class-F^{-1} and class-C^{-1} amplifiers.

In practice, it is important to understand the sensitivity of PA efficiency to the phase and magnitude of the third harmonic termination under the condition of an ideal second harmonic termination. Fig. 3.10 shows PA efficiency as a function of $\angle\Gamma_L(3f_0)$ for the analyzed second and third harmonic cases when $|\Gamma_L(3f_0)| = 1$. The maximum and minimum efficiency when $|\Gamma_L(3f_0)| = 1$ are 81.65% and 76.30%, respectively, demonstrating the importance of terminating the third harmonic in an appropriate angle. Greater than 81% efficiency is achieved within $\pm30.0°$ of a third harmonic short when $z(2f_0) = \infty$ or a third harmonic open when $z(2f_0) = 0$. For the case of a purely resistive $z(3f_0)$, greater than 81% efficiency is achieved when $\Gamma_L(3f_0) \geq +0.9$ for $z_L(2f_0) = 0$ and $\Gamma_L(3f_0) \leq -0.9$ for $z_L(2f_0) = \infty$, as shown in Fig. 3.11. Based upon the simulated results, it is concluded that PA efficiency is less sensitive to both
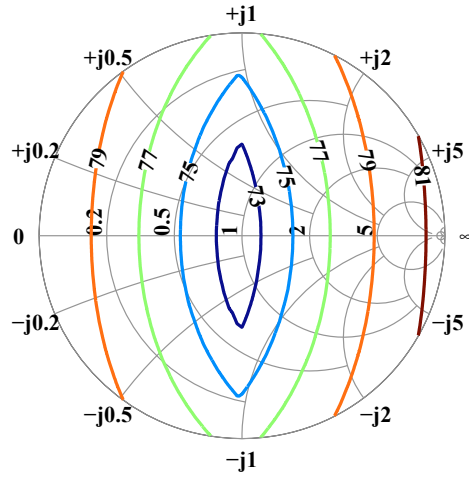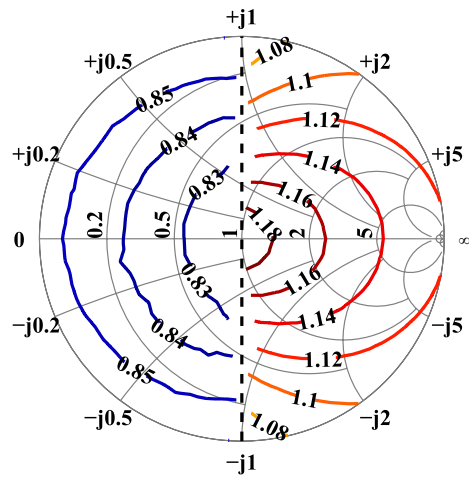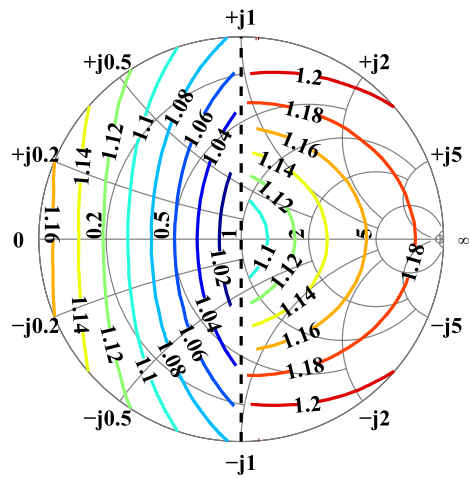
Figure 3.9: (a) Ideal PA efficiency contours vs. $z_L(3f_0)$, $z_L(2f_0) = 0$. The maximum efficiency of 81.65% occurs when $z_L(3f_0) = \infty$. Note how terminating $z_L(3f_0)$ of the third harmonic PA in any impedance improves PA efficiency over the second harmonic only PA. (b) Ideal second & third harmonic PA normalized power $p_{LA}(f_0)$ contours vs. $z_L(3f_0)$, $z_L(2f_0) = 0$. (c) Ideal second & third harmonic PA normalized load resistance $r_{LA}(f_0)$ contours vs. $z_L(3f_0)$, $z_L(2f_0) = 0$. The fundamental frequency impedance $z_L(f_0)$ is purely real.
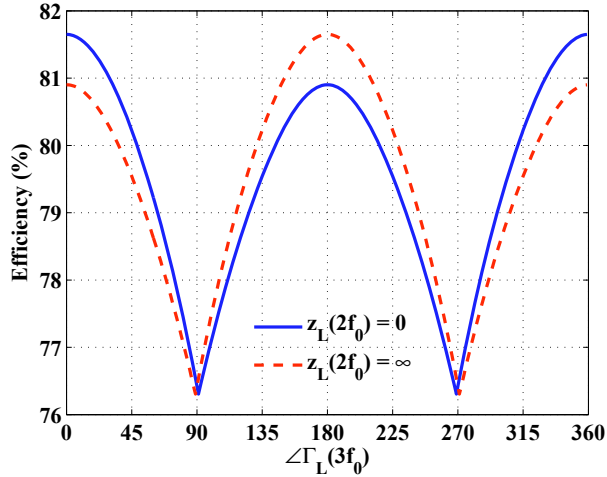
Figure 3.10: Ideal PA efficiency with fixed second harmonic versus $\angle\Gamma_L(3f_0)$, $|\Gamma_L(3f_0)| = 1$. Greater than 81% efficiency is achieved within $\pm30.0°$ of the ideal termination. The fundamental frequency impedance $z_L(f_0)$ is purely real.
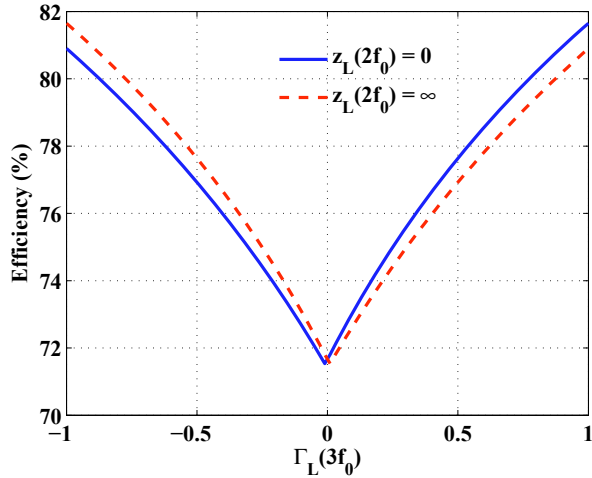
Figure 3.11: Ideal PA efficiency with fixed second harmonic versus $\Gamma_L(3f_0)$ when $\Gamma_L(3f_0)$ is purely real. Greater than 81% efficiency is achieved when $\Gamma_L(3f_0) \geq +0.9$ for $z_L(2f_0) = 0$ and $\Gamma_L(3f_0) \leq -0.9$ for $z_L(2f_0) = \infty$. The minimum efficiency of 71.52% occurs when $z_L(3f_0) \simeq z_L(f_0)$. The fundamental frequency impedance $z_L(f_0)$ is purely real.

$|\Gamma_L(3f_0)|$ and $\angle\Gamma_L(3f_0)$ than $|\Gamma_L(2f_0)|$ and $\angle\Gamma_L(2f_0)$. This is a fortunate result, given that

harmonic terminations become increasingly sensitive and difficult to realize as frequency increases.

3.5 COMPLEX FUNDAMENTAL LOAD IMPEDANCE

This section investigates optimization of the normalized fundamental frequency reactance $x_L(f_0)$ in order to maximize PA efficiency. Further optimization of PA efficiency is done at the expense of normalized output power, given (3.22). The efficiency of an ideal PA restricted to only second harmonic content is again analyzed. Unlike the analysis in the previous section, the normalized fundamental load power $\bar{P}_L(f_0)$ will not remain constant at 1 W for all second harmonic impedances. Efficiency optimization is performed as described in the previous section. However, in this case, $x_L(f_0)$ is an additional optimization parameter, resulting in three optimization parameters for a second-harmonic only PA.

Fig. 3.12, Fig. 3.13, Fig. 3.14(a) and Fig. 3.14(b) show efficiency, fundamental output power, fundamental resistance and fundamental reactance contours, respectively, as a function of second harmonic impedance when $x_L(f_0)$ is an additional optimization parameter.

The efficiency contours are significantly different than those shown in Fig. 3.4(a) and no longer symmetric about the imaginary axis. For the case when $|\Gamma_L(2f_0)| = 1$, an efficiency of 70.71% is obtained regardless of $\angle\Gamma_L(2f_0)$. It is evident that efficiency is significantly improved for much of the Smith Chart at the expense of fundamental output power, where power is reduced by 1.63 dB in the worst case. When comparing Fig. 3.13 with Fig. 3.5(a), one concludes that the fundamental frequency reactance results in an output power reduction. It is evident that the fundamental frequency resistance shown in Fig. 3.14(a) is also impacted by tuning $x_L(f_0)$. Investigation of Fig. 3.14(b) reveals that the optimal fundamental frequency reactance is zero for purely real second harmonic terminations. Given an inductive second harmonic termination, a capacitive fundamental frequency reactance is used to improve PA efficiency. Similarly, under the condition of a capacitive second harmonic termination, an inductive fundamental frequency reactance is used to improve PA efficiency.

Fig. 3.15 shows the voltage and current peaking factors as a function of second harmonic impedance when $x_L(f_0)$ is an additional optimization parameter. It is evident that the peaking factors are, in general, large than when $x_L(f_0)$ is restricted to be zero, as we shown in Fig. 3.7.
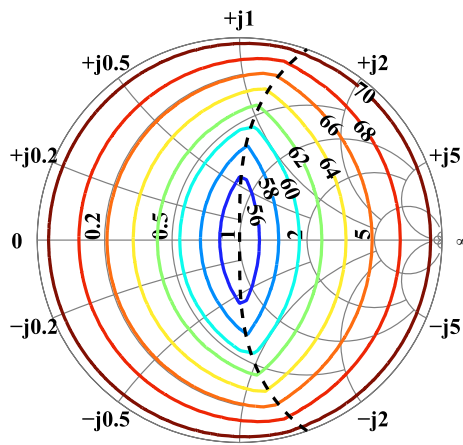
Figure 3.12: Ideal PA efficiency contours vs. $z_L(2f_0)$ when the normalized load reactance $x_L(f_0)$ is optimized in addition to the harmonic Fourier coefficients. The minimum efficiency and maximum efficiency are equivalent to those calculated without optimizing $x_L(f_0)$. However, the regions for which a given high efficiency is obtained are significantly expanded.
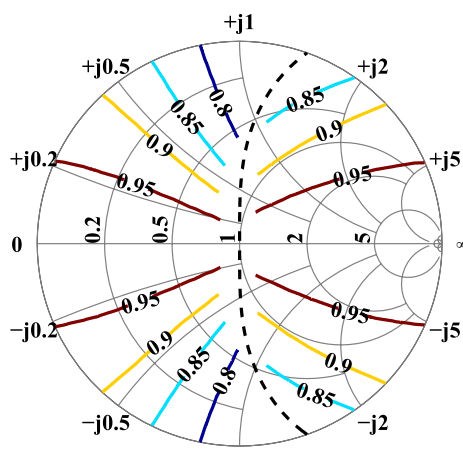
Figure 3.13: Ideal PA $p_{LA}(f_0)$ contours vs. $z_L(2f_0)$ when $x_L(f_0)$ is optimized in addition to the harmonic Fourier coefficients. Power is reduced in order to improve efficiency for much of the Smith Chart. In the worst case, power is reduced by $1.63\,\mathrm{dB}$ relative to class-A output power.
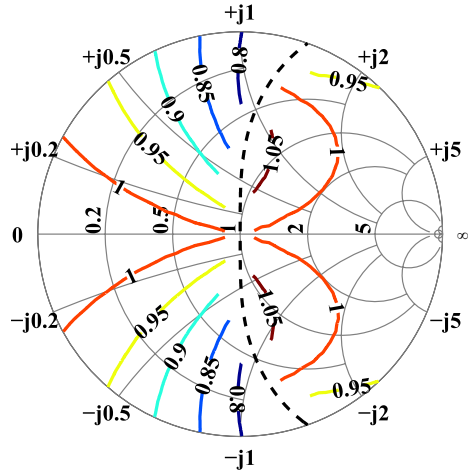
(a)
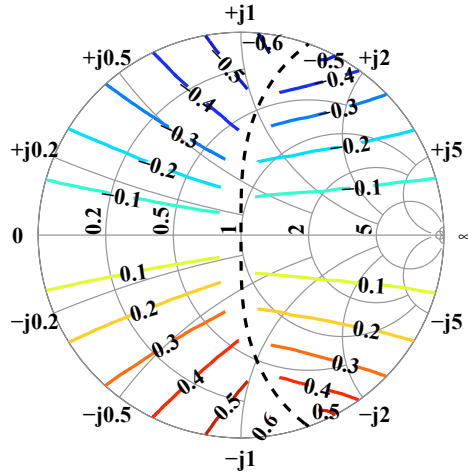
(b)

Figure 3.14: (a) Ideal PA $r_{LA}(f_0)$ contours vs. $z_L(2f_0)$ when $x_L(f_0)$ is optimized in addition to the harmonic Fourier coefficients. Note that the fundamental frequency resistance differs significantly from that shown in Fig. 3.6(a). (b) Ideal PA $x_{LA}(f_0)$ contours vs. $z_L(2f_0)$ when $x_L(f_0)$ is additionally optimized. Fundamental frequency reactance is used to restore PA efficiency under non-ideal harmonic termination conditions.
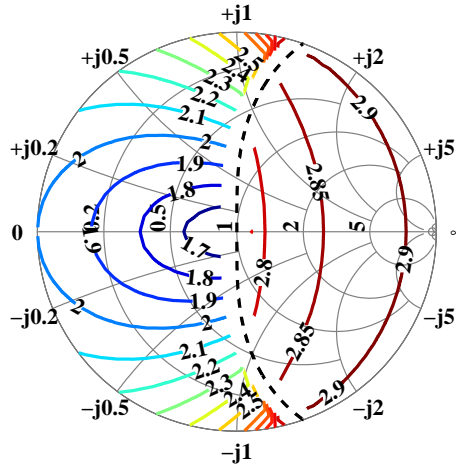
(a)
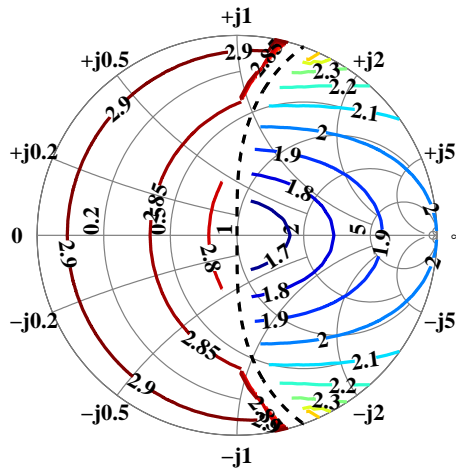
(b)

Figure 3.15: (a) Ideal PA δ_V contours vs. $z_L(2f_0)$ when $x_L(f_0)$ is optimized in addition to the harmonic Fourier coefficients. Note that the voltage peaking factor differs significantly from that shown in Fig. 3.7(a). (b) Ideal PA δ_I contours vs. $z_L(2f_0)$ when $x_L(f_0)$ is optimized in addition to the harmonic Fourier coefficients. Note that the current peaking factor differs significantly from that shown in Fig. 3.7(b).

One can conclude that the restoration of efficiency by tuning $x_L(f_0)$ not only comes at the expense of output power, but also device stress due to the large peaking factors.

In practice, the improvement in efficiency by tuning $x_L(f_0)$ supports class-J amplifier theory [52]. Tuning $x_L(f_0)$ has utility in cases where the PA designer has limited or no control over the harmonic terminations, and is forced to improve efficiency at the expense of output power. However, in the case where ideal harmonic terminations are enforceable at the virtual drain, care should be taken to do so in order to achieve maximum output power for a given PA efficiency. Note that the presented analysis does not directly apply to a class-E PA, where the equivalent output capacitance at the drain is a part of the wave shaping circuit [53].

3.5.1 CONTOUR DISCONTINUITY

During analysis of the second harmonic PA simulation results, it was found that the power, resistance, and reactance exhibited a discontinuity approximately along the parabola defined by

$$r_L(2f_0) = 1 - \frac{x_L^2(2f_0)}{2} \tag{3.43}$$

which is shown by the dashed lines in Fig. 3.12 - Fig. 3.14(b). The parabola is also shown in Fig. 3.16 on rectangular axes. Data near this parabola was subsequently eliminated prior to generation of power, resistance, and reactance contours when fundamental reactance is optimized. As with the results presented for a real fundamental load impedance, the arc defines the transition
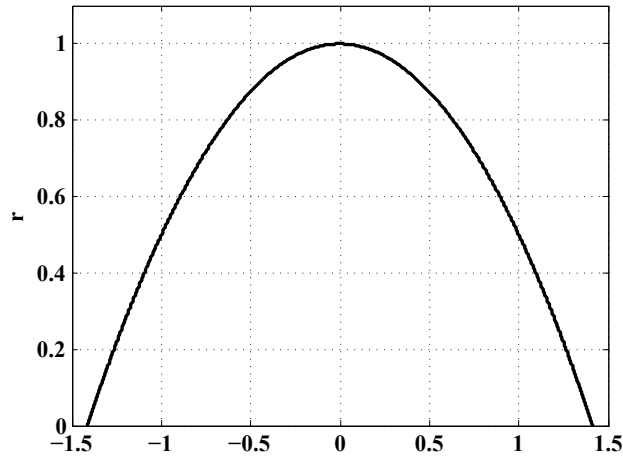
Figure 3.16: Parabolic discontinuity shown on rectangular axes of normalized resistance and normalized reactance.

between current peaking PA classes and voltage peaking PA classes. Although it is not proven that the transition occurs exactly along the arc defined in (3.43), it does provide a good approximation. Deriving the theoretical expression defining the discontinuity would very difficult if not impossible. If one could solve such a problem, then the optimizer would not be required to find the optimal efficiency solutions because this solution would be byproduct of that analysis.

3.6 Extension to Practical PA with Parasitic Output Network

The analysis and results presented in the previous sections correspond to an ideal PA model. In particular, the efficiency and power contours as a function of harmonic impedance are referenced to the impedance at the virtual drain of the transistor, rather than a measurable impedance plane. As shown in [8], the parasitics between the virtual drain and loading network not only transform the impedance, but may significantly increase the phase sensitivity of harmonic terminations at the virtual drain. As a first step towards developing a more realistic model, consider the PA block diagram that includes a constant parasitic device output capacitance C_{out} shown in Fig. 3.17. Though C_{out} can be nonlinear in some devices, it has been shown that the drain-to-source capacitance C_{DS} for a GaN HEMT device is nearly constant [54]. Since the gate-to-drain
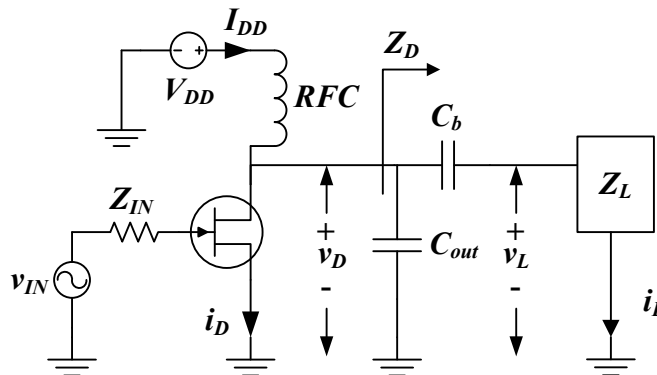
Figure 3.17: Circuit diagram of ideal common source FET-based PA with incorporation of a constant output capacitance C_{out}. The S-parameters of C_{out} represent a transformation between the virtual drain and the measurable plane corresponding to the loading network Z_L.

capacitance is significantly smaller than C_{DS}, C_{out} can be considered to be approximately linear. Another device technology having an approximately constant C_{out} is the GaAs High-Voltage HBT (HVHBT) [55]. Device technologies that have a nonlinear output capacitance would require an analysis procedure different from that presented in this section.

In general, the assumed constant C_{out} can be replaced by any two-port S-parameter model corresponding to an arbitrary linear transformation describing the parasitics. The impedance seen at the virtual drain is no longer equivalent to the impedance presented by the load (i.e. $Z_D(nf_0) \neq Z_L(nf_0)$). For the nth harmonic, the normalized impedance at the virtual drain $z_D(nf_0)$ is translated to an actual impedance $Z_D(nf_0)$ given by

$$Z_D(nf_0) = R_D(f_0)z_D(nf_0) = R_D(nf_0) + jX_D(nf_0) \tag{3.44}$$

where $R_D(f_0)$ is defined in (3.27). Note that (3.27) refers to $R_L(f_0)$, however in the ideal analysis of Section 3.2 $R_L(f_0) = R_D(f_0)$ so the expression is applicable. Additionally, note that $R_D(f_0)$ is a function of the set of harmonic terminations enforced and in general will differ for each unique set of harmonic terminations. Alternatively, $R_D(f_0)$ may be fixed at a specific value without impacting the efficiency contours shown in Fig. 3.4. However, this will result in non-constant maximum voltage and current, along with different power contours than those shown in Fig. 3.5. The reflection coefficient $\Gamma_D(nf_0)$ at the virtual drain is calculated by

$$\Gamma_D(nf_0) = \frac{z_D(nf_0) - 1}{z_D(nf_0) + 1} \tag{3.45}$$

Define the two-port S-parameters at the nth harmonic that represent the parasitic transformation between the virtual drain and a measurable reference plane as $S(nf_0)$, where the characteristic impedance of the ports is $R_D(f_0)\,\Omega$. The reflection coefficient $\Gamma_D(nf_0)$ looking into the two-port network is expressed as

$$\Gamma_D(nf_0) = S_{11}(nf_0) + \frac{S_{12}(nf_0)S_{21}(nf_0)\Gamma_L(nf_0)}{1 - S_{22}(nf_0)\Gamma_L(nf_0)} \tag{3.46}$$

where $\Gamma_L(nf_0)$ is the reflection coefficient at the measurement reference plane. The reflection coefficient $\Gamma_L(nf_0)$ at the measurable plane is calculated by rearranging (3.46) and is given by

$$\Gamma_L(nf_0) = \frac{\Gamma_D(nf_0) - S_{11}(nf_0)}{S_{22}(nf_0)\Gamma_D(nf_0) - \Delta(nf_0)} \tag{3.47}$$

where $\Delta(nf_0)$ is given by

$$\Delta(nf_0) = S_{11}(nf_0)S_{22}(nf_0) - S_{21}(nf_0)S_{12}(nf_0) \tag{3.48}$$

The normalized impedance at the measurable plane $z_L(nf_0)$ is then given by

$$z_L(nf_0) = \frac{1 + \Gamma_L(nf_0)}{1 - \Gamma_L(nf_0)} \tag{3.49}$$

Using (3.47) - (3.49), the efficiency, fundamental power, fundamental resistance and fundamental reactance contours at the virtual drain can be translated to the measurable reference plane. This method enables a theoretical analysis of efficiency and power sensitivity to device and packaging parasitics.

As an explicit example, consider the circuit diagram of Fig. 3.17 where C_{out} exists between the virtual drain and Z_L. The S-parameters of C_{out} assuming the characteristic impedance of the ports is $R_D(f_0)\,\Omega$ are given by

$$S_{11}(nf_0) = S_{22}(nf_0) = -\frac{j\pi nf_0 R_D(f_0)C_{out}}{1 + j\pi nf_0 R_D(f_0)C_{out}} \tag{3.50}$$

$$S_{21}(nf_0) = S_{12}(nf_0) = \frac{1}{1 + j\pi nf_0 R_D(f_0)C_{out}} \tag{3.51}$$

Equations (3.47) - (3.49) may now be used along with the S-parameters in order to calculate PA contours at the loading network plane rather than the virtual drain. Under the assumptions that $f_0 = 2.14\,\text{GHz}$, $R_A = 10\,\Omega$, $X_L(f_0) = 0\,\Omega$ and $C_{out} = 5\,\text{pF}$, the efficiency, power, and resistance contours are calculated as a function of $z_L(2f_0)$ and are shown in Fig. 3.18. Due to the discontinuity in $R_D(f_0)$ about the imaginary axis as discussed in Section 3.4.1, the contours shown in Fig. 3.18 were not evaluated near $\text{Re}\{\Gamma_D(2f_0)\} = 0$. The efficiency, power and resistance contours shown in Fig. 3.4, Fig. 3.5 and Fig. 3.6 experience a significant transformation due to C_{out}.

This simple example illustrates a fundamental problem the PA designer must overcome in order to achieve a high efficiency PA design. The transformation between the virtual drain and a measurable plane must be understood and carefully quantified in order to achieve a high efficiency PA via proper harmonic termination.
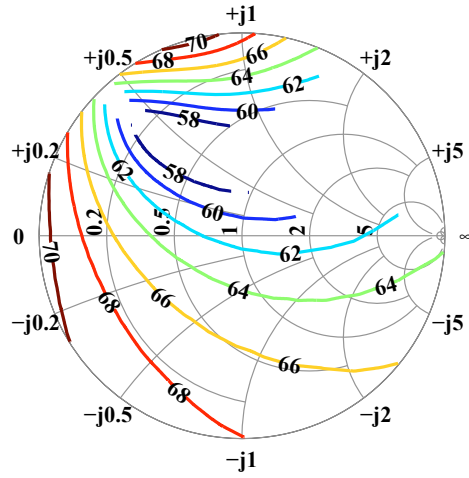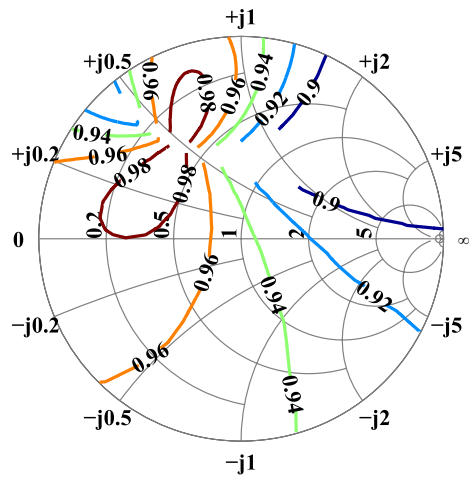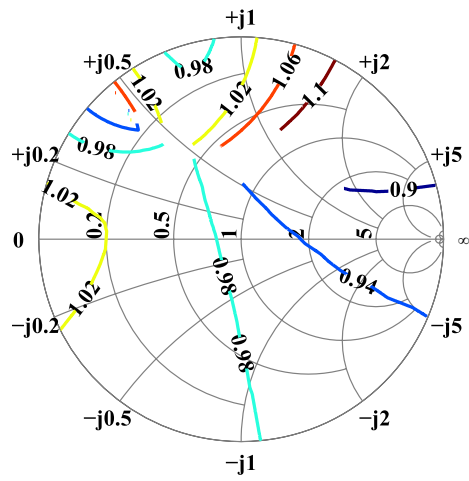
Figure 3.18: (a) Ideal PA efficiency contours vs. $z_L(2f_0)$. (b) Ideal PA $p_{LA}(f_0)$ contours vs. $z_L(2f_0)$. (c) Ideal PA $r_{LA}(f_0)$ contours vs. $z_L(2f_0)$. The contour shapes shown in Fig. 3.4, Fig. 3.5 and Fig. 3.6 are severely distorted given the transformation due to the 5 pF C_{out}.

3.7 Alternate Normalization Conditions

It is important to note that the normalization conditions defined by (3.11) - (4.54) may be redefined in many different ways if desired without impacting the maximal efficiency. However, the fundamental output power and load impedance will be impacted. For instance, it may be useful to normalize to a constant supply voltage V_{DD} and supply current I_{DD}. In this case, the normalization equations are restructured to the forms given by

$$\bar{v}_D(\theta) = \frac{1}{\alpha V_{DD}} v_D(\theta) \quad \text{(V)} \tag{3.52}$$

$$\bar{i}_D(\theta) = \frac{1}{\beta I_{DD}} i_D(\theta) \quad \text{(A)} \tag{3.53}$$

$$\bar{v}_L(\theta) = \frac{1}{\alpha V_{DD}} v_L(\theta) \quad \text{(V)} \tag{3.54}$$

$$\bar{i}_L(\theta) = \frac{1}{\beta I_{DD}} i_L(\theta) \quad \text{(A)} \tag{3.55}$$

where α and β are the redefined scaling factors given by

$$\alpha = \frac{1}{\bar{V}_{DD}} \quad \text{(V}^{-1}\text{)} \tag{3.56}$$

$$\beta = \frac{1}{\bar{I}_{DD}} \quad \text{(A}^{-1}\text{)} \tag{3.57}$$

The normalized output power, fundamental load resistance, and fundamental load reactance defined in (3.26), (3.30) and (3.31), respectively, are now given by

$$p_{LA}(f_0) = \frac{2\bar{P}_L(f_0)}{\bar{V}_{DD}\bar{I}_{DD}} \tag{3.58}$$

$$r_{LA}(f_0) = \frac{\bar{I}_{DD}}{\bar{V}_{DD}} \tag{3.59}$$

$$x_{LA}(f_0) = \frac{\bar{I}_{DD}}{\bar{V}_{DD}} x_L(f_0) \tag{3.60}$$

It is evident that the calculated fundamental output power, load resistance and load reactance will differ from those calculated when normalizing to peak voltage and current. However, it is necessary to understand that this normalization scheme places no limits on the peak voltage and current. Care should be taken to determine which normalization scheme is more appropriate for the problem at hand. As an example, the fundamental output power and resistance contours
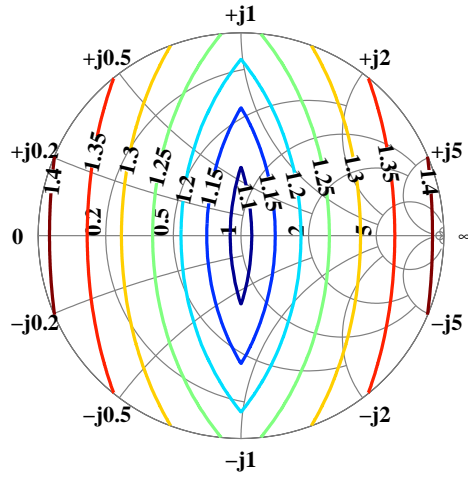
(a)
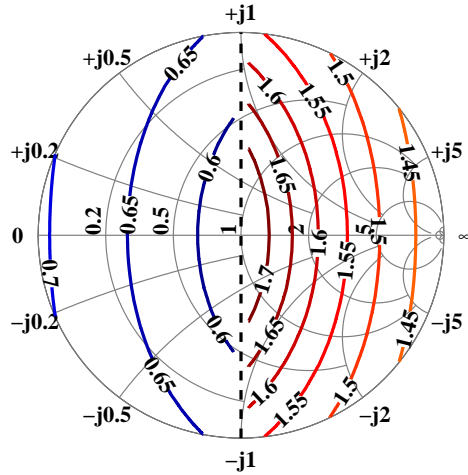
(b)

Figure 3.19: (a) Ideal PA fundamental output power contours vs. $z_L(2f_0)$ when the normalization conditions of (3.52)-(3.55) are applied. (b) Ideal PA fundamental load resistance contours vs. $z_L(2f_0)$ when the normalization conditions of (3.52)-(3.55) are applied.

for an amplifier with real fundamental load impedance limited to second harmonic voltage and current are shown in Fig. 3.19(a) and Fig. 3.19(b), respectively. Note the difference between the contours of Fig. 3.19(a) and Fig. 3.19(b) and their counterparts in Fig. 3.5(a) and Fig. 3.6(a). These differences are strictly due to the applied normalization conditions, therefore they only reflect the differences in the scale of the optimal waveforms rather than the shape.

3.8 Qualitative Experimental Validation

The goal of this chapter is to develop a generalized theoretical description of harmonically terminated power amplifiers. Full experimental verification of the theory requires variation of supply voltage and current in addition to fundamental and harmonic load impedances at the virtual drain of the device. A qualitative experimental validation was performed through load pull measurements on a Triquint TGF2023-10 50 W Discrete Power GaN on SiC HEMT [25]. A fundamental frequency load pull was performed for six unique second harmonic loads at a fixed quiescent supply voltage and current of of 28 V and 300 mA, respectively. The measured results are then de-embedded to the virtual drain of the transistor by accounting for the intrinsic output capacitance and the extrinsic impedance transformation due to the bond wires and fringing capacitance as shown in Fig. 3.20. The extrinsic transformation network was obtained by full wave HFSS simulations. The optimal drain efficiency and associated output power are shown in Fig. 3.21.
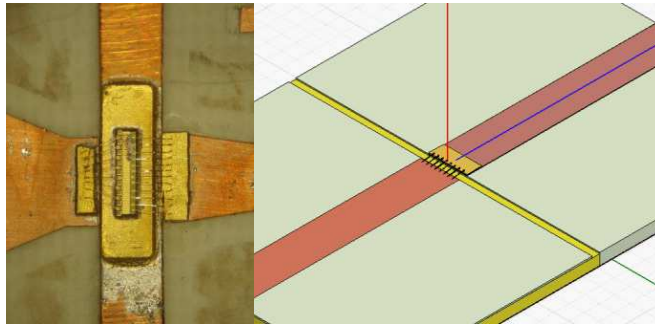
Figure 3.20: Measured device (left) and HFSS model of transformation (right). The transistor die is $824\mu m$ x $2482\mu m$ in size.

The measured data reveals several trends predicted by the theory:

- As the second harmonic termination is swept from a capacitive to inductive, the optimal fundamental impedance sweeps from inductive to capacitive. This is in agreement with the results shown in Fig. 3.14(b).

- The trend of the optimal fundamental resistance as a function of second harmonic termination is in agreement with Fig. 3.14(a).

- When the second harmonic is nearest an open circuit, the drain efficiency is maximum with an approximately real fundamental load impedance.

- High efficiency is achieved over a range of second harmonic termination phase as predicted in Fig. 3.12. For instance, points C and D in Fig. 3.21 show the same measured power, high efficiency, and optimal fundamental impedances which are very close.
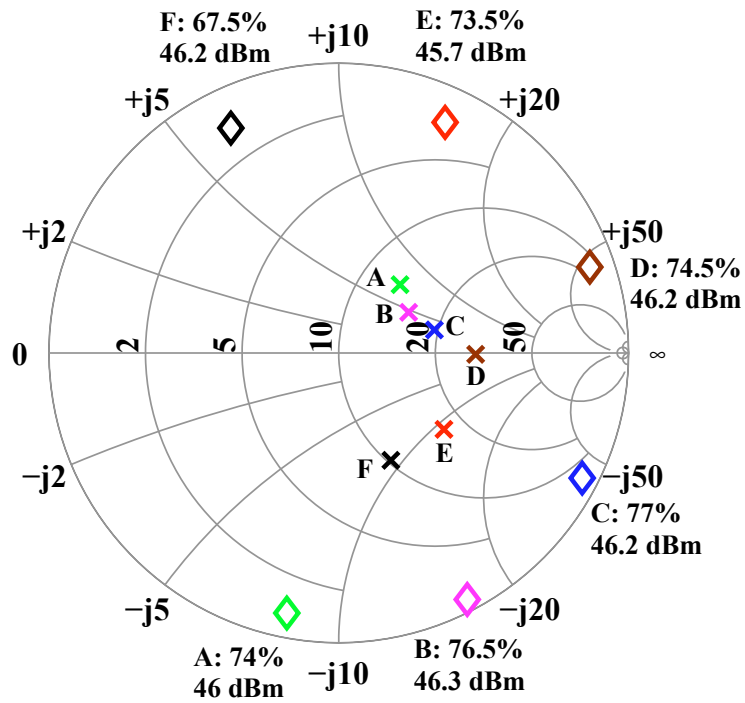
Figure 3.21: Results from harmonic load pull of Triquint $50\,\text{W}$ device on a $10\,\Omega$ Smith Chart. The points denoted by diamonds mark the second harmonic termination at the virtual drain along with resultant peak drain efficiency and associated fundamental output power. The points denoted by an x mark the fundamental load impedance resulting in peak drain efficiency for each respective second harmonic termination.

A practical experiment providing full validation of the optimal drain efficiency, fundamental output power and fundamental load impedance presented in the previous sections would require a large set of measurements, which are not always necessary for practical design. Nevertheless, the presented experimental data shows that the theory is useful for providing design insight and predicting trends.

In summary, this chapter presents a generalized analysis of PA efficiency maximization with associated fundamental output power and fundamental load impedance given arbitrary harmonic terminations. To the best of the authors' knowledge, a general treatment has not been previously presented in literature. Efficiency, fundamental output power and fundamental load resistance contours as a function of second and third harmonic terminations are calculated in Section 3.4 given a real fundamental load impedance, and provide useful guidelines for PA design.

More importantly, the analysis (Section 3.4) gives the designer information about the sensitivity of PA efficiency with respect to the magnitude and phase of the second and third harmonic load reflection coefficients. It is shown that PA efficiency is less sensitive to both $|\Gamma_L(3f_0)|$ and $\angle\Gamma_L(3f_0)$ than $|\Gamma_L(2f_0)|$ and $\angle\Gamma_L(2f_0)$. This is important for practical PA design when the harmonic frequencies are high and the harmonic impedances presented at the virtual drain are sensitive to parasitics. Adjusting the fundamental frequency load reactance $X_L(f_0)$ allows the PA designer to improve efficiency at a reduced output power given non-ideal harmonic terminations. Section 3.5 gives quantitative results for efficiency, output power, resistance and reactance contours for a second-harmonic only PA.

In practical microwave PAs, device and package parasitics can prevent the PA designer from presenting optimal harmonic terminations at the virtual drain. In that case, the results of analysis presented here quantify the fundamental output power and load impedance tradeoffs associated with improving PA efficiency via tuning the fundamental frequency reactance presented to the virtual drain of a given device.

3.9 Conclusion

The specific contributions presented in this chapter are:

- Analysis of ideal PA behavior for arbitrary complex harmonic terminations, which extends existing theory developed by Raab in [40], which was only valid for specific reactive impedances.

- In particular, this method is useful because it predicts the sensitivity of relevant PA parameters to specific impedance terminations at the harmonic frequencies. This is especially important for higher microwave frequency PAs, where the harmonics are in the millimeter-wave range, and parasitic reactances and loss can significantly affect the impedances designed at the harmonics.

- An interesting result from the theory is the limited sensitivity of efficiency and power to harmonic termination phase, which points to the possibility of extending bandwidth through use of appropriate resonant circuits.

- The theoretical approach was validated with qualitative measurements on a $2.14\,\mathrm{GHz}$ class-F^{-1} PA with second and third harmonic terminations.

- In Section 3.6, the theory was extended to include a linear transformation due to C_{out} and was further extended to include bond wires in the experimental validation. In general, the method may be applied to a PA having an arbitrary parasitic output network which is linear and characterized by S-parameters.

- The method in this chapter can be extended to include analysis of PA efficiency, output power, and output load given an arbitrary set of both input and output harmonic terminations.

- The theoretical approach and experimental validation is presented in [10].

CHAPTER 4

SUPPLY MODULATED RADAR TRANSMITTER ANALYSIS & DESIGN

CONTENTS

4.1 Introduction

Long-range system performance of solid-state phased array radar is enabled by a large number of transmit modules that produce very high transmit powers. A typical transmit module has an efficient nonlinear class-C power amplifier (PA) as the output stage [56]. This in turn restricts the transmitted pulse waveform to constant-amplitude rectangular envelopes which inherently have significant spectral content over a large bandwidth, which can interfere with other microwave systems. Amplitude modulation of the envelope provides a means to obtain spectral confinement, and has been experimentally investigated in [57, 58, 59] in an out-phasing PA with a Gaussian envelope shape, with up to a $3\,\mathrm{dB}$ peak-to-average ratio (PAR) waveform and no system efficiency reported. For these experiments, the efficiency was significantly impacted by the out-phasing due to the use of an isolated combiner. However, a Chireix out-phasing technique which uses a non-isolated combiner has potential for improving the efficiency at the expense of implementation complexity [60].

This chapter addresses the implementation of a radar transmitter having the ability to generate pulsed waveforms with both amplitude-modulation (AM) and phase-modulation (PM). The motivation of the introduction of AM to the radar signal is spectral confinement of the radar signal. The impact of the AM on the transmitted spectrum as well as other radar system performance metrics is analyzed in Section 4.2. Specifically, the transmission of a waveform having a Gaussian power envelope is investigated and compared to transmission of a uniform envelope waveform. Additionally, a comparison to applying an analogous weighting function fully on receive is analyzed.

Section 4.3 presents a method for creating spectrally confined radar signals based on Envelope Elimination and Restoration (EER) first introduced in [61]. Extensions of EER are extensively

applied to communication signals and a good overview is presented in [62]. Typical envelope supply modulators are designed for communication signals with PARs up to 10 dB. In contrast to communications signals, the radar signal is typically well known *a priori* to transmission, allowing the use of a high efficiency resonant pulse shaping supply which shapes the signal envelope as it is amplified by a high efficiency PA. A digital pre-distortion technique is used to linearize the system in order to produce envelopes with a programmable PAR. The PA used for testing the AM radar transmitter concept operates at 2.14 GHz with 78 % efficiency at 6 W peak power. A 66.4 % average efficiency over a 14.7 μs pulse with a 4.1dB PAR shaped by a 90 % efficient resonant-pulse envelope supply modulator is demonstrated. For PARs greater than 4.1 dB, the signal envelope can be split between the supply modulator and the PA drive, with up to 25 % improvement in composite efficiency.

4.2 Radar System Performance Metric Analysis

Any proposal to modify a component of a radar system must be accompanied by an analysis of the impact on system performance. The performance metrics of importance for modern radar systems are too numerous to list herein, but are covered extensively in texts such as [29, 63]. This section addresses the key impacts which applying amplitude modulation to a transmitted radar pulse has on radar performance. Specifically, impacts on the transmitted spectrum, time side-lobe level, range resolution and signal-to-noise ratio (SNR) are quantified, with SNR impacting many system metrics such as detection performance and measurement errors. Much of the analysis in the following subsections can be lumped under the discipline of radar signal analysis, and excellent texts on the subject include [64, 65].

The spectrum occupied by a transmitted radar signal has a serious impact on the ability of co-located microwave systems to maintain operability. For instance, a high power S-band radar system operating near 2.45 GHz could seriously impact nearby WiFi systems which operate at 2.45 GHz. Another example is inter-operability of co-located radar systems. Both cases require the spectrum occupied by the radar signal to be limited to allow proper operation of co-located

microwave systems.

The time domain envelope of the signal output from the radar receive filter is of extreme importance to radar system performance analysis, and is typically discussed in terms of its range resolution and time side-lobe level. The range resolution refers to the width of the main-lobe of the radar response measured at a certain level from the peak response, and is a metric which describes the ability of the system to distinguish closely spaced objects. The time side-lobe level is the level of the side-lobes of the radar response relative to the peak response, and is an indictor of the ability of the radar to suppress signal returns offset in time. This is important for preventing the masking of objects having small Radar Cross Section (RCS) by those having large RCS while offset in range.

For the analysis presented, it is assumed that the radar signal has a pulsed Linear Frequency Modulated (LFM) waveform phase modulation [64]. The LFM waveform is a popular waveform used by many modern radar systems where improved range resolution is desired. It has a complex baseband signal representation given by

$$s(t) = \frac{1}{\sqrt{T}} \text{rect}\left(\frac{t}{T}\right) e^{j\pi k t^2} \tag{4.1}$$

where $k = \frac{B}{T}$, T is the pulse-width and B is the swept bandwidth. The rectangular function $\text{rect}(x)$ is defined as

$$\text{rect}(x) = \begin{cases} 0, & |x| > \frac{1}{2} \\ 1, & |x| \leq \frac{1}{2} \end{cases} \tag{4.2}$$

Effectively, the phase is swept quadratically in order to change the frequency linearly as a function of time. As will be seen later, a parameter of importance is the time-bandwidth product γ, defined as $\gamma = BT$. Note that if the swept bandwidth B is set to zero, the signal degenerates to a pulsed continuous-wave (CW) signal.

The analyzed amplitude modulation corresponds to a Gaussian power envelope, which is created by the application of the square root of a Gaussian to the complex baseband signal. This weighting was chosen because it has very attractive spectral confinement properties. Therefore, in the cases where the transmit signal is amplitude modulated, the baseband windowing function

is given by

$$w(t) = \beta\sqrt{e^{-\frac{1}{2}\left(\alpha\frac{2t}{T}\right)^2}} = \beta e^{-\frac{1}{4}\left(\alpha\frac{2t}{T}\right)^2} = \beta e^{-\left(\alpha\frac{t}{T}\right)^2} \tag{4.3}$$

where the parameter α sets the PAR of the transmitted waveform and the parameter β is a normalization factor, as will be discussed in the following subsections.

4.2.1 Transmitted Spectrum

Un-weighted LFM Pulse

Prior to investigating the transmitted spectrum of the AM LFM signal, it is important to understand the spectrum of the LFM signal itself, which will both motivate the use of AM as well as provide results to compare to. The Fourier transform of (4.1) is given by

$$S(j\omega) = \beta \int_{-\infty}^{+\infty} \frac{1}{\sqrt{T}}\text{rect}\left(\frac{t}{T}\right)e^{j\pi k t^2}e^{-j\omega t}dt \tag{4.4}$$

The scaling factor β is defined such that

$$\beta = \frac{1}{\int_{-\infty}^{+\infty}\frac{1}{\sqrt{T}}\text{rect}\left(\frac{t}{T}\right)e^{j\pi k t^2}dt} = \frac{j\sqrt{jB}}{\text{erf}\left(\frac{j\sqrt{j\pi BT}}{2}\right)} \tag{4.5}$$

where the error function $\text{erf}(x)$ is defined as

$$\text{erf}(x) = \frac{2}{\sqrt{\pi}}\int_0^x e^{-t^2}dt \tag{4.6}$$

The definition of β in (4.5) normalizes the spectrum to the baseband DC value. Equation (4.4) simplifies to

$$S(j\omega) = \frac{\beta}{\sqrt{T}} \int_{-\frac{T}{2}}^{+\frac{T}{2}} e^{j\left(\pi k t^2 - \omega t\right)}dt \tag{4.7}$$

The indefinite form of the integral in (4.7) has the form and solution

$$\int e^{j\left(ax^2+bx\right)}dx = \sqrt{\frac{j\pi}{4a}}e^{-j\frac{b^2}{4a}}\text{erf}\left(\frac{\frac{b}{2}+ax}{\sqrt{ja}}\right) \tag{4.8}$$

which was arrived at using the MATLAB® symbolic toolbox. Note that the argument of the error function in (4.8) is complex and must be evaluated as such. By inspection of (4.8) it is evident that

$$a = \pi k$$
$$b = -\omega \tag{4.9}$$

Substituting the results of (4.9) into (4.7) results in

$$S(j\omega) = \frac{\beta}{\sqrt{T}}\sqrt{\frac{j\pi}{4\pi k}}e^{-j\frac{\omega^2}{4\pi k}}\operatorname{erf}\left(\frac{\frac{-\omega}{2}+\pi kt}{\sqrt{j\pi k}}\right)\Bigg|_{-\frac{T}{2}}^{+\frac{T}{2}} \tag{4.10}$$

which simplifies to

$$S(j\omega) = \beta\sqrt{\frac{j}{4B}}e^{-j\frac{\omega^2}{4\pi k}}\left[\operatorname{erf}\left(\frac{\pi B-\omega}{2\sqrt{j\pi k}}\right)+\operatorname{erf}\left(\frac{\pi B+\omega}{2\sqrt{j\pi k}}\right)\right] \tag{4.11}$$

The magnitude of the spectrum is then given by

$$|S(j\omega)| = |\beta|\sqrt{\frac{1}{4B}}\left|\operatorname{erf}\left(\frac{\pi B-\omega}{2\sqrt{j\pi k}}\right)+\operatorname{erf}\left(\frac{\pi B+\omega}{2\sqrt{j\pi k}}\right)\right| \tag{4.12}$$

which through substitution of (4.5) into (4.12) simplifies to

$$|S(j\omega)| = \frac{\left|\operatorname{erf}\left(\frac{\pi B-\omega}{2\sqrt{j\pi k}}\right)+\operatorname{erf}\left(\frac{\pi B+\omega}{2\sqrt{j\pi k}}\right)\right|}{2\left|\operatorname{erf}\left(\frac{j\sqrt{j\pi BT}}{2}\right)\right|} \tag{4.13}$$

Root Gaussian Weighted LFM Pulse

The Fourier transform of the root Gaussian weighted pulse is given by

$$S(j\omega) = \beta\int_{-\infty}^{+\infty}\frac{1}{\sqrt{T}}\operatorname{rect}\left(\frac{t}{T}\right)e^{j\pi kt^2}e^{-j\omega t}e^{-\left(\alpha\frac{t}{T}\right)^2}dt \tag{4.14}$$

where β is defined such that

$$\beta = \frac{1}{\int_{-\infty}^{+\infty}\frac{1}{\sqrt{T}}\operatorname{rect}\left(\frac{t}{T}\right)e^{j\pi kt^2}e^{-\left(\alpha\frac{t}{T}\right)^2}dt} = \frac{\sqrt{\alpha^2-jk\pi T^2}}{\sqrt{\pi T}\operatorname{erf}\left(\frac{\sqrt{\alpha^2-jk\pi T^2}}{2}\right)} \tag{4.15}$$

The magnitude of β expressed as

$$|\beta| = \frac{\left[\alpha^4+(\pi BT)^2\right]^{\frac{1}{4}}}{\sqrt{\pi T}\left|\operatorname{erf}\left(\frac{\sqrt{\alpha^2-j\pi BT}}{2}\right)\right|} \tag{4.16}$$

Equation (4.14) may be expressed as

$$S(j\omega) = \frac{\beta}{\sqrt{T}}\int_{-\frac{T}{2}}^{+\frac{T}{2}}e^{j\left[\left(\pi k+j\left(\frac{\alpha}{T}\right)^2\right)t^2-\omega t\right]}dt \tag{4.17}$$

The indefinite form of the integral in (4.17) has the form and solution

$$\int e^{j\left[(a+jb)x^2+cx\right]}dx = \frac{j}{2}\sqrt{\frac{\pi}{ja-b}}e^{\frac{c^2}{4(ja-b)}}\operatorname{erf}\left(\frac{\frac{c}{2}-jx(ja-b)}{\sqrt{ja-b}}\right) \tag{4.18}$$

By inspection of (4.17) it is evident that

$$a = \pi k$$

$$b = \left(\tfrac{\alpha}{T}\right)^2 \tag{4.19}$$

$$c = -\omega$$

Substituting the results of (4.19) into (4.18) results in

$$\int e^{j\left[(a+jb)x^2+cx\right]}dx = \frac{j}{2}\sqrt{\frac{\pi}{j\pi k - \left(\frac{\alpha}{T}\right)^2}}\,e^{\frac{\omega^2}{4\left[j\pi k - \left(\frac{\alpha}{T}\right)^2\right]}}\,\mathrm{erf}\left(\frac{\frac{-\omega}{2} - jt\left[j\pi k - \left(\frac{\alpha}{T}\right)^2\right]}{\sqrt{j\pi k - \left(\frac{\alpha}{T}\right)^2}}\right) \tag{4.20}$$

Substituting (4.20) into (4.17) results in

$$S(j\omega) = \frac{j\beta}{2\sqrt{T}}\sqrt{\frac{\pi}{j\pi k - \left(\frac{\alpha}{T}\right)^2}}\,e^{\frac{\omega^2}{4\left[j\pi k - \left(\frac{\alpha}{T}\right)^2\right]}}\,\mathrm{erf}\left(\frac{\frac{-\omega}{2} - jt\left[j\pi k - \left(\frac{\alpha}{T}\right)^2\right]}{\sqrt{j\pi k - \left(\frac{\alpha}{T}\right)^2}}\right)\Bigg|_{-\frac{T}{2}}^{+\frac{T}{2}} \tag{4.21}$$

which is equivalent to

$$S(j\omega) = \frac{j\beta}{2\sqrt{T}}\sqrt{\frac{\pi}{j\pi k - \left(\frac{\alpha}{T}\right)^2}}\,e^{\frac{\omega^2}{4\left[j\pi k - \left(\frac{\alpha}{T}\right)^2\right]}}\left[\mathrm{erf}\left(\frac{-\omega + B\pi + j\frac{\alpha^2}{T}}{2\sqrt{j\pi k - \left(\frac{\alpha}{T}\right)^2}}\right) + \mathrm{erf}\left(\frac{\omega + B\pi + j\frac{\alpha^2}{T}}{2\sqrt{j\pi k - \left(\frac{\alpha}{T}\right)^2}}\right)\right] \tag{4.22}$$

The magnitude is then given by

$$|S(j\omega)| = \frac{|\beta|\sqrt{\pi}}{2\sqrt{T}\left[(\pi k)^2 + \left(\frac{\alpha}{T}\right)^4\right]^{\frac{1}{4}}}\,e^{-\frac{\left(\frac{\omega\alpha}{T}\right)^2}{4\left[(\pi k)^2 + \left(\frac{\alpha}{T}\right)^4\right]}}\left|\mathrm{erf}\left(\frac{-\omega + B\pi + j\frac{\alpha^2}{T}}{2\sqrt{j\pi k - \left(\frac{\alpha}{T}\right)^2}}\right) + \mathrm{erf}\left(\frac{\omega + B\pi + j\frac{\alpha^2}{T}}{2\sqrt{j\pi k - \left(\frac{\alpha}{T}\right)^2}}\right)\right| \tag{4.23}$$

Substituting (4.16) into (4.23) and simplifying results in

$$|S(j\omega)| = \frac{e^{-\frac{(\omega\alpha)^2}{4\left[(\pi B)^2 + \left(\frac{\alpha^2}{T}\right)^2\right]}}}{2\left|\mathrm{erf}\left(\frac{\sqrt{\alpha^2 - j\pi BT}}{2}\right)\right|}\left|\mathrm{erf}\left(\frac{-\omega + B\pi + j\frac{\alpha^2}{T}}{2\sqrt{j\pi k - \left(\frac{\alpha}{T}\right)^2}}\right) + \mathrm{erf}\left(\frac{\omega + B\pi + j\frac{\alpha^2}{T}}{2\sqrt{j\pi k - \left(\frac{\alpha}{T}\right)^2}}\right)\right| \tag{4.24}$$

A potentially more insightful form of (4.24) where the spectrum is recast in terms of the time-bandwidth product γ is given by

$$|S(j\omega)| = \frac{e^{-\frac{(\omega T\alpha)^2}{4\left[(\pi\gamma)^2 + \alpha^4\right]}}}{2\left|\mathrm{erf}\left(\frac{\sqrt{\alpha^2 - j\pi\gamma}}{2}\right)\right|}\left|\mathrm{erf}\left(\frac{-\omega T + \pi\gamma + j\alpha^2}{2\sqrt{j\pi\gamma - \alpha^2}}\right) + \mathrm{erf}\left(\frac{\omega T + \pi\gamma + j\alpha^2}{2\sqrt{j\pi\gamma - \alpha^2}}\right)\right| \tag{4.25}$$

EXAMPLE

As an example, assume the pulse width T is $20\,\mu$s, the swept bandwidth B is $1\,$MHz, and α is set such that the PAR of the weighted transmit signal is $8\,$dB. The relationship between α and
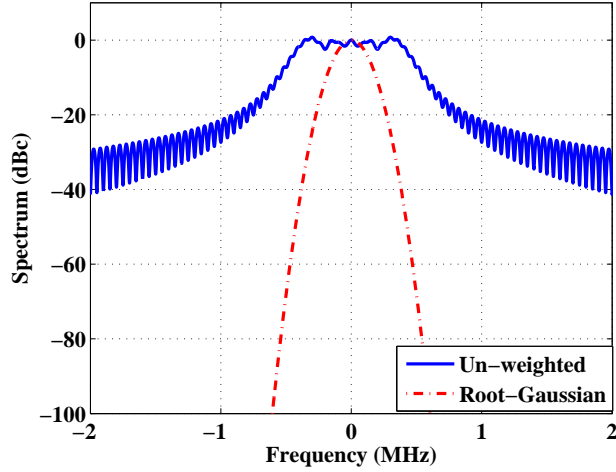
Figure 4.1: Example of un-weighted transmit spectrum versus root Gaussian Weighted transmit spectrum resulting in $8\,\mathrm{dB}$ PAR. The time-bandwidth product γ was set to 20, with the swept bandwidth B set to $1\,\mathrm{MHz}$.

PAR is derived in Section 4.2.3. For this example, (4.13) is used to evaluate the spectrum of the un-weighted transmit pulse and (4.25) is used to evaluate the spectrum of the root Gaussian weighted transmit pulse. To calculate the error function of a complex number in order to evaluate (4.13) and (4.25), [66] was used. Fig. 4.1 shows the resultant spectra. It is evident that applying the root Gaussian weighting function on transmit significantly reduces the occupied spectrum, therefore demonstrating the ability of weighting on transmit to reduce spectral content. The following sections will address the impact on other relevant radar performance parameters.

4.2.2 Received Radar Filter Output

The output of the radar receive filter is given by

$$s_o(t) = s(t) \otimes h(t) \tag{4.26}$$

where $s(t)$ is the complex representation of the transmitted radar signal, $\otimes$ denotes the convolution operator, and $h(t)$ is the complex representation of the impulse response of the receive filter. Expressed in terms of the convolution integral, (4.26) is represented as

$$s_o(t) = \int_{-\infty}^{+\infty} s(\tau)h(t - \tau)d\tau \tag{4.27}$$

When $h(t)$ is implemented as a matched filter, it is represented as

$$h_m(t) = s^*(-t) \tag{4.28}$$

where $*$ indicates the complex conjugate. Note that this definition of the matched filter is not causal, however this definition simplifies the analysis with the only impact being that the maximum of the autocorrelation will occur at $t = 0$ rather than $t = T$. If a weighting window $w(t)$ is applied on receive, then the output of the radar receive filter is given by

$$s_{o,w}(t) = s(t) \otimes (w(t)h(t)) \tag{4.29}$$

The following subsections derive the radar receive filter output for three scenarios: no weighting, weighting on receive-only, and splitting the weighting between transmit and receive. In all cases, an LFM signal is assumed, where in some cases a amplitude weighting function is applied to this phase modulated signal. The received output signal is derived assuming a no Doppler shift. To analyze the radar receive filter output as a function of both time and Doppler shift, it is necessary to investigate the ambiguity function of the radar signal as discussed in [64]. However, the analysis assuming no Doppler shift will prove insightful.

L F M - U N I F O R M   T R A N S M I T   E N V E L O P E - M A T C H E D   F I L T E R I N G

First the output of the radar receive filter will be analyzed given the transmitted waveform is an un-weighted LFM and the radar receive filter is a matched filter. Substituting (4.1) into (4.27) and using the condition of (4.28) yields

$$s_o(t) = \int_{-\infty}^{+\infty} \frac{1}{\sqrt{T}} \text{rect}\left(\frac{\tau}{T}\right) e^{j\pi k \tau^2} \frac{1}{\sqrt{T}} \text{rect}\left(\frac{\tau - t}{T}\right) e^{-j\pi k (\tau - t)^2} d\tau \tag{4.30}$$

which simplifies to

$$s_o(t) = \frac{1}{T} \int_{-\frac{T}{2}}^{+\frac{T}{2}} \text{rect}\left(\frac{\tau - t}{T}\right) e^{j\pi k (2t\tau - t^2)} d\tau \tag{4.31}$$

Define the auxiliary variable $u = \tau - t$ and substitute into (4.31) to yield

$$s_o(t) = \frac{1}{T} \int_{-\frac{T}{2} - t}^{+\frac{T}{2} - t} \text{rect}\left(\frac{u}{T}\right) e^{j\pi k (t^2 + 2tu)} du \tag{4.32}$$

Equation (4.32) can be split up into two regions, given by

$$
s_o(t) = \begin{cases} \frac{1}{T} \int_{-\frac{T}{2}-t}^{+\frac{T}{2}} e^{j\pi k(t^2+2tu)} du, & -T \le t \le 0 \\[3mm] \frac{1}{T} \int_{-\frac{T}{2}}^{+\frac{T}{2}-t} e^{j\pi k(t^2+2tu)} du, & 0 \le t \le +T \end{cases}
\tag{4.33}
$$

which evaluates to

$$
s_o(t) = \begin{cases} -\left(1+\frac{t}{T}\right) \frac{\sin\left[\pi k t T\left(1+\frac{t}{T}\right)\right]}{\pi T k t\left(1+\frac{t}{T}\right)}, & -T \le t \le 0 \\[3mm] -\left(1-\frac{t}{T}\right) \frac{\sin\left[\pi k t T\left(1-\frac{t}{T}\right)\right]}{\pi T k t\left(1-\frac{t}{T}\right)}, & 0 \le t \le +T \end{cases}
\tag{4.34}
$$

Substituting $k = +\frac{B}{T}$ into (4.34) results in

$$
s_o(t) = \begin{cases} -\left(1+\frac{t}{T}\right) \frac{\sin\left[\pi B t\left(1+\frac{t}{T}\right)\right]}{\pi B t\left(1+\frac{t}{T}\right)}, & -T \le t \le 0 \\[3mm] -\left(1-\frac{t}{T}\right) \frac{\sin\left[\pi B t\left(1-\frac{t}{T}\right)\right]}{\pi B t\left(1-\frac{t}{T}\right)}, & 0 \le t \le +T \end{cases}
\tag{4.35}
$$

Equation (4.30) can be expressed as a single equation in the form

$$
s_o(t) = -\left(1-\frac{|t|}{T}\right) \frac{\sin\left[\pi B t\left(1-\frac{|t|}{T}\right)\right]}{\pi B t\left(1-\frac{|t|}{T}\right)}, \quad -T \le t \le +T
\tag{4.36}
$$

whose magnitude is simply

$$
|s_o(t)| = \left| \left(1-\frac{|t|}{T}\right) \frac{\sin\left[\pi B t\left(1-\frac{|t|}{T}\right)\right]}{\pi B t\left(1-\frac{|t|}{T}\right)} \right|, \quad -T \le t \le +T
\tag{4.37}
$$

The expression in (4.37) serves as a reference for comparison to other filtering techniques and transmitted waveform options.

L F M - U N I F O R M T R A N S M I T E N V E L O P E - M I S M A T C H E D F I L T E R I N G

For this analysis, it will be assumed that the receive filter is weighted by the function

$$
w(t) = \beta e^{-\frac{1}{2}\left(\alpha \frac{2t}{T}\right)^2}
\tag{4.38}
$$

It is commonplace to apply weighting to the receive filter in order to control the time side-lobes [65]. The term β is defined such that the response is normalized to have unity signal gain, therefore β is given by

$$
\beta = \frac{1}{\frac{1}{T} \int_{-\frac{T}{2}}^{+\frac{T}{2}} e^{-\frac{1}{2}\left(\alpha \frac{2t}{T}\right)^2} dt}
\tag{4.39}
$$

which evaluates to

$$\beta = \frac{\sqrt{2}\alpha}{\sqrt{\pi}\mathrm{erf}\left(\frac{\alpha}{\sqrt{2}}\right)} \tag{4.40}$$

It is assumed that this weighting function is applied to the receive filter, therefore the radar receive filter response is given by

$$s_o(t) = \beta \int_{-\infty}^{+\infty} \frac{1}{\sqrt{T}}\mathrm{rect}\left(\frac{\tau}{T}\right) e^{j\pi k\tau^2} \frac{1}{\sqrt{T}}\mathrm{rect}\left(\frac{\tau-t}{T}\right) e^{-j\pi k(\tau-t)^2} e^{-\frac{1}{2}\left(\alpha\frac{2(\tau-t)}{T}\right)^2} d\tau \tag{4.41}$$

which reduces to

$$s_o(t) = \frac{\beta}{T} \int_{-\frac{T}{2}}^{+\frac{T}{2}} \mathrm{rect}\left(\frac{\tau-t}{T}\right) e^{j\pi k(2t\tau-t^2)} e^{-\frac{1}{2}\left(\alpha\frac{2(\tau-t)}{T}\right)^2} d\tau \tag{4.42}$$

Define the auxiliary variable $u = \tau - t$ and substitute into (4.42) to yield

$$s_o(t) = \frac{\beta}{T} \int_{-\frac{T}{2}-t}^{+\frac{T}{2}-t} \mathrm{rect}\left(\frac{u}{T}\right) e^{j\pi k(t^2+2tu)} e^{-\frac{1}{2}\left(\alpha\frac{2u}{T}\right)^2} du \tag{4.43}$$

which simplifies to

$$s_o(t) = \frac{\beta e^{j\pi kt^2}}{T} \int_{-\frac{T}{2}-t}^{+\frac{T}{2}-t} \mathrm{rect}\left(\frac{u}{T}\right) e^{j\left[2\pi ktu + j\frac{1}{2}\left(\alpha\frac{2u}{T}\right)^2\right]} du \tag{4.44}$$

Equation (4.44) can be split up into two regions, given by

$$s_o(t) = \begin{cases} \frac{\beta e^{j\pi kt^2}}{T} \int_{-\frac{T}{2}-t}^{+\frac{T}{2}} e^{j\left[2\pi ktu + j\frac{1}{2}\left(\alpha\frac{2u}{T}\right)^2\right]} du, & -T \leq t \leq 0 \\ \frac{\beta e^{j\pi kt^2}}{T} \int_{-\frac{T}{2}}^{+\frac{T}{2}-t} e^{j\left[2\pi ktu + j\frac{1}{2}\left(\alpha\frac{2u}{T}\right)^2\right]} du, & 0 \leq t \leq +T \end{cases} \tag{4.45}$$

The indefinite integral necessary for solution of (4.45) is given by

$$\int e^{j\left(ax+jbx^2\right)} = \frac{1}{2}\sqrt{\frac{\pi}{b}} e^{-\frac{a^2}{4b}} \mathrm{erf}\left(\frac{\frac{a}{2}+jbx}{j\sqrt{b}}\right) \tag{4.46}$$

Equation (4.46) simplifies to

$$\int e^{j\left(ax+jbx^2\right)} = \frac{1}{2}\sqrt{\frac{\pi}{b}} e^{-\frac{a^2}{4b}} \mathrm{erf}\left(\sqrt{b}x - \frac{ja}{2\sqrt{b}}\right) \tag{4.47}$$

By inspection of (4.45) it is evident that

$$a = 2\pi kt$$
$$b = \left(\frac{\sqrt{2}\alpha}{T}\right)^2 \tag{4.48}$$

Therefore, (4.47) simplifes to

$$\int e^{j\left(ax+jbx^2\right)} = \frac{T}{2\sqrt{2}\alpha}\sqrt{\pi}e^{-\left(\frac{\pi ktT}{\sqrt{2}\alpha}\right)^2}\operatorname{erf}\left(\frac{\sqrt{2}\alpha}{T}x - \frac{j\pi ktT}{\sqrt{2}\alpha}\right) \tag{4.49}$$

Define the auxiliary variable A as the product of the integral coefficient in (4.45) and the coefficient in front of the error function in (4.47) which is given by

$$A = \frac{\sqrt{\pi}\beta e^{j\pi kt^2}e^{-\left(\frac{\pi ktT}{\sqrt{2}\alpha}\right)^2}}{2\sqrt{2}\alpha} \tag{4.50}$$

The radar receive filter response is formed by substituting (4.49) and (4.50) into (4.45) resulting in

$$s_o(t) = \frac{\sqrt{\pi}\beta e^{j\pi kt^2}e^{-\left(\frac{\pi ktT}{\sqrt{2}\alpha}\right)^2}}{2\sqrt{2}\alpha}\left[\operatorname{erf}\left(\frac{\alpha}{\sqrt{2}} - \frac{\sqrt{2}\alpha|t|}{T} - \frac{j\pi B|t|}{\sqrt{2}\alpha}\right) + \operatorname{erf}\left(\frac{\alpha}{\sqrt{2}} + \frac{j\pi B|t|}{\sqrt{2}\alpha}\right)\right], \quad -T \leq t \leq +T \tag{4.51}$$

Taking the magnitude of (4.51) yields

$$|s_o(t)| = \frac{\sqrt{\pi}\beta e^{-\left(\frac{\pi Bt}{\sqrt{2}\alpha}\right)^2}}{2\sqrt{2}\alpha}\left|\operatorname{erf}\left(\frac{\alpha}{\sqrt{2}} - \frac{\sqrt{2}\alpha|t|}{T} - \frac{j\pi B|t|}{\sqrt{2}\alpha}\right) + \operatorname{erf}\left(\frac{\alpha}{\sqrt{2}} + \frac{j\pi B|t|}{\sqrt{2}\alpha}\right)\right|, \quad -T \leq t \leq +T \tag{4.52}$$

LFM - Root Gaussian Transmit Weighting - Matched Filtering

The analysis which is most relevant to an AM radar transmitter is next performed, which is applying a matched filter following transmission of a amplitude modulated pulse. The radar pulse is shaped on transmit by a root Gaussian window and the receive filter is implemented as a matched filter. The output of the radar receive filter is given by

$$s_o(t) = \beta \int_{-\infty}^{+\infty}\frac{1}{\sqrt{T}}\operatorname{rect}\left(\frac{\tau}{T}\right)e^{j\pi k\tau^2}e^{-\left(\alpha\frac{t}{T}\right)^2}\frac{1}{\sqrt{T}}\operatorname{rect}\left(\frac{\tau-t}{T}\right)e^{-j\pi k(\tau-t)^2}e^{-\left(\alpha\frac{\tau-t}{T}\right)^2}d\tau \tag{4.53}$$

The term β is defined such that the receive filter has unity signal gain, therefore β is given by

$$\beta = \frac{1}{\frac{1}{T}\int_{-\frac{T}{2}}^{+\frac{T}{2}}e^{-\left(\alpha\frac{t}{T}\right)^2}dt} \tag{4.54}$$

which evaluates to

$$\beta = \frac{\alpha}{\sqrt{\pi}\operatorname{erf}\left(\frac{\alpha}{2}\right)} \tag{4.55}$$

Equation (4.53) simplifies to

$$s_o(t) = \frac{\beta}{T} e^{-\left(\alpha \frac{t}{T}\right)^2} \int_{-\frac{T}{2}}^{+\frac{T}{2}} \mathrm{rect}\left(\frac{\tau - t}{T}\right) e^{j\pi k(2t\tau - t^2)} e^{-\left(\alpha \frac{\tau - t}{T}\right)^2} d\tau \qquad (4.56)$$

Again using the auxiliary variable $u = \tau - t$, (4.56) is expressed as

$$s_o(t) = \frac{\beta}{T} e^{-\left(\alpha \frac{t}{T}\right)^2} \int_{-\frac{T}{2}}^{+\frac{T}{2}} \mathrm{rect}\left(\frac{u}{T}\right) e^{j\pi k(t^2 + 2tu)} e^{-\left(\alpha \frac{u}{T}\right)^2} d\tau \qquad (4.57)$$

which simplifies to

$$s_o(t) = \frac{\beta}{T} e^{-\left(\alpha \frac{t}{T}\right)^2} e^{j\pi k t^2} \int_{-\frac{T}{2}}^{+\frac{T}{2}} \mathrm{rect}\left(\frac{u}{T}\right) e^{j\left[2\pi k t u + j\left(\alpha \frac{u}{T}\right)^2\right]} d\tau \qquad (4.58)$$

At this point we note that the integral is of exactly the same form as the previous section, so we may immediately write

$$s_o(t) = A \left[\mathrm{erf}\left(\frac{\alpha}{2} - \frac{\alpha|t|}{T} - \frac{j\pi B|t|}{\alpha}\right) + \mathrm{erf}\left(\frac{\alpha}{2} + \frac{j\pi B|t|}{\alpha}\right) \right], \quad -T \le t \le +T \qquad (4.59)$$

where in this case

$$A = \frac{\sqrt{\pi} \beta e^{j\pi k t^2} e^{-\left(\frac{\pi k t T}{\alpha}\right)^2} e^{-\left(\alpha \frac{t}{T}\right)^2}}{2\alpha} \qquad (4.60)$$

Plugging in the expression for A yields

$$s_o(t) = \frac{\sqrt{\pi} \beta e^{j\pi k t^2} e^{-\left(\frac{\pi k t T}{\alpha}\right)^2} e^{-\left(\alpha \frac{t}{T}\right)^2}}{2\alpha} \left[\mathrm{erf}\left(\frac{\alpha}{2} - \frac{\alpha|t|}{T} - \frac{j\pi B|t|}{\alpha}\right) + \mathrm{erf}\left(\frac{\alpha}{2} + \frac{j\pi B|t|}{\alpha}\right) \right], \quad -T \le t \le +T$$

$$(4.61)$$

Taking the magnitude yields

$$|s_o(t)| = \frac{\sqrt{\pi} \beta e^{-\left(\frac{\pi B t}{\alpha}\right)^2} e^{-\left(\alpha \frac{t}{T}\right)^2}}{2\alpha} \left| \mathrm{erf}\left(\frac{\alpha}{2} - \frac{\alpha|t|}{T} - \frac{j\pi B|t|}{\alpha}\right) + \mathrm{erf}\left(\frac{\alpha}{2} + \frac{j\pi B|t|}{\alpha}\right) \right|, \quad -T \le t \le +T$$

$$(4.62)$$

Example

As an example, assume the pulse width T is $20\,\mu\mathrm{s}$, the swept bandwidth B is $1\,\mathrm{MHz}$, and α is set such that the PAR of the weighted transmit signal is $8\,\mathrm{dB}$. Let Case A be defined as transmission of an un-weighted LFM and processing the received signal with a matched filter. Let Case B be defined as transmission of an un-weighted LFM and processing the received signal with a matched filter weighted by a Gaussian window having α set as defined above. Let Case C be

109
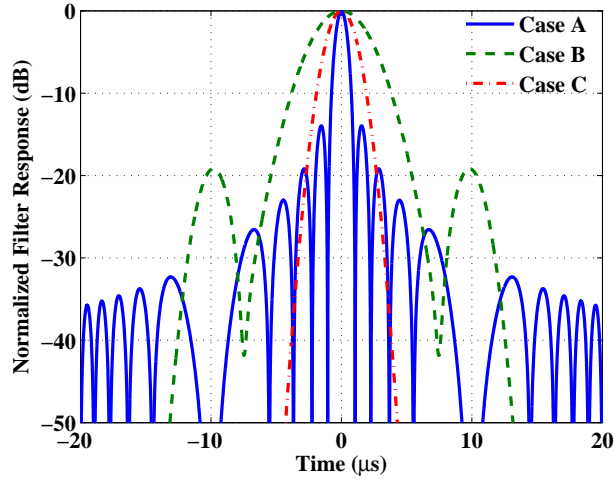
Figure 4.2: Radar receive filter response for Case A, Case B and Case C as defined above.

defined as transmission of a root Gaussian weighted LFM and processing the received signal with a matched filter, with α being set identical to Case B. For Case A, Case B and Case C (4.37), (4.52) and (4.61) are used to evaluate the radar receive filter response, respectively. Fig. 4.2 shows the resultant radar receive filter response. Note how Case A has the narrowest main-lobe, while Case B has the widest. This means that Case A has the best range resolution and largest effective bandwidth, while Case B has the worst range resolution and smallest effective bandwidth. Note that Case C has the best performance in terms of time side-lobes. They are effectively non-existent due to the implementation of the weighting on transmit along with a matched filter. This is a very desirable feature which would eliminate large objects and offset ranges interfering with the measured response.

It is evident that the window applied to the receive filter in Case B is not very productive. I greatly degrades the range resolution while providing only minimal time side-lobe reduction. Additionally, the loss associated with mismatched filtering is significant, which will be discussed in the following subsection. It should also be noted that swept bandwidth for each case could be set uniquely such that the range resolution for each case is equivalent. This will be discussed in a later subsection as well. As a final note, a disadvantage to reduction of the transmit power via amplitude modulation is that the SNR on receive will generally be degraded relative to
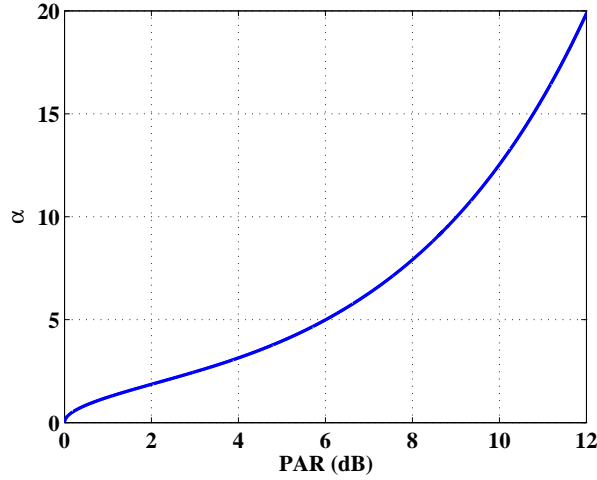
Figure 4.3: Variation of Gaussian parameter α as a function of PAR.

transmitting a uniform envelope. This is due to the average power reduction, which is discussed in the following subsection.

4.2.3 TRANSMIT POWER REDUCTION & RECEIVE FILTER MISMATCH LOSS

To allow a fair comparison of different combinations of transmit signal weighting and receive filter weighting it is necessary to consider the loss factor, which is a combination of the loss due to average power reduction on transmit if a weighting is employed and the loss due to mismatched filtering. The reduction of average power on transmit is simply the Peak-to-Average-Power-Ratio (PAR) of the transmitted signal. When the power envelope on transmit is shaped as a Gaussian using the square root of the window as defined in (4.38), it is easily shown that the PAR is given by

$$PAR = \frac{1}{\frac{1}{T}\int_{-\frac{T}{2}}^{+\frac{T}{2}} e^{-\frac{1}{2}\left(\alpha\frac{2t}{T}\right)^2}dt} = \frac{\sqrt{2}\alpha}{\sqrt{\pi}\mathrm{erf}\left(\frac{\alpha}{\sqrt{2}}\right)} \tag{4.63}$$

Fig. 4.3 shows the variation of α as a function of PAR for up to 12 dB PAR. The receive filter loss comes about when a matched filter is not applied on receive [65]. This loss is expressed as

$$L_m = \frac{\left[\int w(t)dt\right]^2}{T\int w^2(t)dt} \tag{4.64}$$

111
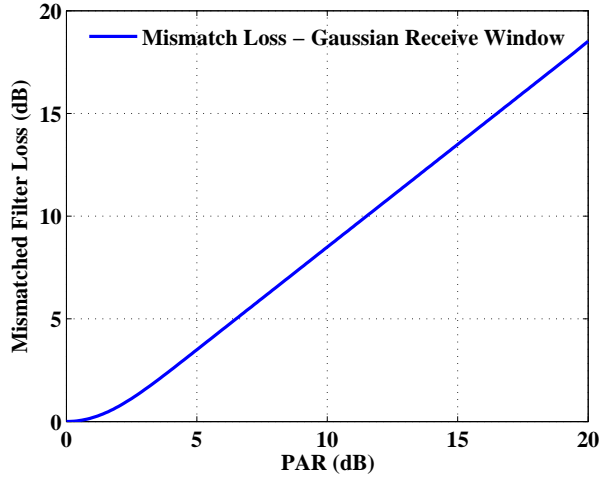
Figure 4.4: Mismatched filter loss when Gaussian window is applied to the radar receive filter as a function of PAR. The PAR corresponds to the PAR that would be achieved on transmit if the root of the window was applied to the transmitted signal, resulting in a Gaussian power envelope.

When a mismatched filter is implemented as a Gaussian filter, the mismatch loss is given by

$$L_m = \frac{\left[\int e^{-\frac{1}{2}\left(\alpha \frac{2t}{T}\right)^2} dt \right]^2}{T \int e^{-\left(\alpha \frac{2t}{T}\right)^2} dt} \tag{4.65}$$

which evaluates as

$$L_m = \frac{\sqrt{\pi}}{\alpha} \frac{\mathrm{erf}\left(\frac{\alpha}{\sqrt{2}}\right)^2}{\mathrm{erf}(\alpha)} \tag{4.66}$$

For a Gaussian window on receive, whose loss factor is given in (4.66), the loss in dB is shown in Fig. 4.4. For large PAR, the loss is approximately $1.5\,\mathrm{dB}$ greater than the PAR. In all cases, the loss is greater than the PAR. Therefore, if the only important metric is SNR, then splitting the window up between transmit and receive will always result in a lower SNR.

4.2.4 Range Resolution & Time Side-lobe Level

The range resolution of a radar corresponds to the width of the main-lobe of the radar receive filter output. In general, the range resolution is not a fixed number, for one could conceivably define it as the points at which the main-lobe decays to any arbitrary level. For the analysis performed below, the $3\,\mathrm{dB}$ range resolution will be investigated, which corresponds to the half-power width of the main-lobe of the radar receive filter output. It is noted that another means by which

the range resolution properties of a radar waveform can be analyzed is calculation of the time resolution constant as discussed in [64]. To perform a general analysis of range resolution, it will be convenient to define the normalized time variable as

$$t_n = \frac{t}{T} \tag{4.67}$$

Substituting this relationship in (4.52) recasts the radar receive filter output from an un-weighted transmit LFM and Gaussian window applied to the matched receive filter as

$$|s_o(t)| = \frac{\sqrt{\pi}\beta e^{-\left(\frac{\pi\gamma t_n}{\sqrt{2}\alpha}\right)^2}}{2\sqrt{2}\alpha} \left| \text{erf}\left(\frac{\alpha}{\sqrt{2}} - \sqrt{2}\alpha|t_n| - \frac{j\pi\gamma|t_n|}{\sqrt{2}\alpha}\right) + \text{erf}\left(\frac{\alpha}{\sqrt{2}} + \frac{j\pi\gamma|t_n|}{\sqrt{2}\alpha}\right) \right|, \quad -1 \le t_n \le +1 \tag{4.68}$$

Substituting the same relationship in (4.62) recasts the radar receive filter output from a root Gaussian weighted transmit LFM processed with a matched receive filter as

$$|s_o(t)| = \frac{\sqrt{\pi}\beta e^{-\left(\frac{\pi\gamma t_n}{\alpha}\right)^2} e^{-(\alpha t_n)^2}}{2\alpha} \left| \text{erf}\left(\frac{\alpha}{2} - \alpha|t_n| - \frac{j\pi\gamma|t_n|}{\alpha}\right) + \text{erf}\left(\frac{\alpha}{2} + \frac{j\pi\gamma|t_n|}{\alpha}\right) \right|, \quad -1 \le t_n \le +1 \tag{4.69}$$

Note that the values of β in (4.68) and (4.69) have different definitions which were defined in (4.40) and (4.55), respectively. To solve for the $3\,\text{dB}$ range resolution it is necessary to find the points at which the magnitude of the radar receive filter output is $\frac{1}{\sqrt{2}}$. Solving the (4.68) and (4.69) for this condition appears intractable, but calculating the $3\,\text{dB}$ range resolution is achievable numerically. Fig. 4.5 shows the range resolution relative to an un-weighted LFM on transmit and receive versus time bandwidth products for a $4\,\text{dB}$ PAR window either fully applied on receive or split on transmit and receive. Note that for low time-bandwidth products, splitting up the Gaussian window on transmit and receive actually results in a better range resolution than does the un-weighted transmit LFM convolved with its matched filter. This is even more evident when the PAR is increased to $12\,\text{dB}$, as shown in Fig. 4.7. The reason for the variation in range resolution is that the effective bandwidth is not equivalent for the uniform LFM and the root-Gaussian weighted LFM. If the effective bandwidths of the two schemes are made equivalent, then the range resolutions of the two schemes will be equivalent. The effective bandwidth, also
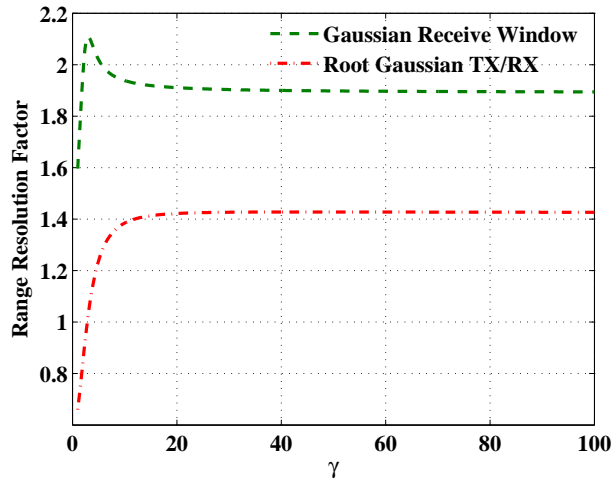
Figure 4.5: Range resolution factor versus time-bandwidth product γ for $4\,\mathrm{dB}$ PAR Gaussian window either full applied on receive or split on transmit and receive. The results are normalized to the range resolution achieved when a un-weighted LFM pulse is processed with its matched filter.
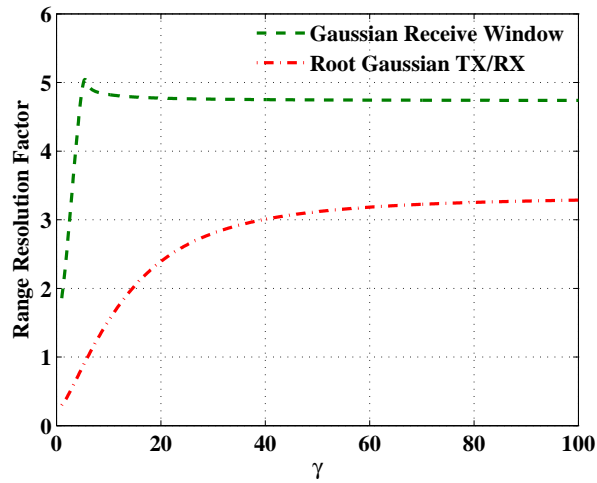
Figure 4.6: Range resolution factor versus time-bandwidth product γ for $8\,\mathrm{dB}$ PAR Gaussian window either full applied on receive or split on transmit and receive. The results are normalized to the range resolution achieved when a un-weighted LFM pulse is processed with its matched filter.
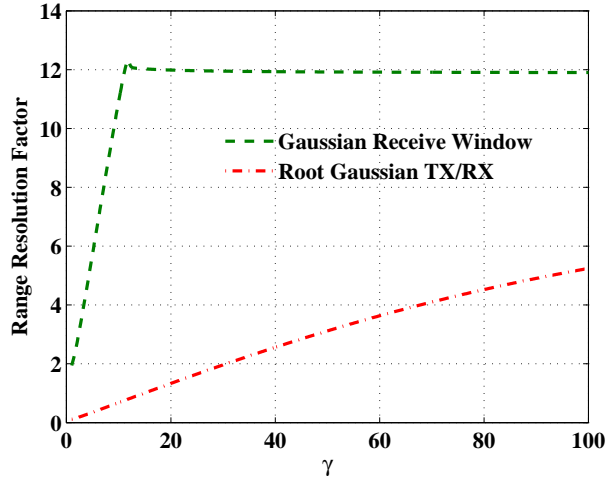
Figure 4.7: Range resolution factor versus time-bandwidth product γ for $12\,\mathrm{dB}$ PAR Gaussian window either full applied on receive or split on transmit and receive. The results are normalized to the range resolution achieved when a un-weighted LFM pulse is processed with its matched filter.

referred to as the rms bandwidth, is given as

$$B_{rms}^2 = \frac{1}{2\pi} \frac{\int_{-\infty}^{+\infty} \omega^2 |S_o(\omega)|^2 d\omega}{\int_{-\infty}^{+\infty} |S_o(\omega)|^2 d\omega} \tag{4.70}$$

where the notation has been modified from [63] to match the notation in this chapter. The term $S_o(\omega)$ corresponds to the signal voltage spectrum at the output of the radar receive filter. Given the the complexity of evaluating (4.70) for the weighted signals discussed in this chapter, a full evaluation is not presented. However, if the rms bandwidth for two different transmission and reception schemes was equivalent, it is expected that the range resolution would be the same. Here is an approximate example demonstrating this. Let us again use the $1\,\mathrm{MHz}$ $20\,\mu\mathrm{s}$ LFM modulation, but for the root-Gaussian weighted pulse we will increase the parameter B until the bandwidth for the two cases is approximately the same. It was found that $5.8\,\mathrm{MHz}$ of swept bandwidth for the $12\,\mathrm{dB}$ PAR root-Gaussian weighted pulse resulted in a nearly identical range resolution and therefore must have approximately the same effective bandwidth. Fig. 4.8 shows the transmitted spectrums for this case with Fig. 4.9 showing the radar receive filter outputs. It is evident that the $3\,\mathrm{dB}$ range resolution is the same for the two cases. However, the spectrum is far better confined with the root-Gaussian transmit pulse and the filter output has far better
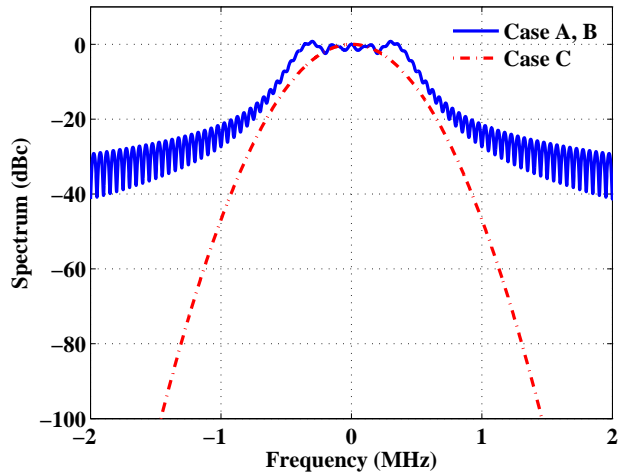
Figure 4.8: Spectrum resulting in same range resolution for cases A,B and C.
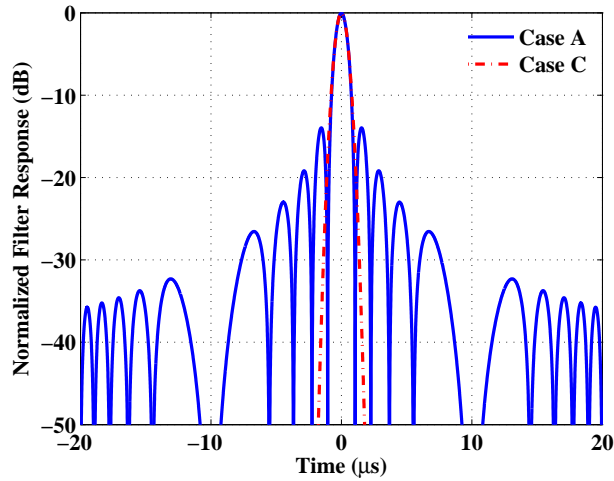
Figure 4.9: Radar receive filter output demonstrating same range resolution.

time side-lobes. The drawback however is the power, since 12 dB of average power was sacrificed to achieve the demonstrated spectrum, which is a very significant amount of power.

The time side-lobe level is also of extreme importance to modern radar systems due to its impact on target masking. For instance, a large RCS object closely spaced to a small RCS object can mask the detection of the small RCS object if the time side-lobe level is not controlled appropriately. It is evident from the presented results however, that the time side-lobe level achieved through application of a root Gaussian window on transmit is more than sufficient, given that the time side-lobes are effectively gone as shown in Fig. 4.9. This implies that the

116

actual time side-lobe level of a radar system will be set by hardware instabilities and errors such as local oscillator phase noise and clock jitter rather than the waveform transmission and processing scheme.

4.3 EFFICIENT AND LINEAR AMPLIFICATION OF SPECTRALLY CONFINED PULSED AM RADAR SIGNALS

This section discusses the implementation of a efficient linear transmitter for generation of pulsed AM radar signals with the goal of spectral confinement in mind. This is accomplished through integration of a high efficiency resonant pulse shaping supply and a high efficiency non-linear PA. Linearization is performed using a two-dimensional static pre-distortion technique which is discussed below.

4.3.1 PULSED RADAR TRANSMITTER ARCHITECTURE

Fig. 4.10 shows the transmitter architecture for creating spectrally confined pulsed radar waveforms. The desired waveform is generated and pre-distorted at baseband. The baseband signal is up-converted and amplified by the PA. The supply voltage of the PA is modulated by the resonant pulse shaping supply which is triggered by the baseband signal generator. Time alignment of the resonant pulse shaping supply and PA input envelope is critical to generating the desired transmitter output signal. When the PA is driven with a constant envelope, the waveform envelope is created by the resonant pulse shaping supply and the gain variation it introduces in the PA. However, the system is not limited to constant input PA drive, allowing for an additional degree of freedom in shaping the waveform envelope.

For this demonstration, a $2.14\,\mathrm{GHz}$ PA was designed with a TriQuint $0.25\,\mu\mathrm{m}$ GaN device, following [9]. The low-frequency stabilization capacitors on the drain bias line need to be removed to allow drain supply modulation. The PA drain bias line is connected to the resonant pulse shaping supply with a low-inductance interconnect as shown in Fig. 4.11.
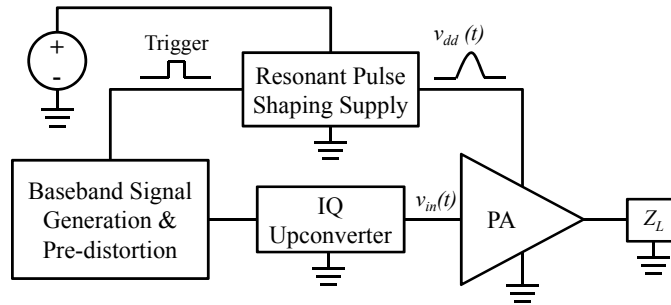
Figure 4.10: Block diagram of radar transmitter with resonant pulse shaping supply for shaping the waveform envelope allowing spectral confinement of the transmitted waveform.
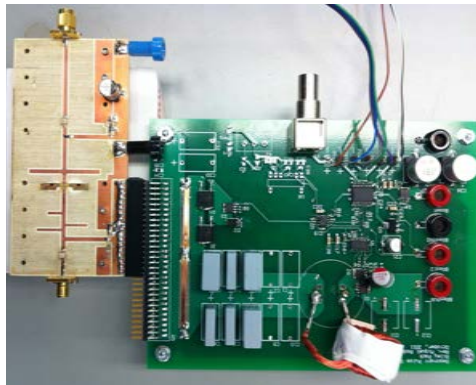
Figure 4.11: Photo of the amplifier integrated with the pulsing circuit.

The implementation of the resonant pulsing circuit is shown in Fig. 4.12. Efficient design of the pulsing circuit requires knowledge of the impedance that the PA presents to the supply, therefore characterization of the PA is required. Upon receipt of a trigger, an FPGA is used to turn on switch M_1. This produces a resonant pulse across the PA which theoretically has a raised cosine shape. Switches M_2 and M_3 are used to actively damp the pulse and improve the output wave shaping. The implemented resonant pulsing circuit has an efficiency of approximately 90 % when driving a resistive load. Further detail on the implementation of the resonant pulsing circuit is given in [11]. Fig. 4.13 shows the measured voltage $v_{DD}(t)$ when connected to the PA, which is well approximated by the square root of a Blackman window [67]. Therefore, the power envelope of the signal may easily be shaped by a Blackman window.

For this proof-of-concept demonstration, a pulse width of approximately 14.7 μs is generated. Changing the pulse width would require modification of the lumped element values indicated in
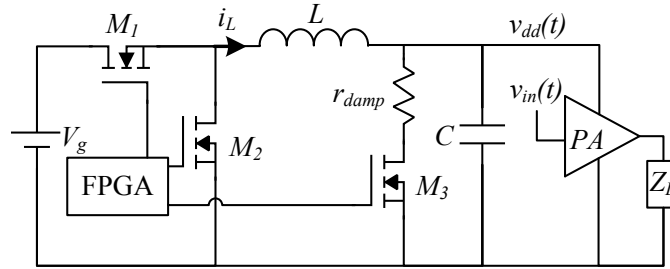
Figure 4.12: Block diagram of resonant pulse shaping supply implementation.
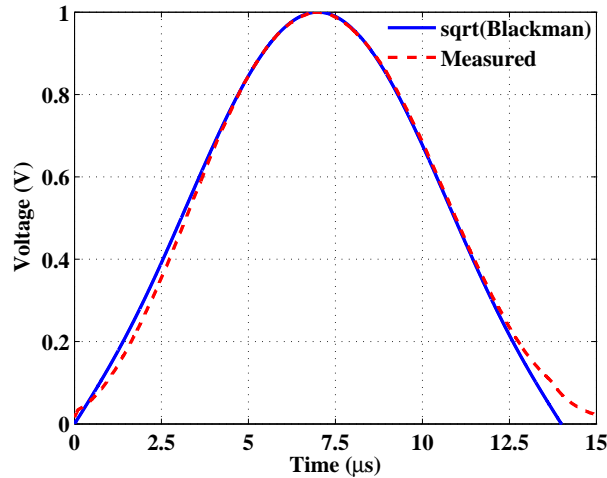
Figure 4.13: Measured supply voltage vs. time. The measured supply voltage is well approximated by the square root of a Blackman windowing function.

Fig. 4.12. However, a system implementation could include several switched resonant pulsing circuits to allow a tunable pulse width.

4.3.2   Static Digital Pre-Distortion Concept

Both envelope shape and phase of the pulse output from the PA need to be controlled in order to achieve spectral confinement of the radar waveform. Digital pre-distortion (DPD) using a Look-Up-Table (LUT) was applied, as a common technique for PA linearization and limiting spectral regrowth, e.g. [68]. Application of LUT-based pre-distortion to the system shown in Fig. 4.10 is not straightforward, since the supply modulator modifies the gain nonlinearity of the transmitter relative to that of the PA alone. Given the time varying nature of the supply waveform, a two-dimensional LUT approach was adopted. In contrast, the LUT would be a
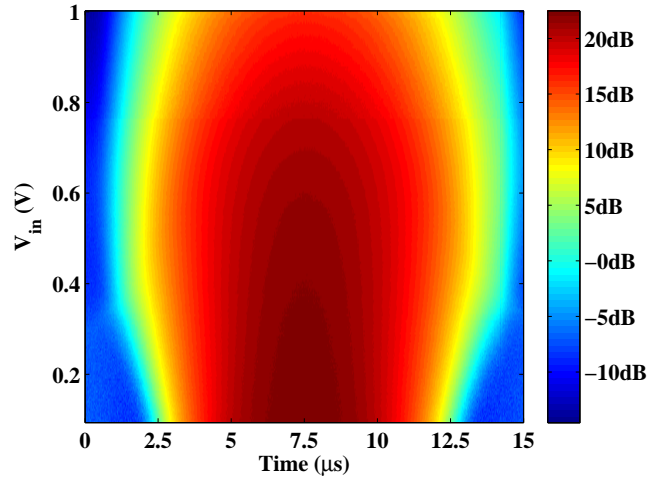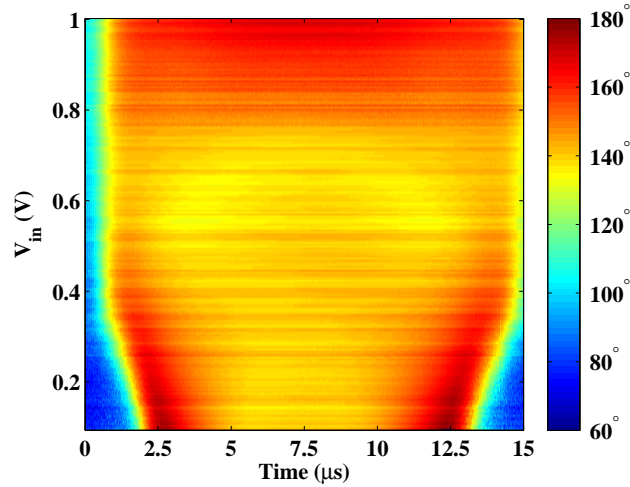
Figure 4.14: (a) Gain magnitude variation as a function of input voltage and time, normalized to peak input voltage. (b) Gain phase variation as a function of input voltage and time, normalized to peak input voltage.

one-dimensional function of input voltage for constant $v_{dd}(t)$.

Initially, the complex voltage gain of the PA connected to the resonant pulse shaping supply as a function of time and input voltage is measured. Fig. 4.14 shows the variation of the measured PA gain and phase over the duration of the pulse as a function input voltage. The input drive waveforms are pre-distorted using this data in order to achieve the appropriate output waveform envelope and phase from the PA based upon the programmed baseband waveform.

4.3.3 Experimental Setup and Measurements

MATLAB® is used to generate the ideal waveforms and apply pre-distortion corrections. The I and Q signals are downloaded to two Agilent 33250A arbitrary waveform generators and upconverted by an Agilent N9310A RF signal generator, whose output is amplified with a linear amplifier, providing the drive to the GaN PA. The output time-domain IQ waveforms are measured with an Agilent E4440A PSA series spectrum analyzer. Power calibration is performed by operating the PA in CW and comparing the spectrum analyzer measurements to those of a power meter. Average input and output power over the pulse are calculated from the spectrum analyzer measurements. Average DC power over the pulse is calculated using average current and voltage measurements input to the resonant pulse shaping supply, and scaling the power using the duty cycle. This is valid given $v_{dd}(t)$ is zero outside the pulse width and therefore the PA consumes no DC power in this region. A 14.7 μs full pulse width was used to be consistent with the approximate full pulse width of the resonant pulse shaping supply. The peak supply voltage is 30 V.

Fig. 4.15 shows the measured spectrum with a Blackman window applied to the power envelope, while the input drive is pulsed CW with slight pre-distortion corrections. Measured and simulated spectra are in good agreement, and the composite PAE is 66.4 % with 6 W peak output power and 4.16 dB PAR. Producing the same pulse shape with the same PA at a constant supply voltage of 30 V results in a PAE of 58.4 %, therefore the system improves the PAE by 13.7 %.

Fig. 4.16 shows the measured spectrum with a Gaussian window with 12 dB PAR applied to the power envelope, requiring the input drive to contain some envelope variation given the resonant supply is limited to 4.16 dB. The measured and theoretical spectra show good agreement, although it is evident that the pre-distortion does not result in the ideal response. The composite PAE in this case is 37.1 % which is a 23.7 % increase over the value obtained using pure drive modulation. Fig. 4.17 shows the efficiencies as a function of PAR, with the 4 dB measurement corresponding to application of a Blackman power window and the remaining measurements corresponding to application of a Gaussian power window with variable PAR. In all cases, the
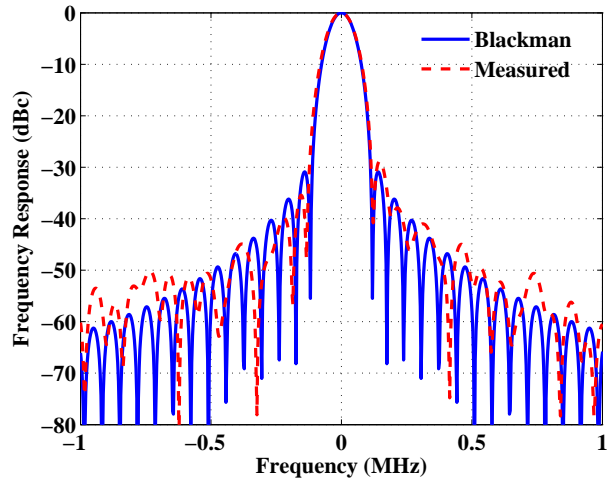
Figure 4.15: Normalized frequency response of the measured power spectrum. The is consistent with the frequency response resultant from shaping the power using a Blackman power window, which is shown in the solid blue curve.
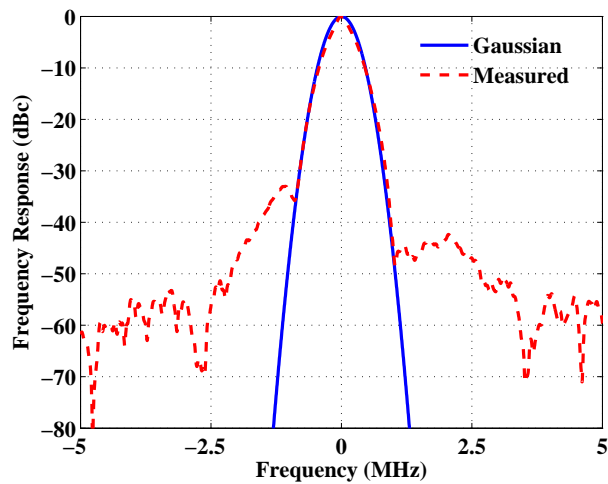
Figure 4.16: Normalized frequency response of the measured power spectrum. The is consistent with the frequency response resultant from shaping the power using a 12dB Gaussian power window, which is shown in the solid blue curve.

first sideband in the spectrum is kept below -40 dBc and the system PAE is improved over that

obtained with pure drive modulation.
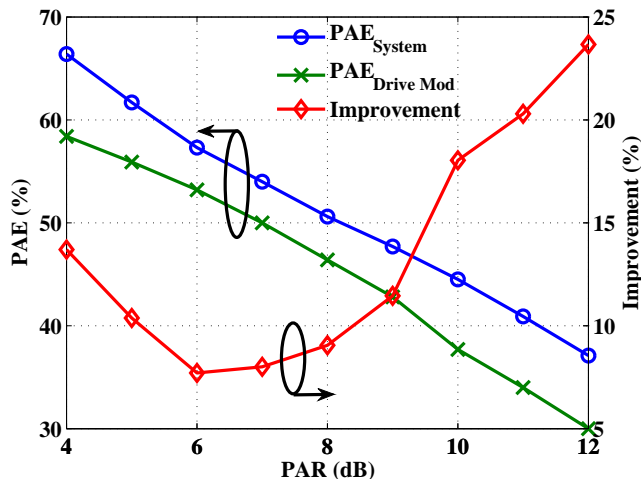
Figure 4.17: Efficiency vs. PAR comparison for 6 W output power.

4.4 Conclusion

In this chapter, a theoretical motivation has been presented for development of a radar transmitter capable of generating amplitude modulated pulses. The spectral confinement properties of a radar system capable of AM signal transmission is superior to that of one limited to constant envelope signals. However, it is also important to understand the impacts which transmission of an AM signal has on other radar performance characteristics, of which some have been investigated in the previous sections. Implementation and measurement of a system capable of high efficiency AM radar signal transmission has been detailed as well, demonstrating the feasibility of such a transmitter. The specific contributions presented in this chapter are:

- Development of theoretical analysis of the impact of amplitude-modulated pulses on radar performance, which was reported in [69].

- In collaboration with Prof. Dragan Maksimović and Dr. Miguel Rodríguez, implemented a simple efficient pulsed supply modulator with an approximately raised cosine amplitude modulation. The supply was characterized with an efficient PA from Chapter 2, with a modified bias line.

- With digital pre-distortion used for linearization, the supply-modulated PA demonstrated

reduced spectral content outside of the band of interest. The PA operates at 2.14 GHz with 78 % efficiency at 6 W peak power, and with 66.4 % average efficiency over a 14.7 μs pulse with a 4.1dB PAR shaped by a 90 % efficient resonant-pulse envelope supply modulator. For PARs greater than 4.1 dB, the signal envelope can be split between the supply modulator and the PA drive, with up to 25 % improvement in composite efficiency.

- This work is reported in [11], where details of the supply modulators are given, as well as a submitted paper to IEEE Microwave and Wireless Components Letters with focus on RF characterization and linearization [12].

CHAPTER 5

HIGH EFFICIENCY MICROWAVE

POWER RECTIFIER ANALYSIS

& DESIGN

CONTENTS

5.1 Introduction

Microwave power rectifiers play an important role in many microwave systems. From a chronological standpoint, the experiments of Nikola Tesla in the transmission and reception of wireless power for lighting applications and the method of obtaining direct from alternating currents performed in the 1890's was the first work performed in transmission and rectification of wireless power [70]. A main application of microwave power rectifiers in the early 1900's was in signal detection where crystals, vacuum tubes or diodes served as the nonlinear element [71, 72]. An excellent discussion of the early history of microwave detectors is provided in [73]. However, the early application of microwave rectifiers was specifically for extraction of information rather than extraction of DC power. The first works in application of microwave rectifiers to extraction of DC power were performed in the 1960's using diode-based rectifiers by Purdue University and Raytheon under funding from the U.S. Air Force Laboratories at Wright Field [74, 75, 76, 77, 78, 79, 80].

Free-space power transmission seemed to find a renewed interest in the early 1970's. A rather interesting microwave rectifier for production of DC power or low-frequency AC power called the Cyclotron-Wave Rectifier was introduced in [81, 82]. This device operates by adding microwave power in the form of beam cyclotron rotation to an electron beam using a Cuccia coupler. A conversion region exists where the magnetic field changes, converting the rotational energy in the cyclotron to longitudinal energy which is recovered as DC power. William C. Brown of Raytheon, one of the original researchers in the field, continued publishing diode-based rectifier work as well as introducing the term rectenna, which corresponds to an antenna for the reception microwave energy integrated with a rectifier [83, 84, 85]. In this time frame, a paper was also published concerning power combining for an array of microwave power rectifiers [86]. Within this paper, the authors inadvertently graze the topic of harmonically terminated rectifiers, of which they seem to hint at a class-F rectifier as will be discussed in detail in Section 5.3.2. A fine history of microwave power transmission was later presented by Brown in 1984 [87].

126

At present time, a plethora of excellent work is going on with diode-based rectifier circuits. Summaries of current work with state of the art rectification efficiencies, as well as excellent bodies of work in their own right include [88, 2]. The topic of rectenna use for low-power RF energy harvesting was fully investigated in [89]. Additional applications where rectifier efficiency is important include microwave power recycling [90], and DC/DC converters with extremely high frequency switching [91]. In many of the reported microwave rectifiers, filtering of the harmonics at both the input and output has been investigated, e.g [92],[93], mainly to reduce re-radiated harmonic power.

The contribution this chapter provides is the identification of the similarity between power rectifiers and power amplifiers. Given the similarity as discussed in 5.2, many of the efficiency improvement techniques developed for power amplifiers may be applied to power rectifiers as well. Particularly, the impact which harmonic terminations have on the rectification efficiency is addressed. A general rectifier analysis approach is presented in 5.3, and several classes of microwave power rectifiers are introduced. An experiment is performed with a Schottky diode-based class-C rectifier in order to demonstrate the impact of harmonic terminations on rectification efficiency. The work presented herein is not limited to use of a diode as the nonlinear rectifying element. Any element which can operate as a switch may be used, which includes transistors [94].

5.2   Relationship to Power Amplifiers

In the opinion of the author, there seems to be less understanding of power rectifiers than power amplifiers. This may be due to the extensive investigation of power amplifiers relative to rectifiers. Most likely this stems from the fact that power amplifiers arguably serve a more practical purpose: increasing the power of a microwave signal. In contrast, microwave power rectifiers seem to make little sense at first glance. Why would one wish to take a microwave signal, which certainly took some DC power to generate, and then rectify it to produce DC power? This seems to be a rather inefficient manner of making DC power in general, but in some cases it becomes necessary. For instance, there are many embedded sensors that required DC power which cannot be reached

to change batteries. These sensors could certainly benefit from wireless powering. Thus, such as in the case of wireless power transmission, the question remains how to do rectification as efficiently as possible and what topologies make sense.

If one simplifies a power amplifier to its absolute basic principle of operation, it can be simply stated that a power amplifier is a DC-RF converter. It takes as inputs microwave power and DC power, and produces as an output microwave power. As is common with most classes of amplifier analysis, the input microwave power is typically ignored, therefore the amplifier is often analyzed as having an input DC power and output microwave power, thus being a DC-RF converter. A seemingly dual problem is where RF power is the input and DC power is the output: a RF-DC converter, or rectifier. Conceptually, this is a very powerful statement because it immediately suggests that, in an ideal sense, a perfectly efficient RF-DC converter would operate in exactly the same manner as a perfectly efficient DC-RF converter. A more succinct way to say this is an efficient power amplifier should behave as an efficient microwave power rectifier, and vice versa.

From the standpoint of analysis, the analogy also suggests that different classes of microwave power rectifiers analogous to different classes of microwave power amplifiers with specific harmonic terminations exist. As will be shown in the following sections, harmonically-terminated rectifiers exhibit analogous behavior. Rectifiers which will be referred to as class-C, class-F and class-F^{-1} are analyzed and shown to have identical waveforms to amplifiers of the same classes.

5.3 POWER RECTIFIER ANALYSIS

Consider the microwave rectifier shown in Fig. 5.1. A sinusoidal microwave power source with voltage magnitude V_s and impedance R_s drives the rectifying element having a resistance $R_D(v_D)$ defined as

$$R_D(v_D) = \begin{cases} \infty, & v_D > 0 \\ 0, & v_D \leq 0 \end{cases} \tag{5.1}$$

where v_D and i_D are the instantaneous voltage across and current through the rectifying element, respectively. The dc load seen by the rectifying element is R_{DC}, while the load at the fundamental
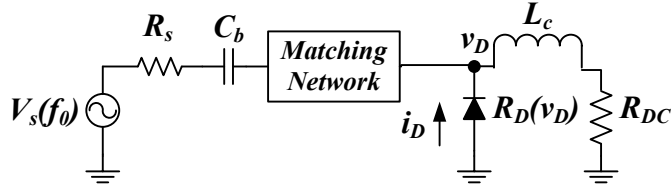
Figure 5.1: Microwave rectifier circuit diagram. An ideal blocking capacitor C_b provides dc isolation between the microwave source and rectifying element. An ideal choke inductor L_c isolates the dc load R_{DC} from RF power.

frequency f_0 and successive harmonics is set by the matching network.

While the rectifying element depicted by $R_D(v_D)$ is shown as a shunt diode in Fig. 5.1, in general it could be replaced by an alternative nonlinear device that acts as a switch, such as a transistor. In some cases presented below, the analysis is extended to include a non-zero on-resistance R_{on} and non-zero threshold voltage V_{tr}. For these cases, the resistance of the rectifying element is given by

$$R_D(v_D) = \begin{cases} \infty, & v_D > -V_{tr} \\ R_{on}, & v_D \leq -V_{tr} \end{cases} \tag{5.2}$$

The analysis of different classes of power rectifiers will now be presented based upon the harmonic terminations presented to the rectifying element, independent of the physical nonlinear device which performs the rectification.

5.3.1 CLASS-C POWER RECTIFIER

Assume the matching circuit of Fig. 5.1 presents $R_s(f_0)$ to the rectifying element with all subsequent harmonics terminated in short circuits. This is equivalent to the harmonic terminations for a canonical reduced conduction angle power amplifier. The reduced conduction angle amplifier with maximum drain efficiency is the class-C amplifier, therefore a rectifier with this set of harmonic terminations will be referred to as a class-C rectifier. The motivation for analyzing short-circuit harmonic terminations rather than opens is the intention to build the rectifier with a Schottky diode which has a significant non-linear junction capacitance. Short-circuiting the

harmonics fixes the harmonic terminations at the intrinsic diode by shorting out the non-linear junction capacitance.

When the incident RF voltage at the ideal rectifier swings negative, it is clipped at zero given (5.1). However, the enforced harmonic terminations force the voltage waveform to contain only a dc and fundamental frequency component. Therefore, a dc component must be produced by the rectifying element such that the voltage waveform maintains its sinusoidal nature. The voltage across the rectifying element can now be expressed as

$$v_D(\theta) = V_{DC} + V_D(f_0)\sin\theta \tag{5.3}$$

where $V_D(f_0)$ is the fundamental frequency component of the voltage across the rectifying element, V_{DC} is the dc component, $V_{DC} = V_D(f_0)$ and $\theta = 2\pi f_0 t$. The current waveform contains infinite frequency components, and is expressed as

$$i_D(\theta) = 2\pi I_{DC}\delta\left(\theta - \frac{3\pi}{2} - 2n\pi\right), \quad n = 0, 1, ..., \infty \tag{5.4}$$

where I_{DC} is the dc current and $\delta(\theta)$ is the Dirac delta function.

When all available input power P_{in} is delivered to the rectifier, the fundamental frequency component of the current through the rectifying element $I_D(f_0)$ is expressed as

$$I_D(f_0) = \frac{2P_{in}}{V_D(f_0)} \tag{5.5}$$

Additionally, since there is no mechanism by which the rectifier itself can dissipate power, all of the available input power must be dissipated in the DC load and the conversion efficiency is 100%. Therefore,

$$P_{in} = V_{DC}I_{DC} \tag{5.6}$$

Substituting in (5.5) and rearranging yields the relationship

$$I_D(f_0) = 2I_{DC} \tag{5.7}$$

Therefore, the optimal dc load is given by

$$R_{DC} = 2R_s(f_0) \tag{5.8}$$

130

When all available input power is delivered to the rectifier, the RF-DC conversion efficiency is 100% because the rectifying element is ideal and cannot dissipate power itself. In order for all available input power to be delivered to the rectifier, it is straightforward to show that the dc load must be set relative to the fundamental frequency load as (5.8).

A harmonic balance simulation of an approximately ideal rectifier with short-circuited harmonic terminations was performed in Microwave Office® using the SPICE diode model with no parasitics (PNIV) as the rectifying element. The device temperature was set to $1°$ K to approximate an ideal switch. The fundamental frequency excitation was set to $1\,\mathrm{W}$ at $1\,\mathrm{GHz}$ with the first 200 harmonics terminated in short-circuits. The diode was presented with $50\,\Omega$ at the fundamental frequency and the dc load was swept from $5\,\Omega$ to $200\,\Omega$. The simulated data was then normalized to generalize the simulation results. The ideal time-domain current and voltage waveforms across the diode are shown in Fig. 5.2 with the RF-DC conversion efficiency as a function of $R_{DC}/R_s(f_0)$ for varying rectifier on-resistance shown in Fig. 5.3. It is clear that the mechanism of operation in the ideal case agrees with the theory presented above. The reduction in RF-DC conversion efficiency when the DC load is not set according to (5.8) is simply due to a fraction of the incident power being reflected due to the impedance mismatch, and is given by

$$\eta = 1 - \left(\frac{R_{DC} - 2R_s(f_0)}{R_{DC} + 2R_s(f_0)}\right)^2 \tag{5.9}$$

The waveforms in Fig. 5.2 are identical to those of a class-C PA as the conduction angle approaches $0°$. The parasitics of realistic rectifying devices such as on-resistance, non-linear capacitance and threshold voltage will cause actual implementations of the harmonically terminated rectifier to deviate significantly from theory, but it is instructional to understand the mechanism of efficient rectification nonetheless.

RECTIFIER CIRCUIT

The Skyworks SMS7630 Schottky diode in the SC-79 package was selected for the half-wave rectifier [95]. Source-pull was performed at $2.45\,\mathrm{GHz}$ with 0-10 dBm available input power for various dc loads in order to identify the combination of input power, fundamental load and
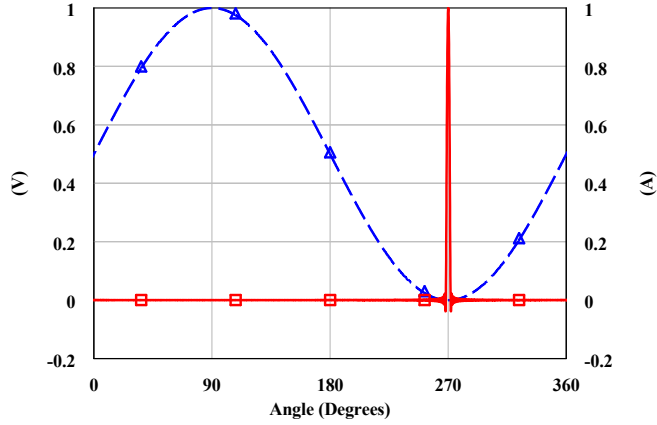
Figure 5.2: Ideal normalized voltage (dashed) and current (solid) waveforms for reduced conduction angle half-wave rectifier. The waveforms have been normalized to their peak values.
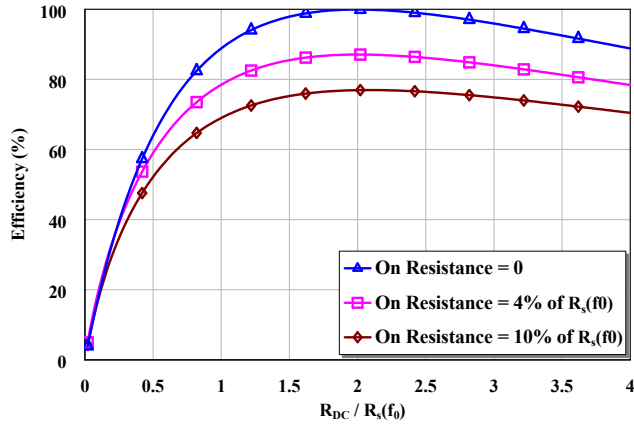
Figure 5.3: Simulated efficiency of reduced conduction angle half-wave rectifier versus $R_{DC}/R_s(f_0)$ for varying rectifier on-resistance.

dc load resulting in highest efficiency. The best case occurred at $6\,\mathrm{dBm}$ input power, with the source-pull contours shown in Fig. 5.4. The on-resistance of the SMS7630 is $20\,\Omega$ with the optimal DC load of $1080\,\Omega$, therefore R_{ON} is approximately 2% of R_{DC} which in theory is 4% of $R_s(f_0)$. From Fig. 5.3, a peak efficiency of 87% occurs with infinite harmonic terminations, therefore the achieved 77.6% is very reasonable considering only the 2nd and 3rd harmonics were explicitly terminated.

Measurements of a rectifier designed using the source-pull data show a maximum RF-DC conversion efficiency of 72.8% when matched to 50Ω being obtained after the $0.6\,\mathrm{dB}$ matching
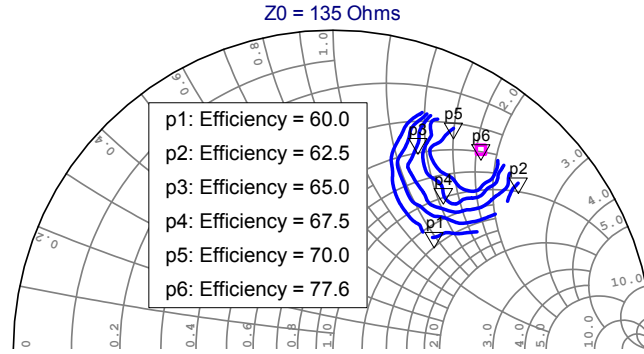
Figure 5.4: Source-pull contours at f_0 with available input power to the diode set to $6\,\text{dBm}$. The $2f_0$ and $3f_0$ harmonics were terminated in short circuits. The impedance is referenced to the junction capacitance of the diode, therefore the lead inductance of the package has been compensated for. Setting R_{DC} to $1080\,\Omega$ was found to result in the optimal efficiency for this input power.
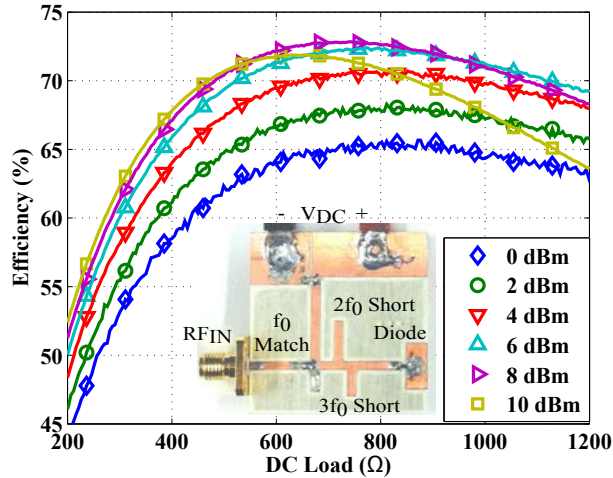
Figure 5.5: RF-DC conversion efficiency versus dc load fixed available input powers with $0.6\,\text{dB}$ matching network loss de-embedded. The maximum efficiency of 72.8% occurred at $8\,\text{dBm}$ with $R_{DC} = 742\,\Omega$, which is lower than the $1080\,\Omega$ found during source-pull. However, the efficiency at $1080\,\Omega$ is 69.9% which is very close to the peak value.

network loss is de-embedded. The fabricated rectifier and dc load sweep measurements are shown in Fig. 5.5. Open circuit shunt stubs were used to present short-circuit terminations at the second and third harmonic as shown in the inset of Fig. 5.5. A shunt capacitor was used for presenting the fundamental frequency impedance to reduce size and allow tunability. The reduction in efficiency relative to the source-pull measurements is due to the matching circuit not presenting the ideal impedance found during source-pull. It is difficult to fabricate a low-loss impedance match which

presents the ideal impedance shown in Fig. 5.4. Additionally, the efficiency is reasonably sensitive to the impedance match, which accounts for the reduction in efficiency demonstrated by the fabricated circuit.

IMPROVING WIRELESS POWERING EFFICIENCY

The class-C rectifier can be applied to improving the efficiency of a wireless powering reception device. We demonstrate the concept on the example of a dual-linearly polarized patch rectenna, with a rectifier circuit for each polarization (Fig. 5.6). In this circuit, the first 5 harmonics are shorted and the impedances are validated by calibrated measurements. Fig. 5.6 shows the simulated vs. experimentally achieved harmonic terminations. Fig. 5.7 shows the simulated time domain waveforms corresponding to these terminations, with higher harmonics not explicitly terminated in the harmonic balance simulation, as compared to the infinite number of shorted harmonics shown in Fig. 5.2. The rectenna is fabricated and measured in a free-space calibrated measurement system, by measuring the incident power density on the rectenna and multiplying by the physical antenna area $(64\,\mathrm{cm}^2)$ to determine incident power on the rectifier [2]. The efficiency calculated from the measured dc output in this case is 56% at $150\,\mu\mathrm{W/cm}^2$ power density $(9.6\,\mathrm{mW}$ total power), which includes antenna and matching circuit losses and is a lower bound on efficiency, and is slightly lower than measured for the rectifier in Fig. 5.5 [13].
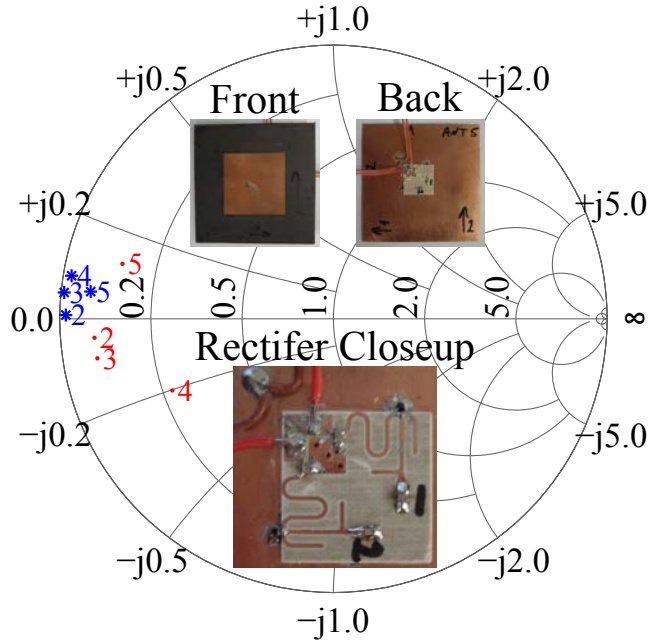
Figure 5.6: Dual-linearly polarized patch rectenna and associated $2f_0$-$5f_0$ terminations ($50\,\Omega$ Smith Chart) [2]. Blue and red indicate the simulated and measured harmonic terminations, respectively. The rectifiers are dc isolated.
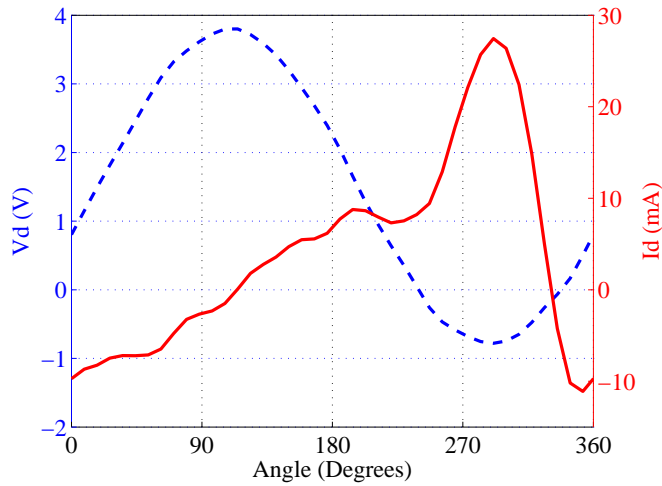
Figure 5.7: Simulated time-domain current and voltage waveforms for rectifier used in dual-polarized patch antenna (using SMS7630 diode) [2]. The frequency and input power were set to $2.45\,\text{GHz}$ and $10\,\text{dBm}$, respectively.

5.3.2 Class-F Power Rectifier

Consider again the rectifier circuit shown in Fig. 5.1 and assume that all even harmonics are terminated in short circuits, while all odd harmonics are terminated in open circuits. This set of harmonic terminations is the same as for a class-F amplifier. Given the harmonic terminations are equivalent to a class-F amplifier, this rectifier will be referred to as a class-F rectifier. The voltage and current waveforms across the rectifying element can now be derived given the assumed set of harmonic terminations. The fundamental frequency component of the voltage across the diode is given by

$$V_D(f_0) = V_s(f_0) \tag{5.10}$$

During the second half of the RF cycle, it is evident that the voltage across the rectifying element must be zero, given (5.1). This condition must be met through the addition of DC and strictly odd harmonic voltage components, given the enforced harmonic terminations. Therefore, the voltage waveform is expressed as

$$v_D(\theta) = \begin{cases} 2V_{DC}, & 0 \le \theta < \pi \\ 0, & \pi \le \theta < 2\pi \end{cases} \tag{5.11}$$

A Fourier expansion of (5.11) expresses the DC component of the voltage waveform as

$$V_{DC} = \frac{\pi}{4} V_D(f_0) \tag{5.12}$$

The current waveform is then expressed as

$$i_D(\theta) = \begin{cases} 0, & 0 \le \theta < \pi \\ -2I_D(f_0)\sin\theta, & \pi \le \theta < 2\pi \end{cases} \tag{5.13}$$

A Fourier expansion of (5.13) expresses the DC component of the current waveform as

$$I_{DC} = \frac{2I_D(f_0)}{\pi} \tag{5.14}$$

For reference, the ideal current and voltage waveforms defined in (5.11) and (5.13) are shown in Fig. 5.8(a). The waveform equations derived are in agreement with a Microwave Office®

136

simulation as shown in Fig. 5.8(b), with the rectifying element modeled as discussed in Section 5.3.1.

Up to this point nothing has been said about the DC load. It can be derived for the optimal rectifier waveforms given that the DC voltage and current are known from (5.12) and (5.12). Effectively, this method of analysis is calculating the required DC load which will result in the
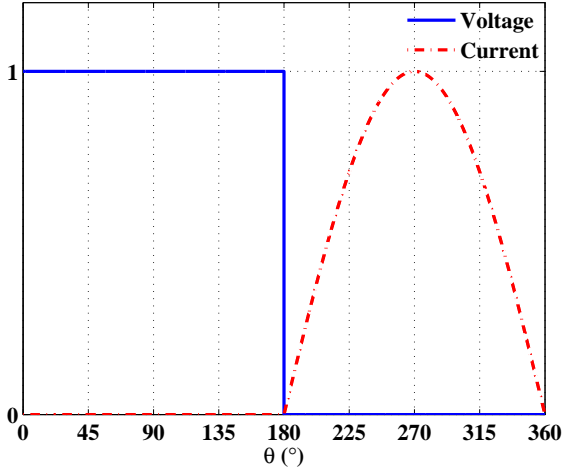
(a)
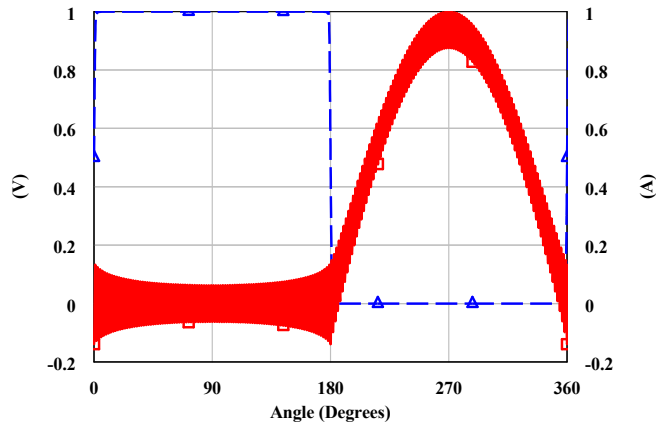
(b)

Figure 5.8: (a) Ideal class-F voltage and current waveforms calculated from (5.11) and (5.13), normalized to their peak respective values. (b) Ideal class-F voltage and current waveforms, normalized to their peak respective values simulated in Microwave Office® using an harmonic balance and an ideal rectifying element.

expressions of (5.11) and (5.13) being valid. Therefore, R_{DC} is given by

$$R_{DC} = \frac{\pi^2 V_D(f_0)}{8 I_D(f_0)} = \frac{\pi^2}{8} R_D(f_0) \tag{5.15}$$

The efficiency of the rectifier may now be determined. Let the efficiency be defined as the ratio of the DC power dissipated in the load resistance to the available fundamental frequency power. This ratio is evaluated as

$$\eta = \frac{P_D C}{P(f_0)} = 2 \frac{V_{DC} I_{DC}}{V_D(f_0) I_D(f_0)} = 2 \frac{\frac{\pi}{4} V_D(f_0) \frac{2}{\pi} I_D(f_0)}{V_D(f_0) I_D(f_0)} = 1 \tag{5.16}$$

Therefore, the ideal class-F half-wave rectifier converts all available RF power to DC power if the the DC loading resistance set to the value given in (5.15). At this point, it is worthy to note that the current and voltage waveforms of the ideal class-F rectifier are equivalent to the ideal class-F power amplifier waveforms, demonstrating the similarity between power rectifiers and power amplifiers as discussed in Section 5.2. The RF-DC conversion efficiency as a function of $R_{DC}/R_s(f_0)$ was simulated in Microwave Office® for varying rectifier on-resistance and is shown in Fig. 5.9. The peak efficiency as a function of on-resistance is higher than for the class-C rectifier, although the efficiency degrades more quickly when the non-ideal DC load is applied. In general, the optimal DC load appears to increase as the on-resistance increases. For zero on-resistance, the optimal DC load is exactly that predicted by (5.15). The reason for the increase in optimal DC load as the on-resistance increases is that by increasing the DC resistance, the current through the on-resistance is reduced, thus reducing the loss. However, there is a penalty paid in reflected power from the rectifying element due to the non-ideal match. This limits the benefit of increasing the DC load infinitely with a fixed fundamental frequency match. Theoretically, if the fundamental and DC loads could be increased infinitely the efficiency would approach 100 % no matter how large the on-resistance became.

Class-F Power Rectifier On-Resistance & Threshold Voltage

With the waveforms for an ideal class-F rectifier derived, the waveforms with a parasitic on-resistance and threshold voltage included in the model may be investigated. Since the rectifier

Figure 5.9: Simulated efficiency of class-F rectifier versus $R_{DC}/R_s(f_0)$ for varying rectifier on-resistance.

impedance is given by (5.2), the time domain voltage and current waveforms are approximated as

$$v_D(\theta) = \begin{cases} V_{max} + I_{max}R_{on}(\sin\theta - 1), & v_D(\theta) > -V_{tr} \\ \\ -V_{tr} + I_{max}R_{on}\sin\theta, & v_D(\theta) \leq -V_{tr} \end{cases} \tag{5.17}$$

$$i_D(\theta) = \begin{cases} 0, & v_D(\theta) > -V_{tr} \\ \\ -I_{max}\sin\theta, & v_D(\theta) \leq -V_{tr} \end{cases} \tag{5.18}$$

where V_{max} is the maximum of the voltage waveform, I_{max} is the maximum of the current waveform, R_{on} is the on-resistance of the rectifying element and V_{tr} is the threshold voltage of the rectifying element. As an example, Fig. 5.10 shows what the current and voltage waveforms look like for a specific set of non-ideal parameters ($V_{tr} = 0.7\,\mathrm{V}$, $V_{max} = 20\,\mathrm{V}$, $I_{max} = 200\,\mathrm{mA}$, and $R_{on} = 5\,\Omega$).

From (5.17), it is evident that the voltage waveform does not have the ideal rectangular shape as in an ideal class-F rectifier. This is due to the on-resistance of the device. When the device is conducting current, it creates a voltage drop across the on-resistance which has a shape equivalent to the shape of the current waveform during this portion of the cycle. To maintain waveform symmetry, this variation in the voltage waveform is also seen when the device is not conducting. If the on-resistance were zero, the only difference between the waveform in (5.17)

139

and the ideal voltage waveform would be the minimum value, which would be $-V_{tr}$ rather than zero. For $\theta = 0$ and $\theta = \pi$, transitions occur in (5.17). A Fourier decomposition of the voltage waveform using the transition points must be performed in order to determine the DC and fundamental components. The DC component is then expressed as

$$V_{DC} = \frac{1}{2\pi} \int_0^{2\pi} v_D(\theta) d\theta \tag{5.19}$$

which expands to

$$V_{DC} = \frac{1}{2\pi} \left(\int_0^{\pi} (V_{max} + I_{max} R_{on}(\sin\theta - 1)) d\theta - \int_{\pi}^{2\pi} (V_{tr} - I_{max} R_{on} \sin\theta) d\theta \right) \tag{5.20}$$

Equation (5.20) evaluates to

$$V_{DC} = \frac{1}{2} \left(V_{max} - V_{tr} - I_{max} R_{on} \right) \tag{5.21}$$

Let the fundamental frequency voltage be expressed as

$$V(f_0) = a_v + jb_v \tag{5.22}$$

where

$$a_v = \frac{1}{\pi} \int_0^{2\pi} v_D(\theta) \cos\theta d\theta \tag{5.23}$$
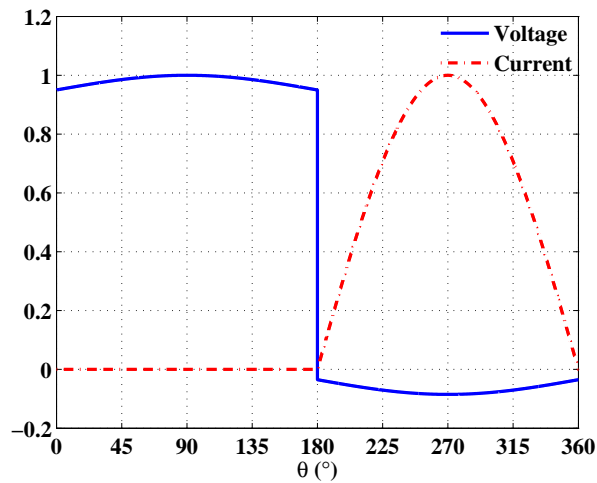
Figure 5.10: Non-ideal class-F voltage and current waveforms, normalized to their peak respective values.

140

$$b_v = \frac{1}{\pi} \int\limits_0^{2\pi} v_D(\theta) \sin\theta d\theta \tag{5.24}$$

First a_v is evaluated as

$$a_v = \frac{1}{\pi} \left(\int\limits_0^{\pi} (V_{max} + I_{max} R_{on}(\sin\theta - 1)) \cos\theta d\theta - \int\limits_{\pi}^{2\pi} (V_{tr} - I_{max} R_{on} \sin\theta) \cos\theta d\theta \right) = 0 \tag{5.25}$$

The value of b_v is then expressed as

$$b_v = \frac{1}{\pi} \left(\int\limits_0^{\pi} (V_{max} + I_{max} R_{on}(\sin\theta - 1)) \sin\theta d\theta - \int\limits_{\pi}^{2\pi} (V_{tr} - I_{max} R_{on} \sin\theta) \sin\theta d\theta \right) \tag{5.26}$$

which is simplified to

$$b_v = \frac{2}{\pi} \left(V_{max} + V_{tr} + \frac{\pi - 2}{2} I_{max} R_{on} \right) \tag{5.27}$$

Now a Fourier decomposition is performed for the current waveform. The DC component of the current waveform is given by

$$I_{DC} = -\frac{1}{2\pi} \int\limits_{\pi}^{2\pi} I_{max} \sin\theta d\theta \tag{5.28}$$

which simplifies to

$$I_{DC} = \frac{I_{max}}{\pi} \tag{5.29}$$

Let the fundamental frequency current be expressed as

$$I(f_0) = a_i + jb_i \tag{5.30}$$

where

$$a_i = \frac{1}{\pi} \int\limits_0^{2\pi} i_D(\theta) \cos\theta d\theta \tag{5.31}$$

and

$$b_i = \frac{1}{\pi} \int\limits_0^{2\pi} i_D(\theta) \sin\theta d\theta \tag{5.32}$$

The fundamental components a_i and b_i are evaluated as

$$a_i = -\frac{1}{\pi} \int\limits_{\pi}^{2\pi} I_{max} \sin\theta \cos\theta d\theta = 0 \tag{5.33}$$

and

$$b_i = -\frac{1}{\pi} \int\limits_{\pi}^{2\pi} I_{max} \sin^2\theta d\theta = -\frac{I_{max}}{2} \tag{5.34}$$

Now that the fundamental frequency components of the current and voltage waveforms have been evaluated, the input power to the rectifying element can be expressed as

$$P_{in} = \text{Re} \left\{ \frac{V(f_0)I(f_0)}{2} \right\} \tag{5.35}$$

Substituting (5.22) and (5.30) into (5.35) results in

$$P_{in} = \frac{\left[\frac{2}{\pi} \left(V_{max} + V_{tr} + \frac{\pi - 2}{2} I_{max} R_{on} \right) \right] \left[\frac{I_{max}}{2} \right]}{2} \tag{5.36}$$

which simplifies to

$$P_{in} = \frac{I_{max}}{2\pi} \left(V_{max} + V_{tr} + \frac{\pi - 2}{2} I_{max} R_{on} \right) \tag{5.37}$$

Rearranging (5.37) in terms of I_{max} results in

$$P_{in} = (V_{max} + V_{tr}) \frac{I_{max}}{2\pi} + \frac{\pi - 2}{4\pi} I_{max}^2 R_{on} \tag{5.38}$$

which may be expressed as

$$\frac{\pi - 2}{4\pi} R_{on} I_{max}^2 + \frac{V_{max} + V_{tr}}{2\pi} I_{max} - P_{in} = 0 \tag{5.39}$$

The solutions to (5.39) are given by

$$I_{max} = -\frac{V_{max} + V_{tr} - \sqrt{(V_{max} + V_{tr})^2 + 4\pi P_{in}(\pi - 2)R_{on}}}{(\pi - 2)R_{on}} \tag{5.40}$$

and

$$I_{max} = -\frac{V_{max} + V_{tr} + \sqrt{(V_{max} + V_{tr})^2 + 4\pi P_{in}(\pi - 2)R_{on}}}{(\pi - 2)R_{on}} \tag{5.41}$$

The correct solution is (5.40) because it is the only solution resulting in $I_{max} > 0$. In the case where R_{on} is zero, (5.39) simplifies to

$$\frac{V_{max} + V_{tr}}{2\pi} I_{max} - P_{in} = 0 \tag{5.42}$$

whose solution is simply

$$I_{max} = \frac{2\pi P_{in}}{V_{max} + V_{tr}} \tag{5.43}$$

Note that in the case of an ideal rectifying element, $V_{tr} = 0$, therefore

$$I_{max,ideal} = \frac{2\pi P_{in}}{V_{max}} \tag{5.44}$$

Given that I_{max} is fully expressed in terms of rectifying element parameters, V_{DC} and I_{DC}, $V(f_0)$ and $I(f_0)$ may be calculated, and from these the DC load, fundamental load, and rectifier efficiency are determined. The DC load is given by

$$R_{DC} = \frac{V_{DC}}{I_{DC}} \tag{5.45}$$

while the load at the fundamental frequency is given by

$$R(f_0) = -\frac{V(f_0)}{I(f_0)} = -\frac{b_v}{b_i} \tag{5.46}$$

The negative impedance in (5.46) indicates that power is delivered to the rectifying element rather than created by the rectifying element. Therefore, (5.46) gives the impedance of the source delivering power to the rectifying element. The rectifier efficiency is given by

$$\eta = \frac{P_{DC}}{P_{in}} = \frac{V_{DC}I_{DC}}{P_{in}} \tag{5.47}$$

An example demonstrating the design procedure should be instructive. Assume the rectifying element has the following parameters: $V_{max} = 10\,\text{V}$, $R_{on} = 5\,\Omega$, $V_{tr} = 0.7\,\text{V}$ and $P(f_0) = 1\,\text{W}$. First, (5.40) is used to calculate I_{max} which evalutes to $516.2\,\text{mA}$. Next, The DC voltage and current are evaluated using (5.21) and (5.29), respectively. These parameters evaluate to $3.36\,\text{V}$ and $164.3\,\text{mA}$ respectively. The fundamental frequency voltage and current Fourier coefficients are then evaluated using (5.22) and (5.30), respectively. These parameters evaluate to $7.409\,\text{V}$ and $-258.1\,\text{mA}$, respectively. The DC and fundamental frequency resistances are then calculated using (5.45) and (5.46) which evaluate to $20.45\,\Omega$ and $28.71\,\Omega$, respectively. The efficiency is then calculated using (5.47) and calculates as $55.20\,\%$. This is not extremely good performance, but again we have chosen the $1\,\text{W}$ input power as a design parameter. If the input power were selected as $0.1\,\text{W}$ rather than $1\,\text{W}$, the resultant efficiency is $82.93\,\%$ instead. The point is that a specific element will always have an approximate input drive level at which it can be most efficient, just as with power transistors in power amplifiers. In the end the goal is always to minimize the amount of power dissipation in the on-resistance of the rectifying element and maximize the power dissipated in the DC load resistor.

5.3.3 Class-F^{-1} Power Rectifier

Consider again the rectifier circuit shown in Fig. 5.1 and assume that all even harmonics are terminated in open circuits, while all odd harmonics are terminated in short circuits. This set of harmonic terminations is the same as for a class-F^{-1} amplifier, therefore this rectifier will be referred to as a class-F^{-1} rectifier. The voltage and current waveforms across the rectifying element can now be derived given the assumed set of harmonic terminations. The fundamental frequency component of the voltage across the diode is again given by (5.10).

During the second half of the RF cycle, it is evident from (5.1) that the voltage across the rectifying element must be zero. This condition must be met through the addition of DC and strictly even harmonic voltage components, given the enforced harmonic terminations. Therefore, the voltage waveform is expressed as

$$v_D(\theta) = \begin{cases} 2V_D(f_0)\sin\theta, & 0 \le \theta < \pi \\ \\ 0, & \pi \le \theta < 2\pi \end{cases} \tag{5.48}$$

The construction of the voltage waveform defined in (5.48) is shown in Fig. 5.11. A Fourier
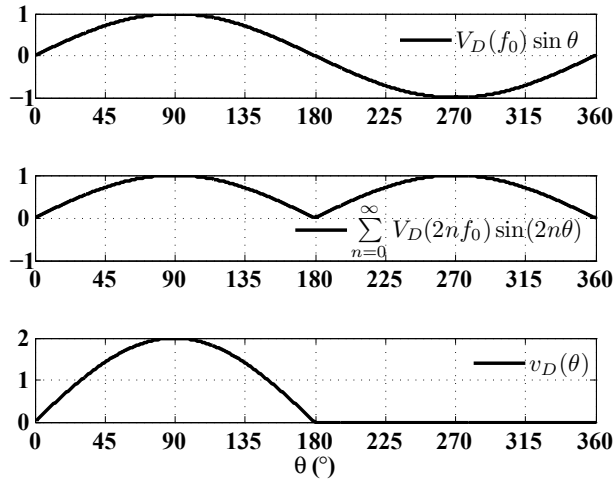
Figure 5.11: Class-F^{-1} half-wave rectifier voltage waveform construction. The voltage is normalized to $v_D(f_0)$.

expansion of (5.48) expresses the DC component of the voltage waveform as

$$V_{DC} = \frac{2V_D(f_0)}{\pi} \tag{5.49}$$

In the first half of the RF cycle, it is evident that the current through the rectifying element must be zero, given (5.1). This condition must be met through the addition of a DC current and strictly odd harmonic current components, given the enforced harmonic terminations. It is well known that any function that may be represented by a Fourier series can be expressed by the sum of an even function and an odd function. Even functions contain only even harmonics, therefore the even function in this case is strictly the DC current. Odd functions contain only odd harmonics, therefore the odd function in this case is the summation of the remaining odd harmonic terms. Given the definition of the current direction in Fig. 5.1, the DC component of the current must be positive. Therefore, in the first half of the RF cycle, the remaining harmonics must sum to a constant value equivalent to the negative of the DC component. Given that the function which is the sum of the remaining harmonics is odd, the second half of the RF cycle must sum to the DC component. The current waveform is then expressed as

$$i_D(\theta) = \begin{cases} 0, & 0 \le \theta < \pi \\ \\ 2I_{DC}, & \pi \le \theta < 2\pi \end{cases} \tag{5.50}$$

A Fourier expanson of (5.50) expresses the DC component of the current waveform as

$$I_{DC} = \frac{\pi}{4}I_D(f_0) \tag{5.51}$$

For reference, the ideal current and voltage waveforms defined in (5.48) and (5.50) are shown in Fig. 5.12. The waveform equations derived are in agreement with a Microwave Office® simulation, with the rectifying element modeled as discussed in Section 5.3.1. The DC load consistent with (5.48) and (5.50) is given by

$$R_{DC} = \frac{8V_D(f_0)}{\pi^2 I_D(f_0)} = \frac{8}{\pi^2}R_D(f_0) \tag{5.52}$$

The efficiency of the rectifier may now be determined. Let the efficiency be defined as the ratio of the DC power dissipated in the load resistor to the available fundamental frequency RF power.

This ratio is evaluated as

$$\eta = \frac{P_DC}{P(f_0)} = 2\frac{V_{DC}I_{DC}}{V_D(f_0)I_D(f_0)} = 2\frac{\frac{2}{\pi}V_D(f_0)\frac{\pi}{4}I_D(f_0)}{V_D(f_0)I_D(f_0)} = 1 \tag{5.53}$$

Therefore, the ideal half-wave rectifier converts all available RF power to DC power if the the DC loading resistance set to the value given in (5.52). The RF-DC conversion efficiency as a function of $R_{DC}/R_s(f_0)$ was simulated in Microwave Office® for varying rectifier on-resistance and is shown in Fig. 5.13. The harmonic balance settings were identical to those used for the class-C rectifier as discussed in Section 5.3.1. The peak efficiency as a function of on-resistance is higher
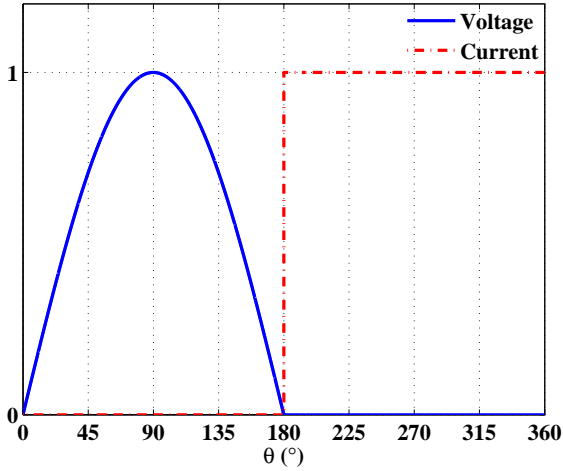
(a)
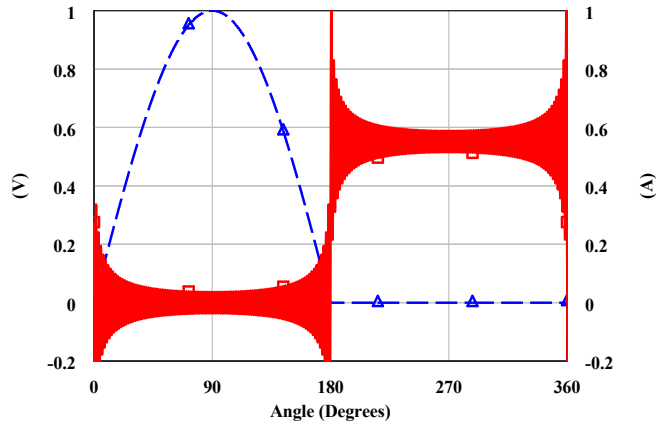
(b)

Figure 5.12: (a) Ideal class-F^{-1} voltage and current waveforms calculated from (5.48) and (5.50), normalized to their peak respective values. (b) Ideal class-F^{-1} voltage and current waveforms, normalized to their peak respective values simulated in Microwave Office® using an harmonic balance and an ideal rectifying element.

than for the class-C rectifier, although the efficiency degrades more quickly when the non-ideal DC load is applied. In general, the optimal DC load appears to increase as the on-resistance increases. For zero on-resistance, the optimal DC load is exactly that predicted by (5.52). The reason for the increase in optimal DC load as the on-resistance increases is that the current through the on-resistance is reduced, thus reducing the loss. However, there is a penalty paid in reflected power from the rectifying element due to the non-ideal match. This limits the benefit of increasing the DC load infinitely with a fixed fundamental frequency match. Theoretically, if the fundamental and DC loads could be increased infinitely the efficiency would approach $100\,\%$ no matter how large the on-resistance became.

Again, as with the class-F rectifier, the current and voltage waveforms of the ideal class-F^{-1} rectifier are equivalent to the ideal class-F^{-1} power amplifier waveforms, demonstrating the similarity between power rectifiers and power amplifiers as discussed in Section 5.2.

Class-F^{-1} Power Rectifier On-Resistance & Threshold Voltage

With the waveforms for an ideal class-F^{-1} rectifier derived, the waveforms given a parasitic on-resistance and threshold voltage may be investigated assuming the rectifier impedance from
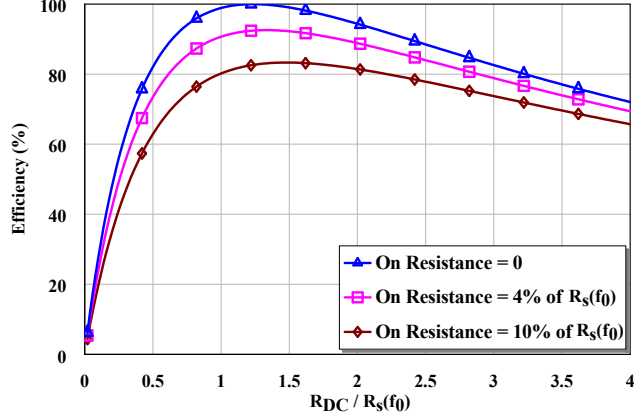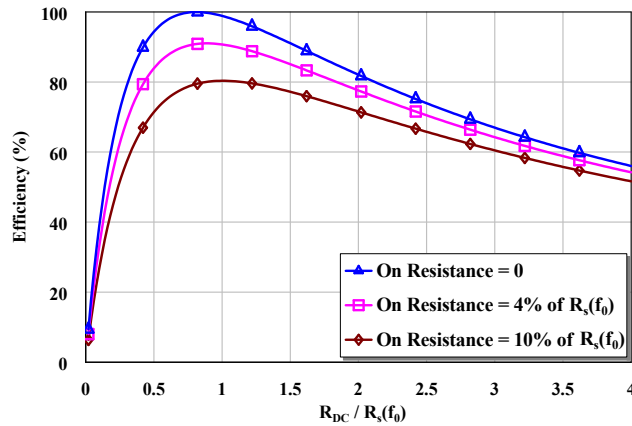

Figure 5.13: Simulated efficiency of class-F^{-1} rectifier versus $R_{DC}/R_s(f_0)$ for varying rectifier on-resistance.

(5.2). The time domain voltage and current waveforms are approximated as

$$v_D(\theta) = \begin{cases} V_{max}\sin\theta, & v_D(\theta) > -V_{tr} \\ \\ -V_{tr} - I_{max}R_{on}, & v_D(\theta) \leq -V_{tr} \end{cases} \qquad (5.54)$$

$$i_D(\theta) = \begin{cases} 0, & v_D(\theta) > -V_{tr} \\ \\ I_{max}, & v_D(\theta) \leq -V_{tr} \end{cases} \qquad (5.55)$$

This analysis is a departure from the efficiency results as a function of on-resistance shown in the previous section. This analysis takes into account that the peak voltage is constrained and that an optimal fundamental matching resistance exists which is a function of both parameters. As an example, Fig. 5.14 shows the current and voltage waveforms for a specific set of non-ideal parameters ($V_{tr} = 0.7\,\mathrm{V}$, $V_{max} = 20\,\mathrm{V}$, $I_{max} = 200\,\mathrm{mA}$, and $R_{on} = 5\,\Omega$).

From (5.54), it is evident that the voltage waveform does not have the ideal clipped sinusoidal shape as in an ideal class-F^{-1} rectifier. This is due to the on-resistance of the device. When the device is conducting current, it creates a voltage drop across the on-resistance which is constant due to the constant current. If the on-resistance were zero, the only difference between the waveform in (5.17) and the ideal voltage waveform would be the minimum value, which
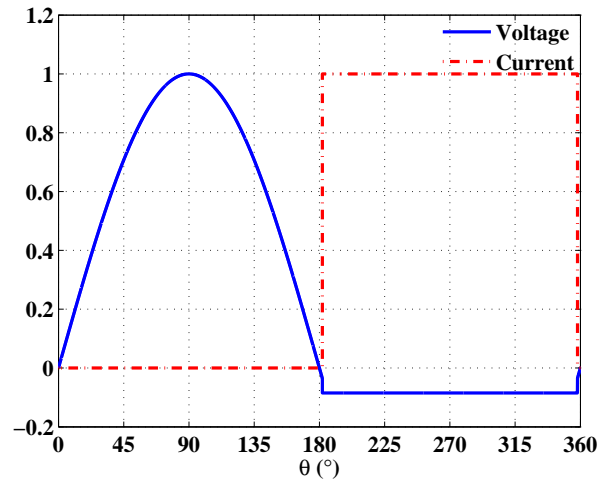
Figure 5.14: Non-ideal class-F^{-1} voltage and current waveforms, normalized to their peak respective values.

would be $-V_{tr}$ rather than zero. The values of θ at which the transition between the conducting and non-conducting regions occurs are given by

$$\sin \theta_{t1} = -\frac{V_{tr}}{V_{max}}$$
$$\sin(\pi - \theta_{t2}) = -\frac{V_{tr}}{V_{max}} \tag{5.56}$$

Solving the transition points in (5.56) in terms of θ expresses the transition angles as

$$\theta_{t1} = 2\pi - \arcsin\left(\frac{V_{tr}}{V_{max}}\right)$$
$$\theta_{t2} = \pi + \arcsin\left(\frac{V_{tr}}{V_{max}}\right) \tag{5.57}$$

A Fourier decomposition of the voltage and current waveforms using the transition points in (5.57) is performed in order to determine the DC and fundamental components. The DC component is expressed in (5.19) which simplifies to

$$V_{DC} = \frac{1}{2\pi}\left(2V_{max}\sqrt{1 - \left(\frac{V_{tr}}{V_{max}}\right)^2} - (V_{tr} + I_{max}R_{on})\left[\pi - 2\arcsin\left(\frac{V_{tr}}{V_{max}}\right)\right]\right) \tag{5.58}$$

The fundamental frequency voltage is expressed in (5.22) with the individual components given in (5.23) and (5.24). First, a_v is calculated as

$$a_v = \frac{1}{\pi}\left(\int_{-\arcsin\left(\frac{V_{tr}}{V_{max}}\right)}^{\pi+\arcsin\left(\frac{V_{tr}}{V_{max}}\right)} V_{max}\sin\theta\cos\theta d\theta - \int_{\pi+\arcsin\left(\frac{V_{tr}}{V_{max}}\right)}^{2\pi-\arcsin\left(\frac{V_{tr}}{V_{max}}\right)} (V_{tr} + I_{max}R_{on})\cos\theta d\theta\right) = 0 \tag{5.59}$$

Then b_v is given by

$$b_v = \frac{1}{\pi}\left(\int_{-\arcsin\left(\frac{V_{tr}}{V_{max}}\right)}^{\pi+\arcsin\left(\frac{V_{tr}}{V_{max}}\right)} V_{max}\sin^2\theta d\theta - \int_{\pi+\arcsin\left(\frac{V_{tr}}{V_{max}}\right)}^{2\pi-\arcsin\left(\frac{V_{tr}}{V_{max}}\right)} (V_{tr} + I_{max}R_{on})\sin\theta d\theta\right) \tag{5.60}$$

which simplifies to

$$b_v = \frac{1}{\pi}\left(V_{max}\arcsin\left(\frac{V_{tr}}{V_{max}}\right) + \frac{\pi V_{max}}{2} + (V_{tr} + 2I_{max}R_{on})\sqrt{1 - \left(\frac{V_{tr}}{V_{max}}\right)^2}\right) \tag{5.61}$$

The DC component of the current waveform is expressed as

$$I_{DC} = \frac{1}{2\pi}\int_{\pi+\arcsin\left(\frac{V_{tr}}{V_{max}}\right)}^{2\pi-\arcsin\left(\frac{V_{tr}}{V_{max}}\right)} I_{max} d\theta \tag{5.62}$$

which simplifies to

$$I_{DC} = \frac{I_{max}}{2\pi}\left(\pi - 2\arcsin\left(\frac{V_{tr}}{V_{max}}\right)\right) \tag{5.63}$$

149

The fundamental frequency current is expressed in (5.30) with the individual components given in (5.31) and (5.32). First, a_i is calculated as

$$a_i = \frac{1}{\pi} \int_{\pi + \arcsin\left(\frac{V_{tr}}{V_{max}}\right)}^{2\pi - \arcsin\left(\frac{V_{tr}}{V_{max}}\right)} I_{max} \cos\theta d\theta = 0 \tag{5.64}$$

The fundamental component b_i is given by

$$b_i = \frac{1}{\pi} \int_{\pi + \arcsin\left(\frac{V_{tr}}{V_{max}}\right)}^{2\pi - \arcsin\left(\frac{V_{tr}}{V_{max}}\right)} I_{max} \sin\theta d\theta \tag{5.65}$$

which simplifies to

$$b_i = -\frac{2 I_{max}}{\pi} \sqrt{1 - \left(\frac{V_{tr}}{V_{max}}\right)^2} \tag{5.66}$$

The input power is expressed in (5.35) simplifies to

$$P_{in} = \frac{k I_{max}}{\pi^2} \left(V_{max} \arcsin\left(\frac{V_{tr}}{V_{max}}\right) + \frac{\pi V_{max}}{2} + (V_{tr} + 2 I_{max} R_{on})k \right) \tag{5.67}$$

where k is defined as

$$k = \sqrt{1 - \left(\frac{V_{tr}}{V_{max}}\right)^2} \tag{5.68}$$

This simplifies to

$$2k R_{on} I_{max}^2 + V_{max} \left(\arcsin\left(\frac{V_{tr}}{V_{max}}\right) + \frac{\pi}{2} + k\frac{V_{tr}}{V_{max}} \right) I_{max} - \frac{\pi^2}{k} P_{in} = 0 \tag{5.69}$$

The solutions to (5.69) when R_{on} is non-zero are given by

$$I_{max} = -\frac{V_{max} \left(\arcsin\left(\frac{V_{tr}}{V_{max}}\right) + \frac{\pi}{2} + k\frac{V_{tr}}{V_{max}} \right)}{4 R_{on} k}$$
$$+ \frac{\sqrt{\left(V_{max} \left(\arcsin\left(\frac{V_{tr}}{V_{max}}\right) + \frac{\pi}{2} + k\frac{V_{tr}}{V_{max}} \right) \right)^2 + 8\pi^2 P_{in} R_{on}}}{4 R_{on} k} \tag{5.70}$$

and

$$I_{max} = -\frac{V_{max} \left(\arcsin\left(\frac{V_{tr}}{V_{max}}\right) + \frac{\pi}{2} + k\frac{V_{tr}}{V_{max}} \right)}{4 R_{on} k}$$
$$- \frac{\sqrt{\left(V_{max} \left(\arcsin\left(\frac{V_{tr}}{V_{max}}\right) + \frac{\pi}{2} + k\frac{V_{tr}}{V_{max}} \right) \right)^2 + 8\pi^2 P_{in} R_{on}}}{4 R_{on} k} \tag{5.71}$$

The correct solution is (5.70) because it is the only solution resulting in $I_{max} > 0$. In the case where R_{on} is zero, (5.69) simplifies to

$$V_{max} \left(\arcsin\left(\frac{V_{tr}}{V_{max}}\right) + \frac{\pi}{2} + k\frac{V_{tr}}{V_{max}} \right) I_{max} - \frac{\pi^2}{k} P_{in} = 0 \tag{5.72}$$

whose solution is simply

$$I_{max} = P_{in} \frac{\pi^2}{kV_{max} \left(\arcsin\left(\frac{V_{tr}}{V_{max}} \right) + \frac{\pi}{2} + k\frac{V_{tr}}{V_{max}} \right)} \tag{5.73}$$

Note that in the case of an ideal rectifying element, $k = 1$ and $V_{tr} = 0$, therefore

$$I_{max,ideal} = \frac{2\pi P_{in}}{V_{max}} \tag{5.74}$$

Now that I_{max} is fully expressed given known rectifier parameters, V_{DC} and I_{DC}, $V(f_0)$ and $I(f_0)$ may be calculated, and the DC load, fundamental load, and rectifier efficiency determined, whose expressions are equivalent to those given in Section 5.3.2.

An example demonstrating the design procedure should be instructive. Assume the rectifying element has the following parameters: $V_{max} = 10\,\text{V}$, $R_{on} = 5\,\Omega$, $V_{tr} = 0.7\,\text{V}$ and $P(f_0) = 1\,\text{W}$. First, (5.70) is used to calculate I_{max} which evaluates to $456.7\,\text{mA}$. Next, The DC voltage and current are evaluated using (5.58) and (5.63), respectively. These parameters evaluate to $1.75\,\text{V}$ and $218.2\,\text{mA}$ respectively. The fundamental frequency voltage and current Fourier coefficients are then evaluated using (5.22) and (5.30), respectively. These parameters evaluate to $6.896\,\text{V}$ and $-290\,\text{mA}$, respectively. The DC and fundamental frequency resistances are then calculated using (5.45) and (5.46) which evaluate to $8.02\,\Omega$ and $23.77\,\Omega$, respectively. The efficiency is then calculated using (5.47) and calculates as $38.18\,\%$. Of course this is not very good performance, but again we have chosen the input power is a design parameter. If the input power were selected as $0.1\,\text{W}$ rather than $1\,\text{W}$, the resultant efficiency is $72.43\,\%$ instead. The point is that a specific element will always have an approximate input drive level at which it can be most efficient, just as with power transistors in power amplifiers. In the end the goal is always to minimize the amount of power dissipation in the on-resistance of the rectifying element and maximize the power dissipated in the DC load resistor.

5.4 Conclusion

This chapter presents an analysis of microwave rectifiers using analogies from power amplifiers with harmonic terminations to improve efficiency. The analysis is confirmed with measured data on several shunt Schottky diode rectifiers, and can be applied to wireless powering which is investigated in [96]. The specific contributions of this chapter are:

- A new approach to rectifier analysis and to increasing efficiency in rectifiers, modeled after efficient power amplifier design, and reported only briefly in [13].

- Experimental verification of the analysis, based on measurements of a class-C 2.45 GHz Schottky-diode rectifier with short-circuit 2nd and 3rd harmonic terminations. A maximum RF-DC conversion efficiency of 72.8% when matched to $50\,\Omega$ is demonstrated. The approach is applied to integration of a rectifier with a dual-polarization patch antenna in a non $50\,\Omega$ environment and free-space measurements demonstrate a lower bound on efficiency of 56% at $150\,\mu\mathrm{W}\backslash\mathrm{cm}^2$ power density which includes matching circuit and mismatch losses [13].

- The details and extensions of the presented theory in [13] will be submitted for journal publication in IEEE Transactions on Microwave Theory & Techniques.

CHAPTER 6

HARMONIC INJECTION POWER AMPLIFIER

CONTENTS

6.1   INTRODUCTION

A large portion of current research in high-power amplification of signals with carriers in the microwave range focuses on improving efficiency and linearity [30]. There are many power amplifier

(PA) topologies which achieve high efficiency by driving the active device into a non-linear region and shaping voltage and current waveforms across the device via proper selection of the output loading network at harmonic frequencies. These techniques, such as class-F and F^{-1} PA topologies [53], rely on the nonlinear active device for harmonic current or voltage generation. The concept of harmonic injection, however, refers to architectures in which power at a harmonic of the operating frequency is supplied externally to either the input, output, or both input and output of the active device.

Analysis of efficiency improvement of tube based PAs using harmonic injection into both the grid (input) and plate (output) has been presented in [97, 98, 99]. A novel harmonic injection scheme referred to as a harmonic reaction amplifier was presented in [100]. The harmonic reaction amplifier uses two parallel devices and effectively acts as a push-pull amplifier with respect to the second harmonic. An experiment demonstrating a 15.2% efficiency improvement of a 2 GHz GaN PA using second harmonic injection at the input was published in [101]. In 1992, a patent was issued for a harmonic injection amplifier in which the harmonic signal created using a frequency multiplier is injected into the transistor output [102]. More recently, a concept for efficiency improvement via injection of harmonics into the output of a class-B/J amplifier was demonstrated [103]. A novel scheme of efficiency improvement of a class-E amplifier using input harmonic injection via a feedback loop was shown in [104].

This chapter presents an analysis of linear amplifiers with second or third harmonic injection. Raab presented a theoretical analysis showing that an ideal PA with only an optimal purely reactive second harmonic termination can have a maximum efficiency of 70.7 % [40]. In this work, a theoretical concept for a second-harmonic-only PA realized with second harmonic injection is presented, showing that the maximum efficiency in this case is 89.9 %. The injection of third-harmonic-only has a maximum efficiency of 65.5 %. Since a separate circuit is required to produce and inject power at the harmonics, it is important to quantify the effect of injector efficiency on the maximum total efficiency of the PA, as well as the sensitivity of PA efficiency to the injected power level. A detailed analysis of the injection circuit is also presented, along with an analysis

of the mechanism for electrical impedance synthesis with harmonic injection.

6.2   Electrical Impedance Synthesis

A harmonic injection amplifier relies on shaping the output waveforms of the active device by electrically synthesizing the proper harmonic impedance at the virtual drain as well as delivering the necessary amount of harmonic power. For example, the harmonic impedance and delivered harmonic power for an ideal second harmonic injection amplifier is presented in Section 6.3. In the case where the virtual drain of the transistor is the ideal terminating impedance at the injected harmonic, no electrical impedance synthesis is required and only the delivered power must be controlled. However, the general case requires control of both. This section provides an analysis of the mechanism by which both the harmonic impedance seen by the virtual drain and delivered harmonic power may be controlled.

Consider the circuit diagram shown in Fig. 6.1. The reference plane depicted by the dashed line is excited by two sources simultaneously, with the incident and reflected waves a_i and b_i, respectively. The characteristic impedances of the media on each side of the reference plane are Z_A and Z_B, respectively. The wave variables a_i and b_i are defined in [105] as

$$a_i = \frac{V_i^+}{\sqrt{Z_{0i}}} \quad b_i = \frac{V_i^-}{\sqrt{Z_{0i}}} \tag{6.1}$$

where $V_i^{\pm}$ are RMS voltages and Z_{0i} is a real normalizing impedance. For the following analysis, it is assumed that Z_A and Z_B are real, therefore $Z_{01} = Z_A$ and $Z_{02} = Z_B$. The input impedance at the reference plane looking into the medium with characteristic impedance Z_B is defined as Z_{IN}. It is assumed that each medium is terminated in its respective characteristic impedance.

A straightforward manner to analyze the circuit in Fig. 6.1 is to apply the principle of superposition. Let the total wave traveling into the media on the left side of the dashed line be defined as b_T. By superposition, the component of b_T due to a_1 can be found by removing the source a_2. Similarly, the component of b_T due to a_2 can be found by removing the source a_1. Then b_T is found by adding the components. The total wave b_T traveling into media Z_A is
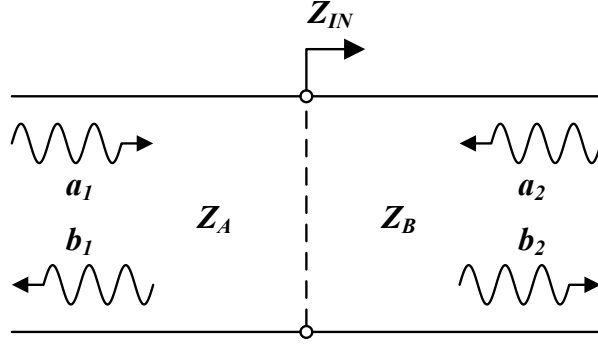
Figure 6.1: Basic impedance synthesis circuit depicting two simultaneous excitations.

expressed as

$$
\begin{aligned}
b_T &= \frac{Z_B - Z_A}{Z_A + Z_B} a_1 + \left[1 + \frac{Z_A - Z_B}{Z_A + Z_B} \right] \sqrt{\frac{Z_B}{Z_A}} a_2 \\
&= a_1 \frac{Z_B - Z_A + 2\sqrt{Z_A Z_B}\frac{a_2}{a_1}}{Z_A + Z_B}
\end{aligned}
\tag{6.2}
$$

The reflection coefficient at the reference plane is then given by

$$
\Gamma_{IN} = \frac{b_T}{a_1} = \frac{Z_B - Z_A + 2\sqrt{Z_A Z_B}\frac{a_2}{a_1}}{Z_A + Z_B}
\tag{6.3}
$$

The input impedance is calculated from the reflection coefficient using the equation

$$
Z_{IN} = Z_A \frac{1 + \Gamma_{IN}}{1 - \Gamma_{IN}}
\tag{6.4}
$$

Substituting (6.3) into (6.4) results in

$$
Z_{IN} = Z_A \frac{1 + \frac{Z_B - Z_A + 2\sqrt{Z_A Z_B}\frac{a_2}{a_1}}{Z_A + Z_B}}{1 - \frac{Z_B - Z_A + 2\sqrt{Z_A Z_B}\frac{a_2}{a_1}}{Z_A + Z_B}}
\tag{6.5}
$$

which simplifies to

$$
Z_{IN} = Z_A \frac{Z_B + \sqrt{Z_A Z_B}\frac{a_2}{a_1}}{Z_A - \sqrt{Z_A Z_B}\frac{a_2}{a_1}} = Z_A \frac{Z_B a_1 + \sqrt{Z_A Z_B} a_2}{Z_A a_1 - \sqrt{Z_A Z_B} a_2}
\tag{6.6}
$$

The resultant input impedance given in (6.6) reveals some very interesting implications of electrical impedance synthesis. First consider the case when there is no incident wave a_1. This case is relevant to the situation in which a transistor does not produce any harmonic content

156

at the virtual drain, or produces extremely little harmonic content. In this case, $Z_{IN} = -Z_A$, independent of the impedance Z_B and the level of the excitation wave a_2. What this reveals is that there is no hope of electrically synthesizing an arbitrary impedance at the reference plane if the first source a_1 is absent. In the case of a harmonic injection amplifier, this means that it is impossible to electrically synthesize an arbitrary harmonic impedance to the virtual drain if the transistor fails to produce harmonic content at the virtual drain. The harmonic content must exist to synthesize an arbitrary impedance, whether it be created by the non-linearity of the transistor, or by injecting harmonic content into the input of the transistor in order to create harmonic content at the output.

However, for the moment let us assume that $a_1 \neq 0$ and the second source a_2 is able to be controlled. Let us investigate the impedances that can be synthesized. For simplicity, assume that the impedances Z_A and Z_B are fixed, and assume the ratio $\frac{a_2}{a_1}$ which we will define as r can be controlled. From (6.6), the input impedance is then re-written as

$$Z_{IN} = Z_A \frac{Z_B + \sqrt{Z_A Z_B} r}{Z_A - \sqrt{Z_A Z_B} r} \tag{6.7}$$

Equation (6.7) can be re-arranged to express r as

$$r = \sqrt{\frac{Z_A}{Z_B}} \left(\frac{Z_{IN} - Z_B}{Z_{IN} + Z_A} \right) \tag{6.8}$$

For a generalized analysis, it is convenient to normalize to the impedance Z_A, therefore the normalized impedance is given by

$$z_{IN} = \frac{z_B + \sqrt{z_B} r}{1 - \sqrt{z_B} r} \tag{6.9}$$

Equation (6.9) contains two free complex variables: r and z_B. Therefore, there are four degrees of freedom due to both variables being complex quantities in general. This gives some freedom in synthesizing an arbitrary input impedance. For an initial investigation, let us fix $z_B = 1$ and investigate the input impedances which may be synthesized as a function of $|r|$ and $\angle r$. This will demonstrate how controlling the relative power and phase of the excitation sources a_1 and a_2 can be used to synthesize an arbitrary impedance. The resultant range of input impedances is

shown in Fig. 6.2 as a function of $|r|$ and $\angle r$. The specific cases when $\angle r = 0°$ and $\angle r = 180°$ are depicted in Fig. 6.3. There are some conclusions that can be drawn from Fig. 6.2 and Fig. 6.3. It is evident that any resistance between $+\infty$ and $-\infty$ can be electrically synthesized at the reference plane by simply adjusting the magnitude and sign of r. Of course this is under the condition where $a_1 \neq 0$.

Up to this point, we have simply addressed the synthesized impedance. However, it is also important to understand the power delivered into medium A under the conditions of the impedance

(a) Re$\{z_{IN}\}$

(b) Im$\{z_{IN}\}$
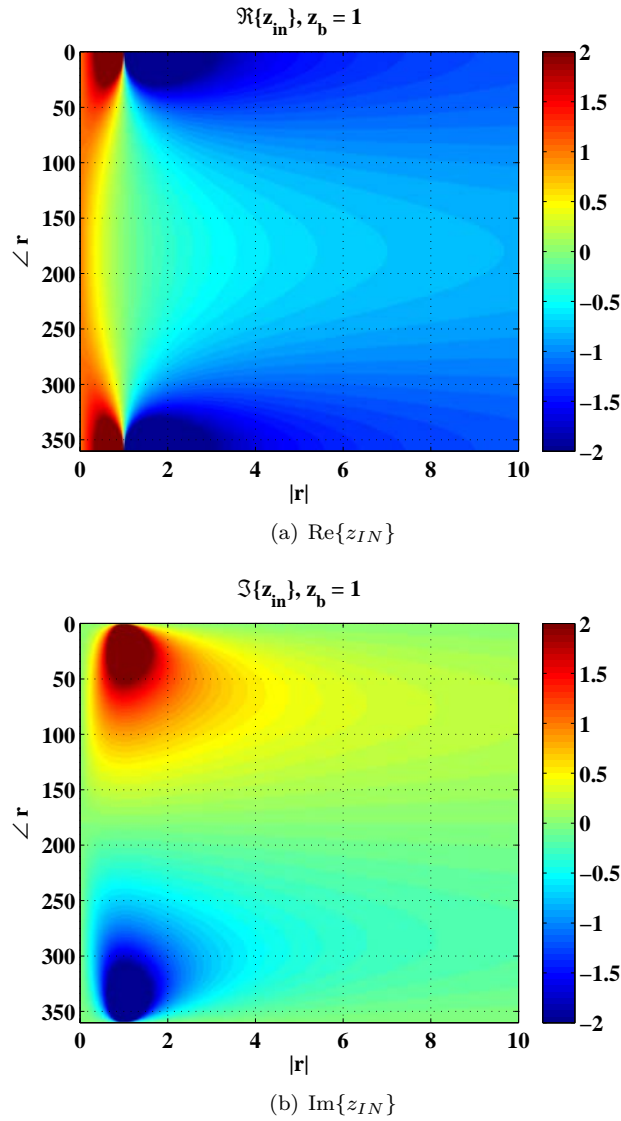
Figure 6.2: z_{IN} versus $|r|$ and $\angle r$ when $z_B = 1$.
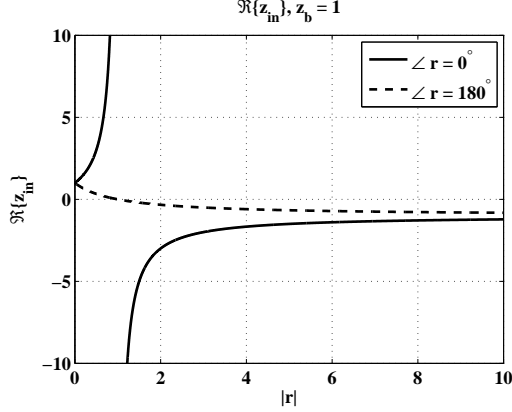
Figure 6.3: Real part of input impedance when $\angle r = 0°$ or $\angle r = 180°$. Note that in this configuration the imaginary part of the input impedance is zero.

synthesis. This can be accomplished through use of the reflection coefficient derived in (6.3). Effectively, this reflection coefficient is used to calculate the average reflected power, given by

$$P_D = |a_1|^2 |\Gamma_{IN}|^2 = |b_T|^2 \tag{6.10}$$

Substituting (6.2) into (6.10), the average power expands to

$$P_D = \left| a_1 \frac{Z_B - Z_A + 2\sqrt{Z_A Z_B}\frac{a_2}{a_1}}{Z_A + Z_B} \right|^2 \tag{6.11}$$

which can also be expressed in the form

$$P_D = |a_2|^2 \left| \frac{(Z_B - Z_A)r^{-1} + 2\sqrt{Z_A Z_B}}{Z_A + Z_B} \right|^2 \tag{6.12}$$

Substituting (6.8) into (6.12) and simplifying yields

$$P_D = |a_2|^2 \frac{Z_B}{Z_A} \left| \frac{Z_A - Z_{IN}}{Z_B - Z_{IN}} \right|^2 \tag{6.13}$$

This expression allows one to determine the power delivered into medium A at the reference plane. This is necessary to characterize for the harmonic injection amplifier because of the specific relationship between fundamental and harmonic Fourier coefficients of the drain voltage and current waveforms. This will be investigated further in the following sections. Finally, the wave amplitude is expressed as

$$|a_2|^2 = \frac{P_D}{\frac{Z_B}{Z_A} \left| \frac{Z_A - Z_{IN}}{Z_B - Z_{IN}} \right|^2} \tag{6.14}$$

159

Under the conditions $Z_A = Z_B$ and $a_1 = 0$, (6.14) reduces to

$$|a_2|^2 = P_D \qquad (6.15)$$

This represents the most efficient use of injected power, because all available power from the injector translates to delivered power at the reference plane. It should be noted that in this case no electrical impedance synthesis is required. This concludes the necessary basic circuit analysis for understanding impedance synthesis using harmonic injection. The most important conclusion is that the transistor must be a harmonic source in order to synthesize an arbitrary impedance. Furthermore, it is necessary to know the amount of harmonic power it is able to generate, as well as the its effective source impedance. Once these things are known, the required input impedance and delivered power may be satisfied for ideal drain voltage and current wave shaping. The main purpose of this analysis has been to understand how to synthesize an impedance having a negative real part if necessary, but is applicable to impedance synthesis in general.

6.3 Second Harmonic Injection Drain Waveforms

Consider the normalized drain voltage and drain current waveforms at the virtual drain of a linear FET PA shown in the block diagram in Fig. 6.4 which are given by

$$\bar{v}_D(\theta) = \bar{V}_{DD} + \sqrt{2}\sin\theta \qquad (6.16)$$

$$\bar{i}_D(\theta) = \bar{I}_{DD} - \sqrt{2}\sin\theta \qquad (6.17)$$

where $\theta = 2\pi f_0 t$, and the bar indicates a normalized quantity. For instance, when $\bar{V}_{DD} = \bar{I}_{DD} = \sqrt{2}$, the normalized class-A output power is $1\,\mathrm{W}$ and the waveforms result in 50% efficiency. If the drain waveforms can be shaped in a manner such that the overlap of the voltage and current is minimized for a given fundamental frequency output power, then drain efficiency will be maximized.

The class-A current and voltage waveforms are symmetrical, and next we consider how the duration of current and voltage waveform overlap, and thus dissipation in the device, can be

Figure 6.4: Block diagram of a linear PA with second harmonic injection at the virtual drain. The three-port network is an ideal passive injection circuit element described in Section 6.5 and further analyzed in Section 6.6. The injector voltage and impedance $Z(2f_0)$ determine the dissipation in the transistor. The matching networks at input and output are designed for a linear PA.

minimized while maintaining time-domain waveform symmetry. This can be accomplished by adding appropriate harmonic components to (6.16) and (6.17). Consider the addition of only a second harmonic term. In order to maintain waveform symmetry following addition of a second harmonic term, only co-sinusoidal components may be added because sinusoidal components are not even functions about $\theta = 180°$. Such a condition will result in a current waveform consistent with a finite harmonic class-B amplifier, with the voltage waveform being the same shape and $180°$ out of phase. The waveforms following addition of a second harmonic term become

$$\bar{v}_D(\theta) = \bar{V}_{DD} + \sqrt{2}\sin\theta + a_2\cos(2\theta) \tag{6.18}$$

$$\bar{i}_D(\theta) = \bar{I}_{DD} - \sqrt{2}\sin\theta + a_2\cos(2\theta) \tag{6.19}$$

It is important to note at this point that these waveforms represent a negative impedance being presented to the virtual drain of the transistor at the second harmonic. Effectively, this requires that power is delivered to the transistor at the second harmonic. The impedance synthesized is the negative of that presented at the fundamental frequency. This can be seen by investigation of (6.18)-(6.19) and noting that the ratio of the second harmonic Fourier coefficients is equivalent to that of the fundamental coefficients, except the sign is reversed.

Next, the optimal value of a_2 is found to maximize the efficiency, taking into account an assumed injector efficiency. First, the critical points of the drain voltage waveform are expressed as

$$\sin \theta_{critical,v} = \sqrt{2}/4a_2 \tag{6.20}$$

and

$$\theta_{critical,v} = \pi/2 + n\pi, \quad n = 0, 1, ..., \infty \tag{6.21}$$

where $\theta_{critical,v}$ corresponds to a point at which the first derivative of the voltage waveform w.r.t θ is equal to zero. Note that (6.20) is only valid when

$$-1 \leq \sin \theta_{critical,v} \leq +1 \tag{6.22}$$

Therefore, (6.20) is only valid when

$$|a_2| \geq \sqrt{2}/4 \tag{6.23}$$

The second derivative of the normalized drain voltage at the critical point described by (6.20) results in

$$\frac{\partial^2 \bar{v}_D(\theta)}{\partial \theta^2} = -4a_2 \tag{6.24}$$

Therefore, if a_2 is negative in sign, then the critical point corresponds to a minimum, while if it is positive in sign, then it corresponds to a maximum. Applying the second derivative test to the critical point described by (6.21) results in

$$\frac{\partial^2 \bar{v}_D(\theta)}{\partial \theta^2} = \sqrt{2}(-1)^{n+1} + 4a_2, \quad n = 0, 1, ..., \infty \tag{6.25}$$

Therefore, the critical point described by (6.21) will be an extremum as follows:

$$a_2 > +\sqrt{2}/4, \quad \bar{v}_D(\theta_{critical,v}) \text{ is a minimum} \tag{6.26}$$

$$a_2 < -\sqrt{2}/4, \quad \bar{v}_D(\theta_{critical,v}) \text{ is a maximum} \tag{6.27}$$

When $-\frac{\sqrt{2}}{4} < a_2 < +\frac{\sqrt{2}}{4}$, the critical points will alternate with n between maxima and minima. If $a_2 \geq -\frac{\sqrt{2}}{4}$, the global minimum occurs at the critical point corresponding to (6.21) with $n = 1$. Otherwise, the global minimum occurs at the critical point corresponding to (6.20).

The normalized total DC power consumed by the PA can now be expressed as

$$\bar{P}_{DC} = \bar{V}_{DD}\bar{I}_{DD} + \frac{a_2^2}{2\eta_{inj}} = \bar{V}_{DD}^2 + \frac{a_2^2}{2\eta_{inj}} \tag{6.28}$$

where η_{inj} is the efficiency of the injection circuit, defined as the ratio of available injector power $P_{inj}(2f_0)$ to the DC power consumed by the injector $P_{inj,DC}$. The highest efficiency is achieved when the DC supply voltage results in a drain voltage waveform minimum of zero. Therefore,

$$\bar{V}_{DD} = -\sqrt{2}\sin\theta_{min,v} - a_2\cos(2\theta_{min,v}) \tag{6.29}$$

The expansion of (6.28) can be written as

$$\bar{P}_{DC} = \begin{cases} \left(\frac{1+4a_2^2}{4a_2}\right)^2 + \frac{a_2^2}{2\eta_{inj}}, & a_2 \leq \frac{-\sqrt{2}}{4} \\[3mm] (\sqrt{2}+a_2)^2 + \frac{a_2^2}{2\eta_{inj}}, & a_2 > \frac{-\sqrt{2}}{4} \end{cases} \tag{6.30}$$

The coefficient a_2 corresponding to the highest efficiency is found by setting the partial derivative of (6.30) to zero:

$$\frac{\partial \bar{P}_{DC}}{\partial a_2} = \begin{cases} 2a_2 - \frac{1}{8a_2^3} + \frac{a_2}{\eta_{inj}} = 0, & a_2 \leq \frac{-\sqrt{2}}{4} \\[3mm] 2\sqrt{2} + 2a_2 + \frac{a_2}{\eta_{inj}} = 0, & a_2 > \frac{-\sqrt{2}}{4} \end{cases} \tag{6.31}$$

The solution for a_2 which optimizes efficiency is:

$$a_2 = \begin{cases} -\dfrac{1}{\sqrt[4]{8\left(2+\frac{1}{\eta_{inj}}\right)}}, & a_2 \leq \frac{-\sqrt{2}}{4} \longrightarrow \eta_{inj} \geq \frac{1}{6} \\[5mm] -\dfrac{2\sqrt{2}}{2+\frac{1}{\eta_{inj}}}, & a_2 > \frac{-\sqrt{2}}{4} \longrightarrow \eta_{inj} < \frac{1}{6} \end{cases} \tag{6.32}$$

A plot of a_2 versus η_{inj} is shown in Fig. 6.5. As expected, the magnitude of a_2 decreases as the injector efficiency decreases. Another interesting parameter to investigate is the ratio of the delivered fundamental output power to the required delivered second harmonic injected power, which is found by calculating $20\log_{10}\left|\frac{a_2}{\sqrt{2}}\right|$, and is also shown in Fig. 6.5.

The normalized DC power is found from (6.30) and (6.32), and is given by

$$\bar{P}_{DC} = \begin{cases} \dfrac{1+2\eta_{inj}}{\eta_{inj}\sqrt{\frac{8}{\eta_{inj}}+16}} + \frac{1}{2}, & \eta_{inj} \geq \frac{1}{6} \\[5mm] \dfrac{2}{2\eta_{inj}+1}, & \eta_{inj} < \frac{1}{6} \end{cases} \tag{6.33}$$

The normalized fundamental output power is 1 W based upon the definition of the fundamental frequency Fourier coefficients, therefore the total efficiency becomes the inverse of the normalized

163
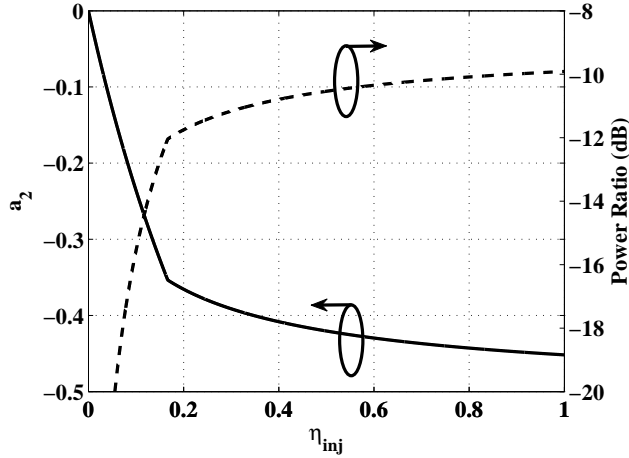
Figure 6.5: Optimal solution for Fourier coefficient a_2 (solid line) and second harmonic delivered power relative to fundamental frequency output power (dashed line) versus second harmonic injection efficiency η_{inj}.

DC power, given by

$$\eta_{total} = \begin{cases} \eta_{inj} \left(\sqrt{\frac{8}{\eta_{inj}} + 16} - 4 \right), & \eta_{inj} \geq \frac{1}{6} \\ \frac{2\eta_{inj}+1}{2}, & \eta_{inj} < \frac{1}{6} \end{cases} \qquad (6.34)$$

A plot of the total efficiency versus injector efficiency is shown in Fig. 6.6. The maximum value

is 89.9%, and it rolls off reasonably slowly with decreasing injector efficiency. This is intuitive

because the power required from the injector is significantly lower than the fundamental output

power of the PA, as shown in Fig. 6.5. As expected, the drain efficiency reaches 50% as injector

efficiency reduces t   on.
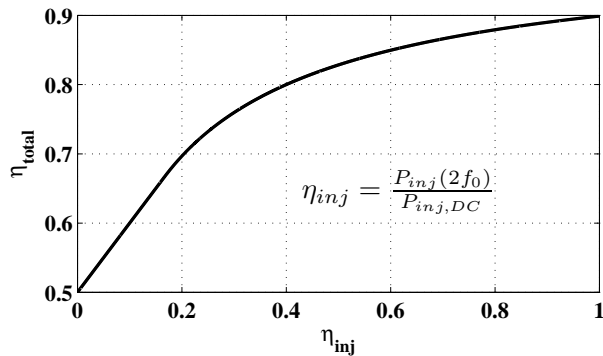
Figure 6.6: Total efficiency η_{total} versus injector efficiency η_{inj}.

As previously mentioned, the load presented to the virtual drain at the second harmonic is

164

the negative of that presented at the fundamental, so the harmonic load resistance normalized to the class-A fundamental load is -1. However, the output power of the PA normalized to class-A output power remains to be found. In order to find this, normalization conditions corresponding to constant peak voltage and current constraints are enforced. $\bar{V}_{DD}$ and $\bar{I}_{DD}$ are now found which will enable determination of the maximum instantaneous normalized voltage $\bar{V}_{max}$ and current $\bar{I}_{max}$. Using $\bar{V}_{max}$ and $\bar{I}_{max}$, the output power normalized to the class-A PA output power is determined. The normalized DC voltage may now be expressed as

$$\bar{V}_{DD} = \begin{cases} -\frac{1+4a_2^2}{4a_2}, & \eta_{inj} \geq \frac{1}{6} \\[2ex] \sqrt{2} + a_2, & \eta_{inj} < \frac{1}{6} \end{cases} \tag{6.35}$$

Due to the symmetry of the current and voltage waveforms, $\bar{V}_{DD} = \bar{I}_{DD}$, and the maximum value of the normalized current waveform is equivalent to the maximum value of the normalized voltage waveform

$$\bar{V}_{max} = \begin{cases} -\frac{1+8a_2^2-4\sqrt{2}a_2}{4a_2}, & \eta_{inj} \geq \frac{1}{6} \\[2ex] 2\sqrt{2}, & \eta_{inj} < \frac{1}{6} \end{cases} \tag{6.36}$$

The output power normalized to class-A is then given by

$$p_{LA}(f_0) = \begin{cases} \dfrac{8}{\left(\frac{1+8a_2^2-4\sqrt{2}a_2}{4a_2}\right)^2}, & \eta_{inj} \geq \frac{1}{6} \\[3ex] \dfrac{8}{(2\sqrt{2})^2} = 1, & \eta_{inj} < \frac{1}{6} \end{cases} \tag{6.37}$$

Fig. 6.7 depicts the fundamental frequency output power reduction relative to a class-A PA versus injector efficiency. This was calculated by computing a_2 as a function of η_{inj}, then computing the output power from a_2 and determining the ratio relative to $1\,\mathrm{W}$. When injection efficiency is 100%, the output power is reduced by $0.13\,\mathrm{dB}$ relative to the class-A PA.

It is of practical interest to plot the supply voltage normalized to class-A supply voltage found as

$$v_{DD,A} = \bar{V}_{DD}/\sqrt{2} \tag{6.38}$$

165
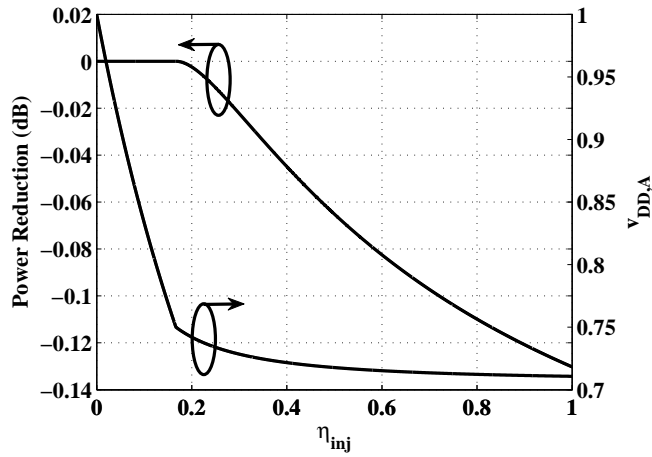
Figure 6.7: Power reduction and normalized supply voltage $v_{DD,A}$ versus injector efficiency η_{inj}.

In this formulation, the normalized supply current is equivalent to the above. Fig. 6.7 shows the supply voltage normalized by the class-A supply voltage as a function of injector efficiency. The value when the injector efficiency is 100% is approximately 0.7107. The resultant normalized ideal drain waveforms (i.e. injector efficiency is 100%) are shown Fig. 6.8. As expected, the current waveform appears as a class-B current waveform with limited harmonic content, while the voltage waveform is identical to the current waveform shifted by 180°.
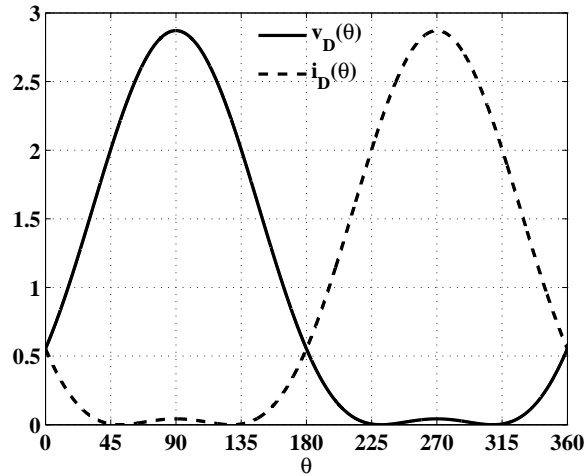
Figure 6.8: Optimal drain current and voltage waveforms when the optimal value of a_2 from (6.32) and $\bar{V}_{DD}$ from (6.35) are calculated assuming $\eta_{inj} = 1$.

166

6.4 Third Harmonic Injection Drain Waveforms

The previous section introduced the second harmonic injection amplifier with the logic behind the selection of the harmonic injection component being to maintain waveform symmetry. This section introduces another idea for a harmonic injection amplifier based upon third harmonic injection. An alternate set of ideal waveforms is considered in order to develop the third harmonic injection concept. Consider shaping the current and voltage waveforms to symmetric square waves. It is well known that a square wave contains only DC, fundamental and odd harmonic components. Therefore, it should be possible to shape the current and voltage waveforms into symmetric square waves using infinite injection of odd harmonics, but let us consider use of only the first odd harmonic (e.g. the third harmonic). In order to maintain waveform symmetry, the third-harmonic-only amplifier normalized drain waveforms are constructed in the form given by

$$\bar{v}_D(\theta) = \bar{V}_{DD} + \sqrt{2}\sin\theta + b_3\sin(3\theta) \tag{6.39}$$

$$\bar{i}_D(\theta) = \bar{I}_{DD} - \sqrt{2}\sin\theta - b_3\sin(2\theta) \tag{6.40}$$

It is interesting to note is that in the case of third harmonic injection, the impedance at the third harmonic is positive rather than negative, so the waveforms of (6.39) and (6.40) can be realized with a passive set of output terminations rather than by electrical impedance synthesis via harmonic injection at the output. However, relying on a passive set of terminations and the third harmonic components generated by the active device is unlikely to realize the optimal levels of harmonic current and voltage. Additionally, the active device would produce some second harmonic current or voltage if it were to produce third harmonic components, which would destroy the waveform symmetry. The third harmonic injection concept suggests the injection be done at the input of the active device with a passive third harmonic termination, allowing the device to operate in its linear region. To analyze the concept, the optimal value of b_3 is found just as a_2 was found in the previous section. The first partial derivative of the voltage waveform in (6.39) w.r.t θ is

$$\frac{\partial \bar{v}_D(\theta)}{\partial \theta} = \sqrt{2}\cos\theta + 3b_3\cos(3\theta) \tag{6.41}$$

Substituting the trigonometric identity

$$cos3\theta = 4cos^3\theta - 3cos\theta \tag{6.42}$$

into (6.41) reduces the partial derivative to

$$\frac{\partial \bar{v}_D(\theta)}{\partial \theta} = 12b_3 \cos^3 \theta + (\sqrt{2} - 9b_3) \cos \theta \tag{6.43}$$

The critical points are determined by setting (6.43) to zero and finding the solutions, which are

$$cos\theta_{critical,v} = \pm\sqrt{\frac{9b_3 - \sqrt{2}}{12b_3}} \tag{6.44}$$

and

$$\theta_{critical,v} = \frac{\pi}{2} + n\pi, \quad n = 0, 1, ..., \infty \tag{6.45}$$

First the solutions of (6.44) are investigated. In order for the solution to be valid, the term under the square root of (6.44) is restricted such that $-1 \leq \cos \theta_{critical,v} \leq +1$. Therefore,

$$\frac{9b_3 - \sqrt{2}}{12b_3} \geq 0 \tag{6.46}$$

and

$$\frac{9b_3 - \sqrt{2}}{12b_3} \leq 1 \tag{6.47}$$

The numerator of (6.46) has a root at $b_3 = \frac{\sqrt{2}}{9}$ and the denominator has a root at $b_3 = 0$. Therefore, the intervals of analysis are $[-\infty, 0)$, $\left(0, \frac{\sqrt{2}}{9}\right]$, and $\left[\frac{\sqrt{2}}{9}, +\infty\right]$. Using the test point method (i.e. picking a test point in each defined interval and checking the sign),

$$\frac{9b_3 - \sqrt{2}}{12b_3} \geq 0, \quad b_3 \left|[-\infty, 0), \left[\frac{\sqrt{2}}{9}, +\infty\right]\right. \tag{6.48}$$

To analyze (6.47), all terms are collected over a common denominator which yields the form

$$\frac{3b_3 + \sqrt{2}}{12b_3} \geq 0 \tag{6.49}$$

The numerator of (6.49) has a root at $b_3 = -\frac{\sqrt{2}}{3}$ and the denominator has a root at $b_3 = 0$. Therefore, the intervals of analysis are $\left[-\infty, -\frac{\sqrt{2}}{3}\right]$, $\left[-\frac{\sqrt{2}}{3}, 0\right)$, and $(0, +\infty]$. Using the test point method,

$$\frac{3b_3 + \sqrt{2}}{12b_3} \geq 0, \quad b_3 \left|\left[-\infty, -\frac{\sqrt{2}}{3}\right], (0, +\infty]\right. \tag{6.50}$$

Therefore, when b_3 is in the interval $\left(-\frac{\sqrt{2}}{3}, +\frac{\sqrt{2}}{9}\right)$, (6.44) does not produce a critical point, and the critical points are strictly defined by (6.45). Which critical points correspond to the minima, maxima, the global minimum, and the global maximum must now be proven. The second partial derivative of the voltage waveform w.r.t θ is

$$\frac{\partial^2 \bar{v}_D(\theta)}{\partial \theta^2} = -36b_3 \cos^2 \theta \sin \theta - (\sqrt{2} - 9b_3) \sin \theta \tag{6.51}$$

which simplifies to

$$\frac{\partial^2 \bar{v}_D(\theta)}{\partial \theta^2} = 36b_3 \sin^3 \theta - (\sqrt{2} + 27b_3) \sin \theta \tag{6.52}$$

First the solution of (6.44) is investigated. Substituting this into (6.52) results in

$$\frac{\partial^2 \bar{v}_D(\theta)}{\partial \theta^2} = 36b_3 \left(\pm\sqrt{1 - \frac{9b_3 - \sqrt{2}}{12b_3}}\right)\left(1 - \frac{9b_3 - \sqrt{2}}{12b_3}\right) - (\sqrt{2} + 27b_3)\left(\pm\sqrt{1 - \frac{9b_3 - \sqrt{2}}{12b_3}}\right) \tag{6.53}$$

which simplifies to

$$\frac{\partial^2 \bar{v}_D(\theta)}{\partial \theta^2} = (2\sqrt{2} - 18b_3)\left(\pm\sqrt{1 - \frac{9b_3 - \sqrt{2}}{12b_3}}\right) \tag{6.54}$$

The best way to analyze (6.54) is to look at the two terms separately. Start by writing (6.54) in the form

$$\frac{\partial^2 \bar{v}_D(\theta)}{\partial \theta^2} = (2\sqrt{2} - 18b_3)\left(\pm\sqrt{\frac{3b_3 + \sqrt{2}}{12b_3}}\right) \tag{6.55}$$

It is evident that the first term is greater than zero when $b_3 < \frac{\sqrt{2}}{9}$ and less than zero when $b_3 > \frac{\sqrt{2}}{9}$. The first term equals zero when $b_3 = \frac{\sqrt{2}}{9}$. The second term is a bit more difficult to analyze. First the range of b_3 over which the inside of the square root is positive must be determined. This is done by analyzing the equation

$$\frac{3b_3 + \sqrt{2}}{12b_3} > 0 \tag{6.56}$$

The numerator of the equation has a root at $b_3 = -\frac{\sqrt{2}}{3}$ and the denominator has a root at $b_3 = 0$. Therefore, the intervals of analysis are $\left[-\infty, -\frac{\sqrt{2}}{3}\right]$, $\left[-\frac{\sqrt{2}}{3}, 0\right)$, and $(0, +\infty]$. Using the test point method,

$$\frac{3b_3 + \sqrt{2}}{12b_3} > 0, \quad b_3 \left| \left[-\infty, -\frac{\sqrt{2}}{3}\right], (0, +\infty] \right. \tag{6.57}$$

169

However, the interval $\left[0, \frac{\sqrt{2}}{9}\right)$ does not contain a valid solution based upon the previous analysis. So subsequent analysis is limited to the intervals $\left[-\infty, -\frac{\sqrt{2}}{3}\right]$ and $\left[\frac{\sqrt{2}}{9}, +\infty\right]$. Combining these results with the analysis of the first term, the properties of the second partial derivative as a function of valid values of b_3 can be stated. When the sign of the square root in (6.54) is positive,

$$\frac{\partial^2 \bar{v}_D(\theta)}{\partial \theta^2} \rightarrow \begin{cases} > 0, & b_3 \left| \left(\frac{\sqrt{2}}{9}, +\infty \right] \right. \\ < 0, & b_3 \left| \left[-\infty, -\frac{\sqrt{2}}{3} \right) \right. \\ = 0, & b_3 = \frac{\sqrt{2}}{9} \end{cases} \tag{6.58}$$

When the sign of the square root in (6.54) is negative,

$$\frac{\partial^2 \bar{v}_D(\theta)}{\partial \theta^2} \rightarrow \begin{cases} < 0, & b_3 \left| \left(\frac{\sqrt{2}}{9}, +\infty \right] \right. \\ > 0, & b_3 \left| \left[-\infty, -\frac{\sqrt{2}}{3} \right) \right. \\ = 0, & b_3 = \frac{\sqrt{2}}{9} \end{cases} \tag{6.59}$$

Now the solution of (6.45) is investigated. Substituting this into (6.52) results in

$$\frac{\partial^2 \bar{v}_D(\theta)}{\partial \theta^2} = 36b_3 \sin^3\left(\frac{\pi}{2} + n\pi\right) - (\sqrt{2} + 27b_3)\sin\left(\frac{\pi}{2} + n\pi\right), \quad n = 0, 1, ..., \infty \tag{6.60}$$

which simplifies to

$$\frac{\partial^2 \bar{v}_D(\theta)}{\partial \theta^2} = (9b_3 - \sqrt{2})(-1)^n, \quad n = 0, 1, ..., \infty \tag{6.61}$$

It is only necessary to investigate the first two solutions corresponding to $n = 0$ and $n = 1$ because the rest correspond to the periodicity of the waveform. When $n = 0$,

$$\frac{\partial^2 \bar{v}_D(\theta)}{\partial \theta^2} \rightarrow \begin{cases} > 0, & b_3 \left| \left(\frac{\sqrt{2}}{9}, +\infty \right] \right. \\ < 0, & b_3 \left| \left[-\infty, -\frac{\sqrt{2}}{3} \right) \right. \\ = 0, & b_3 = \frac{\sqrt{2}}{9} \end{cases} \tag{6.62}$$

When $n = 1$,

$$\frac{\partial^2 \bar{v}_D(\theta)}{\partial \theta^2} \rightarrow \begin{cases} < 0, & b_3 \left| \left(\frac{\sqrt{2}}{9}, +\infty \right] \right. \\ > 0, & b_3 \left| \left[-\infty, -\frac{\sqrt{2}}{3} \right) \right. \\ = 0, & b_3 = \frac{\sqrt{2}}{9} \end{cases} \tag{6.63}$$

170

To identify the global minimum the four known minima must be compared to see which results in the lower value. The known minima are dictated by values of b_3 for which (6.58), (6.59), (6.62) and (6.62) are greater than zero. The voltage minimum corresponding to the critical point in (6.44) with the square root taken as positive is

$$\bar{v}_D(\theta_{critical,v}) = \bar{V}_{DD} + \sqrt{2}\sqrt{1 - \frac{9b_3 - \sqrt{2}}{12b_3}} + b_3 \sin(3\theta_{v,critical}) \qquad (6.64)$$

which through use of the triple angle formula becomes

$$\bar{v}_D(\theta_{critical,v}) = \bar{V}_{DD} + \sqrt{2}\sqrt{1 - \frac{9b_3 - \sqrt{2}}{12b_3}} + b_3 \left[3\sin(\theta_{v,critical}) - 4\sin^3(\theta_{v,critical})\right] \qquad (6.65)$$

which simplifies to

$$\bar{v}_D(\theta_{critical,v}) = \bar{V}_{DD} + \left(\frac{2\sqrt{2}}{3} + 2b_3\right)\sqrt{1 - \frac{9b_3 - \sqrt{2}}{12b_3}} \qquad (6.66)$$

Similarly, if the negative square root of the critical point in (6.44) is taken, the voltage minimum is

$$\bar{v}_D(\theta_{critical,v}) = \bar{V}_{DD} - \left(\frac{2\sqrt{2}}{3} + 2b_3\right)\sqrt{1 - \frac{9b_3 - \sqrt{2}}{12b_3}} \qquad (6.67)$$

The value of the voltage minimum corresponding to the critical point in (6.45) with $n = 0$ is

$$\bar{v}_D(\theta_{critical,v}) = \bar{V}_{DD} + \sqrt{2}\sin\left(\frac{\pi}{2}\right) + b_3 \sin\left(3\frac{\pi}{2}\right) \qquad (6.68)$$

which simplifies to

$$\bar{v}_D(\theta_{critical,v}) = \bar{V}_{DD} + \sqrt{2} - b_3 \qquad (6.69)$$

This is a minimum when b_3 is in the range $\left(\frac{\sqrt{2}}{9}, +\infty\right]$. The value of the voltage minimum corresponding to the critical point in (6.45) with $n = 1$ is

$$\bar{v}_D(\theta_{critical,v}) = \bar{V}_{DD} + \sqrt{2}\sin\left(\frac{\pi}{2} + \pi\right) + b_3 \sin\left(3\frac{\pi}{2} + 3\pi\right) \qquad (6.70)$$

which simplifies to

$$\bar{v}_D(\theta_{critical,v}) = \bar{V}_{DD} - \sqrt{2} + b_3 \qquad (6.71)$$

This is a minimum when b_3 is in the range $\left[-\infty, \frac{\sqrt{2}}{9}\right)$. Now the minima are compared to determine the global minimum as a function of b_3. First, the global minimum when b_3 is in the range

$[-\infty, -\frac{\sqrt{2}}{3}]$ is determined. In this case, there are two minima of interest. Let us try to prove that the minimum corresponding to (6.44) with the positive root taken is the minimum. Then we must prove

$$\left(\frac{2\sqrt{2}}{3} + 2b_3\right)\sqrt{1 - \frac{9b_3 - \sqrt{2}}{12b_3}} < -\sqrt{2} + b_3 \tag{6.72}$$

Direct evaluation of (6.72) proves its invalidity, therefore when b_3 is in the range $\left[-\infty, -\frac{\sqrt{2}}{3}\right]$, the solution to the critical point corresponding to the global minimum is $\theta_{critical,v} = \frac{\pi}{2} + \pi$. The range over which this critical point corresponds to the global minima can be extended to $\left[-\infty, \frac{\sqrt{2}}{9}\right)$ since it is the only minima in this extended range.

Next the global minimum when b_3 is in the range $\left(\frac{\sqrt{2}}{9}, +\infty\right]$ is determined. By direct evaluation, it can be shown that when b_3 is in this region, the solution to the critical point corresponding to the global minimum is given by $cos\theta_{critical,v} = \pm\sqrt{\frac{9b_3 - \sqrt{2}}{12b_3}}$. Now it is fully known how to determine the global minimum of the voltage waveform as a function of b_3. Due to the symmetry of the voltage and current waveforms, the minimum normalized voltage will be equivalent to the minimum normalized current. Therefore, the normalized supply current will be equivalent to the normalized supply voltage, and the normalized voltage global maximum will be equivalent to the normalized current global maximum. Next the normalized supply voltage is found for each potential global minimum. The normalized supply voltage is

$$\bar{V}_{DD} = -\sqrt{2}\sin\theta_{min,v} - b_3\sin(3\theta_{min,v}) \tag{6.73}$$

Through substitution of the appropriate critical points, the normalized supply voltage is expressed as

$$\bar{V}_{DD} = \begin{cases} \sqrt{2} - b_3, & b_3 \left|\left[-\infty, \frac{\sqrt{2}}{9}\right)\right. \\ \left(\frac{2\sqrt{2}}{3} + 2b_3\right)\sqrt{1 - \frac{9b_3 - \sqrt{2}}{12b_3}}, & b_3 \left|\left(\frac{\sqrt{2}}{9}, +\infty\right]\right. \end{cases} \tag{6.74}$$

The consumed DC power is expressed as

$$\bar{P}_{DC} = \bar{V}_{DD}\bar{I}_{DD} + \frac{b_3^2}{2\eta_{inj}} = \bar{V}_{DD}^2 + \frac{b_3^2}{2\eta_{inj}} \tag{6.75}$$

Which in the two regions of b_3 having unique solutions is expressed as

$$\bar{P}_{DC} = \begin{cases} (\sqrt{2} - b_3)^2 + \frac{b_3^2}{2\eta_{inj}}, & b_3 \bigg| \left[-\infty, \frac{\sqrt{2}}{9}\right) \\ \left[\left(\frac{2\sqrt{2}}{3} + 2b_3\right)\sqrt{1 - \frac{9b_3 - \sqrt{2}}{12b_3}}\right]^2 + \frac{b_3^2}{2\eta_{inj}}, & b_3 \bigg| \left(\frac{\sqrt{2}}{9}, +\infty\right] \end{cases} \tag{6.76}$$

which reduces to

$$\bar{P}_{DC} = \begin{cases} (\sqrt{2} - b_3)^2 + \frac{b_3^2}{2\eta_{inj}}, & b_3 \bigg| \left[-\infty, \frac{\sqrt{2}}{9}\right) \\ \sqrt{2}b_3 + \frac{2\sqrt{2}}{27b_3} + b_3^2 + \frac{2}{3} + \frac{b_3^2}{2\eta_{inj}}, & b_3 \bigg| \left(\frac{\sqrt{2}}{9}, +\infty\right] \end{cases} \tag{6.77}$$

Now the DC power is minimized. The partial derivative of (6.77) w.r.t. b_3 is

$$\frac{\partial \bar{P}_{DC}}{\partial b_3} = \begin{cases} -2(\sqrt{2} - b_3) + \frac{b_3}{\eta_{inj}}, & b_3 \bigg| \left[-\infty, \frac{\sqrt{2}}{9}\right) \\ \sqrt{2} - \frac{2\sqrt{2}}{27b_3^2} + 2b_3 + \frac{b_3}{\eta_{inj}}, & b_3 \bigg| \left(\frac{\sqrt{2}}{9}, +\infty\right] \end{cases} \tag{6.78}$$

Note that if the second partial derivative of (6.78) is taken and evaluated for a given b_3, the result is positive, therefore the critical point of the DC power always corresponds to the global minimum. Setting (6.78) equal to zero and solving for b_3 results in

$$b_3 = \frac{2\sqrt{2}}{2 + \frac{1}{\eta_{inj}}}, \quad b_3 \bigg| \left[0, \frac{\sqrt{2}}{9}\right) \tag{6.79}$$

and the purely real positive root of the other expression in (6.78), which is the root of a cubic equation. Notice that b_3 must be greater than zero, given the injector efficiency is always positive. That is the reason for the changed limits of b_3 in (6.79). Also, note that above a certain injector efficiency, the result becomes inconsistent with the range of b_3 over which it is valid. By setting b_3 to the limiting values of the range and solving for injector efficiency, we find that (6.79) is only valid when η_{inj} is in the range $\left[0, \frac{1}{16}\right)$, or in other words up to 6.25% injector efficiency. Above 6.25% injector efficiency, the other solution for b_3 is the valid solution. Fig. 6.9 depicts the optimal solution for b_3 as a function of injector efficiency. This graph was created by parsing together the results from the two different regions of solution. The efficiency may now be calculated as a function of injector efficiency. An analytical expression is not provided because it is complicated due to the root of the cubic equation in (6.78). Fig. 6.10 depicts the total efficiency versus injector efficiency. Fig. 6.11 depicts the optimal drain voltage and current waveforms using third harmonic injection which result from 100% injector efficiency.
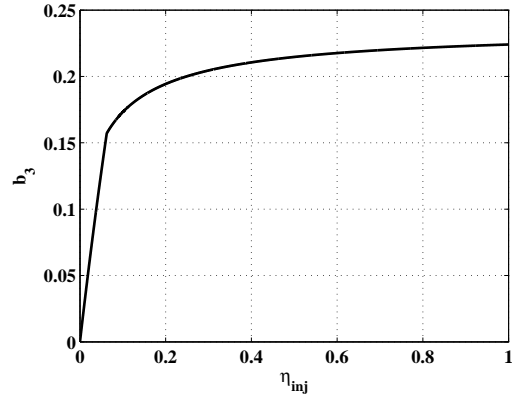
Figure 6.9: Solution for b_3 versus injector efficiency.
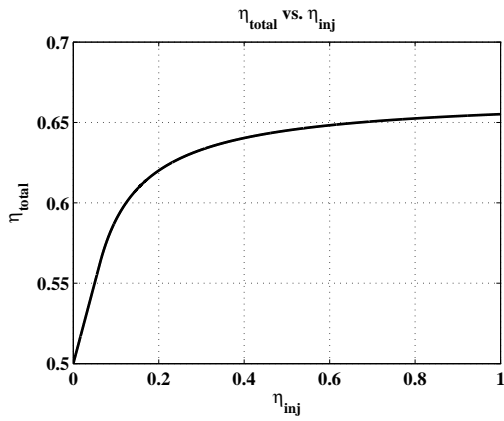
Figure 6.10: Total efficiency versus injector efficiency.
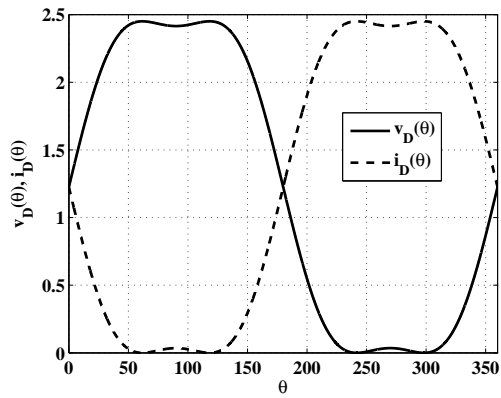
Figure 6.11: Optimal drain current and voltage waveforms for third harmonic injection amplifier.

6.5 Practical Implementation Issues & Limitations

The analysis of the previous sections demonstrates that a high drain efficiency can theoretically be realized via harmonic injection. However, there are several practical issues that must be considered, such as synthesis of the harmonic impedance at the virtual drain of the transistor and the design and influence of the injector passive three port from Fig. 6.4.

The synthesis of a negative second harmonic impedance at the virtual drain can be accomplished using output harmonic injection only in the case where the transistor itself is generating second harmonic content. If the transistor fails to generate second harmonic power and presents an impedance other than that of the fundamental frequency output termination, the necessary negative impedance for optimal injection cannot be synthesized using harmonic injection. In this case, it would be necessary to perform harmonic injection at both the input and output of the transistor.

The ideal passive three port injection circuit shown in Fig. 6.4 is assumed to be lossless in the presented analysis. In general, the ideal S-parameters of the network at the fundamental and harmonic frequencies are given by

$$S(f_0) = \begin{bmatrix} 0 & e^{j\phi_{21}(f_0)} & 0 \\ e^{j\phi_{21}(f_0)} & 0 & 0 \\ 0 & 0 & e^{j\phi_{33}(f_0)} \end{bmatrix} \tag{6.80}$$

$$S(2f_0) = \begin{bmatrix} 0 & 0 & e^{j\phi_{31}(2f_0)} \\ 0 & e^{j\phi_{22}(2f_0)} & 0 \\ e^{j\phi_{31}(2f_0)} & 0 & 0 \end{bmatrix} \tag{6.81}$$

where the S-parameters are assumed to be normalized to the fundamental frequency load impedance. Port-1, port-2, and port-3 are assumed to connect to the device, output load, and harmonic injector, respectively. An example of such a circuit can be found in [103], where the presented multiplexing circuit coupled with the appropriate termination on port-2 obeys (6.80)-(6.81).

6.6 Injection Circuit Analysis

In order to allow for design of a satisfactory injection network, a theoretical design procedure is presented. First assume that there are two individual two-port networks and that their scattering parameters are known. Let the networks be defined as network-A and network-B, with the respective scattering parameters $S_{A,ij}$ and $S_{B,ij}$. The two-port networks are shown on the left side of Fig. 6.12 and the connection scheme resulting in the three-port network is shown on the right side of Fig. 6.12. The goal is to derive the scattering parameters of the three-port network
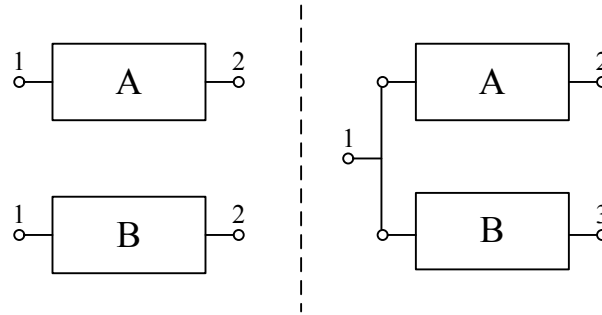
Figure 6.12: Diagram showing construction of a three-port network from two two-port networks.

in terms of the parameters of the two-port networks. A straightforward manner in which to approach the problems is depicted in Fig. 6.13. A signal flow graph analysis could be performed as an alternative approach.

The shunt impedance shown in Fig. 6.13 represents the effective impedance created by the termination of port-2 of either network-A or network-B in a load consistent with the reference impedance for the scattering parameters, which is denoted as Z_0. In the case of analysis of port-1 to port-2, $[S_x] = [S_A]$ while in the case of analysis of port-1 to port-3 $[S_x] = [S_B]$. First, let us derive an expression for the normalized shunt impedance $z_{shunt,x}$. Remember that this represents and normalized input impedance created by two-port network terminated in Z_0. Under the assumption that the scattering parameters of the network are normalized to the reference impedance Z_0, the input reflection coefficient is simply S_{11} of the network. Therefore,

Analysis circuit for port-1 to port-2 and port-1 to port-3

Analysis circuit for port-2 to port-3
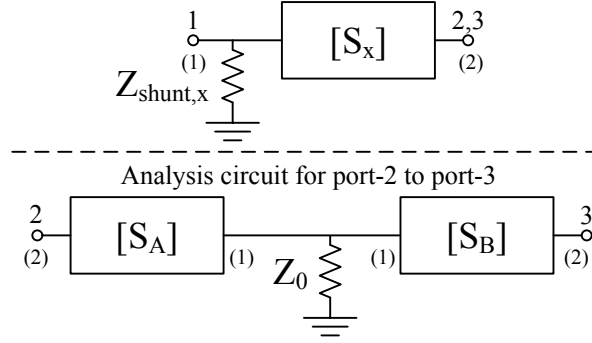
Figure 6.13: Diagram showing the circuits used to determine the three-port scattering parameters. $Z_{shunt,x}$ and $[S_x]$ denote a shunt impedance and scattering parameter block, respectively. Note that in general $Z_{shunt,x}$ and $[S_x]$ will differ for each analysis circuit. For example, $Z_{shunt,x}$ and $[S_x]$ will differ for the analysis of port-1 to port-2 and port-1 to port-3, although they are represented by the same basic circuit in the figure.

the normalized shunt impedance $z_{shunt,x}$ is given by

$$
z_{shunt,x} = \begin{cases} \frac{1+S_{B,11}}{1-S_{B,11}}, & \text{(port-1 to port-2)} \\\\ \frac{1+S_{A,11}}{1-S_{A,11}}, & \text{(port-1 to port-3)} \end{cases} \tag{6.82}
$$

From now on, the normalized shunt impedance presented by network-A as is referred to as $z_{shunt,A}$ and the normalized shunt impedance presented by network-B as $z_{shunt,B}$. Now that an expression for the normalized shunt impedance is obtained, the most straightforward analysis procedure is to analyze the three analysis circuits using ABCD parameters. The ABCD parameters of the shunt impedance are given by

$$
ABCD_{Z_{shunt,x}} = \begin{bmatrix} 1 & 0 \\\\ Y_{shunt,x} & 1 \end{bmatrix} \tag{6.83}
$$

Let the ABCD parameters of the network-A and network-B be defined as

$$
ABCD_A = \begin{bmatrix} A_A & B_A \\\\ C_A & D_A \end{bmatrix} \tag{6.84}
$$

$$
ABCD_B = \begin{bmatrix} A_B & B_B \\\\ C_B & D_B \end{bmatrix} \tag{6.85}
$$

Now we begin to form the scattering parameters. First we analyze port-1 to port-2. In this case

177

the cascaded ABCD parameters are given by

$$ABCD_{12} = \begin{bmatrix} A_A & B_A \\ A_A Y_{shunt,B} + C_A & B_A Y_{shunt,B} + D_A \end{bmatrix} \tag{6.86}$$

Using the formulas in [23] where a real port impedance is assumed, the scattering parameters

are expressed as

$$S_{11} = \frac{2z_{shunt,B}(S_{A,11} + 1)}{2z_{shunt,B} + S_{A,11} + 1} - 1 = \frac{S_{A,11} - \frac{S_{A,11}+1}{2z_{shunt,B}}}{1 + \frac{S_{A,11}+1}{2z_{shunt,B}}} \tag{6.87}$$

$$S_{12} = \frac{2z_{shunt,B}S_{A,12}}{2z_{shunt,B} + S_{A,11} + 1} = \frac{S_{A,12}}{1 + \frac{S_{A,11}+1}{2z_{shunt,B}}} \tag{6.88}$$

$$S_{21} = \frac{2z_{shunt,B}S_{A,21}}{2z_{shunt,B} + S_{A,11} + 1} = \frac{S_{A,21}}{1 + \frac{S_{A,11}+1}{2z_{shunt,B}}} \tag{6.89}$$

$$S_{22} = S_{A,22} - \frac{S_{A,12}S_{A,21}}{2z_{shunt,B} + S_{A,11} + 1} \tag{6.90}$$

Now (6.82) may be substituted to fully express the scattering parameters in terms of the two-port network parameters. However, as we will see later, it is more useful to leave the expressions in the current form. Through an identical analysis, we can also express the port-1 to port-3 results as

$$S_{11} = \frac{2z_{shunt,A}(S_{B,11} + 1)}{2z_{shunt,A} + S_{B,11} + 1} - 1 = \frac{S_{B,11} - \frac{S_{B,11}+1}{2z_{shunt,A}}}{1 + \frac{S_{B,11}+1}{2z_{shunt,A}}} \tag{6.91}$$

$$S_{13} = \frac{2z_{shunt,A}S_{B,12}}{2z_{shunt,A} + S_{B,11} + 1} = \frac{S_{B,12}}{1 + \frac{S_{B,11}+1}{2z_{shunt,A}}} \tag{6.92}$$

$$S_{31} = \frac{2z_{shunt,A}S_{B,21}}{2z_{shunt,A} + S_{B,11} + 1} = \frac{S_{B,21}}{1 + \frac{S_{B,11}+1}{2z_{shunt,A}}} \tag{6.93}$$

$$S_{33} = S_{B,22} - \frac{S_{B,12}S_{B,21}}{2z_{shunt,A} + S_{B,11} + 1} \tag{6.94}$$

Finally, we must analyze the final circuit to arrive at the remaining scattering parameters. The cascaded ABCD parameters are give by

$$ABCD_{23} = \begin{bmatrix} A_A^* & B_A^* \\ C_A^* & D_A^* \end{bmatrix} \begin{bmatrix} 1 & 0 \\ Y_0 & 1 \end{bmatrix} \begin{bmatrix} A_B & B_B \\ C_B & D_B \end{bmatrix} \tag{6.95}$$

$$ABCD_{23} = \begin{bmatrix} A_A^* A_B + B_A^* C_B + B_A^* A_B Y_0 & A_A^* B_B + B_A^* D_B + B_A^* B_B Y_0 \\ C_A^* A_B + D_A^* C_B + D_A^* A_B Y_0 & C_A^* B_B + D_A^* D_B + D_A^* B_B Y_0 \end{bmatrix} \tag{6.96}$$

where the $*$ indicates that the ABCD parameters are calculated with port-1 and port-2 reversed.

After applying the conversion, the remaining scattering parameters are given by

$$S_{22} = S_{A,22} + \frac{2S_{A,12}S_{A,21}(S_{B,11}-1)}{S_{B,11} - S_{A,11}(S_{B,11}-1) + 3} \tag{6.97}$$

$$S_{23} = \frac{2S_{A,12}S_{B,21}}{S_{A,11} - S_{B,11}(S_{A,11}-1) + 3} \tag{6.98}$$

$$S_{32} = \frac{2S_{B,12}S_{A,21}}{S_{A,11} - S_{B,11}(S_{A,11}-1) + 3} \tag{6.99}$$

$$S_{33} = S_{B,22} + \frac{2S_{B,12}S_{B,21}(S_{A,11}-1)}{S_{A,11} - S_{B,11}(S_{A,11}-1) + 3} \tag{6.100}$$

This completes the derivation of the 3-port scattering parameters as a function of the 2-port scattering parameters. Now we start to place requirements on the 2-port scattering parameters based upon the requirements placed on the 3-port scattering parameters given in (6.80) and (6.81). Note that from these requirements we have some commonality between the fundamental and second harmonic scattering parameters. We see that at both frequencies, $S_{11} = S_{32} = S_{23} = 0$. First, based upon (6.87) and (6.91) we have that

$$\frac{2z_{shunt,B}(S_{A,11}+1)}{2z_{shunt,B} + S_{A,11} + 1} - 1 = 0 \tag{6.101}$$

$$\frac{2z_{shunt,A}(S_{B,11}+1)}{2z_{shunt,A} + S_{B,11} + 1} - 1 = 0 \tag{6.102}$$

These may be solved in the following forms

$$z_{shunt,A} = \frac{S_{B,11}+1}{2S_{B,11}} \tag{6.103}$$

$$z_{shunt,B} = \frac{S_{A,11}+1}{2S_{A,11}} \tag{6.104}$$

$$S_{A,11} = \frac{1}{2z_{shunt,B} - 1} \tag{6.105}$$

$$S_{B,11} = \frac{1}{2z_{shunt,A} - 1} \tag{6.106}$$

This gives some guidance about what the two-port networks must present as shunt impedances, or what $S_{A,11}$ and $S_{B,11}$ must be in order to enforced the matched condition at port-1. Next, from the condition that $S_{32} = S_{23} = 0$ we can state using (6.98) and (6.99) that

$$S_{A,12}S_{B,21} = S_{B,12}S_{A,21} = 0 \tag{6.107}$$

179

Given that the two port networks are passive, we have the knowledge that they are reciprocal. Therefore, we can state that for this condition to hold we require that either $S_{A,12} = S_{A,21} = 0$ or $S_{B,12} = S_{B,21} = 0$. Note that these conditions must not be simultaneously true at a given frequency because transmission of energy would never be able to occur between any ports in that case. By inspection of (6.80) and (6.81) with the knowledge of the derived scattering parameters, we conclude that

$$S_{B,21}(f_0) = S_{B,12}(f_0) = 0 \tag{6.108}$$

and

$$S_{A,21}(2f_0) = S_{A,12}(2f_0) = 0 \tag{6.109}$$

We know that we want total transmission from port-1 to port-2 at f_0, therefore

$$|S_{21}(f_0)|^2 = 1 \tag{6.110}$$

which from (6.89) and (6.104) results in

$$\frac{|S_{A,21}(f_0)|^2}{|1 + \frac{S_{A,11}(f_0)+1}{2z_{shunt,B}(f_0)}|^2} = \frac{|S_{A,21}(f_0)|^2}{|1 + S_{A,11}(f_0)|^2} = 1 \tag{6.111}$$

Which expands to

$$\frac{|S_{A,21}(f_0)|^2}{1 + 2\operatorname{Re}\{S_{A,11}(f_0)\} + |S_{A,11}(f_0)|^2} = 1 \tag{6.112}$$

Therefore, for the above to be satisfied we require that

$$|S_{A,21}(f_0)|^2 = 1 \quad |S_{A,11}(f_0)|^2 = 0 \tag{6.113}$$

These requirements further simplify our previous expression for the shunt impedance to

$$z_{shunt,B}(f_0) = \infty \tag{6.114}$$

Similarly, we know that we want total transmission from port-1 to port-3 at $2f_0$, therefore

$$|S_{31}(2f_0)|^2 = 1 \tag{6.115}$$

which results in

$$\frac{|S_{B,21}(2f_0)|^2}{|1 + \frac{S_{B,11}(2f_0)+1}{2z_{shunt,A}(2f_0)}|^2} = \frac{|S_{B,21}(2f_0)|^2}{|1 + S_{B,11}(2f_0)|^2} = 1 \tag{6.116}$$

Which expands to

$$\frac{|S_{B,21}(2f_0)|^2}{1 + 2\operatorname{Re}\{S_{B,11}(2f_0)\} + |S_{B,11}(2f_0)|^2} = 1 \tag{6.117}$$

Therefore, for the above to be satisfied we require that

$$|S_{B,21}(2f_0)|^2 = 1 \quad |S_{B,11}(2f_0)|^2 = 0 \tag{6.118}$$

We can also write that

$$S_{22}(f_0) = 0 \tag{6.119}$$

Therefore

$$S_{A,22}(f_0) - \frac{S_{A,12}(f_0)S_{A,21}(f_0)}{2z_{shunt,B}(f_0) + S_{A,11}(f_0) + 1} = 0 \tag{6.120}$$

which immediately requires that

$$S_{A,22}(f_0) = 0 \tag{6.121}$$

We can also write that

$$S_{33}(2f_0) = 0 \tag{6.122}$$

Therefore

$$S_{B,22}(2f_0) - \frac{S_{B,12}(2f_0)S_{B,21}(2f_0)}{2z_{shunt,A}(2f_0) + S_{B,11}(2f_0) + 1} = 0 \tag{6.123}$$

which immediately requires that

$$S_{B,22}(2f_0) = 0 \tag{6.124}$$

Next we solve for $S_{A,11}(2f_0)$. We know that

$$z_{shunt,B}(2f_0) = \frac{1 + S_{B,11}(2f_0)}{1 - S_{B,11}(2f_0)} = \frac{1 + 0}{1 - 0} = 1 \tag{6.125}$$

Therefore, using (6.105) we may state that

$$S_{A,11}(2f_0) = \frac{1}{2z_{shunt,B}(2f_0) - 1} = \frac{1}{2 - 1} = 1 \tag{6.126}$$

Next we solve for $S_{B,11}(f_0)$. We know that

$$z_{shunt,A}(f_0) = \frac{1 + S_{A,11}(f_0)}{1 - S_{A,11}(f_0)} = \frac{1 + 0}{1 - 0} = 1 \tag{6.127}$$

Therefore, using (6.106) we may state that

$$S_{B,11}(f_0) = \frac{1}{2z_{shunt,A}(f_0) - 1} = \frac{1}{2 - 1} = 1 \tag{6.128}$$

Now we solve for $S_{A,22}(2f_0)$. We require that

$$|S_{22}(2f_0)|^2 = 1 \tag{6.129}$$

First we can simplify (6.90) to the form

$$S_{22}(2f_0) = S_{A,22}(2f_0) - \frac{0}{2 + 1 + 1} = S_{A,22}(2f_0) \tag{6.130}$$

Therefore, we require that

$$|S_{A,22}(2f_0)|^2 = 1 \tag{6.131}$$

Through a similar procedure, it can be shown that

$$|S_{B,22}(f_0)|^2 = 1 \tag{6.132}$$

We have now fully expressed the requirements on the individual two port networks, and they are now summarized below

$$S_A(f_0) = \begin{bmatrix} 0 & e^{j\theta_{A,21}(f_0)} \\ e^{j\theta_{A,21}(f_0)} & 0 \end{bmatrix} \tag{6.133}$$

$$S_A(2f_0) = \begin{bmatrix} 1 & 0 \\ 0 & e^{j\theta_{A,22}(2f_0)} \end{bmatrix} \tag{6.134}$$

$$S_B(f_0) = \begin{bmatrix} 1 & 0 \\ 0 & e^{j\theta_{B,22}(f_0)} \end{bmatrix} \tag{6.135}$$

$$S_B(2f_0) = \begin{bmatrix} 0 & e^{j\theta_{B,21}(2f_0)} \\ e^{j\theta_{B,21}(2f_0)} & 0 \end{bmatrix} \tag{6.136}$$

Investigation of S_A reveals that it represents nothing more that a low-pass filter. However, it represents a special low-pass filter under further inspection due to the requirement on $S_{A,11}(2f_0)$. In the stop-band, the network must look like an open circuit rather than just a reflective

182

termination as is typically the case with a reflective filter. This represents a difficult design challenge, where not only the magnitude of the reflection coefficient must be synthesized but also the phase. This is certainly achievable over a narrow bandwidth, but it is desirable to find a way to achieve it over a broad bandwidth. It is noted that the same stop-band characteristic is required for the network represented by S_B, where in this case the filter is a high-pass filter.

6.7 Conclusion

This chapter presents an analysis of an alternative approach to high-efficiency PA design, using a nominally linear amplifier and injecting harmonic power externally at the load side. The details of second and third harmonic injection are given, along with a discussion of an appropriate network that can be inserted into the output network for harmonic injection. Ground work for experimental verification and appropriate efficiency definitions are also presented. Specific contributions of this chapter include:

- Development of a theory for externally harmonically injected amplifiers for the first time, to the best of our knowledge. It is our plan to submit this work for publication in IEEE Transactions on Microwave Theory & Techniques, along with some experimental validation.

- The theoretical approach shows that from the efficiency and complexity standpoint, it is practical to only consider injection of the second harmonic, and that under ideal conditions the injected amplifier exceeds the theoretical best efficiency of a harmonically terminated amplifier.

- The results are validated with a simple set of experiments and are reported in [14].

- Because a linear amplifier is used as the main amplification mechanism, the overall PA is more linear than a standard harmonically-terminated high efficiency PA, leading to the possibility of achieving linearity with simultaneous high efficiency over a potentially broad bandwidth, assuming a broadband injection circuit can be designed.

- Theoretical analysis of the passive 3-port injection circuit is developed, with a conclusion it needs to behave like interconnected low-pass and high-pass 2-port filters, which act as open circuits in the stop bands. If such a circuit can be designed, simultaneous linearity, efficiency and bandwidth in a PA would be enabled by the harmonic injection architecture.

Chapter 7

Summary and Future Work

Contents

7.1 Summary & Contributions

In summary, the research presented in this thesis addresses techniques for analysis and design of high-efficiency power amplifiers, with extensions to linear high-efficiency transmitters and high-efficiency rectifiers. Specific contributions associated with the material in Chapters 2-6 are summarized below, followed by some obvious directions for future work.

Chapter 2 presented some of the basics of load pull based power amplifier design, including some basic load-pull theory and measurement network design. A method for calibrating and measuring a single slug mechanical tuner was presented and verified with a FOCUS Microwaves tuner. The load pull method is necessary for high-efficiency PA design when good models are not available, which is commonly the case, especially for new device technologies such as GaN used in this thesis. The specific contributions described in this chapter are:

- Application of basic load pull theory to design of a high-efficiency 2.14 GHz cell-phone band PA.

- The resulting design was implemented in a hybrid circuit with a TriQuint 12 W GaN die. This PA was measured independently by Agilent at the 2010 IEEE International Microwave Symposium, resulting in 82.6 % PAE with 38.2 dBm output power and 18 dB large signal gain. This PA won second place at the 2010 IMS PA Student Competition and is also reported in [9].

- The load-pull design method was scaled to 10 GHz in a GaN MMIC test structure with implicit harmonic terminations on-chip. The TriQuint 0.25 μm GaN process was used and resulted in an efficiency of 50 % at 10 GHz with 3.5 W of output power in a test MMIC. The measured results from this test circuit serve as input characterization information for the next iteration of a high-efficiency 10 GHz PA design, with estimated potential PAE of 70 %.

Chapter 3 expands previous work on harmonic terminations for high-efficiency PAs. The analysis of ideal PA behavior for arbitrary complex harmonic terminations is presented, which extends existing theory developed by Raab in [40], which was only valid for specific reactive impedances. Specific conclusions resulting from the analysis can be summarized as follows.

- The method is useful because it predicts the sensitivity of relevant PA parameters to specific impedance terminations at the harmonic frequencies. This is especially important for higher microwave frequency PAs, where the harmonics are in the millimeter-wave range, and parasitic reactances and loss can significantly affect the impedances designed at the harmonics.

- An interesting result from the theory is the limited sensitivity of efficiency and power to harmonic termination phase, which points to the possibility of extending bandwidth through use of appropriate resonant circuits.

- The theoretical approach was validated with qualitative measurements on a 2.14 GHz class-F^{-1} PA with second and third harmonic terminations and is presented in [10].

- In Section 3.6, the theory was extended to include a linear transformation due to C_{out} and was further extended to include bond wires in the experimental validation. In general, the method may be applied to a PA having an arbitrary parasitic output network which is linear and characterized by S-parameters.

- The method in this chapter can be extended to include analysis of PA efficiency, output power, and output load given an arbitrary set of both input and output harmonic terminations.

In Chapter 4, a theoretical motivation has been presented for development of a radar transmitter capable of generating amplitude modulated pulses. The spectral confinement properties of a radar system capable of AM signal transmission is superior to that of one limited to constant envelope signals. However, it is also important to understand the impacts which transmission of an AM signal has on other radar performance characteristics, of which some have been investigated in the previous sections. Implementation and measurement of a system capable of high efficiency AM radar signal transmission has been detailed as well, demonstrating the feasibility of such a transmitter. The specific contributions presented in this chapter are:

- Development of theoretical analysis of the impact of amplitude-modulated pulses on radar performance, which was reported in [69].

- In collaboration with Prof. Dragan Maksimović and Dr. Miguel Rodríguez, implemented a simple efficient pulsed supply modulator with an approximately raised cosine amplitude modulation. The supply was characterized with an efficient PA from Chapter 2, with a modified bias line.

- With digital pre-distortion used for linearization, the supply-modulated PA demonstrated reduced spectral content outside of the band of interest. The PA operates at 2.14 GHz with 78 % efficiency at 6 W peak power, and with 66.4 % average efficiency over a 14.7 μs pulse with a 4.1dB PAR shaped by a 90 % efficient resonant-pulse envelope supply modulator. For

PARs greater than 4.1 dB, the signal envelope can be split between the supply modulator and the PA drive, with up to 25 % improvement in composite efficiency.

- This work is reported in [11], where details of the supply modulators are given, as well as a submitted paper to IEEE Microwave and Wireless Components Letters with focus on RF characterization and linearization [12].

Chapter 5 presents an analysis of microwave rectifiers using analogies from power amplifiers with harmonic terminations to improve efficiency. The analysis is confirmed with measured data on several shunt Schottky diode rectifiers, and can be applied to wireless powering which is investigated in [96]. The specific contributions of this chapter are:

- A new approach to rectifier analysis and to increasing efficiency in rectifiers, modeled after efficient power amplifier design, and reported only briefly in [13].

- Experimental verification of the analysis, based on measurements of a class-C 2.45 GHz Schottky-diode rectifier with short-circuit 2nd and 3rd harmonic terminations. A maximum RF-DC conversion efficiency of 72.8% when matched to $50\,\Omega$ is demonstrated. The approach is applied to integration of a rectifier with a dual-polarization patch antenna in a non $50\,\Omega$ environment and free-space measurements demonstrate a lower bound on efficiency of 56% at $150\,\mu\text{W}\backslash\text{cm}^2$ power density which includes matching circuit and mismatch losses [13].

- The details and extensions of the presented theory in [13] will be submitted for journal publication in IEEE Transactions on Microwave Theory & Techniques.

Chapter 6 presents an analysis of an alternative approach to high-efficiency PA design, using a nominally linear amplifier and injecting harmonic power externally at the load side. The details of second and third harmonic injection are given, along with a discussion of an appropriate network that can be inserted into the output network for harmonic injection. Ground work for experimental verification and appropriate efficiency definitions are also presented. Specific contributions of this chapter include:

- Development of a theory for externally harmonically injected amplifiers for the first time, to the best of our knowledge. It is our plan to submit this work for publication in IEEE Transactions on Microwave Theory & Techniques, along with some experimental validation.

- The theoretical approach shows that from the efficiency and complexity standpoint, it is practical to only consider injection of the second harmonic, and that under ideal conditions the injected amplifier exceeds the theoretical best efficiency of a harmonically terminated amplifier.

- The results are validated with a simple set of experiments and are reported in [14].

- Because a linear amplifier is used as the main amplification mechanism, the overall PA is more linear than a standard harmonically-terminated high efficiency PA, leading to the possibility of achieving linearity with simultaneous high efficiency over a potentially broad bandwidth, assuming a broadband injection circuit can be designed.

7.2 Some Directions for Future Work

The underlining theme of this thesis is Fourier analysis applied to various seemingly unrelated nonlinear microwave circuits such as harmonically terminated saturated PAs, rectifiers and harmonically injected linear PAs. The theory is idealized in most cases, and can be extended to include more practical and non-ideal parameters. A direction for doing this is shown, e.g. in Chapter 3 by including C_{out}, and in Chapter 5 by including V_{tr} and R_{on}.

Follow-up work related to the method described in Chapter 2 is in the direction of GaN MMIC design at X-band and above. TriQuint Semiconductor has developed a 0.15 μm GaN process, and the methodology described in Chapter 2 can be applied to future MMIC designs for high-efficiency PAs. Since this process has limited power available from a single device, power combining on-chip will be necessary, and initial work on including integrated power combiner networks is underway. Specifically, investigation of odd and even mode contributions in a corporate symmetrical power combined MMIC PA is of interest and will be necessary to achieve a stable and efficient GaN
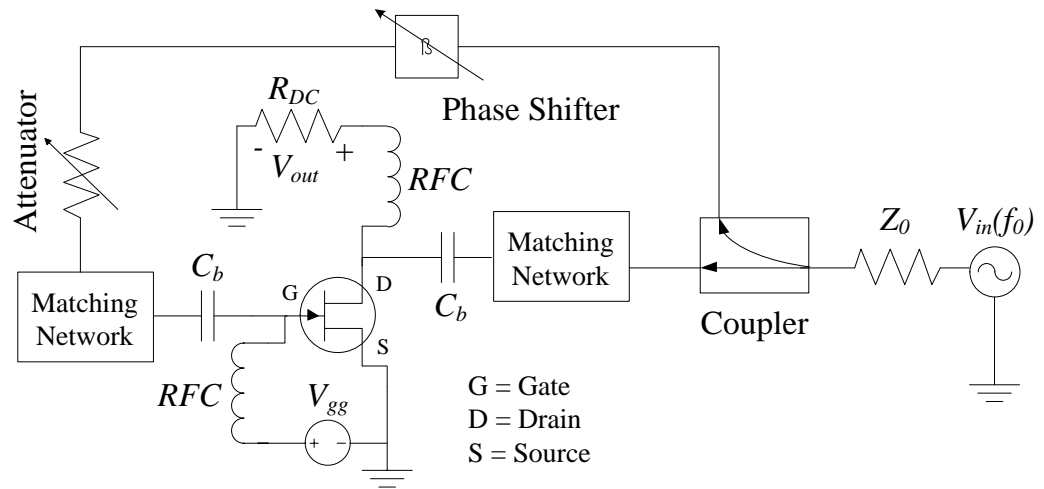
Figure 7.1: Transistor rectifier block diagram. The fundamental frequency RF source shown as $V_{in}(f_0)$ and Z_0 is used to drive both the drain and the gate of the field effect transistor in a common source configuration.

MMIC at 10 GHz.

The microwave power rectifier work presented in Chapter 5 may be extended to transistor rectifiers. Fig. 7.1 shows the basic block diagram of a transistor-based rectifier using a field effect transistor. The drive level at the gate relative to the drain is optimized via the coupling factor of the coupler, phase shifter and attenuator to maximize the RF-DC conversion efficiency. Matching networks are used at the gate and drain in order to present the optimal impedances for RF-DC conversion efficiency. The DC load R_{DC} is also optimized to maximize efficiency. A preliminary rectifier was fabricated and tested at 2.45 GHz using the following procedure. A 25 W TriQuint 0.25 μm GaN die was tested as an amplifier with source pull and load pull measurements subject to second and third harmonic class-F^{-1} terminations. The device was biased at the class-B bias point. Given the dual nature of a microwave amplifier and rectifier as discussed in Chapter 5, it is postulated that the impedances found through this procedure will work well for a microwave rectifier. This method of determining the impedance matching networks was chosen because it greatly simplifies the measurement procedure. If the device were initially tested as a rectifier, the drive level at the gate and drain, as well as the RF impedances and DC load would need to be

optimized. Additionally, the phase of the drive at the gate relative to the drain would need to be optimized. However, when testing the device as an amplifier, only the RF impedances and gate drive level need to be optimized.

When presented with the optimal impedances at the gate and source and bias at $35\,\mathrm{V}$, the rectifier exhibited a $79.7\,\%$ PAE with $42.3\,\mathrm{dBm}$ output power and $14.3\,\mathrm{dB}$ of gain. The optimal fundamental frequency load impedance was $66\,\Omega$, while the ratio of DC supply voltage to DC supply current was $59.25\,\Omega$. Note that the ratio of the fundamental impedance to the DC load is very near that of an ideal class-F^{-1} amplifier. Given the amplifier measurements, the device was then tested as a rectifier, with identical RF matching and the DC load set to $59.25\,\Omega$. After optimization of the gate and drain drive levels and relative phase, the rectifier produced $13.4\,\mathrm{W}$ when driven with a total of $17.7\,\mathrm{W}$, resulting in an RF-DC conversion efficiency of $75.7\,\%$. This efficiency is very close to the PAE of the transistor when used as an amplifier. Additionally, the ratio of the drain drive level to the gate drive level was approximately the gain of the device when operating as an amplifier with optimal PAE ($14\,\mathrm{dB}$). It was noted that the efficiency of the rectifier was sensitive to the phase of the gate drive relative to the drain drive. Investigation of the sensitivity due to the relative phase is a path for future work.

The harmonic injection power amplifier work in Chapter 6 has many possibilities for future work. Initial research in the synthesis of a wide-band injection network is necessary for achieving a broadband amplifier, with a path toward this end being presented in Chapter 6. Investigation of the linearity of the concept is currently underway with some of the work being published in [14]. Further investigation of the linearity of the harmonic injection amplifier when driven with a modulated signal is important research which needs to be performed. Finally, development of a communication transmitter using the harmonic injection amplifier is relevant, with the system performance metrics being of interest.

The research presented in Chapter 4 has several areas in which future work could be performed. Specifically, experimentation with phase and amplitude modulated radar signals is of interest, especially from a linearity standpoint. In order to be more efficient for higher PAR levels, a

modulator needs to be developed which can more drastically swing the drain voltage of the PA. The many challenges of the future work include linearization, the modulator-PA interconnect, and accurate co-characterization. Initial work in this area for communication signals is given in [106] where some parts from Chapter 3 are included.

In summary, the work presented in this thesis demonstrates concepts for improving efficiency of PAs for microwave communication and radar transmitters. The role of the impedance presented to the active device at harmonic frequencies is investigated via a generalized Fourier analysis which may be applied not only to amplifiers with harmonic terminations at the output, but also to microwave rectifiers and power amplifiers with external injection of waves at harmonic frequencies. The challenge of simultaneous efficiency and linearity in a transmitter is addressed for radar waveforms. The harmonic injection amplifier is shown as a possible approach to solving the even more challenging problem of simultaneous efficiency, linearity and bandwidth.

Bibliography

[1] Agilent, "Agilent PN 8720-2 In-Fixture Microstrip Device Measurements Using TRL Calibration." online, accessed 04/01/11, 2000. xiv, 40

[2] E. Falkenstein, *Characterization and Design of a Low-Power Wireless Power Delivery System.* PhD thesis, University of Colorado at Boulder, Boulder, CO, 2011. xxi, 127, 134, 135

[3] S. Mclaughlin, P. Grant, J. Thompson, H. Haas, D. Laurenson, C. Khirallah, Y. Hou, and R. Wang, "Techniques for improving cellular radio base station energy efficiency," *Wireless Communications, IEEE*, vol. 18, pp. 10 –17, october 2011. 2

[4] G. Gonzalez, *Microwave Transistor Amplifiers.* Englewood Cliffs, NJ: Prentice-Hall, 1984. 2

[5] S. Cripps, *RF Power Amplifiers for Wireless Communications.* 685 Canton St. Norwood, MA 02062: Artech House Publishers, 2nd ed., May 2006. 2, 31, 57

[6] I. Bahl, *RF and Microwave Transistor Amplifiers.* 111 River St. Hoboken, NJ 07030: John Wiley & Sons, Inc., 1st ed., June 2009. 2, 10, 31, 57

[7] H. Krauss, C. Bostian, and F. Raab, *Solid State Radio Engineering.* 111 River St. Hoboken, NJ 07030: John Wiley & Sons, Inc., 1st ed., March 1980. 2, 60

[8] J. Hoversten, M. Roberg, and Z. Popovic, "Harmonic load pull of high-power microwave devices using fundamental-only load pull tuners," in *ARFTG Microwave Meas. Symposium Digest*, pp. 1 –4, May 2010. 6, 26, 38, 87

[9] M. Roberg, J. Hoversten, and Z. Popović and, "GaN HEMT PA with over 84% power added efficiency," *Electronics Letters*, vol. 46, pp. 1553 –1554, 11 2010. 6, 11, 55, 117, 186

[10] M. Roberg and Z. Popović, "Analysis of high-efficiency power amplifiers with arbitrary output harmonic terminations," *Microwave Theory and Techniques, IEEE Transactions on*, vol. 59, pp. 2037 –2048, aug. 2011. 6, 96, 187

[11] M. Rodríguez, M. Roberg, R. Pack, P. Fernandez, Z. Popović, A. E., and D. Maksimović, "Resonant pulse-shaping power supply for radar transmitters," in *Power Electronics and Motion Control Conference, 2012. EPE-PEMC 2012 ECCE Europe. 15th International*, 2012. 7, 118, 124, 188

[12] M. Roberg, M. Rodríguez, D. Maksimović, and Z. Popović, "Efficient and linear amplification of spectrally confined pulsed am radar signals," *Microwave and Wireless Components Letters, IEEE*, 2012. Submitted. Available upon request. 7, 124, 188

[13] M. Roberg, E. Falkenstein, and Z. Popović, "High-efficiency harmonically terminated rectifier for wireless power applications," in *Microwave Symposium Digest (MTT), 2012 IEEE MTT-S International*, 2012. Accepted. Available upon request. 7, 134, 152, 188

[14] A. Dani, M. Roberg, and Z. Popović, "Efficiency and linearity of power amplifiers with external harmonic injection," in *Microwave Symposium Digest (MTT), 2012 IEEE MTT-S International*, 2012. Accepted. Available upon request. 8, 183, 189, 191

[15] J. Cusack, S. Perlow, and B. Perlman, "Automatic load contour mapping for microwave power transistors," *Microwave Theory and Techniques, IEEE Transactions on*, vol. 22, pp. 1146 – 1152, dec 1974. 10

[16] R. Stancliff and D. Poulin, "Harmonic load-pull," in *Microwave Symp. Digest, 1979 IEEE MTT-S International*, pp. 185 –187, april 1979. 10

[17] Y. Takayama, "A new load-pull characterization method for microwave power transistors," in *Microwave Symposium, 1976 IEEE-MTT-S International*, pp. 218 –220, 14-16 1976. 10

[18] V. Camarchia, V. Teppati, S. Corbellini, and M. Pirola, "Microwave measurements part ii non-linear measurements," *Instrumentation Measurement Magazine, IEEE*, vol. 10, pp. 34 –39, June 2007. 10

[19] X. Cui, S. J. Doo, P. Roblin, J. Strahler, and R. Rojas-Teran, "High efficiency RF power amplifier designed with harmonic real-time active load-pull," *Microwave and Wireless Components Letters, IEEE*, vol. 18, pp. 266 –268, april 2008. 10

[20] D. Schmelzer and S. Long, "A GaN HEMT class F amplifier at 2 GHz with greater than 80% PAE," *Solid-State Circuits, IEEE Journal of*, vol. 42, pp. 2130 –2136, Oct. 2007. 11

[21] W.L. Pribble et al., "High efficiency class-E amplifier using GaN HEMT technology," in *IEEE Radio and Wireless Symp., 2006*, Jan. 2006. Available: http://www.cree.com/products/pdf/A high efficiency Class-E amplifier utilizing GaN HEMT technology - presentation.pdf. 11

[22] R. Beatty, "Insertion loss concepts," *Proceedings of the IEEE*, vol. 52, pp. 663 – 671, june 1964. 11

[23] D. M. Pozar, *Microwave Engineering.* New York: Addison-Wesley Publishing Comp., Inc., 1990. 16, 18, 178

[24] FOCUS Microwaves, "MPT, a universal Multi-Purpose Tuner." Product Note, 2004. 19

[25] TriQuint Semiconductor, "TGF2023-10 Datasheet." online, accessed 2/21/11, Sep 2010. http://www.triquint.com/prodserv/more_info/ proddisp.aspx?prod_id=TGF2023-10. 26, 93

[26] N. Lopez, J. Hoversten, and Z. Popovic, "Design method for UHF class-E power amplifiers," in *Compound Semiconductor Integrated Circuit Symposium, IEEE Annual*, pp. 1 –4, Oct. 2009. 27

[27] J. Hoversten, *Efficient and Linear Microwave Transmitters for High Peak-to-Average Ratio Signals.* PhD thesis, University of Colorado at Boulder, Boulder, CO, 2010. http://charon.colorado.edu/microwave/theses/Hoversten_Thesis_2sided.pdf. 29

[28] K. Ikossi, "Mtt-5 student high-efficiency pa design competition [tc contest]," *Microwave Magazine, IEEE*, vol. 12, pp. 79 –81, feb. 2011. 31

[29] G. Stimson, *Introduction To Airborne Radar.* 5601 N. Hawthorne Way, Raleigh, NC 27613: Scitech Publishing, Inc., 2nd ed., Jan 1998. 31, 99

[30] F. Raab, P. Asbeck, S. Cripps, P. Kenington, Z. Popovic, N. Pothecary, J. Sevic, and N. Sokal, "Power amplifiers and transmitters for RF and microwave," *Microwave Theory and Techniques, IEEE Transactions on*, vol. 50, pp. 814 –826, Mar 2002. 31, 153

[31] R. Tayrani, "A Spectrally pure 5.0 W, High PAE, (6-12 GHz) GaN Monolithic Class

E Power Amplifier for Advanced T/R Modules," in *Radio Frequency Integrated Circuits (RFIC) Symposium, 2007 IEEE*, pp. 581 –584, Jun 2007. 32

[32] N. Kolias, C. Whelan, T. Kazior, and K. Smith, "Gan technology for microwave and millimeter wave applications," in *Microwave Symposium Digest (MTT), 2010 IEEE MTT-S International*, pp. 1222 –1225, May 2010. 32

[33] C. Campbell, C. Lee, V. Williams, M.-Y. Kao, H.-Q. Tserng, P. Saunier, and T. Balisteri, "A Wideband Power Amplifier MMIC Utilizing GaN on SiC HEMT Technology," *Solid-State Circuits, IEEE Journal of*, vol. 44, pp. 2640 –2647, Oct. 2009. 32

[34] G. Engen and C. Hoer, "Thru-reflect-line: An improved technique for calibrating the dual six-port automatic network analyzer," *Microwave Theory and Techniques, IEEE Transactions on*, vol. 27, pp. 987 – 993, Dec. 1979. 34

[35] TriQuint Semiconductor, "3MI Layout Rules, Rev P." online, accessed 03/31/11, Mar 2011. 35

[36] Cascade Microtech, "Mechanical Layout Rules for Infinity Probes." online, accessed 04/01/11, 2006. 36

[37] TriQuint Semiconductor, "0.25-μm Gallium Nitride 3MI Process Data Sheet." online, accessed 04/01/11, July 2009. 37

[38] J. Vuolevi and T. Rahkonen, *Distortion in RF Power Amplifiers*. 685 Canton St. Norwood, MA 02062: Artech House Publishers, 1st ed., Feb 2003. 38

[39] J. Hallman, L.B., "A fourier analysis of radio-frequency power amplifier wave forms," *Proceedings of the IRE*, vol. 20, pp. 1640 – 1659, oct. 1932. 57

[40] F. Raab, "Class-E, Class-C, and Class-F power amplifiers based upon a finite number of harmonics," *Microwave Theory and Techniques, IEEE Transactions on*, vol. 49, pp. 1462 –1468, Aug 2001. 57, 58, 78, 96, 154, 186

[41] J. Rhodes, "Output universality in maximum efficiency linear power amplifiers," *Int. J. Circ. Theor. Appl.*, vol. 31, pp. 385 –405, 2003. 57

[42] S. Cripps, P. Tasker, A. Clarke, J. Lees, and J. Benedikt, "On the continuity of high efficiency modes in linear rf power amplifiers," *Microwave and Wireless Components Letters, IEEE*, vol. 19, pp. 665 –667, oct. 2009. 57

[43] A. Juhas and L. Novak, "Comments on "class-e, class-c, and class-f power amplifier based upon a finite number of harmonics"," *Microwave Theory and Techniques, IEEE Transactions on*, vol. 57, pp. 1623 –1625, june 2009. 57, 71, 78

[44] S. Cripps, "Grazing zero [microwave bytes]," *Microwave Magazine, IEEE*, vol. 11, pp. 24 –34, Dec 2010. 57

[45] F. Raab, "Class-f power amplifiers with maximally flat waveforms," *Microwave Theory and Techniques, IEEE Transactions on*, vol. 45, pp. 2007 –2012, nov 1997. 64

[46] F. Raab, "Maximum efficiency and output of class-f power amplifiers," *Microwave Theory and Techniques, IEEE Transactions on*, vol. 49, pp. 1162 –1166, jun 2001. 64

[47] J. C. Lagarias, J. A. Reeds, M. H. Wright, and P. E. Wright, "Convergence properties of the nelder–mead simplex method in low dimensions," *SIAM Journal on Optimization*, vol. 9, no. 1, pp. 112–147, 1998. 65

[48] D. E. Goldberg, *Genetic Algorithms in Search, Optimization and Machine Learning.* Boston, MA, USA: Addison-Wesley Longman Publishing Co., Inc., 1989. 65

[49] S. Kirkpatrick, J. Gelatt, C. D., and M. P. Vecchi, "Optimization by Simulated Annealing," *Science*, vol. 220, no. 4598, pp. 671–680, 1983. 65

[50] J. Stewart, *Calculus: Early Transcendentals.* 10 Davis Drive, Belmont, CA 94002: Brooks/Cole, 2nd ed., November 1991. 67

[51] A. S. Houlseholder, *The Theory of Matrices in Numerical Analysis.* New York: Blaisdell, 1st ed., 1964. 68

[52] P. Wright, J. Lees, J. Benedikt, P. Tasker, and S. Cripps, "A methodology for realizing high efficiency class-j in a linear and broadband pa," *Microwave Theory and Techniques, IEEE Transactions on*, vol. 57, pp. 3196 –3204, dec. 2009. 86

[53] S. Kee, I. Aoki, A. Hajimiri, and D. Rutledge, "The class-e/f family of zvs switching amplifiers," *Microwave Theory and Techniques, IEEE Transactions on*, vol. 51, pp. 1677 – 1690, jun. 2003. 86, 154

[54] J. H. Kim, G. D. Jo, J. H. Oh, Y. H. Kim, K. C. Lee, and J. H. Jung, "Modeling and Design Methodology of High-Efficiency Class-F and Class- F^{-1} Power Amplifiers," *Microwave Theory and Techniques, IEEE Transactions on*, vol. 59, pp. 153 –165, Jan 2011. 87

[55] J. Jeong, D. Kimball, M. Kwak, P. Draxler, C. Hsia, C. Steinbeiser, T. Landon, O. Krutko, L. Larson, and P. Asbeck, "High-efficiency wcdma envelope tracking base-station amplifier implemented with gaas hvhbts," *Solid-State Circuits, IEEE Journal of*, vol. 44, pp. 2629 –2639, Oct 2009. 88

[56] M. I. Skolnik, *Radar handbook*, ch. 11. New York, NY: McGraw-Hill, 3rd ed., Jan 2008. 98

[57] R. Chen and B. Cantrell, "Highly bandlimited radar signals," in *Radar Conference, 2002. Proceedings of the IEEE*, pp. 220 – 226, 2002. 98

[58] H. Faust, B. Connolly, T. Firestone, R. Chen, B. Cantrell, and E. Mokole, "A spectrally clean transmitting system for solid-state phased-array radars," in *Radar Conference, 2004. Proceedings of the IEEE*, pp. 140 – 144, april 2004. 98

[59] J. de Graaf, H. Faust, J. Alatishe, and S. Talapatra, "Generation of spectrally confined transmitted radar waveforms: experimental results," in *Radar, 2006 IEEE Conference on*, p. 8 pp., april 2006. 98

[60] H. Chireix, "High power outphasing modulation," *Proceedings of the Institute of Radio Engineers*, vol. 23, pp. 1370 – 1392, nov. 1935. 98

[61] L. Kahn, "Single-sideband transmission by envelope elimination and restoration," *Proc. of the IRE*, vol. 40, pp. 803 –806, july 1952. 98

[62] K. Bumman, M. Junghwan, and K. Ildu, "Efficiently amplified," *Microwave Magazine, IEEE*, vol. 11, pp. 87 –100, aug. 2010. 99

[63] D. Barton, *Radar System Analysis and Modeling*. 685 Canton St. Norwood, MA 02062: Artech House, 2nd ed., Nov 2005. 99, 115

[64] C. Cook and M. Bernfeld, *Radar Signals: An Introduction to Theory and Application*. 685 Canton St. Norwood, MA 02062: Artech House, 1st ed., Dec 1993. 99, 100, 105, 113

[65] N. Levanon and E. Mozeson, *Radar Signals*. 111 River St. Hoboken, NJ 07030: John Wiley & Sons, Inc., 1st ed., Jul 2004. 99, 106, 111

[66] Marcel Leutenegger, "Error function of complex numbers." online, accessed 2/08/12, January 2008. http://www.mathworks.com/matlabcentral/fileexchange/18312-error-function-of-complex-numbers. 104

[67] A. Nuttall, "Some windows with very good sidelobe behavior," *Acoustics, Speech and Signal Processing, IEEE Transactions on*, vol. 29, pp. 84 – 91, feb 1981. 118

[68] K. Muhonen, M. Kavehrad, and R. Krishnamoorthy, "Look-up table techniques for adaptive digital predistortion: a development and comparison," *Vehicular Technology, IEEE Transactions on*, vol. 49, pp. 1995 –2002, sep 2000. 119

[69] M. Roberg, J. Hoversten, and Z. Popovic, "Efficient and linear transmitter concept for future high-power solid-state radar systems," Invited presentation at the 2010 CNC/USNC/URSI Radio Science Metting, Boulder, CO, 2011. 123, 187

[70] T. C. Martin and N. Tesla, *The inventions, researches and writing of Nikola Tesla: with special reference to his work in polyphase currents and high potential lighting.* Milwaukee, WI: Lee Engineering Co., 1952. 126

[71] E. Peterson and F. Llewellyn, "The operation of modulators from a physical viewpoint," *Proceedings of the Institute of Radio Engineers*, vol. 18, pp. 38 – 48, jan. 1930. 126

[72] J. Nelson, "Some notes on grid circuit and diode rectification," *Radio Engineers, Proceedings of the Institute of*, vol. 20, pp. 989 –1003, june 1932. 126

[73] C. Edwards, "Microwave converters," *Proceedings of the IRE*, vol. 35, pp. 1181 – 1191, nov. 1947. 126

[74] R. George and E. Sabbagh, "An efficient means of converting microwave energy to dc using semiconductor diodes," *Proceedings of the IEEE*, vol. 51, p. 530, march 1963. 126

[75] W. Brown, "Experiments in the transportation of energy by microwave beam," in *IRE International Convention Record*, vol. 12, pp. 8 – 17, mar 1964. 126

[76] W. Brown, J. Mims, and N. Heenan, "An experimental microwave-powered helicopter," in *IRE International Convention Record*, vol. 13, pp. 225 – 235, mar 1965. 126

[77] O. E. Maynard, W. C. Brown, A. Edwards, J. T. Haley, G. Meltz, J. M. Howell, and A. Nathan, "Microwave power transmission studies. volume 1: Executive summary," Tech. Rep. 19760008506, NASA, 1975. 126

[78] O. E. Maynard, W. C. Brown, A. Edwards, J. T. Haley, G. Meltz, J. M. Howell, and A. Nathan, "Microwave power transmission studies. volume 2: Introduction, organization,

environmental and spaceborne systems analyses," Tech. Rep. 19760008507, NASA, 1975. 126

[79] O. E. Maynard, W. C. Brown, A. Edwards, J. T. Haley, G. Meltz, J. M. Howell, and A. Nathan, "Microwave power transmission studies. volume 3: Mechanical systems and flight operations," Tech. Rep. 19760008508, NASA, 1975. 126

[80] O. E. Maynard, W. C. Brown, A. Edwards, J. T. Haley, G. Meltz, J. M. Howell, and A. Nathan, "Microwave power transmission studies. volume 4: Sections 9 through 14 with appendices," Tech. Rep. 19760008509, NASA, 1975. 126

[81] D. Watson, K. Talbot, and C. Johnson, "A cyclotron-wave microwave power converter," *Proceedings of the IEEE*, vol. 53, pp. 1797 – 1798, nov. 1965. 126

[82] D. Watson, R. Grow, and C. Johnson, "A cyclotron-wave rectifier for s-band and x-band," *Electron Devices, IEEE Transactions on*, vol. 18, pp. 3 – 11, jan 1971. 126

[83] W. C. Brown, "High power, efficient, free-space microwave power transmission systems," in *Microwave Conference, 1973. 3rd European*, vol. 2, pp. 1 –4, sept. 1973. 126

[84] W. Brown and C. Kim, "Recent progress in power reception efficiency in a free-space microwave power transmission system," in *Microwave Symposium Digest, 1974 S-MTT International*, vol. 74, pp. 332 – 333, jun 1974. 126

[85] W. Brown, "The design of large scale terres trial rectennas for low-cost production and erection," in *Microwave Symposium Digest, 1978 IEEE-MTT-S International*, pp. 349 –351, june 1978. 126

[86] R. Gutmann and J. Borrego, "Power combining in an array of microwave power rectifiers," *Microwave Theory and Techniques, IEEE Transactions on*, vol. 27, pp. 958 – 968, dec 1979. 126

[87] W. Brown, "The history of power transmission by radio waves," *Microwave Theory and Tech., IEEE Trans. on*, vol. 32, pp. 1230 – 1242, sep 1984. 126

[88] J. Hagerty, *Nonlinear Circuits and Antennas for Microwave Energy Conversio.* PhD thesis, University of Colorado at Boulder, Boulder, CO, 2003. 127

[89] J. Hagerty et. al., "Recycling ambient microwave energy with broad-band rectenna arrays," *Microwave Theory and Tech., IEEE Trans. on*, vol. 52, pp. 1014 – 1024, march 2004. 127

[90] X. Zhang et. al., "Analysis of power recycling techniques for rf and microwave outphasing power amplifiers," *Circuits and Systems II: Analog and Digital Signal Processing, IEEE Trans. on*, vol. 49, pp. 312 – 320, may 2002. 127

[91] S. Djukic et. al., "A planar 4.5-ghz dc-dc power converter," *Microwave Theory and Tech., IEEE Trans. on*, vol. 47, pp. 1457 –1460, aug 1999. 127

[92] S. Imai et. al., "Efficiency and harmonics generation in microwave to dc conversion circuits of half-wave and full-wave rectifier types," in *2011 IEEE MTT-S International*, pp. 15 –18, may 2011. 127

[93] H. Takhedmit et. al., "A 2.45-ghz low cost and efficient rectenna," in *Antennas and Propagation (EuCAP), 2010 Proceedings of the Fourth European Conference on*, pp. 1 –5, april 2010. 127

[94] W. Chen, K.-Y. Wong, W. Huang, and K. J. Chen, "High-performance algan/gan lateral field-effect rectifiers compatible with high electron mobility transistors," *Applied Physics Letters*, vol. 92, pp. 253501 –253501–3, jun 2008. 127

[95] Skyworks, "SMS7630 series, Mixer and Detector Schottky Diodes." online, accessed 2/21/09, January 2010. http://www.skyworksinc.com/uploads/documents/200041U.pdf. 131

[96] E. Falkenstein, M. Roberg, and Z. Popović, "Low-power wireless power delivery," *Microwave Theory and Techniques, IEEE Transactions on*, 2012. Accepted. Available upon request. 152, 188

[97] Z. Zivkovic and A. Markovic, "Increasing the efficiency of the high-power triode hf amplifier -why not with the second harmonic?," *Broadcasting, IEEE Transactions on*, vol. BC-32, pp. 5 –10, march 1986. 154

[98] Z. Zivkovic-Dzunja and A. Markovic, "Plate and grid modulated hf high-power tuned amplifier with increased efficiency," *Broadcasting, IEEE Transactions on*, vol. 35, pp. 97 –107, Mar. 1989. 154

[99] A. Juhas, L. Novak, and S. Kostic, "Signals with flattened extrema in balance power analysis of hfhpta: theory and applications," *Broadcasting, IEEE Transactions on*, vol. 47, pp. 38 –45, Mar. 2001. 154

[100] S. Nishiki and T. Nojima, "Harmonic reaction amplifier - a novel high-efficiency and high-power microwave amplifier," in *Microwave Symposium Digest, 1987 IEEE MTT-S International*, vol. 2, pp. 963 –966, june 1987. 154

[101] H. Matsubara, F. Kawanabe, and T. Nojima, "A 2-ghz band experiment on efficiency enhancement of a gan power amplifier using 2nd harmonic injection," in *Microwave Conf., APMC. Asia-Pacific*, pp. 1 –4, dec 2008. 154

[102] D. Williams et al., "High efficiency harmonic injection power amplifier," December 1991. 154

[103] A. AlMuhaisen, P. Wright, J. Lees, P. Tasker, S. Cripps, and J. Benedikt, "Novel wide band high-efficiency active harmonic injection power amplifier concept," in *Microwave Symposium Digest (MTT), 2010 IEEE MTT-S International*, pp. 1 –1, May 2010. 154, 175

[104] H. R. Bae, C. S. Cho, and J. W. Lee, "Efficiency enhanced class-e power amplifier using the second harmonic injection at the feedback loop," in *Microwave Conference (EuMC), 2010 European*, pp. 1042 –1045, sept 2010. 154

[105] Z. Popović and E. F. Kuester, *Principles of RF and Microwave Measurements*, p. 29. Boulder, CO: Course Notes, 2009. 155

[106] J. Hoversten, S. Schafer, M. Roberg, M. Norris, M. D., and Z. Popović, "Co-design of pa, supply and signal processing for linear supply-modulated rf transmitters," *Microwave Theory and Techniques, IEEE Transactions on*, 2012. Accepted. Available upon request. 192